Experimental characterisation and numerical modelling of the assembly of welded thermoplastic composite structures' behaviour from quasi-static to dynamic

Pauline Bourda

COLLEGE SCIENCES
DOCTORAL DE L'INGENIERIE
PAYS DE LA LOIRE ET DES SYSTEMES

CENTRALE NANTES

MÉMOIRE DE DOCTORAT DE

L'ÉCOLE CENTRALE DE NANTES

ÉCOLE DOCTORALE N° 602
Sciences de l'ingénierie et des systèmes
Spécialité : *Génie mécanique*

Par
Pauline BOURDA

Experimental characterisation and numerical modelling of the assembly of welded thermoplastic composite structures' behaviour from quasi-static to dynamic

Projet de recherche doctoral présenté et soutenu à Nantes, le 11 mai 2023
Unité de recherche : UMR 6183, Institut de Recherche en Génie Civil et Mécanique (GeM)

Rapporteurs avant soutenance :

Federica DAGHIA	Maître de conférence HDR, École Normale Supérieure Paris-Saclay, Gif-sur-Yvette
Franck LAURO	Professeur des Universités, Université Polytechnique Hauts-de-France, Valenciennes

Composition du Jury :

Présidente :	Xiaojing GONG	Professeure des Universités, Université Toulouse III - Paul Sabatier, Tarbes
Examinateurs :	Federica DAGHIA	Maître de conférence HDR, École Normale Supérieure Paris-Saclay, Gif-sur-Yvette
	Franck LAURO	Professeur des Universités, Université Polytechnique Hauts-de-France, Valenciennes
Dir. de recherches doctorales :	Patrick ROZYCKI	Professeur des Universités, École Centrale de Nantes
Co-enc. de recherches doctorales :	Mamadou Abdoul MBACKÉ	Ingénieur de recherche, IRT Jules Verne, Bouguenais

REMERCIEMENTS

La thèse n'est pas un long fleuve tranquille ; néanmoins, le chemin est plus agréable lorsque l'on est bien accompagné.

Je remercie fortement Federica Daghia et Franck Lauro d'avoir accepté de rapporter ce mémoire. Vos commentaires et questions ont été des éléments importants afin d'améliorer la prise en recul quant à mes travaux. Je tiens également à remercier Xiaojing Gong pour avoir présidé le jury. Enfin, merci à vous trois pour la richesse des échanges lors de la soutenance de thèse.

Patrick et Mamadou, je tiens à vous remercier de m'avoir fait confiance pour réaliser ces travaux de recherches à vos côtés. Vous avez su m'accompagner pour faire mes premiers pas dans la recherche et à prendre en main des éléments complexes qui m'étaient encore obscurs au début de ma thèse, notamment sur la partie numérique. Je vous remercie par ailleurs de m'avoir guidé tout en me laissant une certaine autonomie. Je souhaite enfin souligner que vos qualités humaines font de vous des collègues d'exception.

J'adresse aussi toute ma reconnaissance aux membres de mon comité de suivi de thèse, Steven Marguet et Hervé Le Sourne. Que ce soit en présentiel ou à distance, merci pour les échanges que l'on a pu avoir ainsi que pour vos conseils.

J'adresse un grand merci à Valérie Donal et Stéphanie Colliou qui m'ont aussi fait confiance pour rejoindre l'IRT Jules Verne en tant que doctorante. Merci également à Nathalie pour la partie administrative, aux collègues de l'équipe Modélisation et Simulation : Tuan Linh, Simon, Yves, Yvan, Rachid, Nihad, ainsi qu'aux autres doctorants PERFORM.

Je tiens à remercier Cynthia, Cannelle, Marine, Émilie et Éric pour la gestion administrative et informatique tout au long de ma thèse de doctorat. Je souhaite aussi remercier plusieurs collègues permanents du GeM pour leur accueil, leur aide et leur bienveillance : Pascal, Laurent G., Rian, Julien, Alexis, Grégory, Laurent S., Thomas. Je remercie grandement Jean-Michel pour sa disponibilité pour l'utilisation des différents équipements de la Hall composite et sa façon de relativiser les choses qui m'ont grandement aidées à avancer. Je tiens à remercier ceux qui m'ont aidé pour la réalisation des essais : Pierrick et Franck. Un grand merci également à Yannick Benoît pour la prise d'images au MEB.

Je remercie également les enseignants de l'option MATEPRO qui m'ont transmis cette volonté de poursuivre mes études d'ingénieur par une thèse : Sébastien, Bertrand, Erwan, Michel, Christophe et Adrien. Merci pour la qualité de vos cours, votre dynamisme et votre persévérance dans la promotion du doctorat à vos étudiants.

Il est maintenant temps de remercier ceux sans qui cette thèse aurait été un peu plus terne, mes merveilleux collègues, doctorants et docteurs, qui sont devenus au fil du temps des amis. Tout d'abord les anciens qui ont quitté le laboratoire : Elie, Raphaël, Audrey, Soukaïna, Adrien, Ivanna, Shaoqi. Vous êtes devenus des exemples pour moi, à la fois pour la qualité de vos travaux, mais aussi pour vos qualités hu-

maines. Une mention spéciale pour Vasu : "World best *office mate*". Je ne saurais suffisamment te remercier pour toutes les discussions qu'on a pu avoir pendant ces trois ans et demi, quelles soient scientifiques ou non, et toute l'aide que tu m'as apportée. Un grand merci à ceux arrivés en cours de route : Ghita, Raphael, Saba, Annie, Nour, Noémie, Lucie, Mathis, Hugo, Hadi, Lara, merci pour tous ces repas et discussions partagées et bon courage pour la suite ! Je remercie également mes amis pour leurs encouragements tout le long de ces trois ans de travail.

Ce travail n'aurait pas été possible sans le support de mes proches : Mireille, Clara, Morgan, Jérémy, Quentin, Martin, Yves, Valérie. Je vous remercie tous pour vos encouragements et votre présence qui m'ont permis de mener à bien ce travail, et ce, malgré les difficultés de la vie rencontrées pendant ces trois ans. Une de mes pensées s'adresse à Jean-Pierre, qui a su m'accueillir chaleureusement parmi les siens tout en m'aidant à me dépasser, ce dont je lui suis reconnaissante. Enfin, je dédie ce travail à mes parents, Marie-France et Bernard, que je remercie de tout mon cœur pour leur soutien sans faille depuis toujours. Je vous remercie de toujours être là pour m'épauler et de m'avoir accompagné tout au long de ces travaux.

Ce travail a pu aboutir également grâce à Thomas, mon compagnon, que je remercie pour sa résilience, ses encouragements et son support quotidien qui m'ont aidé à traverser ces trois années et à me redonner confiance dans les moments de doute.

TABLE OF CONTENTS

NOTATIONS

Abbreviations

Composites

TS	Thermoset	
TP	Thermoplastic	
PA	Polyamide	
PA6	Polyamide 6	
PA66	Polyamide 66	
PPS	Polyphenylene Sulphide	
PEEK	Polyethertherketone	
CF	Carbon fibre	
GF	Glass fibre	
UD	Unidirectional	
GF/PA66	Glass fibre 2×2 twill woven reinforced polyamide 66	
RVE	Relative volume elementary	

Environmental conditions

RH	Relative humidity	%
T_g	Glass transition temperature	°C
T	Testing temperature	°C

Mechanical testing

DCB	Double Cantilever Beam
ENF	End Notch Flexure
SLJ	Single lap joint
SLS	Single lap shear
DLJ	Double lap joint
DLS	Double lap shear
LSS	Lap shear strength
Mode I	Normal opening mode
Mode II	Sliding shear mode
Mode II	Scissoring shear mode
F-U curve	Load-displacement curve
DIC	Digital image correlation

Composite welding

HAZ	Heat affected zone
EDs	Energy directors
S_{welded}	Welded joint cohesive fracture area
US welding	Ultrasonic welding
Cohesive/FMD	Combination of cohesive fracture and fibre/matrix debonding

Numerical

FE	Finite Elements
TSL	Traction-separation law
VUMAT	User-defined mechanical material behaviour for Abaqus/Explicit

Symbols for mechanical characterisation and modelling

Geometry and testing

l	Specimen width	m
L_0	Initial gauge length	m
L	Current gauge length	m
ΔL	Elongation	m
S_0	Initial specimen section	m^2
S	Current specimen section	m^2
F	Load	N

Behaviour and constitutive model

ψ	Helmholtz free energy	J
ε	Strain	(-)
σ	Stress	Pa
ρ	Density	$\mathrm{kg\,m^{-3}}$
E	Young's modulus	Pa
G	Shear Modulus	Pa
ν	Poisson's ratio	(-)
$\underline{\underline{\mathrm{C}}}$	Stiffness matrix	
p	Accumulated plastic strain	(-)
f_p	Plastic yield surface function	Pa
β and m	Hardening law parameters	Pa and (-)
R	Isotropic hardening stress	Pa
σ^0	Yield stress	Pa
Y	Thermodynamic dual to damage variable	Pa
$\overline{Y}$	Upper bound of the released energy rate	Pa
ν^*	Contraction coefficient	(-)
d	Damage variable	(-)
Y_{12}^M	Released energy rate at transition between logarithmic and linear evolution of damage	Pa
d_{12}^M	Damage transition value between logarithmic and linear evolution	(-)
α_1, α_2	Longitudinal and transverse damage evolution parameters	$\mathrm{Pa}^{-1/2}$
α_{12}^1	Shear damage evolution parameters for the logarithmic evolution	$\sqrt{\mathrm{Pa}}$
α_{12}^2	Damage evolution parameters for the linear evolution for shear behaviour	$\mathrm{Pa}^{-1/2}$
σ^R	Fracture stress	Pa
$\underline{\underline{Q}}_2^+$	Transition matrix	
$F_X^{1/2/3}$	Viscous function parameters for the property 'X'	(-)
$\dot{\varepsilon}$	Strain rate	s^{-1}
$\dot{\varepsilon}_p$	Plastic strain rate	s^{-1}
$\dot{\lambda}$	Plasticity multiplier	(-)
$\dot{\varepsilon}^{norm}$	Normalised strain rate	(-)

Cohesive elements

δ_j	Displacement jump / separation in mode j	m
σ_j	Traction in mode j	Pa
K_j	Traction-separation law stiffness in pure mode 'j'	$\mathrm{Pa\,m^{-1}}$

σ_j^0	Damage initiation stress in pure mode j	Pa
δ^0	Separation at damage initiation	m
δ^f	Separation at fracture	m
δ_s	Shear separation	m
δ_m	Effective separation	m
δ^{max}	Maximum separation reached during loading	m
β	Mixed mode ratio	(-)
G_{jc}	Fracture toughness in mode j	$\mathrm{J\,m^{-2}}$
G_c	Fracture toughness for mixed mode	$\mathrm{J\,m^{-2}}$
η	BK criterion power	(-)
$\delta_{j,m}^0$	Mode j separation at damage initiation for mixed-mode loading	m
$\delta_{j,m}^f$	Mode j separation at fracture for mixed-mode loading	m
e	Thickness of the cohesive element	m
D	Damaged stiffness matrix	Pa
f	Viscous function	(-)

Reference systems, indices and exponents

Reference system

$\{x, y, z\}$	Global frame of the tensile test
$\{1, 2, 3\}$	Local frame of a ply

Indices

xx	Longitudinal direction (parallel to the load)
yy	Transverse direction (perpendicular to the load)
11	Warp direction
22	Weft direction
33	Out-of-plane/through-thickness direction
12	Shear direction in plane (1,2)
13	Shear direction in plane (1,3)
23	Shear direction in plane (2,3)
j	Value of the loading mode considered

Exponents

eng	Engineering value
true	True value
0	Value at damage initiation / the end of the elastic domain
i	Value for the cycle or the increment i
QS	Value for quasi-static loading
e	Elastic part of a quantity
p	Plastic part of a quantity
R	Quantity at fracture
max	Maximum of the quantity

INTRODUCTION

The transport industry is a sector that is constantly evolving to adapt to economic and environmental conditions, whether in the aviation, automotive or maritime sectors. New regulations insist on reducing the fuel consumption of transport vehicles for environmental reasons. This can be achieved by improving engine efficiency and limiting structural weight. Therefore, the appeal to composite materials has been growing over the years in these sectors. This attractiveness is justified by the high performances and low densities of the organic-based composites reinforced by carbon or glass fibre. Thermoset composites have been the preferred materials these last decades to lighten structural parts in aeronautics and semi-structural parts in the automotive sector. However, these composites may present drawbacks with long manufacturing processes requiring the matrix curing in an autoclave for several hours. In addition, the storage requirements (expiration date, controlled storage temperature) and high costs of thermoset matrices are key elements leading to the study of thermoplastic composites, which are more flexible in these respects. Consequently, interest in thermoplastic composites has grown over the last years for their high performances under impact loadings, faster manufacturing processes out of the autoclave and potential recyclability enabled by the matrix's melting or softening ability. The development of bio-based thermoplastic matrices also reinforced this appeal.

Expansion of the study of thermoplastic composites has led to the investigation of composite welding, a joining process adapted to these materials and limiting the increase in structures' weight as opposed to bolted joints, for example. Joining substructures is an essential aspect of the structures' design because the joint may be a significantly weak zone in the event of inadequate joining technology. Classical joining methods (riveting, bolted joints, adhesives, etc.) may present drawbacks when applied to thermoplastic composites because of stress concentration, increased delamination risk due to hole drilling, extensive surface preparation or long resin curing durations. Welding is presented as a fast joining process for thermoplastic composites (durations in the order of a second), adapted for simple geometries and creating continuity between both joined parts. However, despite the extensive literature about the improvement and control of welding processes, investigating the weld's mechanical behaviour is still limited, especially for dynamic loadings or variations in environmental conditions. On that first point, several thermoplastic matrices are strain rate sensitive, and structures in the transport industry can suffer dynamic loadings in-service. On the second point, temperature and humidity can significantly influence the thermoplastic matrices' behaviour for quasi-static and dynamic loadings. Thereby, a significant influence of these parameters on a weld's behaviour can be reasonably supposed. In that respect, knowledge about the dynamic behaviour of thermoplastic composite welded joints is needed for several environmental conditions to be applied to structural parts. In addition, modelling the weld's behaviour under these conditions and loadings improves the design of structures using simulations.

This thesis is a collaboration between the institut de Recherche en Génie civil et Mécanique (GeM) and Institut de Recherche Technologique Jules Verne (IRT Jules Verne) with funding from the PERFORM thesis program of IRT Jules Verne. Identification and modelling of the strain rate and temperature influences on a welded composite's behaviour are the two main scientific challenges that initially led to this thesis. The final application of these research works was modelling an impact test - such as a bird strike test - on a welded aeronautical structure (skin/stringer structure, for example). However, the lack of initial data

about the quasi-static behaviour of welds (for the composite considered) and the composite's dynamic behaviour induced a reconsideration of the works' aims to be able to perform both characterisation and modelling of the weld's behaviour. Therefore, the composite studied was fixed to a glass fabric-reinforced polyamide 66, for which quasi-static and dynamic behaviours are known and modelled. Furthermore, the objectives were limited to investigating the strain rate influence on composite weld's behaviour and its modelling at room temperature. As far as the author is aware, no study has addressed this issue in the literature so far. The aims of this thesis contribute to the field with the dynamic testing of welded composites and the inclusion of strain rate dependence in the weld's constitutive model.

Modelling welded joints' behaviour over a wide range of strain rates requires experimental results constituting a reference to define a model and identify its parameters. For this reason, the characterisation of welded thermoplastic composite specimens is proposed for several loading speeds, ranging from quasi-static to moderate values using lap joint samples. These experiments provide the welded composite's behaviour from quasi-static to dynamic and highlight the strain rate effect on welded composites. However, they do not allow the direct identification of the weld's behaviour. Subsequently, the numerical modelling of the weld is conducted using cohesive zone model, and the model's parameters are determined by inverse analysis. This method can be applied based on experimental knowledge of the welded composite behaviour and accurate modelling of the unwelded composite's behaviour under quasi-static and dynamic conditions. The final step is to include the strain rate dependence in the weld's constitutive model and validate the numerical simulations.

The manuscript is structured into four chapters to study experimentally the behaviour of welded thermoplastic joints and model it from quasi-static to dynamic loadings.

Chapter 1 draws a literature review about thermoplastic composites, welding and strain rate influences on composites and their interfaces. The chapter is divided into four sections: strain rate sensitivity of thermoplastic composites, development of ultrasonic welding for composites, characterisation of interface behaviour for high loading speeds and the modelling of composite and interface behaviours from quasi-static to dynamic. The first section introduces the behaviour of composites, and the influence of strain rate on their behaviour, focusing on polyamide-based and fabric-reinforced composites. The second part on ultrasonic welding presents a review of the process and its control. There is also a focus on the mechanical behaviour of welds, which has been an area of development over the last decade. However, research still needs to be done about these joints with loading rate influence investigation for crashworthiness applications. The review of strain rate sensitivity of composite interfaces focuses on adhesive and delamination, as they are both close to welded joints. The testing methodologies used and the strain rate influences observed are presented. Finally, the modelling strategies employed to describe the dynamic behaviour of composites and joints are developed in the last section. This review aims to introduce the different elements studied and used in this work. It also highlights the missing parts in the literature that led to this work.

Chapter 2 presents the knowledge acquired during the COPERSIM-Crash project (project of IRT JV) about the composite used in this work: Polyamide 66 reinforced by 2×2 glass-fibre twill weave. The investigation of strain rate, temperature and humidity influences on the laminate behaviour was used as a foundation to study the behaviour of these composite welded joints, experimentally and numerically. Moreover, the constitutive model developed and implemented in Abaqus with a user subroutine VUMAT is used for the laminate modelling in the welded specimen's model (Mbacké & Rozycki, 2018). Due to the material storage in an uncontrolled environment, and so submitted to cycles of temperature and humidity (potential chemical ageing), some tensile tests were conducted to validate the laminate behaviour determined previously. This investigation permits securing the knowledge about the substrates of the

welded structures and thus getting an adequate understanding of their behaviour. It is also essential to thoroughly model and control the behaviour of the substrates to properly model the welded specimens.

Chapter 3 is dedicated to the experimental characterisation of the welded composite behaviour over a large range of loading speeds. The substrate behaviour is well-known for this study, and the measurements of quantities in the welded joint are highly complicated experimentally. Therefore, the choice was made to work on the welded structure behaviour, and use an inverse method to determine the weld's behaviour from the results obtained on structures. The experimental characterisation required the definition of suitable processing parameters of the ultrasonic welding process chosen for this study. A short experimental study for several levels of welding energy permits fixing the processing parameters and welding the specimens for experimental characterisation. The weld performance in shear is studied from quasi-static $(1.2\,\mathrm{mm\,s^{-1}})$ to dynamic loadings $(7\,\mathrm{m\,s^{-1}})$ using lap shear tests. These results constitute a first step in the study of welded composites dynamic behaviour and make it possible to analyse the evolution of the structure's behaviour and performance as a function of the loading speed (Bourda et al., 2023). A fractography analysis is also conducted to understand the fracture mechanisms occurring in a welded joint. Finally, this experimental characterisation provides information to define a constitutive model for the welded interface: inputs and reference tests for the model validation.

Chapter 4 introduces the modelling strategy used for the welded specimens and presents its application. The welded interface is modelled by cohesive elements, as the fracture path is known to propagate through the weld. Their constitutive model is defined using a bilinear traction-separation law with strain rate dependence of the parameters (viscous functions). The constitutive law parameters are identified by an inverse method on quasi-static tests, using the experimental results as a reference. Then, simulations are performed for dynamic loadings to validate the parameters; in case of a significant relative error between experiments and numerical results, the parameters are re-identified for the loading speed considered. Afterwards, the viscous functions describing the parameters' evolution with strain rate are identified from the numerical results. Finally, the strain rate dependent behaviour defined for the weld is validated.

This manuscript concludes with a synthesis of the primary outcomes of these research investigations on the dynamic behaviour of a welded composite. These conclusions are put into perspective with essential studies to improve and extend the knowledge of thermoplastic composite welds' behaviour.

Chapter 1

Literature review

Abstract: *These research works study the welded composites' behaviour from quasi-static to dynamic loadings. These structures are composed of substrates (composite laminates) and a matrix-rich zone, constituting the weld, which may be strain rate dependent due to the viscous behaviour of the polyamide matrix studied in this work. The potential strain rate sensitivity leads to a review of composites' and matrices' behaviour from quasi-static to high strain rates. The first section of the literature review highlights the significant influence of strain rate on laminate among temperature and moisture dependencies. The second section presents the joining methods used in the industry for composites. In more detail, the welding technologies are presented to have an overview of the process, its control and the current knowledge on the welds' behaviour, which lack results on their dynamic behaviour. Consequently, experimental testing was required in this work to obtain results on the behaviour of welded structures for a wide range of dynamic loadings. Therefore, the methods for composite interface testing for quasi-static and dynamic loadings have been reviewed in the third section to define the methodology used in this work. Finally, numerical elements are presented in the fourth section knowing the observed behaviours of substrates and joined structures. The strain rate influence inclusion in the constitutive models of composites and interfaces is presented. Finally, the research interests are presented in light of the literature review.*

Contents

Introduction

This work aims to investigate the behaviour of **T**hermo**P**lastic (TP) composite welded joints from quasi-static to dynamic loadings and to model the joint's behaviour on this loading range. Due to the difficulties of experimentally measuring quantities in the welded joint, the choice was made to work with a global structure on which it is easier to make measurements. This choice was also based on the extensive knowledge acquired on the laminate for quasi-static and dynamic loadings and from experimental and numerical points of view (Mbacké & Rozycki, 2018; Dau, 2019; Rozycki et al., 2019). If required, an inverse method can be implemented to identify the welded joint behaviour from the global structure and laminate behaviours.

The first section of the literature review highlights the experimental knowledge about polymer composite behaviour from quasi-static to dynamic loadings. The mechanisms observed in quasi-static are introduced. Then, the strain rate influence on the matrix and reinforcement is presented together with its effect on the laminate. A focus is made on the woven composites to be as close as possible to the material studied in this work. The joining methods are presented in the second section with a short introduction to classical joining technologies, followed by a presentation of the **U**ltra**S**onic (US) welding process. The performance of welded interface is reviewed for the several loading conditions already investigated (quasi-static, temperature, moisture). However, the author found no study on the loading speed influence on welded joints. Therefore, a database must be constituted with experimental results on welded specimens for quasi-static and dynamic tests to be able to model the welded joint behaviour. As a consequence, a review was done on the testing strategies used to characterise composite interfaces for modelling objectives; the specimen and testing rigs used are presented in the third section. Finally, the modelling of composites and interfaces is presented for structures' crashworthiness. Models were developed to describe the strain rate influence on composites, bonded interfaces and delamination, and they will be used in this work.

Terminology

Two terms are used in this manuscript to investigate the materials' time dependence: strain rate and loading speed. In general, the strain rate is used to define the time dependence of a material, and the loading speed is more frequently used to refer to a testing machine parameter. Taking two materials loaded at the same loading speed will result in different strain rate levels in the specimen because of their distinct behaviours. Strain rate is the intrinsic quantity to compare quasi-static and dynamic behaviours. However, measurement of strain rate for joints (welds, adhesive, delamination) is complicated experimentally, so most investigations are done analysing behaviours with respect to the loading speed instead of strain rate. This expression of "loading speed" will be used in this work because the investigation focuses on only one material; hence, if the loading speed increases, the strain rate is also supposed to increase. Finally, strain rates may be studied during the numerical investigations on the welded joint.

1.1 Behaviour of polymer composites and influence of strain rate

Structures in automotive and aeronautic areas must resist static and dynamic loadings in service. It is essential to characterise materials and their assemblies at different strain rates to determine whether and to what extent this affects their behaviour. These elements can then be used to validate the behaviour of structures submitted to tool drops or impact loadings. The present section introduces polymer composites and primarily the material under study. Then behaviours of the composites are presented from quasi-static to high strain rates. More details are given for woven thermoplastic composites as polyamide 66/glass fibre 2×2 twill woven is studied in this work. This part of the literature review stays limited as the principal element of these research works is investigations on welded joints.

1.1.1 Introduction on the polymer composites behaviour

Polymer composites are materials widely used in the energy and transport industry: automotive, aeronautical, space or wind turbine. These materials consist of at least two components: a matrix and a reinforcement. The addition of fibre reinforcement improves the mechanical properties of the pure matrix. The matrix transfers the load to the fibres and ensures that the reinforcement is held in position.

Two families of organic matrices exist for composites:

— **T**hermo**S**et (TS) matrix such as epoxy: They have strong energy bonds between molecules resulting from the curing process. The cross-link obtained makes the material infusible and insoluble. These matrices are well-suited for high temperatures applications. TS composites were mainly studied and used these past decades for their high performances. However, the manufacturing costs and durations are relatively high compared to the processes used for TP composite forming.

— **T**hermo**P**lastic (TP) matrix such as **P**oly**A**mides (PA) or **P**oly**P**henylene **S**ulphide (PPS): These matrices are characterised by lower energy bonds between molecules. These matrices can be melted/soften (for crystalline/amorphous phases, respectively) after the structure shaping for repair, reuse or recycling. In addition, they are good impact absorbers and they have good chemical, thermal and electrical resistance (Reis et al., 2020; Hsissou et al., 2021).

The high toughness of TP resins and composites (Figure 1.1) is an advantage to increase the bearing strength of structures and reduce the extent of delamination for low velocities impacts (Vieille et al., 2012; Vieille et al., 2013). However, their notched behaviour may deteriorate under severe conditions due to mechanical properties degradation.

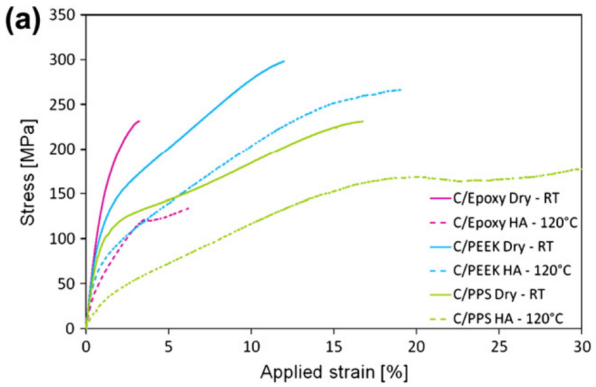

Figure 1.1 – Tensile behaviour of $[45]_7$ TP and TS laminates - RT 'room temperature', Dry 'RH 0 %' and HA 'Hygrothermal ageing' (Vieille et al., 2012)

TP resins are semi-crystalline structures. The ratio of amorphous and crystalline zones depends on the material, the cooling rate and the fibre quantity (Frihi et al., 2016). Fast cooling during manufacturing can lead to mostly amorphous material, while a slow cooling rate gives time for the macromolecules to organise. The crystallinity ratio affects the mechanical properties of TP resins, as observed by Felder et al. (2020) on PA6 resin. An increase in elasticity modulus, hardening, yield stress and relaxation time was

observed for a larger crystalline ratio.

Multiple reinforcements exist to meet the industry's needs. Concerning the material used, synthetic **G**lass and **C**arbon **F**ibres (GF and CF) are used for the majority of composites because of their high tensile and compressive strength in association with polymers (Hsissou et al., 2021). Their high tensile performances and low sensitivity to temperature and moisture are valuable qualities for automotive and aeronautic applications. Nowadays, the use of vegetal fibres is studied to improve the material carbon footprint and reduce the density (Saheb & Jog, 1999). Unlike synthetic fibres, these vegetal reinforcements are highly sensitive the environmental conditions and can have a significant range of mechanical behaviour depending on the fibre quality. Although, high performances have been shown with a suitable choice for weave (Aisyah et al., 2021). Long fibre reinforcements are mainly used for structural parts as **U**ni-**D**irectional (UD), cross-ply or woven. The fabric weave choice drives the final stiffness of the reinforcement and the composite. Figure 1.2 shows three fabrics from the most to the less stiff. Woven reinforcement can be quasi-equilibrated to have similar longitudinal and transverse behaviours [1].

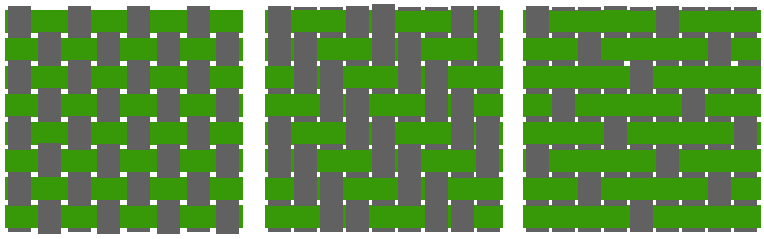

a) taffeta b) 2x2 twill woven c) 5-harness satin fabric

Figure 1.2 – Example of woven reinforcements

A four-ply laminate PA66 reinforced by 2×2 glass fibre twill woven composite (GF/PA66) is studied in this work. In the end, this material was chosen for the strong knowledge of its behaviour from quasi-static to dynamic loadings. The COPERSIM-Crash project, conducted by IRT Jules Verne, GeM and other partners, investigated the characterisation and modelling of this composite behaviour for crash applications at several temperatures and **R**elative **H**umidity (RH) conditions (Mbacké & Rozycki, 2018; Dau, 2019; Rozycki et al., 2019). Therefore, this thesis work used the experimental and numerical results on the laminate as a solid foundation to study the welded joints' behaviour. Concerning the technical aspects of the laminate, the volumetric fibre fraction is $50\,\%$ and $70\,\%$ in weight. COPERSIM-Crash project highlighted GF/PA66 and PA66's significant sensitivity to temperature, RH and strain rate. The behaviour of this composite material will be described in the following sections under quasi-static and dynamic conditions.

1.1.2 Quasi-static behaviour of woven polymer composites

The warp and weft directions behaviours are generally elastic-fragile-damage because fibres drive the composite behaviour for these orientations (Figure 1.3). The off-axis behaviours are mainly dominated by the matrix behaviour; thus, larger strains are reached (Figure 1.4). This ductility of the off-axis directions and elastic-fragility of in-axis orientations is observed for several composites: CF/epoxy, CF/PPS, GF/PSS, CF/PEEK... (Vieille et al., 2012; Berthe, 2013; Pivdiablyk et al., 2020). Irreversible strains are significant for the off-axis directions. In addition, the woven faces fibre bundles re-orientation during tensile tests on $[\pm 45]_x$ specimens about 12 to $20\,\%$ for GF/PA6, for example (most of the time indirectly considered in shear behaviour modelling) (Pivdiablyk, 2019). Figure 1.4 shows that temperature and moisture significantly affect the GF/PA66 shear behaviour. This matrix can absorb a relatively high quantity of water compared to other TP matrices; moisture interacts with the material and affects its properties. First of all, the **G**lass transition **T**emperature (T_g) decreases for higher RH level: $+60\,°C$ in dry state and

1. The weaving method does not allow for equal fabric properties in the warp and weft directions. The warp yarns are fixed while the weft yarns are undulating between the warp yarns to form the weave pattern. Nevertheless, the properties can be considered quasi-equal in some cases.

+23 °C at RH 50 % for PA66/GF (Dau, 2019). The behaviour is more ductile for high moisture uptakes. Similar observations are made with temperature; indeed, the composite shear behaviour is more and more ductile with the increase in temperature. As the temperature approaches the T_g, the mechanical properties drop drastically. Similar behaviours are observed for other TP composites such as GF/PPS (Pivdiablyk et al., 2020).

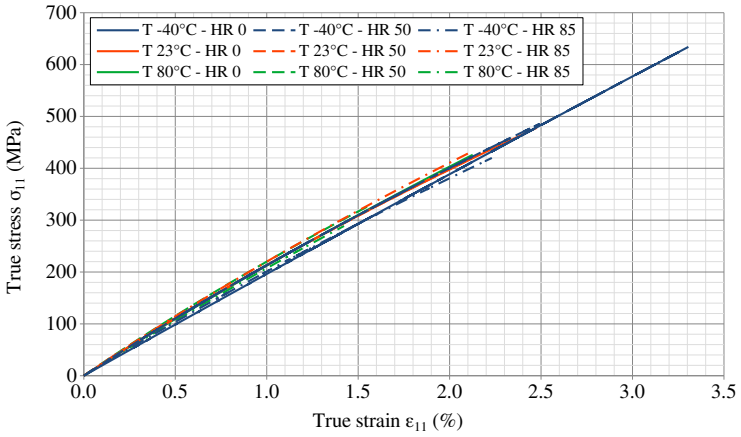

Figure 1.3 – GF/PA66 longitudinal behaviour for several temperature/RH couples (Rozycki et al., 2019)

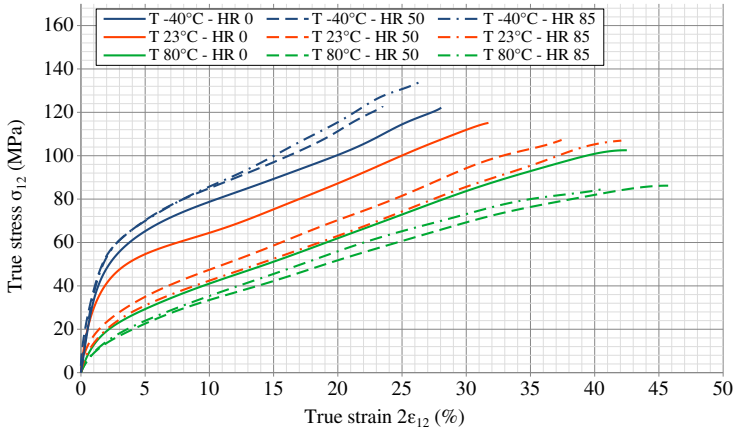

Figure 1.4 – GF/PA66 shear behaviour for several temperature/RH couples (Rozycki et al., 2019)

In addition to these effects, damage propagates in the composite until fracture. All these elements lead to the complex behaviour observed in Figure 1.5.

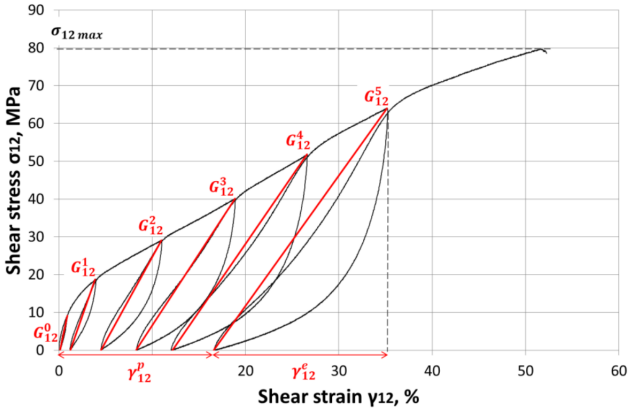

Figure 1.5 – Cycled tensile test on a TP woven composite (Pivdiablyk, 2019)

Mechanical properties can be evaluated from these tensile tests, such as elasticity modulus, yield stress, fracture stress and damage evolution. Damage can be considered in any direction of the laminate to model different degradations evolving in the material: matrix cracking, fibre matrix debonding, and fibre fracture. Damage mechanism is highlighted by several authors with the use of cycled tensile tests for the off-axis directions and evaluating the intersecting modulus for longitudinal/transverse behaviours (Ladeveze & LeDantec, 1992; Coussa, Renard, Joannes, et al., 2017; Pivdiablyk et al., 2020). The evolution

of the loading-unloading loops or current vs initial modulus allows the calculation of a damage variable d for each cycle i (Equation 1.1 and Equation 1.2).

$$d^i_{11/22} = 1 - \frac{E^i_{11/22}}{E^0_{11/22}} \tag{1.1}$$

$$d^i_{12} = 1 - \frac{G^i_{12}}{G^0_{12}} \tag{1.2}$$

1.1.3 Dynamic behaviour of woven polymer composites

The strain rate sensitivity of matrices and reinforcement is reviewed to identify their influence on the global behaviour of laminates. Then, the strain rate sensitivity of composites is presented.

Influence of strain rate on thermoplastics behaviour

Part of TP and TS resins are sensible to strain rate. This characteristic is widely studied in the literature due to the increasing use of these polymers as composites' matrices for automotive and aerospace structures. In the case of polyamides, PA6 and PA66, a strong strain rate influence is observed on the tensile behaviour at several RH levels and temperatures (Shan et al., 2007a; Dau, 2019; Felder et al., 2020). Strain rate positively influences the yield stress and tensile modulus of PA66 (Dau, 2019). Other authors reported only a strain rate dependence of the PA6 hardening (Shan et al., 2007a; Felder et al., 2020). Moreover, the fracture strain tends to decrease for higher strain rates. Beyond the evolution of the polymer's mechanical properties, a change in the behaviour is also observed with strain rate evolution depending on the moisture content. Figure 1.6 illustrates this phenomenon with a behaviour evolution from ductile to brittle in a dry state, while the behaviour stays ductile from $3.64 \times 10^{-3}\,\mathrm{s}^{-1}$ to $240\,\mathrm{s}^{-1}$ at RH $85\,\%$. According to the author, the ductile behaviour observed at the highest RH level is the consequence of the difference between the testing temperature T and the glass transition temperature T_g.

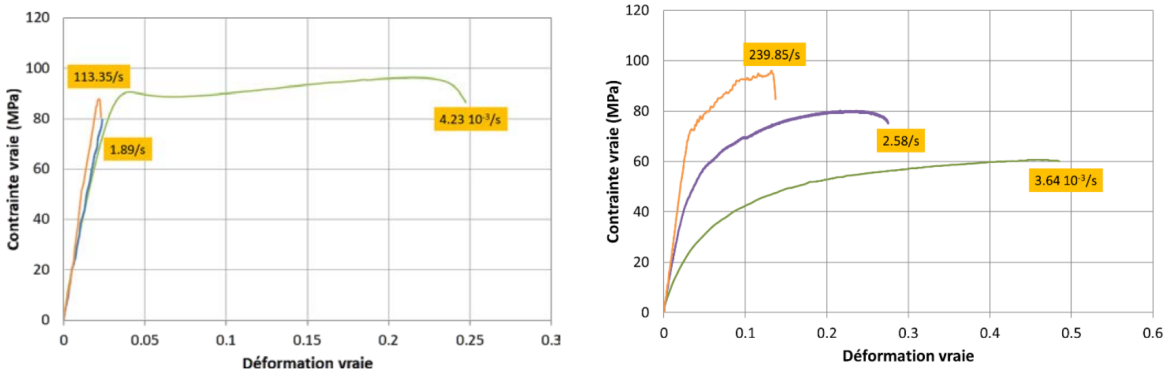

(a) 23 °C - RH 0% (b) 23 °C - RH 85%

Figure 1.6 – PA66 behaviour for several strain rates dans RH levels (Dau, 2019)

Poly**E**ther**E**ther**K**etone (PEEK) resin undergoes strain rate and temperature influences. Several authors investigated the tensile behaviour of this aeronautic matrix, and the results highlight an improvement of elastic modulus and yield stress with the increase of strain rate (Garcia-Gonzalez et al., 2015; Barba et al., 2020). Other authors only reported a strain rate influence on the yield stress with sometimes a change in behaviour from ductile to brittle (Béguelin et al., 1991; Abbasnezhad et al., 2018). Moreover, the strain rate influence depends on the testing temperature; a more significant increase in yield stress is observed at ambient temperatures ($20\,^{\circ}\mathrm{C}$), whereas the elastic modulus is more sensitive at high temperatures. A significant modification is observed between the quasi-static and dynamic tensile tests: it is the transition from isothermal to adiabatic tests (Cady et al., 2003; Barba et al., 2020). In

quasi-static, the heat generated by inelastic dissipation is removed from the material through conduction and convection. However, concerning dynamic loadings, the material temperature also increases during the test due to inelastic dissipation, but the test speed does not allow the heat to escape by conduction or convection. Hence, strain rate hardening and thermal softening compete within the polymer (Cady et al., 2003; Barba et al., 2020). This behaviour was modelled by Garcia-Gonzalez et al. (2015) using the Johnson-Cook model (parameters in Table 1.1).

A (MPa)	B (MPa)	n (-)	$\dot{\varepsilon}_0{}^{\mathrm{p}}$ (s^{-1})	C (-)	m (-)
132	10	1.2	0.001	0.034	0.7

Table 1.1 – Thermo-visco-plastic parameters for Johnson-Cook model describing PEEK plasticity (Garcia-Gonzalez et al., 2015)

Fabre et al. (2018) studied the equivalence of the strain rate, temperature and RH influence of the PA66 behaviour. The full description of the PA66 behaviour between the α-transition region and rubbery state cannot be done using only a temperature/humidity equivalence and requires the addition of time dependence.

Influence of strain rate on glass and carbon fibres

The majority of polymer composites are reinforced by glass or carbon fibres. These reinforcements have high tensile properties, and their behaviour is elastic-fragile. Carbon fibre tensile behaviour is reported as strain rate insensitive in most studies. For example, T700 fibres were studied by Zhou et al from $10^{-3}\,\mathrm{s}^{-1}$ to $10^{3}\,\mathrm{s}^{-1}$ and no sensitivity to the testing speed was reported (Figure 1.7a) (Zhou et al., 2010). Taniguchi et al. (2012) confirmed this result for T300 carbon fibres. However, the strain rate sensitivity is observed on glass fibres with an increasing fibre bundle strength (Figure 1.7b) (Yuanming et al., 1994; Z. Wang & Xia, 1998; Arao et al., 2012). In addition, an influence on the elastic modulus is noticed only in some studies (Z. Wang & Xia, 1998).

Figure 1.7 – Behaviour of fibres for several strain rates

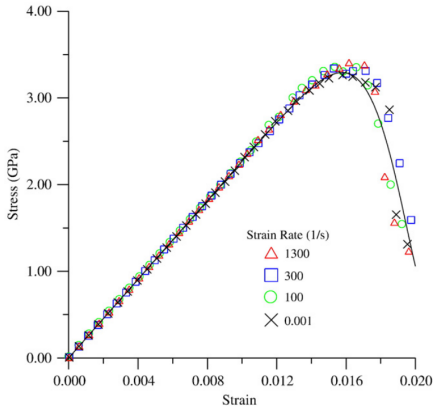

(a) Carbon fibres T700 (Zhou et al., 2010)

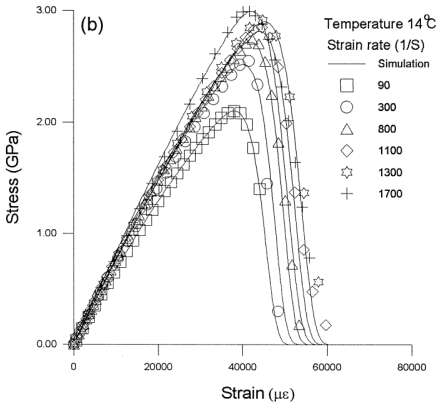

(b) E-glass fibres (Z. Wang & Xia, 1998)

Influence of strain rate on the behaviour of woven polymer composites

Strain rate influence on UD and woven TS composites was studied by several authors these last decades (Weeks & Sun, 1998; Rozycki, 2000; Kawai et al., 2001; Goldberg & Stouffer, 2002; Rozycki & Coutellier, 2002; Marguet, 2007; Berthe, 2013; Chen et al., 2018). Tensile tests conducted on several fibres orientation exposed an effect of the strain rate on longitudinal but also shear behaviour of E-GF/Epoxy UD composites (Rozycki & Coutellier, 2002). As expected from the separated behaviours of matrix and fibres, the longitudinal behaviour of woven or UD composites is almost strain rate insensitive, while the off-axis are significantly rate-sensitive (Dau, 2019), as the matrix mainly dominates their behaviour.

Several authors studied the strain rate influence on GF/PA66 woven composite, and results show a significant change in the material properties in shear. Coussa and Dau presented in separate studies the enhancement of shear modulus and fracture strength for higher strain rates (Figure 1.8) (Coussa, 2017; Coussa, Renard, Joannès, et al., 2017; Dau, 2019). In addition, the specific device developed by Coussa to perform cycled tensile tests at moderated strain rate (Coussa, Renard, Joannes, et al., 2017) shows that the damage initiation of GF/PA66 is strain rate dependent. However, the damage evolution and the inelastic strains are not influenced by the strain rate (Coussa, 2017).

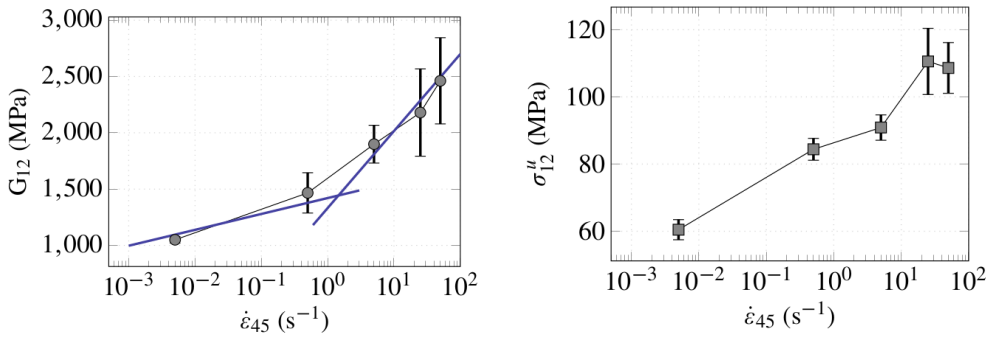

(a) Shear modulus (b) Fracture stress

Figure 1.8 – Evolution of PA66/woven GF properties with the increase of strain rate (Coussa, 2017)

In addition to the rate sensitivity of GF/PA66 woven composite, primarily in shear, the behaviour is also affected by moisture and temperature (Rozycki et al., 2018; Dau, 2019). As observed by Fabre et al. (2018) for neat PA66, temperature and RH have a softening influence on the GF/PA66 shear behaviour. As the moisture level affects the matrix T_g by reducing its value as the RH increases, a higher ductility is observed for "wet" conditions (Pivdiablyk, 2019).

1.1.4 Conclusions

The PhD subject is to study the behaviour of TP composite welded joints from quasi-static to dynamic loads and to propose, more specifically, a strain rate dependent model for the weld zone. As there are no studies on this topic in the literature review, we have chosen a two-step methodology: the first one will consist in performing experiments on welded composite laminates to identify the welded structure's behaviour. The second step is composed of numerical simulations of these experiments: assuming full knowledge of the substrates' behaviour, it is then possible to isolate the considered zone numerically and identify the parameters of a weld's model using comparisons to the experimental results. Therefore, the laminate's behaviour, which surrounds the welded joint, must be known and suitably modelled to be in a position to extract the weld's behaviour. This first section of the literature review shows that several studies investigated the behaviour in quasi-static and on a wide strain rate range. The in-plane tensile behaviour divides into two categories: elastic-fragile-damage behaviour for the longitudinal and transverse orientation; and an elastoplastic with damage behaviour in shear, inherited by the matrix ductility. Concerning the time dependency of these materials, and more precisely for the glass woven/PA66 studied in this work, the stiffness and strength of the shear behaviour increase with the strain rate while its influence on the in-axis behaviour is negligible. Finally, the polyamide matrix confers a dependence on temperature and moisture to polyamide-based composites. Therefore, special care should be taken before the mechanical investigation of the material to ensure the control of these two environmental conditions. The laminate behaviour time-dependence was studied during the COPERSIM-Crash project for several temperature and RH conditions (Mbacké & Rozycki, 2018; Dau, 2019; Rozycki et al., 2019) with some results presented in this section. These results constitute the basis of this work with valuable experimental and numerical results on the laminate behaviour, including strain rate influence; they will be

presented in more detail in Chapter 2.

1.2 TP composites joining: from classical methods to welding

TP composites have advanced mechanical performances adapted for the automotive and aeronautics industries. Their high impact resistance, high strength, low density and potential recyclability make them first choice materials (Reis et al., 2020). In addition to these characteristics, the ability of thermoplastic matrices to melt/soften enables the weldability of structures. This joining method is extensively studied for its speed of processes and the high strength of the welds. A short introduction to classical joining methods starts the section by presenting their advantages and drawbacks, which led to the development of welding processes for TP composites. The following sections present several welding methods used and studied for industrial applications. Subsequently, a focus is made on ultrasonic welding, the technology used in this work. Then, the behaviour and performances of welded interfaces under quasi-static loadings are presented. Moreover, the influence of environmental conditions (temperature and humidity) on joint performance is reviewed to improve the understanding and predict joints' in-service behaviour. The author found no studies investigating the dynamic behaviour of welded TP composites.

1.2.1 Short review about the joining methods for composite materials

Mechanical joints were initially used to assemble metallic parts mainly used for automotive and aeronautical structures. The aim was to have high-strength structures and joints, with the possibility to disassemble parts. Technologies improved with time to adapt to the evolution of materials. Joining methods requiring hole drilling are partially replaced to improve the joining efficiency for composites.

Riveted joint and bolted joint

Bolted joints need to drill the composite before assembling (Figure 1.9). Some TP composites have a significant hole sensitivity with large irreversible strains, which might lead to extensive damage in the laminate (Vieille et al., 2012). Nevertheless, TP composite double lap bolded joints performance is suitable with a higher bearing capability than TS composites. What is more, the fastener adds a significant through-the-thickness reinforcement for peeling mode, which cannot be found with adhesive or welded joints (Zhao et al., 2017). However, the addition of the fastener can be detrimental to the lightening of structures, and the drill step may increase the risk of delamination.

Figure 1.9 – Example of bolted single lap joint

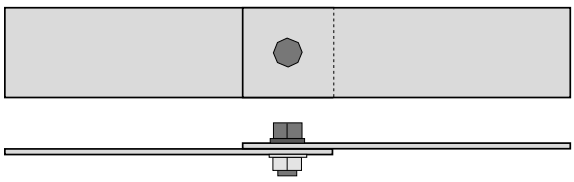

Riveted joints are extensively used for aeronautic parts. Indeed, the associated process spreads because of its fastness for metal assemblies to lighten the structures. They are mainly used to join composite with metal, not for composite/composite joints. This joining method induces damage in the composite due to the rivet insertion, but also because of rivet rotation during loading (Li et al., 2001). Moreover, rivets can be associated with bonded joints, as for the self-piercing rivet (Figure 1.10).

These two joining methods increase stress concentration around the bolt or rivets; hence, joints constitute the weak zones of the structures with large damaged areas observed around the joint after fracture (Li et al., 2001). Nevertheless, these methods are well suited for large thicknesses joints but also to assemble dissimilar materials (metal/polymer composite) even with high fatigue performance (Esmaeili et al., 2014).

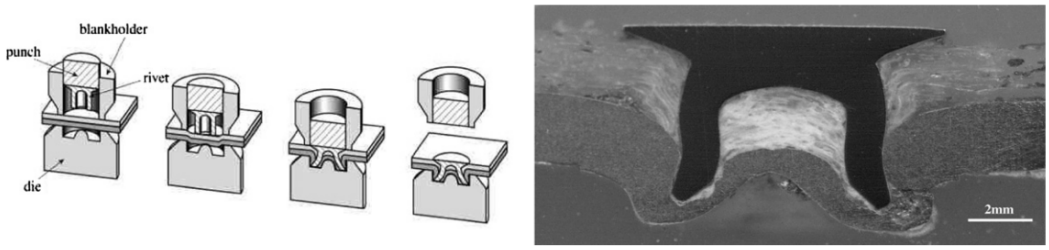

Figure 1.10 – Self-piercing rivet (Di Franco et al., 2012)

Z-pinning and CMT pins

Other technologies have been developed in these last decades to reinforce interfaces and reduce the stress concentration at the interfaces. Composite materials suffer from low out-of-plane strength and high delamination risk, especially for impact loadings. Z-pinning is a technology offering an out-of-plane reinforcement for composites by the addition of metallic or CF pins in the pre-pregs (Partridge & Cartié, 2005; Francesconi & Aymerich, 2018). The pins are placed orthogonally to the composite plates (Figure 1.11). The intralaminar fracture is reduced and limits the fracture propagation in the laminates. However, the in-plane tensile properties are reduced. Z-pinning does not delay the damage initiation, although it increases the reaction load when fracture propagates (Partridge & Cartié, 2005). Moreover, these advantages depend on the stacking sequence considered. Francesconi and Aymerich (2018) observed an improvement of impact resistance of sequence promoting interlaminar fracture between two plies, while configurations facing small delamination at multiple interply zones were not improved by Z-pinning. One main drawback is the consistency needed for pin placement requiring a large part of preparation before curing.

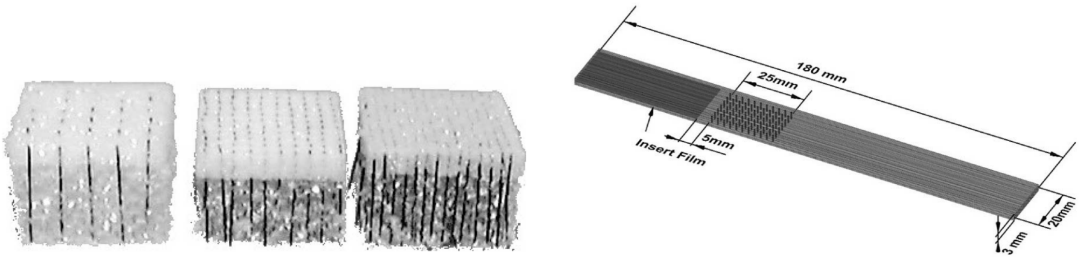

(a) Z-pinning for several pins density (b) Example of Z pinned DCB/ENF test specimen

Figure 1.11 – Z pinning of composites (Partridge & Cartié, 2005)

CMT pinning is a recent method to assemble metallic parts with composites. Metallic pins are placed on the metal part then the composite polymerisation is made in contact with the pinned structure (Figure 1.12). This method leads to strong adhesion and avoids deterioration of the composite with pin hammering. Strong joints can be obtained between metallic and composite structures (Paroissien, 2016).

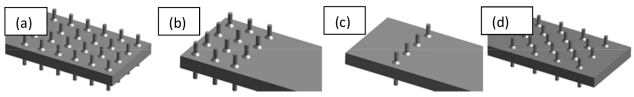

Figure 1.12 – CMT pins for several pins quantity and DLJ configuration (Paroissien, 2016)

Adhesive joint

The large use of adhesive joints in the transport industry comes from the many advantages of this method. Polymer resins, such as an epoxy-based adhesive, allow the strong joining of two parts from the same or dissimilar materials. Stresses in the composites are transferred through the adhesive layer over the entire interface; the stress concentration is relatively small compared to riveting. Major drawbacks of

this method have prompted researchers to investigate other joining processes. The surface preparation is a crucial point of the adhesive joining process. It requires strict protocols, which can be time-consuming and require operators. Moreover, the adhesive resin needs to cure to meet its strength. These curing cycles can last from some hours to an entire week to complete (Argoud et al., 2016).

Welded joint

TP composites can be welded since their matrix is fusible. As for metals, the material is melted at the interface to create intimate contact between both parts. The main interest of these joining processes is to have a continuity between both substrates through the weld made of the same matrix as the composite. Hence, welding (or fusion bonding) is, on paper, the closest technology to co-consolidation. It is particularly suitable for the assembly of simple geometries. These technologies will be presented in more detail in Section 1.2. Compared to composite structure bonding, welding does not require extensive surface preparation, and the joining process is faster as no curing step is needed. Compared to mechanical fastening, fusion bonding limits stress concentration and difference in coefficient of expansion between components; also, it does not require drilling of the substrates, an operation that increases the risk of delamination in the adherents (Yousefpour et al., 2004).

1.2.2 Welding methods

Several welding methods exist based on different techniques to heat the interface (Figure 1.13). The three families of fusion bonding are thermal welding, friction welding and electromagnetic welding. Three processes stand out by their efficiency and high-quality welds: induction, resistance and ultrasonic welding (Ageorges et al., 2001; Yousefpour et al., 2004). These methods have advantages and drawbacks and are not adapted for the same types of structures to join or materials. All these methods are based on the same phenomenon: elements are placed at the interface to heat the interface or to concentrate the heating energy in the interface, the substrate's matrix melts in the first ply in contact with the interface, and macromolecules can then diffuse and make the interface vanish (Figure 1.14). Finally, a solidification phase is used to fix the weld structure.

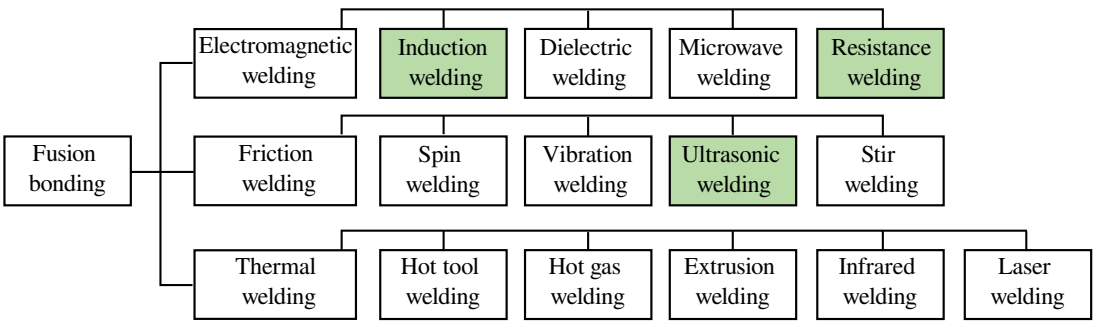

Figure 1.13 – Welding methodologies organised depending on the technology (based on (Reis et al., 2020))

Resistance and induction welding processes require the addition of an insert to heat the interface. Concerning resistance welding, a metallic mesh coated with chemicals and surrounded by neat matrix films constitutes the heating element (Figure 1.15). Usually, the use of coating improves the adhesion between the mesh and organic matrix (Rohart, 2020). A pre-preg ply might also be used as a heating element (Stavrov & Bersee, 2005). The relatively low process cost and the possibility of automatisation for up-scaling are the main advantages of this method. However, metal mesh use can induce difficulties caused by metal oxidation, and care must be taken to limit deconsolidation in the interface. Finally, resistance heating might serve to heat the welded interface to ease the joint disassembly (Frederick et al.,

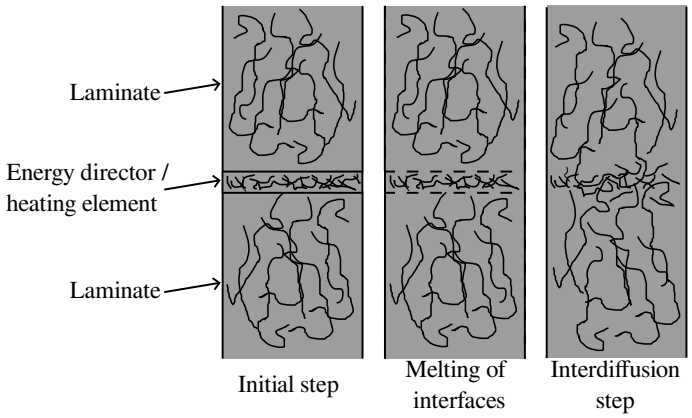

Figure 1.14 – Main steps of the adhesion process

2021). The temperature increase in the interface reduces the weld strength and facilitates the separation of both parts. Nevertheless, this method can be applied for recycling, but the application to structural repairs seems limited.

Figure 1.15 – Resistance welding setup

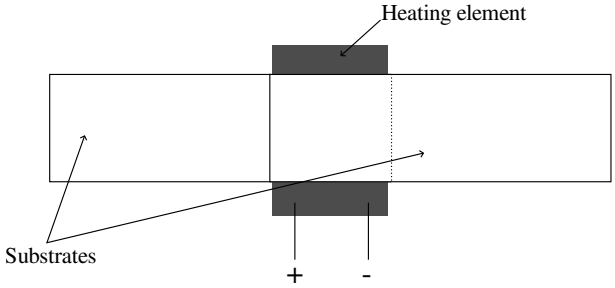

Concerning induction welding, the insert is made of matrix and ferromagnetic elements (iron particles, stainless steel). The susceptors are submitted to a magnetic field using a coil, and the induction field heats the insert by eddy currents. The temperature increase melts/softens the matrix around susceptors. The solidification phase is done with pressure applied on the joint to limit deconsolidation. The coil and susceptor designs are crucial for this process because a non-uniform magnetic field leads to non-homogeneous heating of the interface, so to a heterogeneous welding quality. Moreover, this process is expensive due to the susceptors; nevertheless, its interest is significant for continuous welding. Finally, the welding process choice depends on the geometry to weld and the material (Gouin O'Shaughnessey et al., 2016).

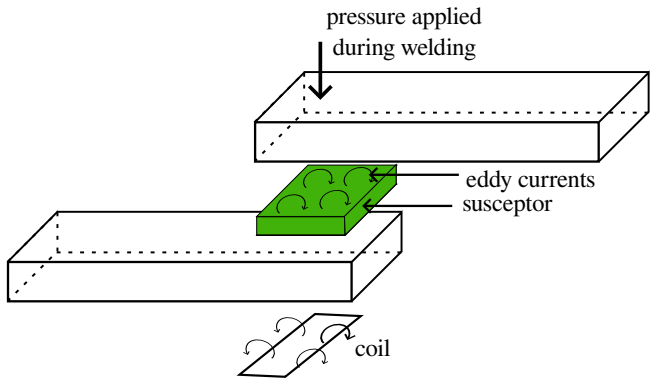

Figure 1.16 – Induction welding setup (based on (Ahmed et al., 2006))

These two methods are fast and can be applied to long and thin structures to join. However, foreign material addition (metal mesh, for example) might weaken the interface in case of poor adhesion with the matrix. It is one of the main reasons for the development of ultrasonic welding, which does not need a heating element at the interface. Thus, this process is theoretically the closest to co-consolidation.

1.2.3 Knowledge about ultrasonic welding

Ultra**S**onic (US) welding is a fast process which does not require a foreign material in the interface compared to resistance or electromagnetic welding. A sonotrode vibrates at high frequency and low amplitude to heat the interface by friction and viscous dissipation (Levy et al., 2014). **E**nergy **D**irectors (EDs) are usually placed at the interface to improve the weld quality. These are neat matrix lines over-moulded on the interface or pure matrix films that concentrate the dissipated energy at the interface and limit the extension of the **H**eat-**A**ffected **Z**one (HAZ). The stiffness and thickness of these elements are smaller than the substrates, then the loading is more significant on these parts. Another objective of EDs is to improve the weld quality by adding some matrix to the adhesion process. Indeed, depending on the composite, the matrix quantity at the interface can be insufficient to ensure strong adhesion.

Two types of US welding exist, the static process (one specimen welded at a time) and the continuous process (dynamic welding along a line). The US welding static process is described, which is currently the most controlled method. Before welding, substrates to join are placed on a specific tooling to avoid in-plan elements shifting (Figure 1.17). Three main steps constitute the process:

— Bringing the sonotrode into contact with the specimen.
— Application of the welding force on the assembly and emission of ultrasounds simultaneously. Ultrasound stops when the target is reached.
— Application of a holding force during a specified time to enable solidification of the interface and limit deconsolidation.

The thickness of the weld at the final stage is about ten times the interply thickness. This data may vary depending on the control process and the type of substrate.

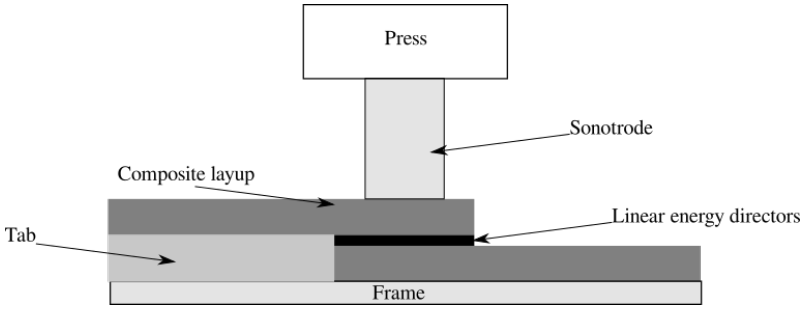

Figure 1.17 – Schematic diagram of the static ultrasonic welding process

The continuous welding process is developed to extend US welding to large dimensions structures. The aim is to weld parts along a line, so the sonotrode has to move linearly during the process (Figure 1.18). The main difficulties are the co-existence of the matrix at different steps (intact EDs, melted matrix and consolidated matrix) and the high risk of deconsolidation as the sonotrode has to stay for an appropriate amount of time for solidification. Despite these elements, studies showed the viability of this process using **F**lat **E**nergy **D**irectors (Flat EDs) or even woven polymer mesh EDs to improve the adhesion (Senders et al., 2016; Jongbloed, Teuwen, Benedictus, et al., 2020; Jongbloed, Teuwen, Palardy, et al., 2020). The performances of continuously welded interfaces are as good as the static ones.

EDs' distribution has a considerable influence on weld quality. It determines the heat generation and homogeneity at the interface. Two types of ED can be used: linear (triangular or semi-circular shaped) or flat (Figure 1.19). The orientation of linear EDs influences the size of the welded area, especially when a rectangular overlap is welded (Villegas & Bersee, 2010). Transverse ED lead to a larger welded area and a smaller scatter. The multiplicity of EDs at the interface improves the weld quality by increasing the welded zone and, more importantly, by reducing the pressure on the ED tips, resulting in a lower disturbance of the outermost ply reinforcement. EDs melting and collapsing is twice faster in the case of triangular ones than for a flat ED (Fernandez Villegas & Palardy, 2017). The triangular EDs start to

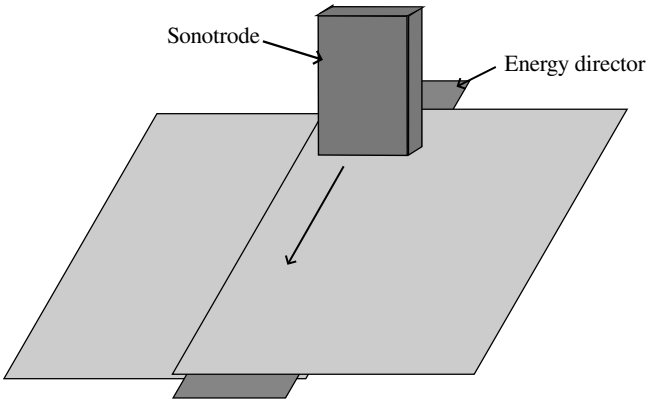

Figure 1.18 – Schema of continuous US welding setup

melt at the tip (Figure 1.20); after the first matrix flow at the interface, the matrix solidifies because of the contact with cold substrates. It is followed by a second heating step that melts the EDs matrix and outermost ply substrates matrix to create adhesion in the interface. The total welding duration is similar using linear EDs or flat EDs. Nevertheless, flat EDs ease the welding process by reducing the preparation time of specimens, which is a tremendous issue for industrial applications.

Figure 1.19 – Triangular and flat ED configuration before welding

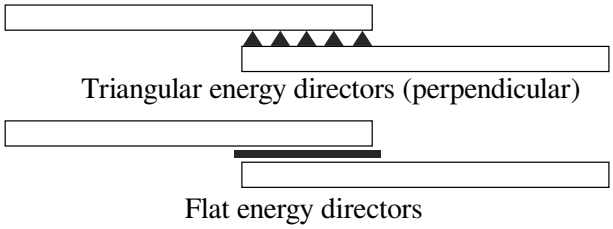

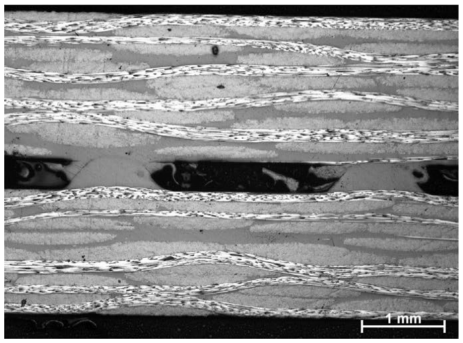

Figure 1.20 – Triangular ED early melting (Fernandez Villegas & Palardy, 2017)

The use of EDs is essential to improve weld quality. For PA66/CF composites, Goto et al. (2019) investigated the influence of the flat ED use on the shear and peeling behaviours of welded interfaces, for cross-ply and twill laminates. For the shear behaviour, flat ED improved the welding efficiency of twill laminates, meaning that a larger surface is welded; for the cross-ply joint, it improved the welding quality, which corresponds to the weld strength. Concerning the opening behaviour, flat ED contributes to higher performances of the two joints considered but in a smaller fraction than in shear. In addition, flat ED can reduce the indentation caused by the sonotrode for cross-ply specimens. Research is performed to have an improvement of US welding control and avoid the use of EDs (Tutunjian et al., 2018; Tutunjian et al., 2020). This methodology seems promising for the industry, but it is still barely used at the moment.

The orientation of the composite reinforcement also influences the weld strength. When fibres are mainly oriented along the loading direction, the strength is higher (Villegas & Bersee, 2010; Shi et al., 2013). This phenomenon might be explained by the higher number of fibre bundles to break when they are parallel to the load. Moreover, the fracture type observed differs depending on the apparent orientation. Shi et al. (2013) observed intralaminar fracture for all the GF/**P**oly**E**ther**I**mide (PEI) specimens

tested; however, the warp yarn orientation mainly faced fibre/matrix debonding while the weft yarn orientation suffered laminate tearing. Hence, the fracture caused by fibre/matrix debonding is sensitive to the adhesion between these components.

ED are still essential elements to obtain good-quality welds for the current industrial processes, whether it be for the static or continuous welding process. Moreover, the orientation of the reinforcement in contact with the weld can considerably affect the weld strength. Other parameters can influence the behaviour of the weld, such as the processing parameters. The next part presents their influence and the weld performance for several loading conditions.

1.2.4 Behaviour of welded interfaces

The more extended part of the literature about US welding of TP composites focuses on the process and the influence of processing parameters on weld quality. The quality evaluation is assessed by tensile tests on **S**ingle **L**ap **J**oint (SLJ) specimens (**S**ingle **L**ap **S**hear - SLS tests), which were defined first for bonding quality evaluation in shear. In addition, the failure mechanisms are investigated through fractography analysis. Finally, the influences of environmental conditions on performances are presented.

Influence of processing parameters

The main parameters used to control the US welding process are welding and holding forces, vibration amplitudes, welding time and energy. The definition of a processing window is essential to get strong and reproducible welds. Hence, many authors focused on the parameters' influence study on weld quality and performance. Several parameters need optimisation, depending on the method employed to control the process, for example, welding energy or welding time. Nevertheless, the welding amplitude and the holding and welding forces are the process parameters shared by all the control methods.

Researches show that the increase in welding energy, the energy supplied by the generator to the sonotrode, leads to an improvement in the welds' performance. However, beyond a certain energy level, the interface starts deteriorating due to a larger HAZ and to the development of voids in the weld and at the interface between fibres and matrix (K. Wang et al., 2017; Goto et al., 2019). The welding time is also a critical parameter similarly affecting the weld performance as the welding energy. The vibration phase prolongation results in better weld performances up to the properties degradation mainly caused by voids (Tao et al., 2019; Choudhury & Debnath, 2020). Several authors suggested explanations for the formation of the voids. Tao et al. (2019) present this phenomenon as a result of the thermal expansion coefficient difference between matrix and fibres. A longer welding time conducts to a HAZ enlargement, and thus laminate reinforcement is affected by the heat resulting in voids formation during the heating and cooling phases (Figure 1.21). In this respect, ED also helps reduce the extent of the HAZ and the defects quantity in that zone. Another origin of voids comes from the moisture in the laminates that might evaporate, and for higher welding time, these voids could be the consequence of matrix deterioration (Shi et al., 2013). Finally, the initial residual stresses may cause the generation of the voids during the joining process (Amedewovo et al., 2022).

The strategy used to control the US welding process may strongly affect the quality of the weld and scatter of performances. Authors choose the strategy mainly depending on the material under study on which the process relies. Fernandez Villegas et al. (2015, 2014) presented the advantages of a displacement-controlled process on CF/PEI and CF/PPS. The output power and displacement of the generator and sonotrode, respectively, are valuable indicators to follow the welding process. In (Fernandez Villegas et al., 2015) and (Fernandez Villegas, 2014), five welding steps are distinctly identified. This study showed that the displacement-controlled process permits the identification of an optimum travel value to obtain the maximum **L**ap **S**hear **S**trength (LSS), for the force and amplitude considered. In addition,

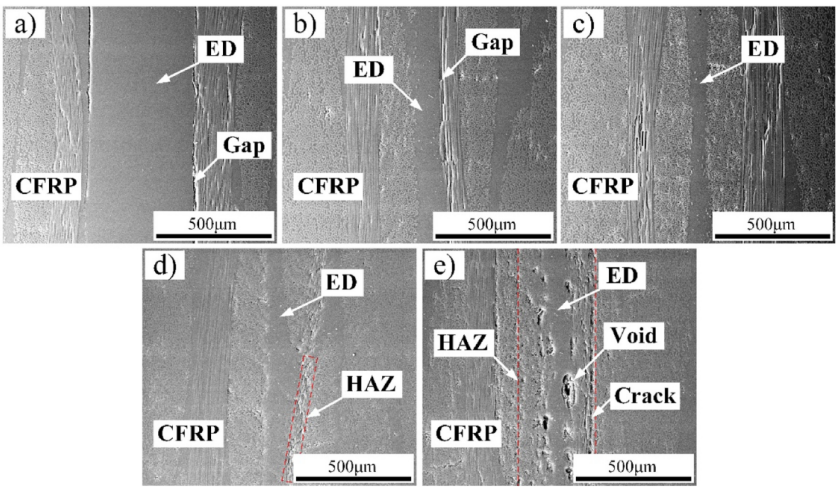

Figure 1.21 – Mesoscopic aspect of the weld with flat ED for different welding times and with corresponding defects (Tao et al., 2019)

this method of control is more reliable because it reduces the dispersion of the weld's performance; furthermore, amplitude variations slightly affect the process. According to Fernandez Villegas (2014), the displacement-controlled process is thus certainly more robust than the time-controlled. The main argument is the different travels that can be reached after one vibration time, leading to different steps in the welding process and so unreproducible weld. What is more, this process control applied to CF/PEI presented a low sensitivity to variation in the couple welding force/amplitude. High values for this couple result in the decrease of welding time and HAZ extent but with higher power dissipation. Nevertheless, other authors show on CF/PA66 that energy-controlled welding can produce high-quality welds with a low scatter of performances with an example on PA6/CF (Goto et al., 2019).

Welded joint testing and fractography

The mechanical testing of composite welded joints is essentially done in shear using SLJ specimens. The main reason is the simplicity of specimen manufacturing and testing. SLJ samples are used to evaluate the joint shear strength and to compare different process settings of the US welding (Fernandez Villegas, 2014; Fernandez Villegas et al., 2015; Goto et al., 2019; Choudhury & Debnath, 2020). Only one study reported results from tests on double lap joint specimens to qualify the weld performance in pure shear (Zhao et al., 2017). The use of these lap shear tests is questionable as there are designed for bonded joints characterisation. Beyond the performance evaluation through the weld strength, a study of the joint fracture, weld mesostructure, and adherent behaviour are necessary to have a global joint performance evaluation (Fernandez Villegas & Rans, 2021).

Different joint fractures might occur and they are linked to the weld quality (Figure 1.22). Both on the first line correspond to a poor quality weld and a weld stronger than the adherents, respectively called adhesive fracture and coupon fracture. The intralaminar fracture corresponds to the main fracture observed for high-quality welds. It is a fracture occurring along the weld and propagating in both adherents, or only in one with delamination, or even in the matrix-rich layer at the interface. As the weld thickness is small, the last intralaminar fracture is rarely observed.

Intralaminar fracture is characterised by fibre/matrix debonding, fracture of fibre bundles and laminate tearing (Figure 1.23). Most of the authors observed this fracture type which is linked to strong adhesion between EDs and substrates' matrix (Shi et al., 2013; Fernandez Villegas, 2014; Zhao et al., 2017; Goto et al., 2019; Fernandez Villegas & Rans, 2021). Moreover, in the case of SLJ specimens welded ultrasonically, the fracture is localised in the first outermost ply of the substrates in contact with the welded

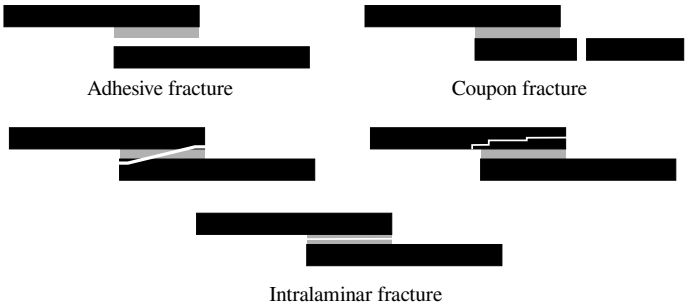

Figure 1.22 – Fracture types observed for lap shear tests

interface. Figure 1.23a illustrates the fibre/matrix debonding for cross-ply composites, with identifiable zones where the matrix is ripped off the fibres. In Figure 1.23b, fibre/matrix debonding is also noticed with fibre bundle fracture for woven composite's weld. In the case of over-welded joints, fibre bundles may be deformed because of the HAZ extent. It results in deep laminate tearing and a decrease in LSS, most likely caused by voids at the edges of the overlap acting as initiation elements for interface fracture.

Figure 1.23 – Post-mortem specimen - intralaminar fracture (Goto et al., 2019)

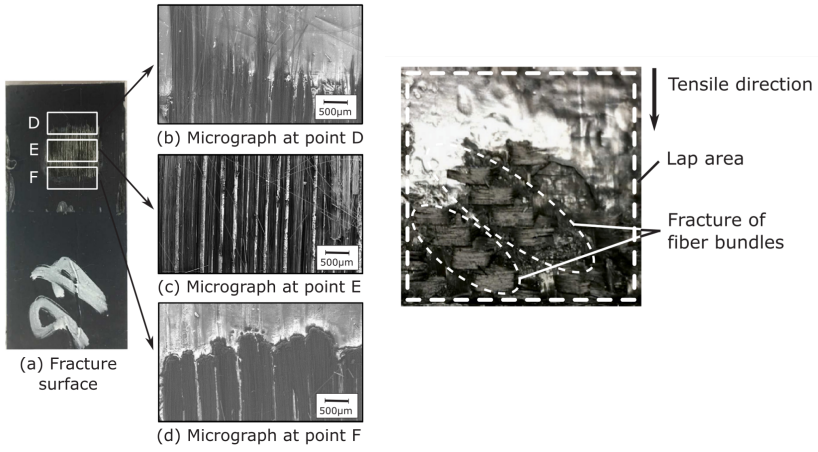

(a) Cross-ply laminates (b) Twill laminates

In the literature, other specimens were studied to characterise pure mode I and mode II weld behaviours. **D**ouble **C**antilever **B**eam (DCB) and **E**nd-**N**otched **F**lexure (ENF) were used by Harras et al. (1996) on CF/PEEK and showed better results than for compression moulded specimens (higher shear fracture toughness). This result is surprising as the weld is not supposed to be stronger than the original material due to the defects that might result from the welding process. This larger fracture toughness is attributed to the delamination occurring during the weld fracture, tortuous fracture path and plastic strains in the matrix-rich layer at the interface. Delamination and fibre bridging are the main reasons why the DCB test is not the most appropriate test for the pure mode I characterisation of welds (Stavrov & Bersee, 2005). Pull-through tests have been conducted successfully by other authors to study the weld opening (Zhao et al., 2017; Goto et al., 2019). This test is not standardised, unlike the DCB; however, it is possible to evaluate the fracture toughness through an inverse method.

Influence of the joint thickness

The joint thickness is a substantial parameter for an adhesive study. Several studies showed experimentally and numerically that the failure load increases when the joint's thickness decreases for SLJ specimens (Da Silva et al., 2006; Castagnetti et al., 2011; Banea et al., 2015). This element is linked to the reduction of the stress peaks at the overlap edges for thinner adhesives, whether they are ductile or fragile. Moreover, a decrease in the interface average stresses is observed for ticker adhesive joints.

However, Banea et al. (2015) noticed an increase in G_{Ic} for thicker adhesive joints as the polymer can face plastic strains before fracture. Despite the joint performances increase with thinner joints, an optimum thickness value seems to exist because degradation of the interface properties is observed for a large decrease in thickness.

Concerning the welded joints, an influence of the thickness is reported in (Villegas & Bersee, 2010; Fernandez Villegas, 2014). These joints are, by definition, significantly thinner than adhesive joints because they tend to be as thin as a matrix-rich zone between laminate plies. An excessive matrix-rich zone thickness can lead to a reduction of the weld strength. Moreover, a weld thickness diminution is associated with an adhesion improvement, in addition to the strength improvement observed for the adhesive joints. Finally, the weld quality at the edges is also significantly important as it can facilitate fracture initiation (Fernandez Villegas & Palardy, 2017).

Influence of temperature and relative humidity

For similar processing parameters, weld thickness and fracture type, the weld strength may be affected by other factors, such as environmental conditions. During service, structures face changes in the environment: temperature and hygrometry. These environmental conditions can significantly influence the behaviour of several TP matrices and composites, as seen in Section 1.1.2. For example, the behaviour of PA66 and PA6 depends on both the temperature and RH (Dau, 2019; Pivdiablyk, 2019). PA66 softens with an increase in temperature and RH (Figure 1.6). Besides, the ductile properties are enhanced for higher temperatures or moisture levels, along with an ultimate strain increase.

The weld is a matrix-rich zone between two reinforcement plies. Thus, its behaviour might be sensitive to environmental conditions as the neat matrix. Results of SLS tests show the degradation of welded CF/PPS joints performance with the increase of testing temperature (observed for resistance and US welding) (Koutras et al., 2018; Koutras et al., 2021). For the resistance welded joints, an improvement of 28 % is observed for tests conducted at -50 °C compared to room temperature and a decrease of 35 % is observed at 150 °C (Koutras et al., 2018). The same trends are observed for ultrasonically welded CF/PPS (Figure 1.24) (Koutras et al., 2021). Hygrometry influence was reported to be limited compared to temperature for the same composite (Figure 1.25). However, PSS can only absorb a limited quantity of moisture against other thermoplastics as polyamides (Rohart et al., 2020). The influence of this environmental condition might be of greater importance for other welded thermoplastic composites.

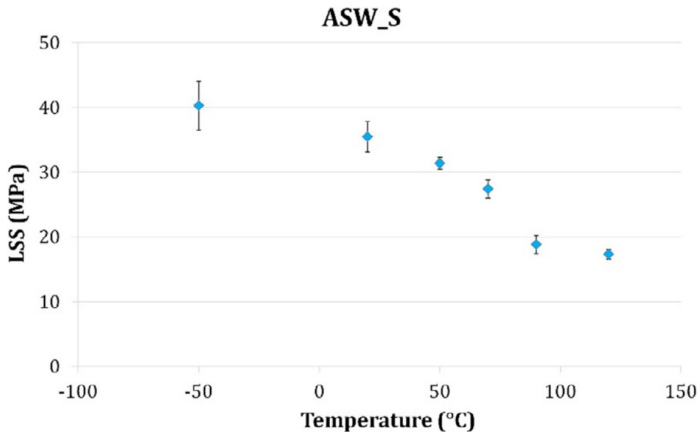

Figure 1.24 – Lap Shear Strength for several testing temperatures on CF/PPS US welds (Koutras et al., 2021)

The sensitivity of welded specimens' strength to temperature and moisture is linked to the dependence of the matrix to these two environmental parameters. In addition, the decrease in the substrate in-plane strength with the increase in temperature is also denoting that the interfacial shear strength deteriorates, as highlighted by several studies (Madhukar & Drzal, 1991; Deng & Ye, 1999). This decrease in interfacial strength is also presented as a major effect in the evolution of joint performance at high

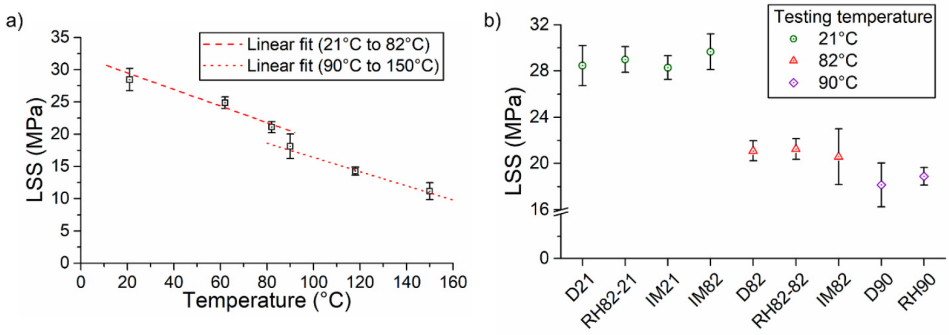

Figure 1.25 – Lap Shear Strength for several testing temperatures (a) and RH levels (b) on CF/PPS US welds (Rohart, 2020)

temperatures (Koutras et al., 2018).

Moreover, Koutras et al. (2021) studied the influence of weld crystallinity on the weld's performances. Despite the effect of the crystallinity ratio on the tensile behaviour of the matrix, the weld crystallinity influence is limited from room temperature to below glass temperature in dry conditions for CF/PPS SLJ specimens. Nevertheless, amorphous welds' performance improves at low temperatures, while crystalline welds are more suitable for high temperatures (Figure 1.26). These effects are most likely caused by the higher ductility of the amorphous matrix and the higher stiffness of high crystallinity PPS that improves the fibre/matrix interfacial strength.

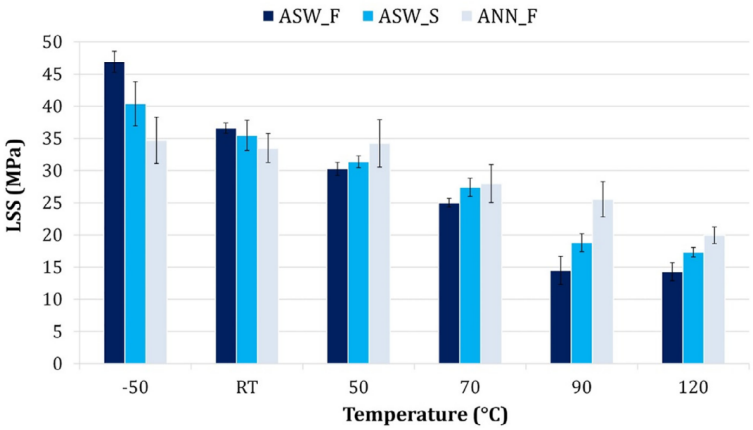

Figure 1.26 – Lap Shear Strength for several testing temperatures and three crystallinity levels on CF/PPS US welds (ASW for As welded, F and S for fast and slow welding and ANN for annealed specimens) (Koutras et al., 2021)

Comparison of performances with bolted joints

The previous paragraphs focused on the surface welded joint, but US welding can also be used for spot welding depending on the sonotrode size. Some authors studied the behaviour of these particular joints and compared their performance with the mechanically fastened joints, extensively employed in the industry. First, a single welded spot was tested in Zhao et al. (2017) for shear and peeling loads using double lap shear and pull-through tests. The results show that spot-welded joints can compete with fastening, especially in shear. More importantly, this study underlines the limited area damaged by the weld fracture, which is one main advantage of US welding. The welded area and the adherent outermost ply correspond to the damaged zones, while other parts of the substrates are intact after a shear or peel loading. Hence, substrates could be repaired or reused after the joint fracture. Nevertheless, the opening performances of welded spots are much smaller than fastened joints because the weld does not offer through-the-thickness reinforcement, unlike pins.

Mechanically fastened joints are also used in rows to increase joint strength. The multi-row spot welding performances were thus studied in (Zhao et al., 2019). Despite the low opening performances of welds, the multi-row spot welds have only a 10 % smaller strength than mechanical joints. Moreover, their

behaviour shows a high stiffness and limited secondary bending caused by the shape of SLJ specimens. As observed for the fastened joint, the distance between welded spots and the number of spots in a row influences the bearing capacity: a higher number and larger spaces lead to higher joint strength. Finally, work still needs to be done to fix the design rules for the multi-spot US welding.

US welding of TP with TS composites

US welding is a powerful method for joining parts made of the same material. However, classical joining methods such as adhesives or fasteners can join dissimilar materials. Hence, some studies try to develop the US welding of TP composites with TS. This joining needs the use of a TP coating on the TS to prevent thermal degradation of the matrix (Villegas & Rubio, 2015). Moreover, US welding seems to be the most appropriate welding process to obtain these mixed assemblies as the heating process must stay short (less than one second) to avoid some degradations of the TS matrix.

1.2.5 Conclusions

The three most promising welding technologies for TP composites have been presented in this section, with a focus on the process employed in this work, i.e. the US welding. This fast process is well controlled, especially for static welding (spot and larger zone) and woven composites. The extensive investigations on the influence of processing parameters improved the knowledge of this method to obtain high-strength welds and reduce the void content, non-welded zones and reinforcement perturbation at the interface. US welding, used for spot welding, competes with bolted joints with high strength and smaller damaged areas.

The predominant fracture mechanism linked to high-strength weld is the intralaminar fracture. This mechanism is driven by fibre/matrix debonding and ductile matrix fracture with limited fibre breakage. Consequently, the use of DCB tests for the fracture toughness evaluation in mode I is altered as fibre fractures and bridging increase artificially the fracture toughness. Environmental conditions affect the weld's behaviour according to the TP matrix dependence. For PPS, the temperature increase reduces the weld strength, and the moisture effect is moderate. These observations could have been expected as PPS is sensitive to temperature, but it absorbs a limited quantity of moisture. Hence, its influence is not significant for this material but could be for others. Moreover, the fracture mechanisms observed highlight the significance of interfacial shear strength as fibre/matrix debonding is the primary fracture mechanism observed.

Research still needs to be done on US welding. The use of Flat ED needs to be improved just like the continuous welding process because they are essential elements to upscale the process for the industry. What is more, improving the TP/TS composite welding may be interesting to facilitate the use of this joining method without changing the TS structures to TP. Finally, the strain rate influence is not yet taken into account in the research, despite its importance for structure study and the strain rate influence on TP matrices and composites. The next section focuses on the strain rate influence on the adhesive joints and intralaminar fracture. These two phenomena are close to composite welds with a high-adhesion process and similar polymers employed but with different interface thicknesses.

1.3 Interface characterisation and behaviour for dynamic loadings

This section presents the testing methodologies used in the literature to characterise the dynamic behaviour of interfaces: structure bonds or delamination. The first part presents the difficulties that can be faced for pure mode characterisation caused by inertia effects and wave propagations. New specimens have been developed to improve testing at a high strain rate but still present drawbacks. The second and third parts of this section introduce the

behaviour of bonded structures and delamination for moderate to high loading speeds. A focus is made on TP composites, but results of metallic structures bonding and delamination of TS composites are also presented. There is little research on TP composites; thus, a large part of the literature review considers results on TS composites.

1.3.1 Dynamic testing of interfaces

Dynamic testing of interfaces (bonded, welded or interlaminar zone) needs suitable specimens and testing devices to reach high strain rates and not be affected by inertia effects. The interface rupture can be divided into three main failure modes: normal opening, sliding shear and scissoring shear (Figure 1.27).

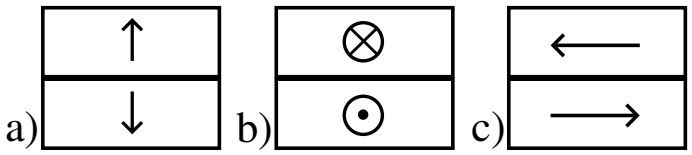

Figure 1.27 – Failure modes: a) mode I normal opening, b) mode II sliding shear and c) mode III scissoring shear - front view

Mechanical testing of interfaces is performed to determine their performances, but it can also be done to define a numerical model. Thus, different tests exist to determine, for example, the fracture toughness (G_c) for the three modes presented above or to determine the interface strength.

Testing setups and specimens used for the characterisation

Mode I and mode II characterisation specimens are the most used to determine the fracture toughness of interfaces. Some mixed mode characterisation specimens exist for mode I/II characterisation.

Mode I

DCB is highly used for the identification of mode I fracture toughness (G_{Ic}) of bonded joints or interlaminar fracture of composites (ASTM, 2013). The specimen is constituted of two beams bonded or co-cured with crack initiation at one edge. Then, one arm end is loaded on the crack edge side, and the other arm end is fixed. Methodologies have been developed to calculate the G_{Ic} from beam geometry, load and arm displacement. The main issue with DCB testing for dynamic loadings is the unsymmetrical opening of the specimen. Figure 1.28 shows tests for different loading speeds. The symmetrical opening is observed for the lower speed ($0.8\,\mathrm{m\,s^{-1}}$), and it becomes unsymmetrical at $6\,\mathrm{m\,s^{-1}}$ loading speed. The symmetry loss is caused by inertia effects (flexural waves in both specimen arms) (Brunner et al., 2008; May, 2016). Hence, the fracture toughness for pure mode I loading cannot be measured. Moreover, issues may occur while applied to composite welded interfaces as their fracture implies fibre breakage even for quasi-static loadings (Yousefpour et al., 2004).

Other testing methods have been employed to overcome this issue at high strain rates. Figure 1.29 presents the wedge-loaded DCB which aims to force the symmetrical opening by inserting a wedge between specimen arms (Kusaka et al., 1998; May, 2016; Oshima et al., 2018; Ponnusami et al., 2018; Manterola et al., 2020). This test's major drawback is the friction occurring between the wedge and the arms. Data reduction methods are proposed by several authors based on the crack length and the opening distance (Kusaka et al., 1998; Oshima et al., 2018). Some authors determine the mechanical interface properties by an inverse method, as done by Ponnusami et al. (2018) using cohesive elements and results from their experimental campaign.

Alternatives to DCB specimens were developed for the strain rate influence investigation on mode I behaviour. Multiple tests exist to characterise mode I, such as the Arcan test developed to test the interface through different directions. The setup can be oriented in the tensile test machine to load the interface in pure mode I, mixed mode I/II and pure mode II. However, the facility is relatively heavy and cannot be directly used for dynamic tensile tests due to inertia effects. Then, the original test was adapted to

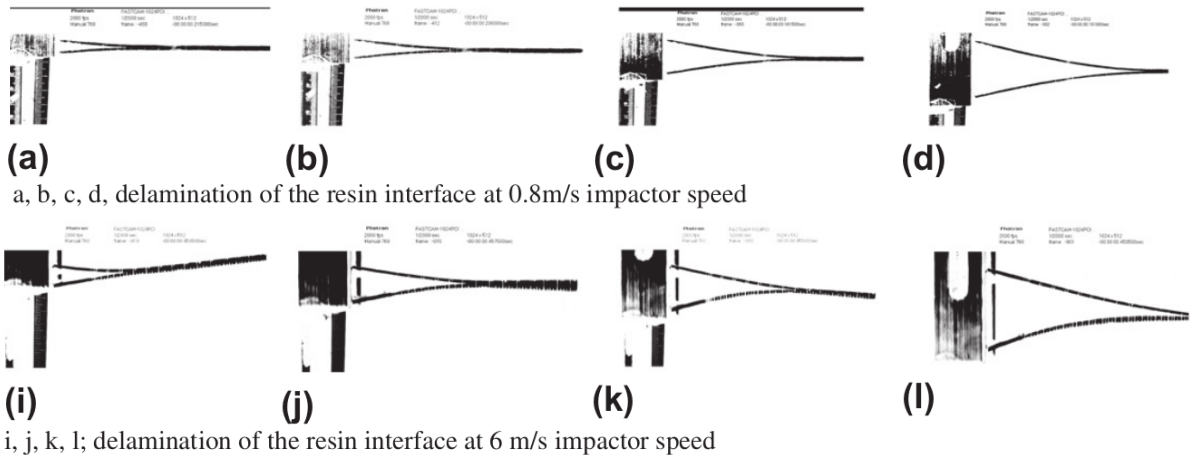

Figure 1.28 – Side view of DCB tests for several dynamic loadings (Figure from (de Verdiere, Skordos, May, et al., 2012))

Figure 1.29 – Schematic representation of wedge loaded DCB (Oshima et al., 2018)

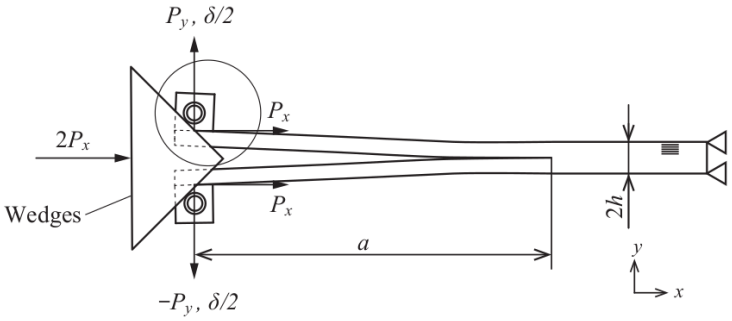

lighten the installation and characterise interfaces at high strain rates. Double U configuration was used by Argoud et al. (2016) to test the behaviour of bonded composites for pure traction, traction-shear and pure shear (Figure 1.30). Nevertheless, this type of setup was only used for low loading rates (up to $500\,\mathrm{mm\,min^{-1}}$). Finally, an Arcan test setup was developed for adhesive testing and showed suitable results for strain rates between $4 \times 10^2\,\mathrm{s^{-1}}$ and $1 \times 10^3\,\mathrm{s^{-1}}$ on drop weight tower (Valès, 2017).

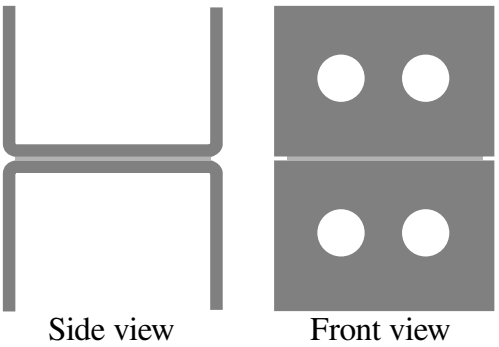

Figure 1.30 – Multiaxial specimen and test setup for interface characterisation (Morin, 2010; Argoud et al., 2016)

Mode II

ENF test is highly used to identify the mode II fracture toughness (ASTM, 2014b). Usually, a three-point bending setup is implemented for this specimen testing; four-point bending is also employed. The application can be done for high strain rates on several testing rigs such as Split Hopkinson bar (Figure 1.31). Nevertheless, some difficulties are experienced due to inertial effects resulting from the impactor. Moreover, the instability of crack propagation may affect the G_{IIc} evaluation (May et al., 2020).

SLJ specimens are used to quantify the performance of the bonded structure in shear (Figure 1.32)

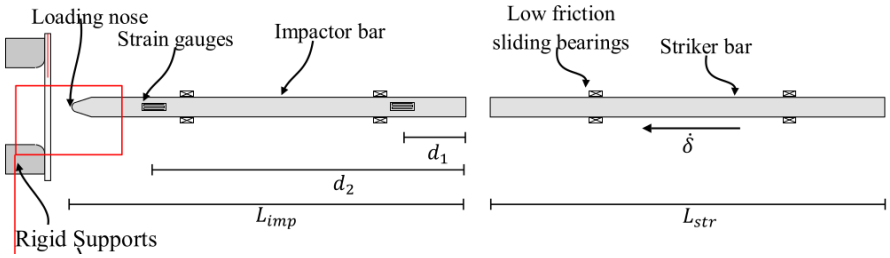

Figure 1.31 – ENF testing on Split Hopkinson bar (Yasaee et al., 2017)

(Adamvalli & Parameswaran, 2008; Galliot et al., 2012; Heimbs et al., 2013; Avendaño et al., 2016; Dufour, 2017; Machado, Gamarra, et al., 2018; Viana et al., 2018; Grefe et al., 2020; Ramaswamy et al., 2020). However, in practice, the loading mode is mixed I/II due to the bending induced by the loading eccentricity. They are widely used because the specimens are simple to manufacture and test. However, SLS tests are not standardised for the fracture toughness evaluation but for the bond integrity investigation. Most of the time, the tensile tests are analysed using the force-displacement curve and the joint strength (maximum load divided by the bonded surface area). SLJ testing is also relatively easy for dynamic loading tests as it does not need a specific gripping or impacting device. Wu et al. also used an SLJ specimen tested on a three-point bending bench (Wu et al., 2013).

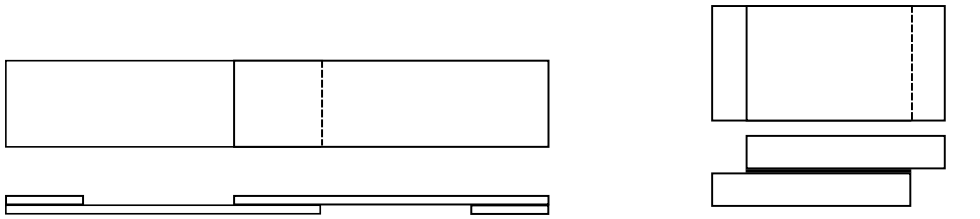

(a) Tensile test specimen (b) Compression test specimen

Figure 1.32 – Single lap joint specimens for dynamic loading

Double **L**ap **J**oint (DLJ) specimens are an extension to SLJ specimens (Figure 1.33). The specimen symmetry permits the interfaces testing for a quasi-pure mode II loading (Challita et al., 2011; May et al., 2015). These specimens are employed to evaluate the pure shear performance of the interface. As the SLJ specimens, they can be loaded in tension or compression. A double thickness of the internal part may be used to reinforce the specimen and limit the risk of coupon fracture (fracture of the intern substrate orthogonally to the interfaces).

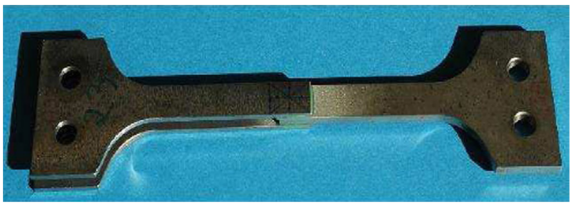

Figure 1.33 – Double lap joint tensile test (Challita et al., 2011)

Mode I/II

Mixed mode I/II is also studied to identify the modes coupling for a complex loading. This test may be used to determine parameters for a constitutive model of the interface. **M**ixed **M**ode **B**ending (MMB) test configuration is a standardised test for mixed loading at low loading speeds (Brunner et al., 2008; ASTM, 2014a). Figure 1.34 shows the scheme of the configuration and its application. The mixed mode ratio can be changed by modifying the moment of the loading arm. It is the main configuration used for the mixed mode characterisation.

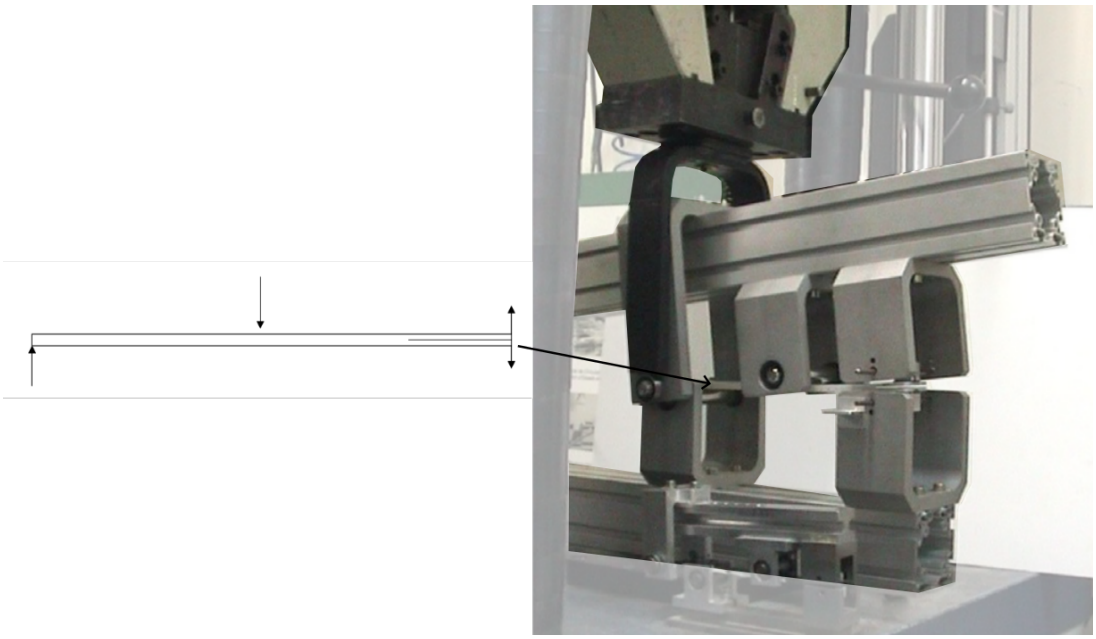

Figure 1.34 – Mixed mode bending test configuration (Brunner et al., 2008)

Loading system used for the characterisation

Several rigs may be used to characterise material or interface behaviour at moderate to high strain rates. The choice depends on the strain rate target for the characterisation, which can be reached with the mainly used devices (Table 1.2).

Testing rig	Screw-driven tensile test machine	Servo-hydraulic machine	Drop weight tower	Split Hopkinson bar
Strain rate reached (s^{-1})	10^{-4}	10^{-3} to 10^{2}	10^{2}	10^{2} to 10^{4}
Application	Quasi-static	Quasi-static to moderate strain rates	Moderate to high strain rates	

Table 1.2 – Device used depending on the strain rate and applications concerned

Screw-driven tensile test machines are commonly used for material characterisation. They are adapted for low loading speeds and are driven by displacement most of the time. The loading speed can be fixed and precisely controlled. However, the strain rate reached in the material depends on its mechanical properties.

Servohydraulic tensile test machines can reach velocities up to $10\,\mathrm{m\,s^{-1}}$ to $20\,\mathrm{m\,s^{-1}}$. For high loading speed, the loading speed required for the test cannot be reached instantaneously because of the feature inertia leading to a progressive increase of the velocity. This issue is fixed using loss travel for the grip applying the load (Figure 1.35a). The bar translates along a fixed value of distance to reach the desired loading speed. Then, the bar drives the loading speeds by a system of cylinders in most cases (Blackman et al., 1995; Blackman et al., 2012). Moreover, the load signal obtained for dynamic loading can be noised and may need to be filtered. High strain rates can be obtained in polymer composites and metal using this device.

Drop-weight towers are used for moderate loading speeds. A weight is dropped from a defined height, dependent on the study, and impacts a structure placed on an appropriate fixture. For tests pre-

sented in the previous paragraphs as DCB or SLS tests, the mass impacts a grip which loads the specimen (Figure 1.35) (Galliot et al., 2012; Machado, Gamarra, et al., 2018; Viana et al., 2018).

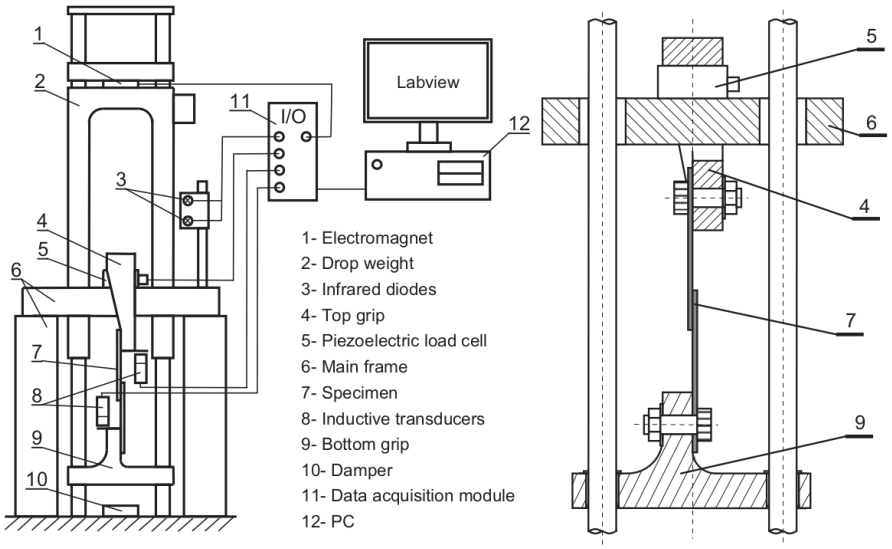

Figure 1.35 – Scheme of drop weight tower for SLS test (Galliot et al., 2012)

Split Hopkinson bars can be used for tensile or compression testing at high loading speeds. This device is more specific than the three presented above and is not a widespread rig in all test centres. An air gun accelerates the striker bar, which impacts the input bar with the necessary kinetic energy. The input bar loads the specimen at the required loading speed. The reaction force is measured on the output bar in contact with the specimen using a strain gauge bridge placed at specific zones (Kusaka et al., 1998; Machado et al., 2017; Yasaee et al., 2017). Finally, the specimen size is limited due to inertia effects.

Most studies use high-speed cameras to measure strains and displacements. Depending on the loading speed and testing configuration (DCB or ENF, for example), the acquisition frequency can be significantly different. Despite the efficiency of this method, it can be complex to apply due to the frequencies and resolutions required. Other measuring methods are employed in the literature, such as acoustic emissions or electric monitoring (May, 2016). Hence, the strain rate influence on composite interfaces can be investigated using the appropriate tensile or compressing rig and specimens. Literature results about the effect on bonded interfaces and delamination are presented in the following subsections.

1.3.2 Behaviour of bonded structures

Structural bonding is a joining method highly used in the industry because it permits the joining of dissimilar materials and is not a damaging process, unlike riveting or bolted joints, as presented in Subsection 1.2.1. Hence, bonding is preferred for some applications. Multiple substrate/adhesive couples are studied in the literature for dynamic applications, and they reveal different behaviour depending on the constituents. The main adherent types studied are metallic structures, CF/epoxy and CF/PEEK. Concerning adhesives, a large part of studies focuses on epoxy-based adhesives. Investigations of bonded joint behaviour usually start with tests on the bulk adhesive tensile behaviour, especially when the final aim is to model the joint behaviour (May et al., 2015; Borges et al., 2020). The second step is the bonded structure testing using DCB, ENF, SLJ specimens or equivalent at several loading speeds.

Results from Blackman et al. (1995; 2012) on CF/epoxy and CF/PEEK bonded structures with structural epoxy adhesive, tested with DCB and ENF from $10^{-5}\,\mathrm{m\,s^{-1}}$ to $15\,\mathrm{m\,s^{-1}}$, showed a slight negative influence of the loading speed on the mode I fracture toughness of the joints. However, the mode II fracture toughness is independent of time effects. Nevertheless, the loading speed influence on adhesive joint behaviour differs between studies, sometimes because of changes in the fracture toughness identi-

fication for dynamic loadings (Blackman et al., 2012). The inclusion of stability or instability in the crack propagation during the DCB or ENF test is important for the calculation of dynamic G_c. Moreover, using the load signal to calculate G_{Ic} may distort the results because of the dynamic effect on the signal measured. Figure 1.36 shows that a wrong calculation could lead to an overestimation of G_{Ic} at high loading speeds.

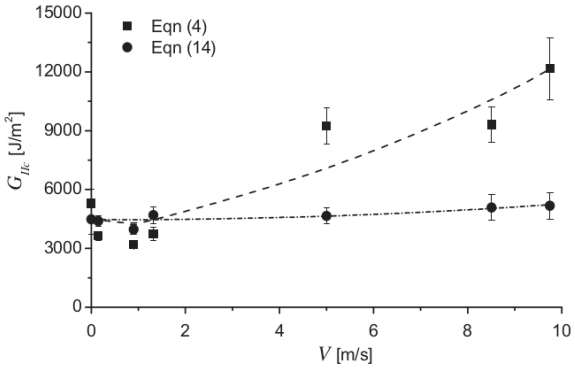

Figure 1.36 – Evolution of the fracture toughness with the loading speed for the load dependant calculation (squared points) and a load independent (circled points) (Blackman et al., 2012)

Most of the time, the several influences are only caused by the mechanical differences of the adhesive studied. Borges et al. (2020) investigated the behaviour of two epoxy-based adhesives with tensile tests on bulk and DCB/ENF tests using metallic substrates. Results highlight the mode I loading speed sensitivity with an increase of G_{Ic} from $2.5\,\mathrm{N\,mm^{-1}}$ at $0.2\,\mathrm{mm\,min^{-1}}$ to $4.5\,\mathrm{N\,mm^{-1}}$ at $180 \times 10^3\,\mathrm{mm\,min^{-1}}$. Other authors studied CF/epoxy bonded with epoxy-based adhesive with SLS tests conducted with drop weight towers up to $3\,\mathrm{m\,s^{-1}}$ (Galliot et al., 2012; Machado, Gamarra, et al., 2018). Both studies reported an increase in the maximum force for impact tests compared to quasi-static. Moreover, Galliot et al. (2012) exhibited the increase of the joint performances for several stacking sequences (Figure 1.37) (quasi-isotropic quasi-homogeneous, isotropic stiffness for membrane and orthotropic for bending...).

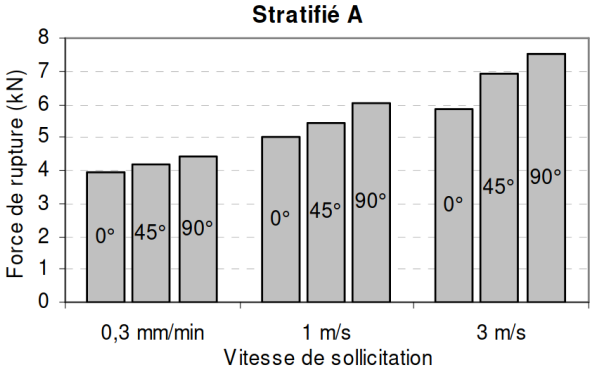

Figure 1.37 – Failure load for several loading rate for a CF/epoxy composite bonded with epoxy-based adhesive - multiple quasi-isotropic sequences considered (Galliot et al., 2007)

GF/PA66 bonded structures were tested by Argoud et al. (2016) using a multiaxial testing device similar to the Arcan method. The use of a polyurethane hyperelastic leads to a loading speed dependency of the joint in traction, shear and mixed traction-shear loadings. In addition, a stiffening behaviour is observed without any decrease in the ultimate failure displacement. Finally, all these elements show that multiple bonded joints are loading speed sensitive.

1.3.3 Delamination of composites

Mode I loading

Epoxy/CF and PEEK/CF are the primary composites studied in the literature for the delamination behaviour at high strain rates. Most studies investigate the strain rate or loading speed influence on composite delamination by the fracture toughness measurements in modes I and II. Impact tests can

also be done on plates to evaluate the damaged area extent under several impact speeds and energies.

DCB testing is chosen for mode I characterisation despite the drawback of its use for dynamic loadings. Studies on CF/epoxy and CF/PEEK reported a diminution of G_{Ic} for high loading speeds (Mall et al., 1987; Smiley & Pipes, 1987a; Béguelin et al., 1991; Kusaka et al., 1998; Fracasso et al., 2001; Zabala et al., 2015). Other studies observed no influence of loading speed on the mode I fracture toughness (Blackman et al., 1995; Govender et al., 2013). Some TP composites present an influence of the loading speed on the delamination behaviour as the ballistic composite studied by May and Lässig (2017) (Figure 1.38). In this case, the in-plane behaviour of the composite studied is known as strain rate dependent. As far as the author knows, no studies were published about the mode I delamination behaviour of GF/PA66 composites for dynamic loadings.

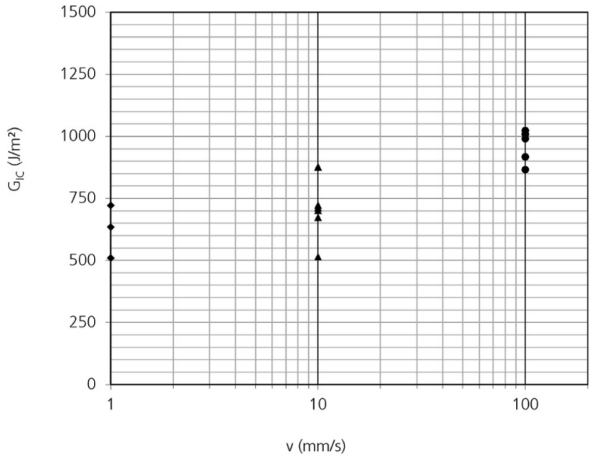

Figure 1.38 – Evolution of G_{Ic} with the loading speed for a ballistic composite (May & Lässig, 2017)

The loading speed influence is supposedly caused by the strain rate sensitivity of the matrix, which confers a strain rate sensitivity to the composites and their interfaces (Jacob et al., 2005). The strain rate in the interface may increase through tests at higher loading speeds. In other cases, the influence of strain rate on delamination is reported as an outcome of the fracture mechanism evolution. Zabala et al. (2015) illustrated this phenomenon on woven CF/epoxy with a change from stick/slip propagation (fibre/matrix fracture) to unstable propagation linked to brittle matrix crack. Similar phenomena were observed by Kusaka et al. (1998) with larger damaged zones for low-velocity loadings. What is more, fibre bridging is a significant issue in fracture toughness measurement (Brunner et al., 2008). The increase of G_{Ic} with the increasing loading speed might result from a modification in the specimen loading mode from pure mode I to mixed I/II (de Verdiere, Skordos, May, et al., 2012).

Mode II loading

Similar observations were made on mode II behaviour without consensus for some materials. A decrease of G_{IIc} for higher strain rates was observed by Smiley and Pipes (1987b) and Machado et al. (2017). Figure 1.39 illustrates this result for several testing temperatures on a CF/epoxy. The authors explained this decrease from the matrix behaviour, ductile at low strain rates, which becomes more fragile for higher values. It is consistent with the observation made by Machado et al. (2017) on the temperature influence; higher matrix ductility at high temperature, hence the G_{IIc} increases.

Strain rate insensitivity was observed by several authors for mode II loading (Fracasso et al., 2001; de Verdiere, Skordos, Walton, et al., 2012). A limited increase is also observed for epoxy-based composite, but it is not significant (Yasaee et al., 2017). Jacob et al. (2005) suggested in their review about the influence of strain rate on polymer composite fracture toughness that the lack of consensus toward this topic might be caused by the absence of time-dependency of this property.

Todo et al. (1999) presented results about mode II fracture toughness of CF/PA6 and GF/PA6 for

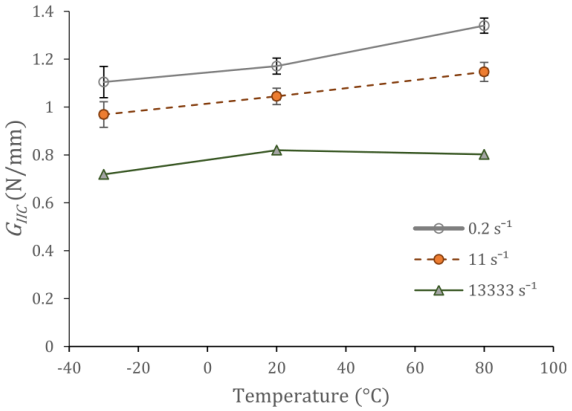

Figure 1.39 – Influence of strain rate and temperature on the mode II fracture toughness of a CF/epoxy (Machado et al., 2017)

quasi-static and $1.1\,\mathrm{m\,s^{-1}}$ loading speeds. G_{IIc} is loading speed sensitive for both materials, but the influence is positive for CF/PA6 and negative for GF/PA6. The reason underlying such a phenomenon is the difference between fracture mechanisms. CF/PA6 faced matrix fracture, while GF/PA6 experienced fibre/matrix debonding. As presented in Section 1.1.3, PA6 behaviour is influenced by strain rate with an increasing yield stress, then Todo et al. supposed that the fibre/matrix interface loses strength for higher loading speeds.

1.3.4 Conclusions

Interface testing is extensively studied in the literature and standardised for adhesive joints and delamination of composites tested in quasi-static. A diversity of testing rigs and specimens can be used to investigate the composite interface behaviour from quasi-static to moderated and high strain rates. If the testing processes are standardised for quasi-static testing, issues are still unsolved for the dynamic loadings. The use of classical tests for the fracture toughness evaluation as DCB configuration faced complications resulting in a mixed mode loading I/II because of the unsymmetrical specimen opening. Mode II testing also faced difficulties with force measurements complicated to use due to noise in the signal and instability of crack propagation. Nevertheless, using SLJ and DLJ specimens to evaluate the joint performances (mostly bonded joints) is easier for dynamic loadings.

Delamination lacks consensus on the effect of dynamic loading on fracture toughness for several materials. According to some authors, some influences obtained by other studies come from a wrong evaluation of the quantity using the force signal, which is unreliable in some cases. In most cases, for high performances composites (CF/epoxy, CF/PEEK), a decrease in fracture toughness is observed for dynamic loadings, and some studies report no influence. Concerning bonded interfaces, the possibility of performing tests on the bulk adhesive leads to a good comprehension of the material at the interface. Finally, the joint strength results obtained from SLJ and DLJ specimens are not questioned. However, it is the combined results of the joint and substrates' strength. The interface performance can be defined numerically from that result using an inverse method.

1.4 Modelling the dynamic behaviour of composite materials and interfaces

The three previous sections focused on the experimental phenomena concerning TP composites, ultrasonic welding process and strain rate influence on interfaces. The following section presents the numerical methods used to describe these several elements. The first part introduces the modelling of strain rate sensitive composite behaviour. The focus is made on the constitutive model used in this work because this model is suitable for quasi-static and

dynamic studies, and the main objective is to study the welded joint. The second part describes the numerical modelling for composite interfaces and the addition of strain rate sensitivity. Again, several methods are presented because no model was initially privileged for this study.

1.4.1 Constitutive models for composite materials

Constitutive models for quasi-static behaviour of polymer composites

As presented in Subsection 1.1.2, composite behaviour is a combination of elastic and inelastic behaviours, in particular for off-axis directions. A description of the damage evolution was proposed at the LMT in Cachan by Ladeveze and LeDantec (1992). This model was initially developed for UD elementary ply and then applied to several types of composites (TS and TP-based, woven reinforcement); the differences between UD and woven composites will be detailed afterwards. For UD composites, irreversible strains are represented in shear and for in-plane transverse direction, and damage is taken into account for longitudinal, transverse and shear directions. The damage variables represent fibres fracture, matrix microcracking and fibre/matrix debonding. In addition to the constitutive model, a strategy of parameters' identification is proposed in (Ladeveze & LeDantec, 1992). Hence, from tensile tests on $[0,90]_{2s}$, $[\pm 45]_{2s}$ and $[\pm 67{,}5]_{2s}$, all the parameters are experimentally determined. A suitable correlation between experiments and numerical results is obtained (Figure 1.40).

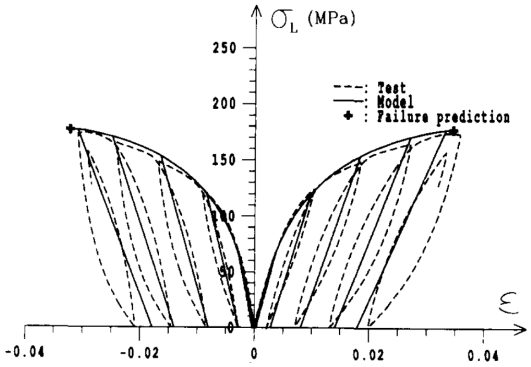

Figure 1.40 – Comparison of experimental and numerical results for $[\pm 45]_{2s}$ (Ladeveze & LeDantec, 1992)

This model was extended by Rozycki and then Marguet to woven composites, on a GF/epoxy laminate (Rozycki, 2000; Marguet, 2007). Irreversible strains only concern the shear behaviour because of the fibres oriented in the warp and weft directions. The damage is linked to the fibre tensile strength for warp and weft directions; then, the matrix drives the damage and fracture for the shear direction. Hence, the damage variables can be uncoupled contrarily to the UD model. Therefore, it requires testing of $[0]_{2s}$ and $[\pm 45]_{2s}$; tests should also been performed on $[90]_{2s}$ in case of not equilibrated reinforcement. This model was finally extended to describe the behaviour of GF/PA66 during the COPERSIM-Crash project (Mbacké & Rozycki, 2018). This model will be used in this work as it successfully defines the elastic and irreversible behaviours of laminates.

Addition of the strain rate sensitivity

The addition of the strain rate influence on the elastic and plastic behaviour may be done by several methods. Johnson-Cook model is an example of the strain rate sensitivity for metals (Johnson, 1983). This empirical model describes viscoplasticity and can be used for adiabatic transient dynamic tests because it considers the temperature's influence on hardening.

Rozycki (2000) introduced a strain rate dependence of mechanical properties for composites crashworthiness. GF/Epoxy is described as a viscous elastoplastic material. The rate-sensitive mechanical properties become a function of the strain rate with a formulation of viscous functions; this modelling choice is close to the Johnson-Cook model. The quantities and strain rate are normalised using a reference

strain rate. Damage is expressed as a function of the energy released rate: linear functions are considered for longitudinal and transverse damages while a logarithmic function is better describing shear damage evolution for woven composites. Linear functions suitably define damage evolutions for UDs.

Based on this model, Mbacké and Rozycki (2018) adapted the laws for GF/PA66 woven 2×2 twill. Larger shear strains are reached for this type of material because of the thermoplastic matrix. In addition, significant fibre bundle reorientation is observed during the tensile test, which affects the damage variable's evolution. In contrast with the model developed for GF/epoxy, a logarithmic function could not describe the damage evolution until the fracture; consequently, the damage evolution in shear is described with a function defined by pieces with a logarithmic and then a linear function. Figure 1.41a shows that this damage evolution associated with the irreversible behaviour considered results in a suitable description of the GF/PA66 shear behaviour. Finally, this model was developed and validated for several couples of temperature and relative humidity in the material, from $-40\,°C$ to $80\,°C$ and from RH $0\,\%$ to RH $85\,\%$ respectively. Coussa (2017) proposed another model for this material based on the dynamic cycled loading tests. Instead of the function defined by pieces suggested by Mbacké and Rozycki, a continuous function describing the exponential increase of crack density is used. Moreover, the damage evolution does not depend on strain rate according to the measurements, contrary to the assumptions made in the previous model. Coussa's model (Figure 1.41b) also gives a suitable description of GF/PA66 strain rate dependency for large strains.

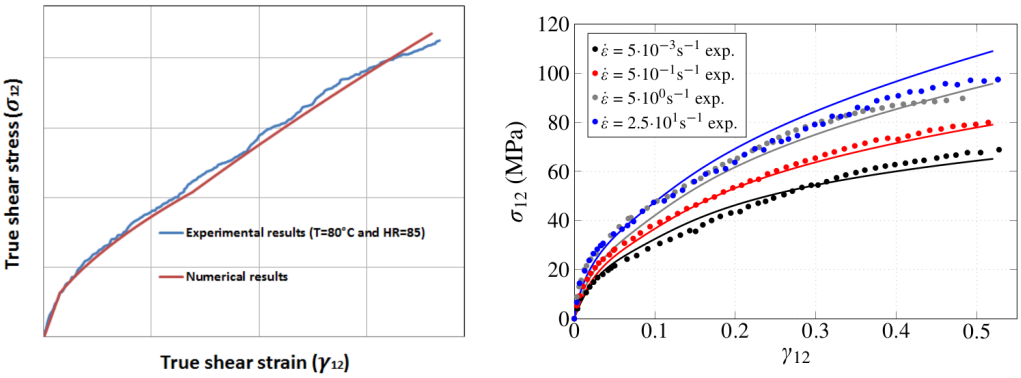

(a) T 80 °C - RH 85 % (Mbacké & Rozycki, 2018) (b) (Coussa, Renard, Joannès, et al., 2017)

Figure 1.41 – Numerical modelling of GF/PA66 shear behaviour for several strain rates

1.4.2 Constitutive models for interfaces

A wide variety of models exist to describe the behaviour of interfaces. Continuum mechanics, fracture mechanics, e**X**tended **F**inite **E**lement **M**ethod (X-FEM) or damage mechanics can be used to model the rupture of materials or interfaces. As the fracture path is known in advance for welded composite joints, with a fracture between outermost plies in quasi-static for a suitably-controlled process, the use of a cohesive zone model seems appropriate, based on damage mechanics. Cohesive elements are presented in this subsection, from the quasi-static definition to the addition of strain rate influence. Moreover, several constitutive models that can be used are described.

Cohesive zone models defined by traction-separation laws

Cohesive zone models are used to describe interface behaviour or cracks until fracture along a path known before fracture. Hence, these elements are adapted to describe the composite delamination or the facture of adhesive joints. This formulation is based on the work of Dugdale (1960) and Barenblatt (1962) to represent irreversible mechanisms ahead of the crack tip. This method uses the displacement

jump δ (separation) between adjacent continuous elements, i.e. displacement between two faces of the cohesive element (Figure 1.42). The separation δ is linked to the strain by Equation 1.3. Three other physical quantities are needed to describe the behaviour: the stress threshold σ^0, the energy dissipated by the cohesive elements G_c (fracture toughness) and the damage d. These quantities can be linked by a traction-separation law, otherwise known as the cohesive law. Different forms are generally used for the traction-separation law. The most used is the bilinear law (Figure 1.43).

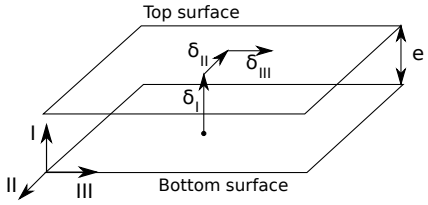

Figure 1.42 – Decohesion model

$$\delta = \varepsilon e \tag{1.3}$$

Figure 1.43 – Bilinear traction-separation law

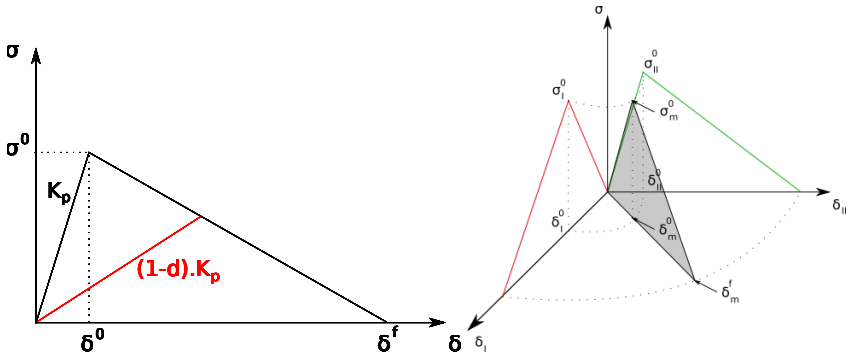

(a) Pure mode (b) Mixed modes

The law above can be used to describe the behaviour of an interface in mode I or pure mode II or III. However, some types of loading result in mixed-mode loading. Therefore, the cohesive element must be able to describe this behaviour if several modes are coupled (Figure 1.43b).

Influence of the traction-separation law shape

Different forms of traction-separation law are currently used in the literature. In the previous section, the bilinear law was presented as it is the most commonly used, which is generally included in finite element codes such as LS DYNA or Abaqus. The trapezoidal and exponential laws can also be used to describe more ductile or fragile interfaces (Figure 1.44).

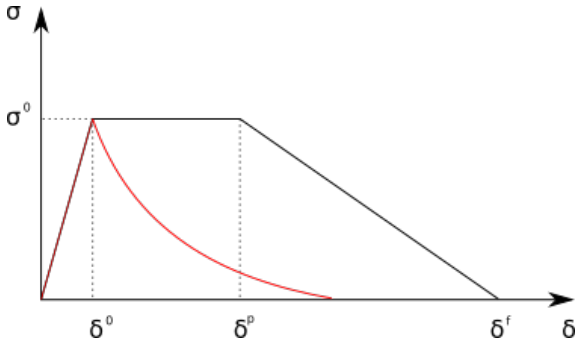

Figure 1.44 – Trapezoidal and exponential traction-separation laws

Damage evolution of the trapezoidal law is presented in Equation 1.4 and in Equation 1.5 for exponential law.

$$d = 1 - \frac{\delta^0}{\delta}\left(1 - \frac{1 - e^{-\alpha(\delta-\delta^0)/(\delta^f-\delta^0)}}{1 - e^{-\alpha}}\right) \quad (1.4)$$

$$d = \begin{cases} 1 - \frac{\delta^0}{\delta}, & \text{if } \delta^0 \leq \delta \leq \delta^p \\ 1 - \frac{m\delta+b}{K\delta}, & \text{if } \delta^p < \delta \leq \delta^f \end{cases} \quad (1.5)$$

with m and b defined by Equation 1.6 and Equation 1.7, and α a parameter.

$$m = \frac{-\sigma^0}{\delta^f - \delta^p} \quad (1.6)$$

$$b = \frac{\sigma^0.\delta^f}{\delta^f - \delta^p} \quad (1.7)$$

The choice of the cohesive law shape must be made according to the interface behaviour. Campilho et al. (2013) investigated the influence of the traction-separation law shape on numerical results. Tensile tests on SLJ specimens were used as reference results to determine which law shape is the most appropriate for a given adhesive [2]. The tests were carried out on composites bonded with two epoxy adhesives: one ductile and one brittle. From a numerical point of view, three laws were used: bilinear, trapezoidal and exponential. The laws' parameters were determined from tests carried out on the pure adhesives. The results comparison showed that the choice of the law shape has a limited effect on the results for the brittle adhesive (Figure 1.45). A bilinear traction-separation law is suitable for describing the interface behaviour. However, significant differences were observed depending on the law in the case of the ductile adhesive. Better results, especially on the maximum stress value, are obtained for trapezoidal and bilinear laws. A trapezoidal law is more suitable for describing the ductile behaviour of the interface due to the plateau. Thus, the law shape seems to have a significant influence in the case of a ductile material in the interface compared to a brittle material.

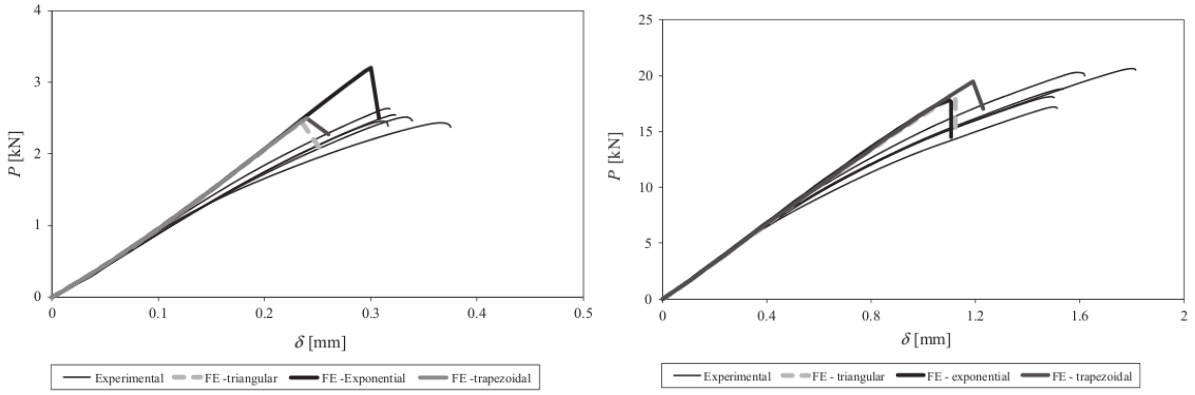

(a) Ductile adhesive (b) Fragile adhesive

Figure 1.45 – Comparison of experimental and numerical results for different σ-δ law shapes (Campilho et al., 2013)

In the case of a mixed-mode description of the interface behaviour, different laws can be used for each mode: a bilinear law was used to describe the behaviour of the bonded interface loaded in mode I and a trapezoidal for mode II (May et al., 2014). The plateau length is used to define the degree of plasticity of the interface (Figure 1.46a). Finally, the mixed mode behaviour for bilinear behaviour in mode I and trapezoidal behaviour in mode II is described in Figure 1.46b.

Addition of the strain rate influence in cohesive elements

Marzi et al. (2009) proposed a model of a cohesive zone depending on the strain rate. This model has been used by May et al. (2014) to model the behaviour of bonded metallic and composite structures but

2. The adherents used here are unidirectional carbon/epoxy composites $[0]_{16}$

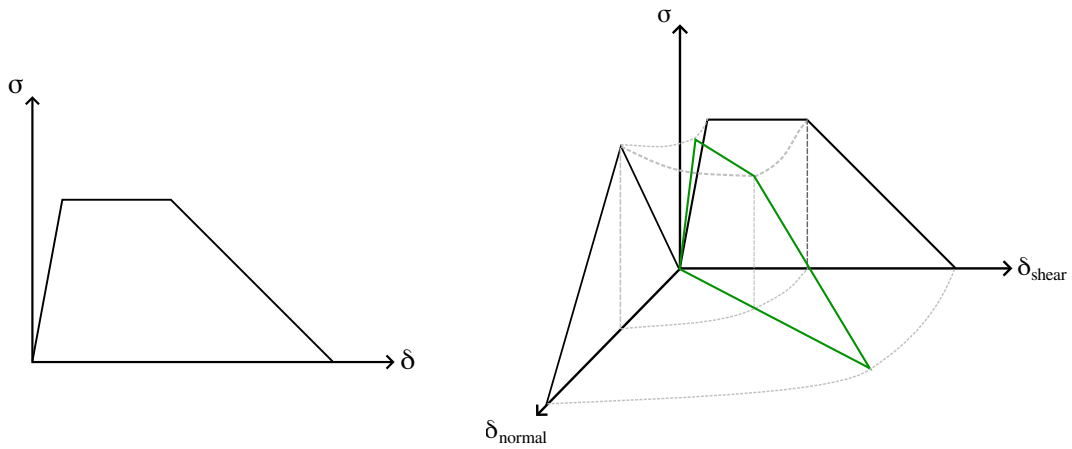

(a) Trapezoidal σ-δ law (b) Coupling of a bilinear and trilinear σ-δ laws

Figure 1.46 – Application of trapezoidal traction-separation law (based on (May et al., 2014))

also for delamination. This model is based on the evolution of two properties of the cohesive zone (G_c and σ^0) as a function of the strain rate.

The evolution of the damage initiation stress is proposed using viscous functions (Equation 1.9). The strain rate is defined in the cohesive elements with the following expression:

$$\dot{\varepsilon}_j = \frac{d\varepsilon_j}{dt} \tag{1.8}$$

with $j = \{I, II\}$ corresponding to mode I (normal mode) and mode II (shear mode), respectively and ε_j the strain corresponding to the mode j.

$$\sigma_j^0(\dot{\varepsilon}_j) = \begin{cases} \sigma_j^{0,QS} & \text{if } \dot{\varepsilon}_j \leq \dot{\varepsilon}_{j,ref} \\ \sigma_j^{0,QS}.\left(1 + C.ln\left(\frac{\dot{\varepsilon}_j}{\dot{\varepsilon}_{j,ref}}\right)\right) & \text{if } \dot{\varepsilon}_j > \dot{\varepsilon}_{j,ref} \end{cases} \tag{1.9}$$

The fracture toughness is also described with viscous functions (Equation 1.10).

$$G_{jc}(\dot{\varepsilon}_j) = \begin{cases} G_{jc}^{QS} & \text{if } \dot{\varepsilon}_j \leq \dot{\varepsilon}_{j,ref} \\ G_{jc}^{QS}.\left(1 + m.ln\left(\frac{\dot{\varepsilon}_j}{\dot{\varepsilon}_{j,ref}}\right)\right) & \text{if } \dot{\varepsilon}_{j,ref} < \dot{\varepsilon}_j \leq \dot{\varepsilon}_{j,max} \\ G_{jc}^{max} & \text{if } \dot{\varepsilon}_j > \dot{\varepsilon}_{j,max} \end{cases} \tag{1.10}$$

Other laws can be used depending on the interface modelled and the influence of loading speed. The most suitable evolution can be determined from tests carried out on the material at the interface by plotting the evolution of the maximum stress and the critical energy restitution rate as a function of the strain rate. Several authors define the damage initiation stress evolution with a logarithmic law (Marzi et al., 2009; May et al., 2014; May et al., 2015; Liu et al., 2018; Borges et al., 2020). An exponential law was used by Marzi et al. (2009) to describe the evolution of critical energy. These laws can also be more complex such as the use of polynomial laws by May and Lässig (2017).

Thus, the dynamic traction-separation law is described by Figure 1.47. The black curve corresponds to the quasi-static traction-separation law, and the red curve describes the behaviour for a higher strain rate. The formulation of the strain rate influence on the initiation stress and the critical energy restitution rate makes it possible to describe an increasing effect of these properties with the strain rate but also a decrease when the strain rate increases, depending on the sign of the parameters C and m. No strain rate

dependence of the stiffness is considered in this model.

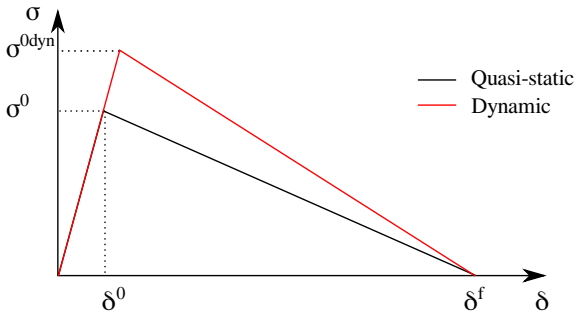

Figure 1.47 – Bilinear traction-separation law with strain rate sensitivity

In this model, once the damage is initiated, the traction-separation law is fixed; i.e. after σ^0, the curve no longer evolves as a function of the current strain rate. An extension of this model has been proposed in (May, 2015; May et al., 2015) to take into account the strain rate influence before and after the damage initiation. The strain rate may vary during a test even after the damage initiation, so it may be interesting to integrate this influence into the model. The main assumption is that the energy release rate achieved at the moment of failure corresponds to the critical energy for the current strain rate. At that time, the currently damaged stiffness is used to change from the dashed-dotted curve to the dotted curve. Once the strain is reached, the dotted curve describes the damage in the interface.

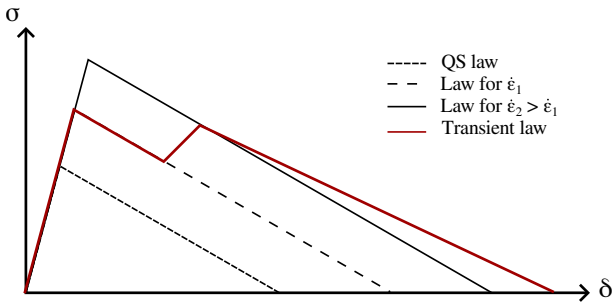

Figure 1.48 – Traction-separation law with influence of strain rate on all the domain (May et al., 2015)

This model was initially used to model the behaviour of structural steel bonds in (May et al., 2015). Experimental tests and numerical simulations show that, in the case of this adhesive, the use of a strain rate sensitive model until failure neither deteriorates nor improves the numerical results obtained with the strain rate dependent model until damage initiation. In the second step, it was possible to study the delamination of composites from a numerical point of view (May, 2015). It appears that the addition of the strain rate influence on the whole traction-separation curve affects the size of the delaminated zone. The extension of the model proposed by May et al. (2014) could be interesting in cases such as delamination if the original model does not allow a suitable description of the damaged area.

May et al. have implemented this model to describe the mode II delamination behaviour of a PEEK/CF composite. On the one hand, this study shows that it is necessary to integrate the influence of the strain rate in the interface behaviour model. On the other hand, the model proposed accurately describes the behaviour of a DCB test for dynamic loading. Figure 1.49 shows that the strain rate independent cohesive zone model does not correctly predict the crack length evolution for the highest loading rates (Liu et al., 2018).

Jiang et al. (2007) considered another damage evolution. The cohesive zone model is described with a bilinear law, but the damage evolution is linear (Equation 1.11) in contrast to the classical definition of the Equation 1.12, which uses a polynomial function. In this model, the damage directly influences the stress and does not affect the stiffness, unlike the model previously described. The idea here is to have an indicator of the interface state. In addition, a linear damage evolution could simplify the stability issues encountered with non-linear laws while maintaining a bilinear traction-separation law. The damage increases slowly with increasing displacement jump (Figure 1.50). Initially defined for quasi-static,

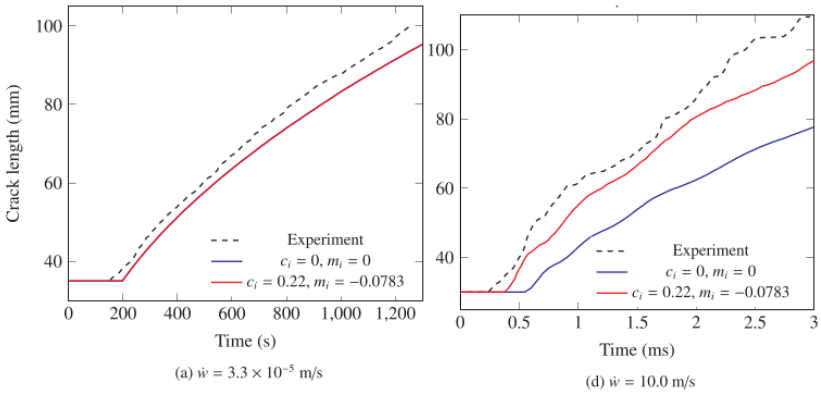

Figure 1.49 – Crack length obtained experimentally and numerically for a DCB test on a CF/PEEK for several loading speeds, with and without strain rate effect for the cohesive elements (Liu et al., 2018)

this model was taken up by May and Lässig (2017) to consider the strain rate influence on the maximum stress and the energy restitution rate (using parabolic functions on a semi-logarithmic scale here). This cohesive zone model allows the delamination behaviour of ballistic composites to be modelled.

$$d = \begin{cases} 0 & \text{if } \delta^{max} \leq \delta^0 \\ \dfrac{\delta^{max} - \delta^0}{\delta^f - \delta^0} & \text{if } \delta^0 \leq \delta^{max} \leq \delta_f \\ 1 & \text{if } \delta^{max} \geq \delta^f \end{cases} \quad (1.11) \qquad d = \begin{cases} 0 & \text{if } \delta^{max} \leq \delta^0 \\ \dfrac{\delta^f}{\delta^{max}} \dfrac{\delta^{max} - \delta^0}{\delta^f - \delta^0} & \text{if } \delta^0 \leq \delta^{max} \leq \delta_f \\ 1 & \text{if } \delta^{max} \geq \delta^f \end{cases} \quad (1.12)$$

with $\delta^{max} = \underset{t>0}{max}\{\delta(t)\}$.

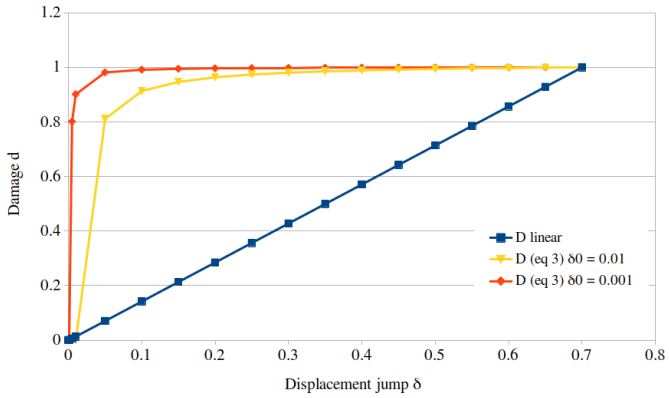

Figure 1.50 – Evolution of damage depending on the displacement jump for a classical definition and linear one (graph plotted from (Jiang et al., 2007))

Cohesive elements using other laws

Another method used in the literature defines the traction-separation law from a rheological model. This definition may be helpful to describe the fracture of bulk material. Indeed, it permits the development of a constitutive model for the crack consistent with the material behaviour model. Moreover, the strain rate influence can be included. Musto and Alfano (2013) used a rheological model (Figure 1.51) to describe the propagation of a crack in rubber. Results show a suitable correlation with experiments performed at high strain rates. Nevertheless, the viscoelastic model used in this example is relatively simple (one relaxation time) and describes the behaviour only for two decades of strain rate.

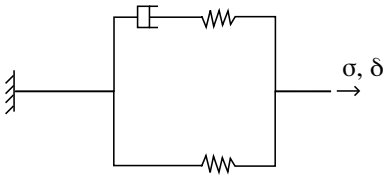

Figure 1.51 – Rheological model used to describe the fracture of a rubber in mode I (Musto & Alfano, 2013)

These model limit discontinuities caused by the strain rate evolution during the loading in contrast to

the models proposed in (May et al., 2015). However, this model was developed only for mode I loading on rubber without considering mixed modes.

Bilinear and trilinear traction-separation laws have drawbacks, especially in dynamic explicit, because of the singularities of their definition (transition between elastic and damaged domain or even during the rupture). In that respect, some authors tried to address this issue using continuous laws. Pinho et al. (2006) implemented two continuous laws in the finite element software LS DYNA, the first is order 3 polynomial (Equations 1.13 and 1.14) and the second is linear-polynomial (Equations 1.13 and 1.15). Figure 1.52 presents that for both models proposed by Pinho et Al., fracture and damage initiation are smoother than the bilinear model. A numerical trial was made on DCB and MMB tests for CF/ epoxy; it showed that polynomial and linear/polynomial laws are more stable than the triangular law. These two models have not been used to include the strain rate influence to the author's knowledge.

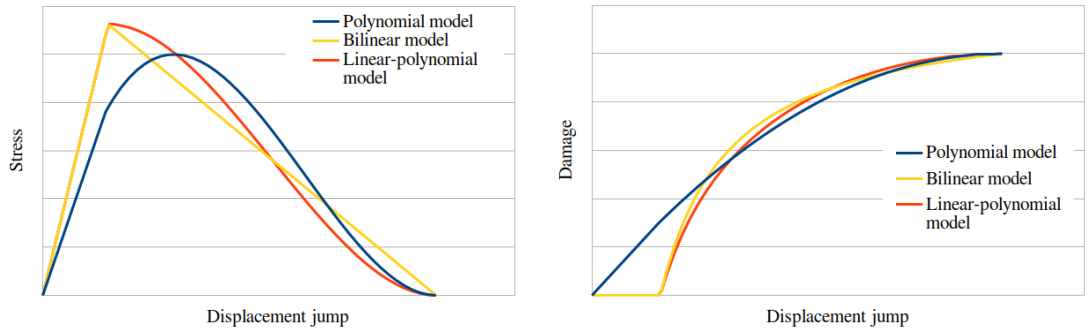

(a) Traction-separation laws (b) Evolution of damage

Figure 1.52 – Comparision of both model described in (Pinho et al., 2006) and bilinear traction-separation law

$$\sigma = K\delta\,(1-d) \qquad (1.13) \qquad d = 2\frac{\delta}{\delta^f} - \left(\frac{\delta}{\delta^f}\right)^2 \text{ for } \delta \leq \delta^f, 1 \text{ for } \delta > \delta^f \qquad (1.14)$$

$$d = 1 - \frac{\delta^0}{\delta}\left[1 + \left(\frac{\delta-\delta^0}{\delta^f-\delta^0}\right)^2\left(2\frac{\delta-\delta^0}{\delta^f-\delta^0} - 3\right)\right] \text{ for } \delta^0 < \delta \leq \delta^f, 0 \text{ for } \delta \leq \delta^0 \text{ and } 1 \text{ for } \delta > \delta^f \qquad (1.15)$$

1.4.3 Conclusions

The purpose of this section was to present existing models to describe the behaviour of composites and interfaces for several rates. The constitutive model proposed by the LMT offers a relatively simple description of the elementary ply, which has been successfully adapted for woven composites and extended to include strain rate dependency. This model was also successfully employed to describe the behaviour of TP composite dependent on humidity and temperature. This modelling strategy will be used in this work to describe the composite behaviour. Concerning interface modelling for several loading speeds, cohesive elements are well-suited to describe the interface fracture. The traction-separation law can be defined according to the material behaviour at the interface (ductile or fragile), and the strain rate sensitivity may be included using viscous functions for the time-dependent mechanical properties.

1.5 Research interests

The use of welding methods is growing in the transport industry for TP composite structures. In that context, the use of these joining methods for structures validating a high level of crashworthiness requires experiments, and the weld's modelling to be able to use numerical predictions. Experiments can

feed the model to simulate the performance of welds from quasi-static to moderate loading speeds and thus validate the structure before final experiments. As presented in the literature review, the strain rate sensitivity of several TP matrices and composites raises questions about the possible strain rate sensitivity of composites' welds. The same interrogations can be valid for temperature and RH sensitivities for TP composite affected by these environmental conditions, which have already been investigated for CF/PPS welds (US and resistance welding). In addition, some studies on bonded joints and delamination for quasi-static and dynamic loadings report a loading speed influence on the behaviour. Nevertheless, no study in the literature investigates the loading speed influence on the welded TP composite joints. Therefore, experimental characterisation of these joints is required from quasi-static to dynamic loadings to create a database and define a numerical model on the strain range considered for the welded joints' behaviour.

The literature review about interface testing at high loading speed highlights the difficulties measuring the fracture toughness in pure mode I or II using DCB or ENF specimens. Therefore, simple specimens will be used in this work to study mixed mode and shear loadings: traction-loaded SLJ and DLJ specimens, respectively. The welded specimen's global behaviour is studied in light of the experimental and numerical knowledge of the laminate behaviour. The experimental results and the constitutive model developed for GF/PA66 during the COPERSIM-Crash project are used and provide knowledge on the elastic and irreversible behaviour of the laminate considering damages and, more importantly, its strain rate dependence. The weld behaviour is identified using an inverse method because SLJ and DLJ do not allow a separation of the joint and substrates' behaviour from simple operations on experimental measurements. Inverse methods involve having a suitable description of the substrate behaviour and boundary conditions to let only the weld behaviour to determine. These conditions apply to this work with the COPERSIM-Crash project results for the laminate (Chapter 2) and the characterisation of welded specimens (Chapter 3).

The composite used in this work was characterised in a previous project, experimentally and numerically, and then it was stored in an uncontrolled environment. Some tensile tests were performed here to validate the behaviour after storage (temperature and moisture cycles over the years) because of the possible chemical ageing phenomenon, even if it should be limited (Bernstein & Gillen, 2010). The constitutive model developed in (Mbacké & Rozycki, 2018) was used; some mechanical properties and model parameters were adjusted based on the results of the tensile tests. An extensive description of the substrate is presented in Chapter 2, from the data obtained in the project COPERSIM-Crash to the validation of the constitutive model parameters after storage. The database on the dynamic behaviour of welded TP composites is opened with an experimental testing campaign of two weld configurations, proposed in Chapter 3. The mechanical performance of joints is assessed by tensile tests on single-lap and double-lap joint specimens for loading speeds from $2 \times 10^{-5}\,\mathrm{m\,s^{-1}}$ to $7\,\mathrm{m\,s^{-1}}$. Tests could not be done at higher loading speeds due to the specimen geometry and the tensile test machine used. The mesoscopic aspect of the weld and the fractography were analysed to improve the understanding of the mechanical results. These experimental results serve as a basis for defining a constitutive model for the weld valid on the range of loading speed tested. Chapter 4 introduces the model used for the weld using cohesive elements and the methodology implemented to identify the parameters using an inverse method. The parameters are identified for quasi-static tests. Then, the model parameters are applied to dynamic tests. In case of a significant difference between numerical and experimental results, a suitable set of parameters are identified for the loading speed considered. Based on these results, a strain rate dependent model is defined and validated. Finally, the conclusions of the work, with the combined views of experimental and numerical results, are presented in the last chapter with the perspectives.

Chapter 2

Behaviour of GF 2×2 twill woven/PA66

Abstract: *The major experimental study of this work is done by investigating welded specimens' global behaviour. It is necessary to have a strong knowledge of the laminate behaviour to analyse the results and apply an inverse method to identify the weld's constitutive model parameters. This chapter describes the knowledge acquired about GF/PA66 during the COPERSIM-Crash project (Mbacké & Rozycki, 2018; Rozycki et al., 2018; Dau, 2019) and this PhD thesis. The composite behaviour was studied experimentally from quasi-static up to* $60\,\mathrm{s}^{-1}$ *and* $470\,\mathrm{s}^{-1}$ *in longitudinal and shear directions, respectively. In addition, several temperatures and moisture levels were studied. The experimental results are summarised in the first section. The data post-processing and the constitutive model developed and implemented during the project are also presented (Mbacké & Rozycki, 2018). This model has been used for the substrates' modelling in numerical simulations of welded specimens. All these results highlight the strain rate sensitivity of the laminate; in consequence, the suggested model includes this phenomenon. Tensile tests were performed for the current work to verify that no ageing or other phenomenon affected the composite behaviour due to its storage for five years. The present results are compared to the previous project results to validate the laminate behaviour after storage, which is required for the welded specimen's modelling.*

Contents

Introduction to the characterisation and modelling of GF/PA66

The study of welded TP composites requires experimental work to extract the weld's behaviour and define its constitutive model. Unfortunately, measurements could not be made directly on welds as they are part of structures. Lap joint specimens' behaviour under tensile tests is a combination of substrate and interface behaviours that cannot be separated easily. Therefore, the welded joint's behaviour identification should be achieved using numerical simulations of the experiments. Hence, a proper comprehension, description and modelling of the non-welded laminates were required to control the laminate behaviour in the welded composite model. Thus, it let only the welded joint constitutive model as the unknown, which may be defined using an inverse method.

Poly**A**mide 66 reinforced by a **G**lass **F**abric 2×2 twill woven (GF/PA66) was studied during the COPERSIM-Crash project for several conditions of temperature, moisture and strain rate. First, the aim was to quantify the influence of these three conditions on the composite behaviour for longitudinal and shear directions. Second, a constitutive model was developed to predict the crashworthiness of GF/PA66 structures, considering the laminate strain rate dependence for several thermal and moisture conditions. The constitutive model properties were defined from the experimental data.

The first section reviews the knowledge acquired experimentally on the composite at room temperature, from quasi-static to dynamic loadings and for three moisture levels. It also motivates the choice of environmental conditions for the current work. The second section describes the constitutive model developed and implemented by Mbacké and Rozycki (2018) for the GF/PA66, validated from quasi-static to dynamic loadings with a subroutine (VUMAT) in the **F**inite **E**lement (FE) software Abaqus (*ABAQUS / Dynamic User's Manual*, 2019). The protocol used to define the model parameters from experimental and dynamic results is also explained. Following that review, some tensile tests were performed to verify that no phenomena linked to the material storage have led to a modification of the elementary ply behaviour.

2.1 Knowledge about GF/PA66 in-plane behaviour

The composite of interest is a GF/PA66 with 50 % of fibres in volume and 70 % in weight. A four-ply laminate was manufactured by compression moulding (Solvay company). The reinforcement and so the ply is quasi-balanced. Therefore, for the rest of the study, the transverse direction behaviour is assumed to be equal to the longitudinal one. Tensile tests were performed for several temperatures, RH, orientations and strain rates. The two laminates tested are a $[0]_4$ and $[45]_4$ used to study the longitudinal and shear behaviour of the elementary ply, respectively. First, the specimen used for quasi-static is presented with the protocol adopted for specimen conditioning (desorption and ageing). Then, the quasi-static in-plane behaviour is introduced with its elastic-damage longitudinal behaviour and elastoplastic-damage shear behaviour. The influences of the temperature and RH on these behaviours are summarised. Second, the dynamic behaviour of the laminate is presented. All the results in this section were obtained during the COPERSIM-Crash project (Dau, 2019; Rozycki et al., 2019).

2.1.1 Specimen's geometry and conditioning

Tensile tests were conducted on rectangular specimens (Figure 2.1) using a quasi-static tensile test machine (Instron 5584 - 150 kN), an experimental device from the **C**entre de **R**essources en **E**ssais **D**ynamiques (CRED) at Centrale Nantes. The specimen dimensions were selected to ensure that 1.5 **R**epresentative **V**olume **E**lementary (RVE) is contained in the width to be able to extract the elementary ply behaviour. The RVE size is 15 mm × 15 mm for 0°-oriented specimen and 10.6 mm × 10.6 mm for 45°-oriented specimen.

PA66 matrix is known for its sensitivity to temperature and RH due to the presence of amide groups,

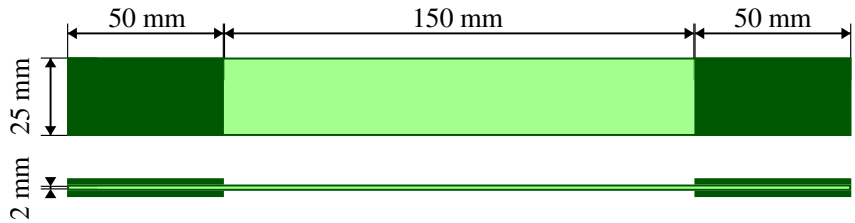

Figure 2.1 – Rectangular specimens for quasi-static characterisation of GF/PA66 (Rozycki, 2017)

principally in the amorphous part (Obeid, 2016). Knowledge about these environmental conditions is essential for using this laminate in the transport industry. Therefore, three temperature levels were investigated in the COPERSIM-Crash project ($-40\,°C$, $+23\,°C$ and $+80\,°C$) and three RH levels (RH $0\,\%$, RH $50\,\%$ and RH $85\,\%$). The temperature influence was investigated using a thermal chamber surrounding the specimen on the tensile test machine. Concerning the relative humidity level, drying and ageing processes were carried out prior to the test to achieve the required moisture level in the material. Therefore, a desorption and ageing protocol for GF/PA66 was defined in the COPERSIM-Crash project.

Desorption protocol

Specimens are placed in a desiccator (BINDER Vacuum drying chamber - Figure 2.2a) at a fixed temperature, superior to ambient temperature. This choice accelerates the desorption phenomenon but makes it necessary to check whether or not this affects the mechanical properties. Desorption temperature is fixed to $+90\,°C$ as preconise by the material manufacturer. Several temperatures were used by Pivdiablyk (2019) for the desorption of PA6/GF ($+50$, $+70$ and $+90\,°C$), and all the samples showed the same mechanical tensile properties regardless of the drying temperature. For this reason, a temperature of $+90\,°C$ appears to be appropriate from both points of view: maintaining the mechanical properties and reducing the total desorption duration. Furthermore, this desiccator was linked to a vacuum pump to accelerate and improve drying. This method breaks molecule bonds and reaches a deeper level of drying. At the end of the desorption process, a small amount of water may remain in the sample due to the material structure whose elements (polymeric chains particles, fibrous reinforcement) block the elimination of remanent water molecules (Silva et al., 2013); thus, the RH level is not exactly $0\,\%$. Nevertheless, the moisture level is very close to dry as moulded state; hence, RH $0\,\%$ will be used in the remainder of this manuscript to refer to this RH state.

(a) Desiccator BINDER Vacuum drying chamber (b) Specimens placement on racks

Figure 2.2 – Desiccation devices

A gravimetric method is used to measure the moisture desorbed by a sample over time. Three spe-

cimens are weighed at different times during the desorption process to determine the evolution of the mass loss over time (Equation 2.1). When this mass loss reaches the first plateau, the RH is commonly assumed to be close enough to a dry state ('RH 0 %' theoretically).

$$C(t) = \frac{m(t) - m_0}{m_0} \tag{2.1}$$

Figure 2.3 presents a desorption curve measured during the COPERSIM-Crash project. The mass loss starts stabilising after four days ($600\sqrt{s}$) for the three specimens, and the desorption was extended to seven days to ensure the drying of all the specimens in the desiccator.

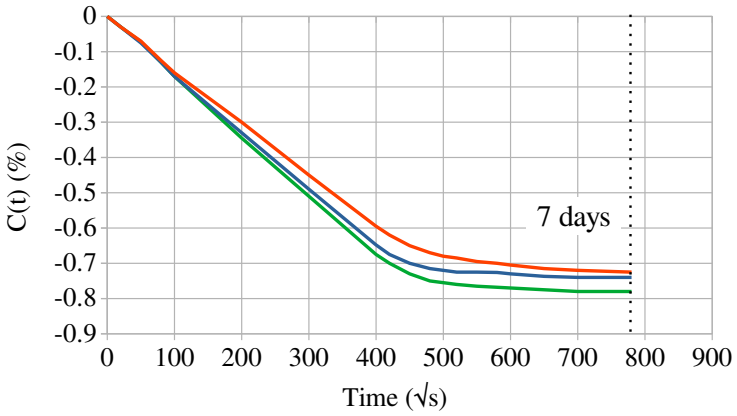

Figure 2.3 – Desorption curve for GF/PA66 0°-oriented (Rozycki, 2017)

Ageing protocol

The ageing protocol is conducted with a climatic chamber (Binder Constant climate chambers KMF 115). The specimens are placed in the chamber at a temperature of +70 °C and an RH level corresponding to the target (RH 50 % and RH 85 %). A similar protocol to the desorption is followed by tracking the mass of reference specimens using Equation 2.1. The moisture uptake is presented in Figure 2.4. Fourteen days ($1100\sqrt{s}$) are required to reach the moisture uptake plateau at RH 50 % and RH 85 %. However, three days were added, as in the desorption process, to ensure the target's safety. Specimens were stored in specific sealed bags to avoid variation in the RH level.

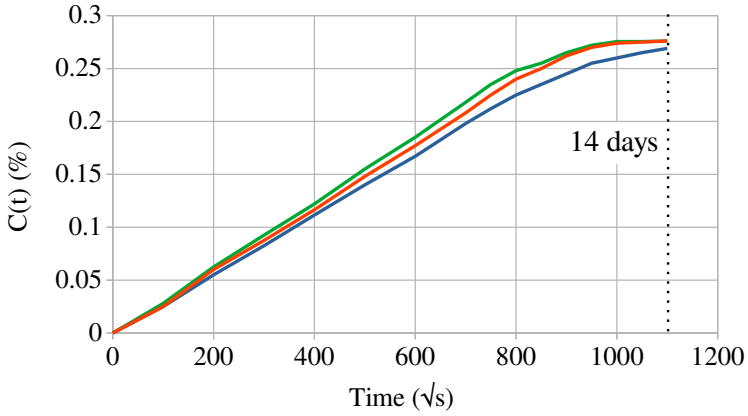

Figure 2.4 – Moisture uptake curve for GF/PA66 45°-oriented (Rozycki, 2017)

Important note on the conditioning protocol duration

Four months were necessary to age the 170 specimens due to the limited size of the climatic chamber and to the separated protocol for RH 50 % and RH 85 % (specimens cannot be aged at the same time for both moisture level). In addition, two months were required to dry the specimens to reach the RH

0 % condition and to prepare the specimens for ageing. These elements showed that despite the acceleration of the drying and ageing processes due to the temperature (compared to room temperature), the duration remains long to prepare the characterisation test samples.

2.1.2 Quasi-static behaviour of GF/PA66 and influence of temperature and hygrometry

Longitudinal behaviour

The longitudinal behaviour is elastic-fragile with damage (Figure 2.5). This orientation is dominated by the weave longitudinal behaviour, leading to a significant elastic modulus and strength and a limited fracture strain. A slight decrease in stiffness is noticed during the tensile test and is caused by damage propagating in the laminate. This damage is located in the glass fibres and at the interface between fibres and matrix. The matrix micro-cracking is limited during the tensile test because the reinforcement carries most of the load. The longitudinal in-plane stress-strain curves of GF/PA66 show no significant influence of the temperature or RH level. The elastic moduli are similar for the three levels of moisture and the three temperatures tested. Finally, for each condition tested, a standard deviation of 6 % on average was observed for the elastic modulus and about 13 % for the strength, which highlights the acceptable reproducibility of the tensile tests for crash applications (the scatterings are commonly larger than for quasi-static tests).

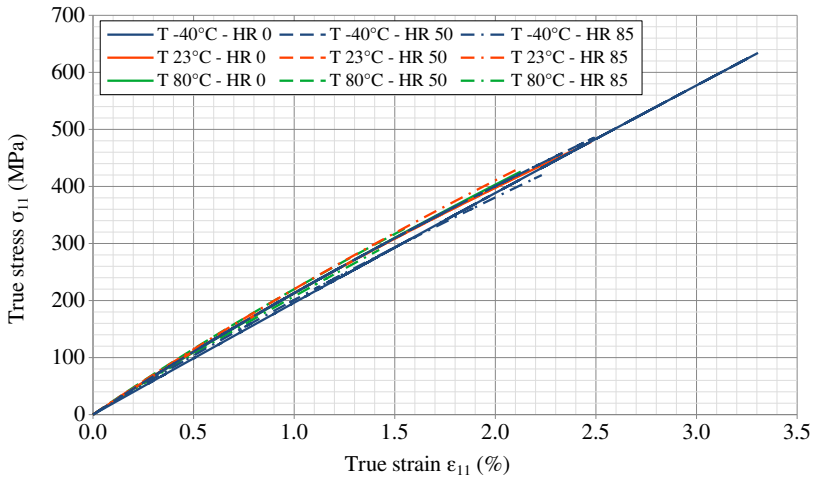

Figure 2.5 – Longitudinal stress - strain curves for several RH and temperature conditions in quasi-static (Rozycki et al., 2019)

Shear behaviour

The shear behaviour is identified from tensile tests on $[45]_4$, first with the envelope curve in red (Figure 2.6 - T 23 °C and RH 0 % results presented as an example). The stress-strain curve highlights an elastoplastic behaviour with damage inherited by the matrix, which dominates the response in this direction. Large strains are reached due to the mechanical properties of the PA66 matrix.

Figure 2.6 shows a cycled tensile test used to quantify the elastic and irreversible strains, composing the total strain measured and damage which affects the shear modulus. Less than six loading-unloading loops were done to avoid fatigue loading. Once the purely elastic domain is exceeded, the slope of loops allows the identification of the damaged shear modulus and the ratio of elastic/irreversible strains as presented for the last loop (Figure 2.6). The post-processing of each cycle provides data for the evolution of the irreversible strains, yield function and damage. These data calculations will be presented in Subsection 2.2.2 with the constitutive model parameters identification.

The shear behaviour is significantly affected by both environmental conditions, with a loss in stiffness observed when the temperature and RH increase (Figure 2.7). 45°-oriented specimens behaviour mainly

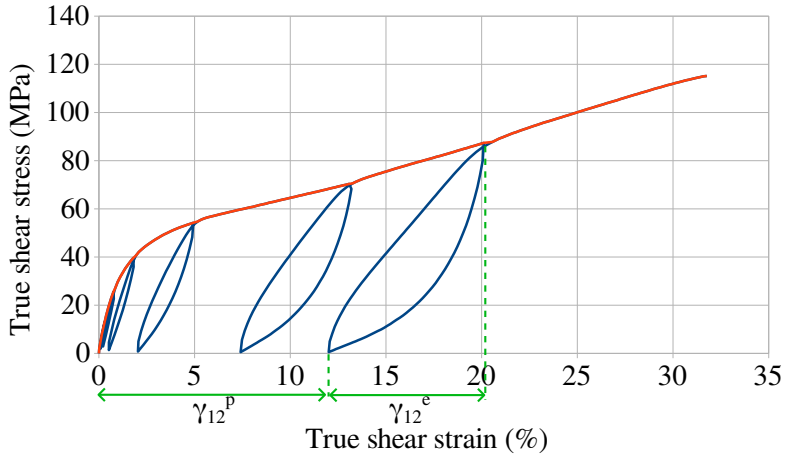

Figure 2.6 – Cycled tensile test on $[45]_4$ - QS shear behaviour - T 23 °C - RH 0 % (Dau, 2019)

relies on the matrix behaviour, which is significantly affected by temperature and RH. As the authors explain, it is linked to the difference between the testing temperature and the glass transition temperature T_g. The T_g values are presented in Table 2.1 for three moisture levels in the laminate. The material is more ductile when the difference between T and T_g is small and when the temperature is higher than T_g, as the material state changes from glassy to rubbery. Moreover, T_g strongly depends on the RH level in the material with smaller values at higher RH levels. An increase in the fracture strain and a decrease in strength join this loss of stiffness.

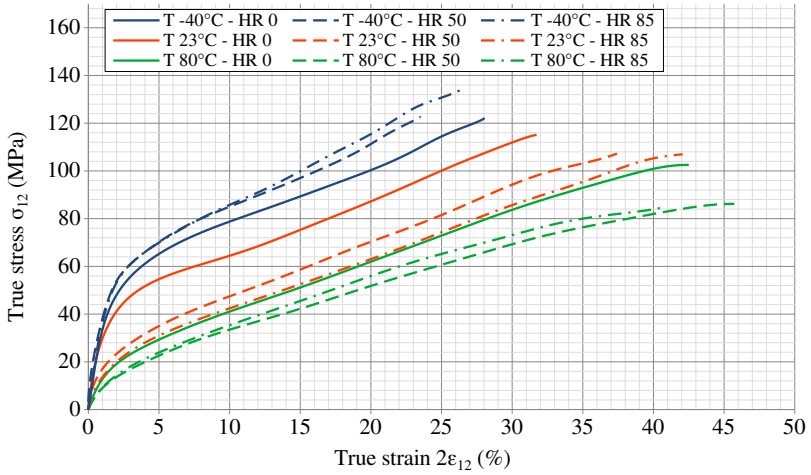

Figure 2.7 – Shear stress - strain curves for several RH and temperature conditions in quasi-static (Rozycki et al., 2019)

Table 2.1 – Glass transition temperatures (T_g) for several RH levels (Dau, 2019)

RH 0 %	RH 50 %	RH 85 %
+60 °C	+23 °C	−10 °C (estimation)

Choice of temperature and RH conditions for the study

As presented in Section 2.1.1, seven days are required for desorption plus fourteen days of ageing for the specimens conditioned at 50 % or RH 85 %, and only a limited number of samples can be aged simultaneously because of the climatic chamber size. In addition, a question may arise concerning the ageing of welded specimens: how to ensure a uniform moisture distribution in the sample (substrates and weld)? Therefore, RH 0 % and room temperature are chosen for the welded specimens' characterisation based on the duration of the conditioning protocol and to provide a uniform RH level within the specimen. Furthermore, due to issues with the welded material supply (beyond our control and that of the company conducting the specimens' welding), the experimental work was postponed and could not be further delayed by the specimens' ageing.

2.1.3 Dynamic behaviour of GF/PA66

Dynamic tensile tests were performed on shorter specimens to promote the strain rates in the specimens (Figure 2.8). The size of the sample was defined to have 1.5 RVE in the loaded area. Moderate strain rates (around $60\,\mathrm{s}^{-1}$ to $470\,\mathrm{s}^{-1}$) can be reached for this type of material with tensile test conducted at $10\,\mathrm{m\,s}^{-1}$, depending on the direction considered.

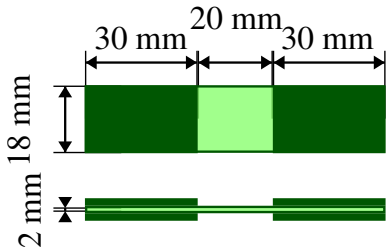

Figure 2.8 – Rectangular specimens for dynamic characterisation of GF/PA66 (Rozycki, 2017)

Concerning the dynamic behaviour of GF/PA66, tensile tests were conducted at four loading speeds in addition to the quasi-static tests ($2\,\mathrm{mm\,s}^{-1}$, $200\,\mathrm{mm\,s}^{-1}$, $2\,\mathrm{m\,s}^{-1}$ and $10\,\mathrm{m\,s}^{-1}$). Dynamic tests up to moderate strain rates ($60\,\mathrm{s}^{-1}$ and $470\,\mathrm{s}^{-1}$ for longitudinal and shear directions) were performed only at room temperature and for the same three RH levels as in quasi-static. The use of a thermal chamber for dynamic tests was not possible for the two highest strain rates tested.

A limited sensitivity of the longitudinal behaviour to strain rate was reported in Dau's thesis, as previously noticed for temperature and moisture influence. This phenomenon can be observed in Figure 2.9 for the longitudinal behaviour at room temperature and RH $0\,\%$. It is caused by the reinforcement behaviour, which carries most of the load in that direction and has been negligibly strain rate sensitive in comparison to the matrix. Even if the strain rate influence seems limited for this orientation compared to shear, it was considered in the constitutive model in the COPERSIM-Crash project to obtain a model as complete as possible.

Figure 2.9 – Longitudinal stress - strain curves for five strain rates at T 23 °C-RH $0\,\%$ (Dau, 2019)

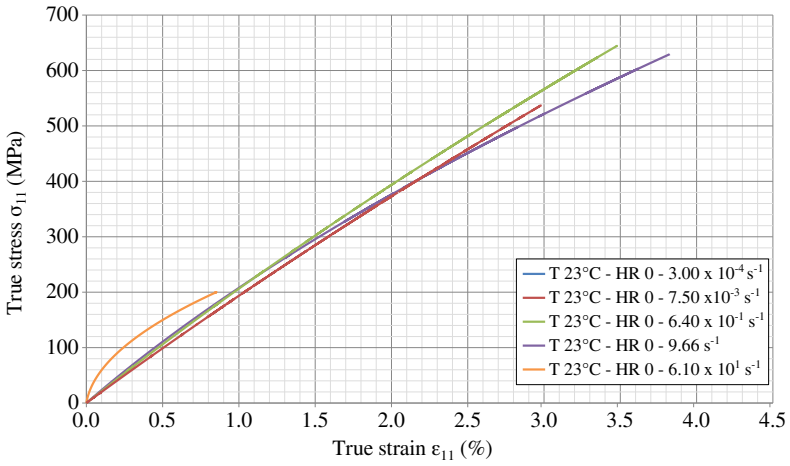

In contrast, the shear behaviour is significantly influenced by temperature, RH and strain rate; it results from the matrix strain rate sensitivity. Figure 2.10 shows the stress-strain curve in shear for several strain rates at RH $0\,\%$. As explained by Dau, a stiffening behaviour is observed up to a critical strain rate (around $60\,\mathrm{s}^{-1}$) from which a softening behaviour is noticed. This change is assumed to result from the material self-heating caused by the adiabatic conditions of the dynamic tensile test. The softening behaviour, resulting from the temperature increases, faces the stiffening caused by strain hardening. For a tensile test at $477\,\mathrm{s}^{-1}$, an averaged temperature of $+60\,°\mathrm{C}$ was measured using an infrared camera for the three RH levels tested. This self-heating leads to the T_g being exceeded in the dry state (Table 2.1), the T_g was already reached or overpassed for RH $50\,\%$ and $85\,\%$. The softening is observed above a critical strain rate for both other RH conditions tested and are presented in Appendix A. In addition, the

surrounding temperature may have been affected by the use of spot lighting which generate heat, and then can modify the testing conditions.

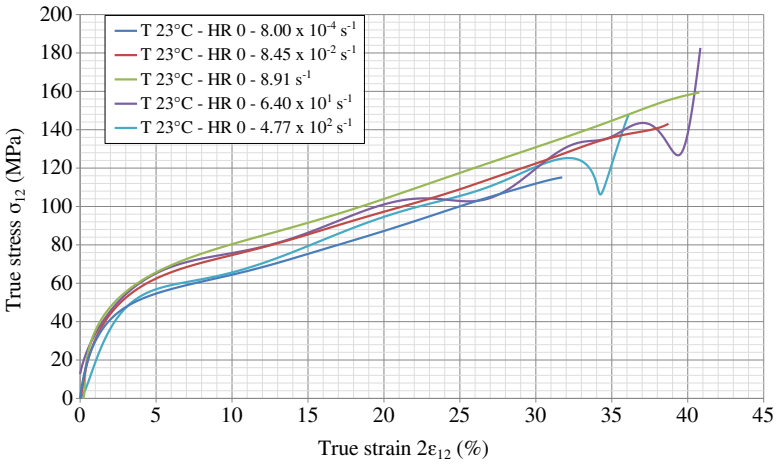

Figure 2.10 – Shear behaviour for five strain rates at T 23 °C-RH 0 % (Dau, 2019)

During the tensile tests, the use of bonded end tab led to specimen slippage in some cases due to a weak adhesion of the end tab with the laminate. This weak adhesion may be caused by poor execution of the end-tab bonding process (non-uniform distribution of the adhesive on the surface) that was subcontracted or by an influence of the conditioning process on the behaviour of the adhesive. Therefore, the end tabs were punctually replaced by sandpaper placed between the grip and the laminate to enhance the adhesion and avoid specimen slippage, especially for the dynamic tests on 0°-oriented specimens.

2.1.4 Conclusions on the COPERSIM-Crash experimental results

To summarise the experimental results obtained during the COPERSIM-Crash project, the longitudinal behaviour is elastic-fragile with damage leading to a limited loss of stiffness up to fracture. In addition, the temperature and RH influences may be neglected. The limited strain rate dependence of the longitudinal behaviour is considered for the post-processing of results. The shear behaviour is characterised by elastoplastic-damage behaviour on a large strain range. Damage and inelastic strains were identified with cycled tensile tests. Temperature and moisture significantly affect the shear behaviour with an increase in stiffness at low RH levels or temperatures. The higher ductility at high temperatures or moisture content is caused by the PA66 matrix being highly sensitive to environmental conditions and dominating the shear behaviour, as reported by Dau (2019). The lower T_g at a high moisture level is responsible for the high ductility in shear. Strain rate affects the shear behaviour for a wide range of RH levels (from RH 0 % to RH 85 %). A strengthening behaviour is observed up to a strain rate threshold (about $60\,s^{-1}$), followed by softening caused by material self-heating that creates a competition between strain hardening and thermal effects. Nevertheless, GF/PA66 shear behaviour is significantly strain rate sensitive, with an increase in strength and shear modulus as the strain rate increases. Some specimens' slippage caused by poorly bonded end tabs may have conducted to the scattering observed especially for the longitudinal tensile strength. The variation may also be caused by the fracture location observed in the specimen's effective zone or near the grips.

COPERSIM-Crash project provides strong experimental knowledge about GF/PA66 composites with its characterisation on large ranges of temperature, hygrometry and strain rate. These results show that the study about the strain rate influence on welded laminates behaviour is relevant for the three moisture levels studied during the COPERSIM-Crash project as they highlight strain rate sensitivity. Moreover, a significant strain rate influence could be expected for high moisture levels as the laminate strain rate sensitivity is exacerbated. However, the conditioning protocol followed to reach the RH levels can be

long, especially in the case of a large specimen quantity. First, a desorption phase is required to have a similar and controlled RH level, close to a dry state, in all the specimens. Second, moisture uptake is carried out in a climatic chamber with controlled conditions. This step can last for several months due to the capacity of the climatic chamber. Moreover, the uniformity of moisture distribution within the welded specimens can raise questions, while a dry state can ensure a homogeneous moisture level in the sample. Therefore, a dry state is chosen for the welds' characterisation in this work to reduce the conditioning duration, only requiring the drying phase. Room temperature is chosen for thermal conditions.

From all these tensile test results, a constitutive model was developed in (Mbacké & Rozycki, 2018) and implemented in the commercial FE software Abaqus. Section 2.2 presents the constitutive model developed for the elementary ply. Moreover, the tensile test post-processing is described from the experimental data to identify the model's parameters.

2.2 Constitutive model for GF/PA66

The GF/PA66 constitutive model is based on the work of Ladevèze and Le Dantec on the elastoplastic-damage behaviour of UD composites (Ladeveze & LeDantec, 1992). This model was adapted by Rozycki (2000) and then by Marguet (2007) to include the strain rate dependence of the elementary ply for UD and woven TS composites. Afterwards, Mbacké and Rozycki (2018) modified the strain rate sensitive model for TP woven composites, which can undergo significant shear strains compared to TS composites, and they validated the constitutive model for several temperature and moisture conditions. For this purpose, the damage evolution was adapted for this wide range of strains for dynamic loadings. The model is presented in this section based on the thermodynamic formulation. The post-processing of tensile tests is specified with the protocol used to identify the several laminates' mechanical properties and the inputs of the constitutive model.

2.2.1 Description of the GF/PA66 elementary ply model

Mbacké and Rozycki (2018) originally developed the constitutive model for GF/PA66, then it was implemented in a VUMAT user subroutine and used in Abaqus with the Dynamic/Explicit solver (*ABAQUS / Dynamic User's Manual*, 2019). The model is written under the assumption of plane stresses and is based on the Helmholtz free energy ψ as thermodynamic potential (Equation 2.2). It is decomposed in elastic (ψ^e) and irreversible energies (ψ^p) (Equation 2.3 and Equation 2.4).

$$\psi\left(\varepsilon^e, d_i, p, \beta\right) = \psi^e + \psi^p \tag{2.2}$$

$$\rho\psi^e = \frac{1}{2}\left(C_{11}^0(1-d_{11})(\varepsilon_{11}^e)^2 + C_{22}^0(1-d_{22})(\varepsilon_{22}^e)^2 + 2\nu_{12}^0 C_{11}^0 \varepsilon_{11}^e \varepsilon_{22}^e + G_{12}^0(1-d_{12})(2\varepsilon_{12}^e)^2\right) \tag{2.3}$$

$$\rho\psi^p = \frac{\beta}{m+1}p^{\beta+1} \tag{2.4}$$

The constitutive model (Equation 2.5) is deduced from the Equation 2.3. In this definition, damage operates on the stiffness matrix diagonal and not directly on the elasticity moduli. Abaqus/Explicit solver is based on the calculation of the strain increments at the beginning of each time step, then the stresses are calculated according to the constitutive model defined. Therefore, the definition used for damage ease the calculations because it uncouples in the calculation of damage and released energy rate Y, its

thermodynamic dual.

$$\begin{Bmatrix} \sigma_{11} \\ \sigma_{22} \\ \sigma_{12} \end{Bmatrix} = \underline{\underline{C}} \begin{Bmatrix} \varepsilon^e_{11} \\ \varepsilon^e_{22} \\ 2\varepsilon^e_{12} \end{Bmatrix} = \begin{bmatrix} C^0_{11}(1-d_{11}) & \nu^0_{12}C^0_{22} & 0 \\ \nu^0_{21}C^0_{11} & C^0_{22}(1-d_{22}) & 0 \\ 0 & 0 & G^0_{12}(1-d_{12}) \end{bmatrix} \begin{Bmatrix} \varepsilon^e_{11} \\ \varepsilon^e_{22} \\ 2\varepsilon^e_{12} \end{Bmatrix} \tag{2.5}$$

With $C^0_{11} = \dfrac{E^0_{11}}{1-\nu^0_{12}\nu^0_{21}}$ and $C^0_{22} = \dfrac{E^0_{22}}{1-\nu^0_{12}\nu^0_{21}}$.

E^0_{11}, E^0_{22} and G^0_{12} are the elasticity modulus, ν^0_{12} and ν^0_{21} the Poisson ratios and d_{11}, d_{22} and d_{12} are the damage variables. This last variable takes values between 0 and 1 to describe the degradation of stiffnesses during traction. Moreover, the orthotropic stiffness matrix is noted $\underline{\underline{C}}$.

Y_{11}, Y_{12} and Y_{22} are the thermodynamical variables associated with the damage variables obtained by taking the derivative of ψ to the corresponding damage variable. They are expressed as follows:

$$Y_{12} = -\rho\frac{\partial\psi^e}{\partial d_{12}} = \frac{1}{2}G^0_{12}(2\varepsilon^e_{12})^2 \tag{2.6}$$

$$Y_{11} = -\rho\frac{\partial\psi^e}{\partial d_{11}} = \frac{1}{2}C^0_{11}(\varepsilon_{11})^2 \tag{2.7}$$

$$Y_{22} = -\rho\frac{\partial\psi^e}{\partial d_{22}} = \frac{1}{2}C^0_{22}(\varepsilon_{22})^2 \tag{2.8}$$

Released energy rates are defined to be increasing versus time with Equation 2.9, Equation 2.10 and Equation 2.11, to store the damage level reached during the loading history of the material.

$$\overline{Y}_{12}(t) = \sup_{\tau\leq t}(Y_{12}(\tau)) \tag{2.9}$$

$$\overline{Y}_{11}(t) = \sup_{\tau\leq t}(Y_{11}(\tau)) \tag{2.10}$$

$$\overline{Y}_{22}(t) = \sup_{\tau\leq t}(Y_{22}(\tau)) \tag{2.11}$$

The evolution of damage variables depends on their associated variable (Equation 2.12). The function f is selected based on the experimental results. The square root function have been first introduced for UD composites as they appears to be the best suited for the description of the damage evolution.

$$d_{ij} = \alpha_{ij}f_{ij}\left(\sqrt{\overline{Y}_{ij}}\right) \tag{2.12}$$

Concerning GF/PA66 elementary ply, damage for shear direction is defined using two types of evolution laws based on the experiments; the first is logarithmic, and the second is linear (Equation 2.13). This continuous function by parts permits a suitable description of the experimental damage evolution. The logarithmic function describe correctly the damage evolution until a threshold Y^M_{12} (as classically used for shear direction), then the evolution is limited until fracture which required the definition of a linear evolution. The longitudinal and transverse damage evolutions are well described by linear evolutions as classically used for these materials (Equations 2.14, 2.15) (Ladeveze & LeDantec, 1992; Rozycki,

2000; Marguet, 2007).

$$d_{12} = \begin{cases} 0 & \text{if } \overline{Y}_{12} \leq Y_{12}^0 \\ \left(log\left(\sqrt{\overline{Y}_{12}}\right) - log\left(\sqrt{Y_{12}^0}\right)\right) \alpha_{12}^1 & \text{if } Y_{12}^0 < \overline{Y}_{12} \leq Y_{12}^M \\ \left(\sqrt{\overline{Y}_{12}} - \sqrt{Y_{12}^0}\right) \alpha_{12}^2 + d_{12}^M & \text{if } Y_{12}^M < \overline{Y}_{12} < Y_{12}^R \\ d_{12}^{max} & \text{otherwise} \end{cases} \tag{2.13}$$

$$d_{11} = \begin{cases} 0 & \text{if } \overline{Y}_{11} \leq Y_{11}^0 \\ \left(\sqrt{\overline{Y}_{11}} - \sqrt{Y_{11}^0}\right) \alpha_1 & \text{if } Y_{11}^0 < \overline{Y}_{11} < Y_{11}^R \\ d_{11}^{max} & \text{otherwise} \end{cases} \tag{2.14}$$

$$d_{22} = \begin{cases} 0 & \text{if } \overline{Y}_{22} \leq Y_{22}^0 \\ \left(\sqrt{\overline{Y}_{22}} - \sqrt{Y_{22}^0}\right) \alpha_2 & \text{if } Y_{22}^0 < \overline{Y}_{22} < Y_{22}^R \\ d_{22}^{max} & \text{otherwise} \end{cases} \tag{2.15}$$

The inelastic shear behaviour is introduced by the definition of a dissipation potential (plastic yield surface). An isotropic hardening function ($R(p)$) is considered with plastic yield surface defined by the function f_p (Equation 2.16). Only the effective shear stress leads to plastic deformation in the material.

$$f_p(\sigma_{12}, R) = \left| \frac{\sigma_{12}}{1 - d_{12}} \right| - R(p) - \sigma_{12}^0 \text{ with } R(p) = \beta p^m \tag{2.16}$$

β and m are material properties for hardening and σ_{12}^0 is the yield stress.

Yield conditions are defined by Equation 2.17 following the normality condition ($f_p = 0$ and $\dot{f}_p = 0$) with the plasticity multiplier $\dot{\lambda} \leq 0$:

$$\begin{cases} \dot{\varepsilon}_{12}^p = \dot{\lambda} \dfrac{\partial f_p}{\partial \sigma_{12}} \\ \dot{p} = \dot{\lambda} \dfrac{\partial f_p}{\partial R} \end{cases} \tag{2.17}$$

The plasticity multiplier is zero for $f_p < 0$ and takes the following value during plastic flow considering the consistence condition $\dot{f}_p = 0$:

$$\dot{\lambda} = \frac{f}{\dfrac{\partial f_p}{\partial \sigma_{12}} 2G_{12}(1 - d_{12}) \dfrac{\partial f_p}{\partial \sigma_{12}} + \dfrac{\partial f_p}{\partial R} \dfrac{\partial R}{\partial p} \dfrac{\partial f_p}{\partial R}} \tag{2.18}$$

In the original model, strain rate dependencies are defined for longitudinal, transversal and shear directions. Viscous functions are defined for each material parameters affected by strain rate ($E_{11/22}^0$, $Y_{11/22}^0$ and $Y_{11/22}^R$ for longitudinal and transverse directions and G_{12}^0, σ_{12}^0, d_{12}^M, α_{12}^1 and Y_{12}^R for shear direction). These functions consider the quasi-static value of the property X^{QS} and F_X^1, F_X^2 and F_X^3 the coefficients of the polynomial evolution equation for property "X" (Equation 2.19). In addition, the strain rates are normalised to the strain rate assessed for the quasi-static test (Equation 2.20). These normalised strain rates were the most appropriate laws to describe the experimental evolutions. $\dot{\varepsilon}_{ij}^{exp}$ is a quantity defined to improve the polynomial regression for the several properties affected by the strain rate.

$$X_{ij} = X_{ij}^{QS} \left(1 + F_X^1 \dot{\varepsilon}_{ij}^{norm} + F_X^2 (\dot{\varepsilon}_{ij}^{norm})^2 + F_X^3 (\dot{\varepsilon}_{ij}^{norm})^3\right) \text{ with } ij = \{11, 22, 12\} \tag{2.19}$$

$$\dot{\varepsilon}_{11}^{norm} = \left(\frac{\dot{\varepsilon}_{11}}{\dot{\varepsilon}_{11}^{ref}}\right)^{\dot{\varepsilon}_{11}^{exp}} ; \dot{\varepsilon}_{22}^{norm} = \left(\frac{\dot{\varepsilon}_{22}}{\dot{\varepsilon}_{22}^{ref}}\right)^{\dot{\varepsilon}_{22}^{exp}} ; \dot{\varepsilon}_{12}^{norm} = \left[\ln\left(\frac{\dot{\varepsilon}_{12}}{\dot{\varepsilon}_{12}^{ref}}\right)\right]^{\dot{\varepsilon}_{12}^{exp}} \tag{2.20}$$

All the elements of the constitutive model have been presented. The identification method from the experimental results is described in the following subsection.

2.2.2 Identification of the model settings from experimental data

The post-processing method for analysing the tensile tests performed and evaluating the mechanical properties of the elementary ply RVE is presented in this subsection. The complete calculation of the stress-strain curve, from the camera images and force signal, is detailed for the several directions of the fabric. The last part presents the constitutive model parameters identification. All these elements have been set up during the COPERSIM-Crash project and are used in the present work.

Extraction of engineering strains using Digital Image Correlation (DIC) and virtual gauges and calculation of true quantities

Several technologies can be used during a tensile test to measure material strains, for example, gauges or DIC. Strain gauges are used for low-speed tests, though their application is limited when strains are large and unsuitable for dynamic tests. Therefore, DIC and virtual gauges will be employed here for all composite characterisation tests and loading speeds. Two methods were used: measurements of the strain field with VIC-2D software (*VIC-2D CS Software*, 2009) and measurements from virtual gauges with point tracking software TEMA (*TEMA Motion 3.4*, n.d.). The engineering strains are used to compare the results obtained with DIC and virtual gauges. The strains are extracted on a zone corresponding to 1.5 RVE for both methods. The first software is used to measure the strain field over a given area, the second is used to obtain an average value of the strains on virtual gauges and, above all, to measure the reorientation of the fibres. VIC-2D software measures the strains in a zone chosen by the user (to be approximately 1.5 RVE here), placed in the centre of the specimen (Figure 2.11a). The engineering (or conventional) strain field is measured on all the tensile test duration, and then these fields are averaged at each time step for further post-processing. Three longitudinal and three transverse virtual gauges are drawn with TEMA to cover 1.5 RVE. For this purpose, eight points are placed and then connected in pairs (Figure 2.11b). The ninth point is placed in the centre to measure the yarn reorientation during the tensile tests. Once the distance provided for these gauges is extracted, it is possible to calculate the strains by subtracting the initial length and then dividing this elongation by the initial gauge length. This post-processing permits the calculation of engineering (or conventional) values.

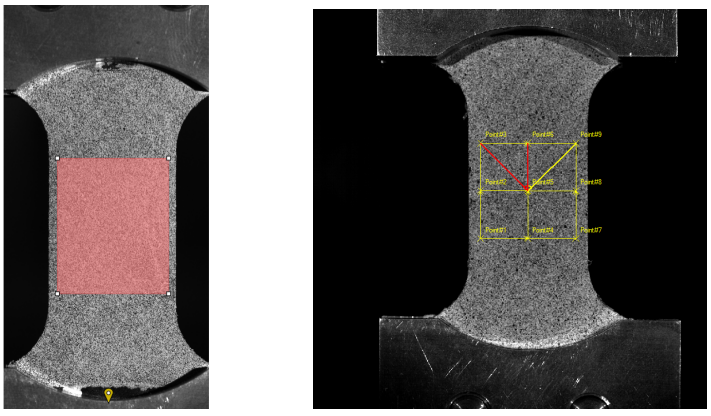

(a) VIC-2D (b) TEMA

Figure 2.11 – Extraction of engineering strains using DIC and point tracking

The strains considered here are relatively large, and the application of the constitutive model is crashworthiness; hence it is necessary to work with the true (or rational) stresses and strains calculated from the engineering quantities. The engineering strains are obtained by DIC as explained above. This quantity is defined by Equation 2.21 using the elongation ΔL and the initial length L_0. The true strains are calculated with the current length L; it can also be calculated from the engineering values with Equation 2.22 (Lemaitre et al., 2020).

$$\varepsilon^{eng} = \frac{\Delta L}{L_0} \qquad (2.21) \qquad\qquad \varepsilon^{true} = \frac{\Delta L}{L} = \ln\left(1 + \varepsilon^{eng}\right) \qquad (2.22)$$

Considering F, the reaction force obtained by the tensile machine load cell and S_0, the initial section of the narrowest zone of the specimen, the engineering stress is defined by Equation 2.23. The true stress is established from the current section, which evolves during the test and whose evolution over time can be difficult to measure (Equation 2.24).

$$\sigma^{eng} = \frac{F}{S_0} \qquad (2.23) \qquad\qquad \sigma^{true} = \frac{F}{S} \qquad (2.24)$$

The true stress can be calculated from the engineering stress by Equation 2.25, with ν^* corresponding to the contraction coefficient. For incompressible materials, such as metals, this coefficient is approximately $1/2$ (Lemaitre et al., 2020). In the case for which the assumption of incompressibility is not verified, then $\nu^* = -\dot{\varepsilon}_{yy}/\dot{\varepsilon}_{xx}$ must be taken into account in the calculation of the engineering stress according to Equation 2.25.

$$\sigma^{true} = \sigma^{eng}\left(1 + \varepsilon^{eng}\right)^{2\nu^*} \qquad (2.25)$$

From global to local frame

Two frames characterise the system studied: the global frame corresponding to the main directions of the tensile test machine and the local frame associated to the weave orientation. The transition from the global to the local strain frame (Figure 2.12) is given by Equation 2.26.

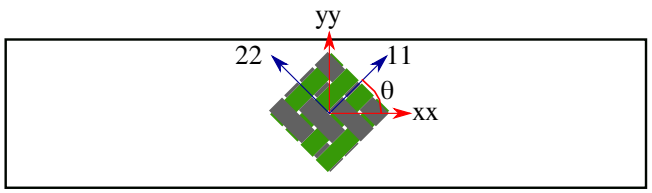

Figure 2.12 – Global and local frames of a specimen

$$\begin{pmatrix} \varepsilon_{11} \\ \varepsilon_{22} \\ 2\varepsilon_{12} \end{pmatrix} = \begin{bmatrix} cos^2\theta & sin^2\theta & sin\theta cos\theta \\ sin^2\theta & cos^2\theta & -sin\theta cos\theta \\ -2sin\theta cos\theta & 2sin\theta cos\theta & cos^2\theta - sin^2\theta \end{bmatrix} \begin{pmatrix} \varepsilon_{xx} \\ \varepsilon_{yy} \\ 2\varepsilon_{xy} \end{pmatrix} = \underline{\underline{Q_2}}^{+} \begin{pmatrix} \varepsilon_{xx} \\ \varepsilon_{yy} \\ 2\varepsilon_{xy} \end{pmatrix} \qquad (2.26)$$

Thus, for the $0°$-oriented ply, the transition from global to local deformations is determined by Equation 2.27.

$$\begin{pmatrix} \varepsilon_{11} \\ \varepsilon_{22} \\ 2\varepsilon_{12} \end{pmatrix} = \begin{pmatrix} \varepsilon_{xx} \\ \varepsilon_{yy} \\ 0 \end{pmatrix} \qquad (2.27)$$

For the 45°-oriented ply, transition is defined by Equation 2.28.

$$\begin{pmatrix} \varepsilon_{11} \\ \varepsilon_{22} \\ 2\varepsilon_{12} \end{pmatrix} = \begin{pmatrix} \dfrac{\varepsilon_{xx}+\varepsilon_{yy}}{2} \\ \dfrac{\varepsilon_{xx}+\varepsilon_{yy}}{2} \\ \varepsilon_{xx}-\varepsilon_{yy} \end{pmatrix} \tag{2.28}$$

The equation for the transition from the global to the local stress frame is similar to Equation 2.26 for laminates composed of plies all oriented at the same angle (Equation 2.29). However, the transition relationship is more complex for symmetrical laminates, appealing to laminate theory.

$$\begin{pmatrix} \sigma_{11} \\ \sigma_{22} \\ \sigma_{12} \end{pmatrix} = \begin{bmatrix} cos^2\theta & sin^2\theta & 2sin\theta cos\theta \\ sin^2\theta & cos^2\theta & -2sin\theta cos\theta \\ -sin\theta cos\theta & sin\theta cos\theta & cos^2\theta - sin^2\theta \end{bmatrix} \begin{pmatrix} \sigma_{xx} \\ \sigma_{yy} \\ \sigma_{xy} \end{pmatrix} \tag{2.29}$$

Thus, for a $\pm$ 45° laminate with each ply equilibrated, the relationship between the shear stress and the longitudinal stress in the global frame (Equation 2.30) can be defined from the Equation 2.29, for uniaxial traction ($\sigma_{yy} = \sigma_{xy} = 0$). For the longitudinal behaviour, the longitudinal stress is defined by Equation 2.31.

$$\sigma_{12} = \mp\frac{1}{2}\sigma_{xx} \tag{2.30}$$

$$\sigma_{11} = \sigma_{xx} \tag{2.31}$$

Identification of elasticity moduli and yield stress

Tensile properties are determined from the true stress-strain data because these values are used for dynamic loading studies with Abaqus/Explicit. The shear and longitudinal elasticity modulus (G_{12} and E_{11}, respectively) are defined as the value of a slope of $\sigma^{\text{true}}(\varepsilon^{\text{true}})$ curve in the elastic domain for the orientation considered (Figure 2.13). The parameters are calculated for the several tests (repeatability specimens) performed for a fixed loading speed. A protocol is implemented to have a reproducible process with limited user interventions.

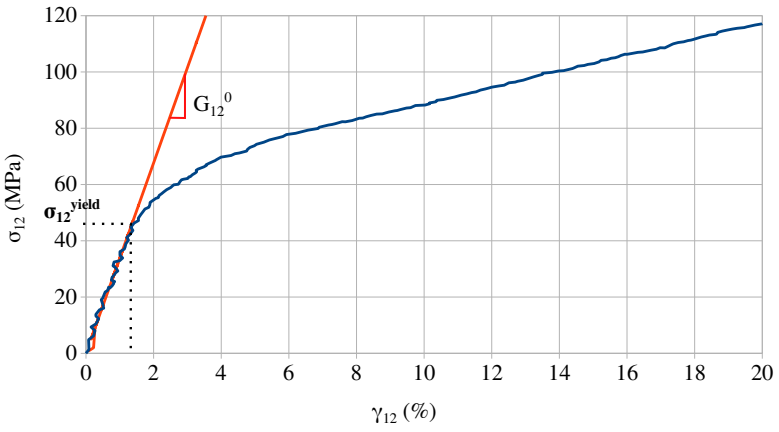

Figure 2.13 – Identification of the shear modulus and yield stress on the stress-strain curve

First, a coefficient of determination (R^2) for linear regression is defined as a target value to ensure a reproducible method for the elastic modulus identification between the several curves treated. Secondly, linear regressions are calculated between the curve origin and the current point. Thirdly, the R^2 closest to the target value is identified. This time step is assumed to be the end of the purely elastic domain. It permits the identification and the calculation of yield stress ($\sigma_{12}^{0,true}$), elasticity moduli ($G_{12}^{0} = \sigma_{12}^{0,true}/\gamma_{12}^{0,true}$

or $E_{11}^0 = \sigma_{11}^{0,true}/\varepsilon_{11}^{0,true}$ at the identified time step for the current orientation) and the Poisson's ratio $\nu_{12}^0 = \nu_{21}^0$. Curves were interpolated, before the linear regressions' calculations to ensure a high number of points in the elastic domain, especially for the highest strain rates. This method is reproducible to determine the elasticity modulus. Finally, the strain rate is calculated as the current strain rates average over the whole tensile test.

Identification of hardening law and damage

The mechanical properties of the elementary ply are identified for the longitudinal and shear behaviours in this study. The identification of material parameters is more extensive for the shear behaviour than for the longitudinal behaviour due to the irreversible behaviour caused by the ductility of the matrix in addition to the damage.

Longitudinal properties

Concerning the longitudinal damage, the tensile test are not cycled to identify damage because of the small strains and damage values for this orientation; the use of cycled test would only add complexity to the tensile test and difficulties in post-processing. Hence, the damage variable is calculated using the intersecting and initial elasticity modulus (Equation 2.32 and Figure 2.14). The released energy rate is calculated with Equation 2.33. Damage law parameters α_1 (Equation 2.14) and α_2 (Equation 2.15) are identified from linear regression between d_{11} and $\sqrt{Y_{11}}$[1]. Y_{11}^0 and Y_{22}^0 are calculated from the value of the strain at damage initiation (Equation 2.33).

$$d_{11}^i = 1 - \frac{E_{intersecting}^i}{E^0} \tag{2.32}$$

$$\sqrt{Y_{11}^i} = \sqrt{\frac{E_{11}^0}{2\left(1-\nu_{12}\nu_{21}\right)}{\varepsilon_{11}^i}^2} \tag{2.33}$$

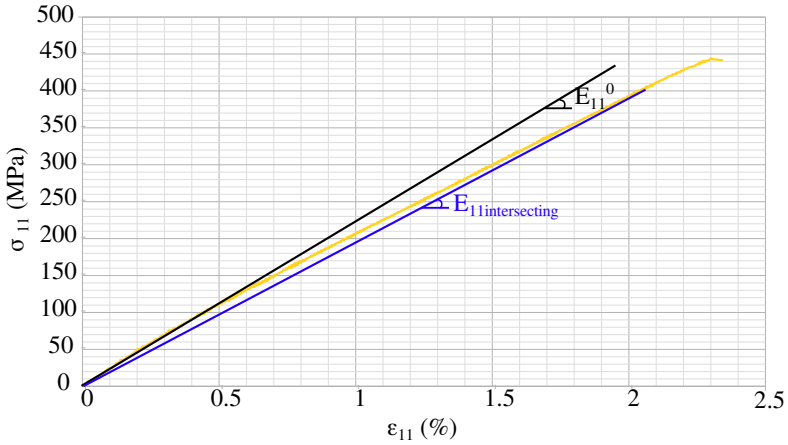

Figure 2.14 – Identification of initial and intersecting longitudinal elastic moduli from longitudinal stress-strain curve

Shear properties

Concerning the shear direction, the damage is identified from cyclic tensile tests only in quasi-static (Figure 2.15). The evolution of the current shear modulus, denoted by G_{12}^i with i $\geq$ 0, permits the evaluation of the damage variable d_{12} (Equation 2.34) and the released energy rate (Equation 2.35) to define the damage evolution $d_{12} = f(\sqrt{Y_{12}})$ (Equation 2.13). The modulus is identified as the slope between the starting point of the unloading and the beginning of reloading.

1. As a reminder, longitudinal and transverse behaviour are considered equal; hence transverse parameters are defined from the longitudinal results.

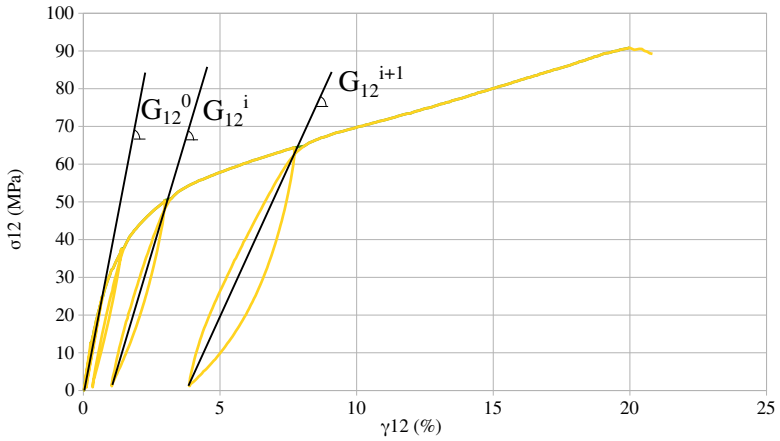

Figure 2.15 – Stress-strain curve for a quasi-static cycled tensile test

$$d_{12}^{i} = 1 - \frac{G_{12}^{i}}{G_{12}^{0}} \tag{2.34}$$

$$\sqrt{Y_{12}^{i}} = \sqrt{\frac{1}{2} G_{12}^{0} \left(2\varepsilon_{12}^{e\ i}\right)^{2}} \tag{2.35}$$

In practice, the indexes of unloading and reloading starts are identified for all the cycles in the tensile test. From this information, elastic $(2\varepsilon_{12}^{e})$ and irreversible $(2\varepsilon_{12}^{p})$ strains are calculated, as well as damage and the released energy rate.

$$\begin{cases} 2\varepsilon_{12}^{e\ i} = \dfrac{\sigma_{12}^{i}}{G_{12}^{i}} \\ 2\varepsilon_{12}^{p\ i} = 2\varepsilon_{12}{}^{i} - 2\varepsilon_{12}^{e\ i} \end{cases} \tag{2.36}$$

At that point, the irreversible strain reached in cycle i is known, as well as the yield stress σ_{12}^{0}. Hence, the cumulated inelastic strain p and the hardening stress can be calculated (Equation 2.37 and Equation 2.38, respectively).

$$p^{i} = \int_{0}^{\varepsilon_{p}^{i}} (1 - d_{12}^{i}) d\varepsilon_{12}^{p} \tag{2.37}$$

$$R^{i} = \frac{\sigma_{12max}^{i}}{1 - d_{12}^{i}} - \sigma_{12}^{0} \tag{2.38}$$

These parameters calculation is done for every cycle of the tensile test. Then hardening function parameters m and β are identified from R and p data obtained for each cycle using a linear regression between $ln(R)$ and $ln(p)$. The same applies to the damage evolution parameters, α_{12}^{1}, α_{12}^{2}, d_{12}^{M} and d_{12}^{max}. This identification protocol for hardening law and damage can be done in quasi-static with cycled tests.

Application for dynamic loadings

The identification of the elastic properties and fracture parameters is done as explained for the quasi-static tests. However, the protocol is modified for the identification of damage evolution because only monotonic tests were performed for dynamic loadings. In addition, only some parameters defined as strain rate dependent are identified from the dynamic tests (E_{11}^{0}, $Y_{11/22}^{0}$, $Y_{11/22}^{R}$, G_{12}^{0}, σ_{12}^{0}, Y_{12}^{R}, α_{12}^{1} and d_{12}^{M}). Consequently, only α_{12}^{1} and d_{12}^{M} cannot be identified from tensile tests using the protocol presented for quasi-static test; they are obtained by an inverse method.

The strain rate influence is disabled in the constitutive model and simulations are done at a fixed strain rate. The parameters known at the strain rate considered are defined in the model, and α_{12}^{1} and

d_{12}^M are replaced by parameters to be optimised. In the present work, the optimisation of α_{12}^1 and d_{12}^M is done using the "Particle swarm" optimisation function in Matlab following the scheme Figure 2.16. The function defines the parameters to test, then the value is replaced in the Abaqus model input file, and the Abaqus calculation is done and post-processed to obtain the stress-strain curve. The numerical curve is interpolated based on the experimental strain range, and the error is calculated between numerical and experimental results with Equation 2.39 defining the objective function. Particle swarm optimisation proposes a pair of parameters and converges after several calculations to the parameters minimising the objective function.

$$F_{gap} = \sum_{i=0}^{n} \left| \frac{\sigma_{12}^{num,i} - \sigma_{12}^{exp,i}}{\sigma_{12}^{exp,i}} \right| \tag{2.39}$$

n is the number of points for the experimental curve. The optimisation function ends if the relative evolution in the best objective function is less than 10^{-6} over 20 iterations. This calculation is done for all the strain rates tested.

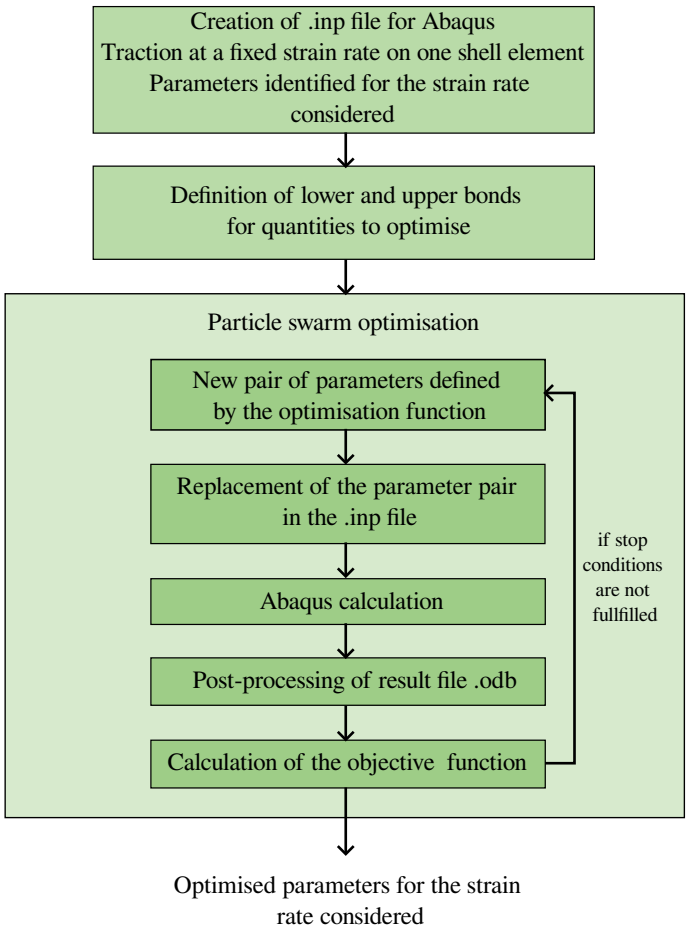

Figure 2.16 – Scheme of the process for VUMAT parameters optimisation (d_{12}^M and α_{12}^1)

Identification of viscous functions

The viscous functions are identified from the evolution of the material parameters as a function of the normalised strain rate. The following properties are influenced by strain rate: G_{12}^0, σ_{12}^0, σ_{12}^R, d_{12}^M and α_{12}^1 in shear and $E_{11/22}^0$, $Y_{11/22}^0$ and $Y_{11/22}^R$ for longitudinal direction. The value of each parameter is known for the strain rates tested. Order 3 polynomial functions were identified during the COPERSIM-Crash project to suitably describe the parameter's evolution with a normalised strain rate. As explained previously, strain rates are normalised to develop viscous functions. Below the reference strain rate $\dot{\varepsilon}_{ref}$,

material parameters are not influenced by strain rate and keep their quasi-static value; above the reference value viscous function affects the property value (Equation 2.41). $\dot{\varepsilon}^{exp}$ is a coefficient defined before the polynomial regression between X^{norm} (Equation 2.40) and $(\dot{\varepsilon}_{norm})^{\dot{\varepsilon}^{exp}}$ to determine F_X^1, F_X^2 and F_X^3. Only the strain rate dependence of the shear behaviour will be considered in this work based on the experimental results and to limit the computing time.

$$X^{norm}(\dot{\varepsilon}) = \frac{X(\dot{\varepsilon})}{X(\dot{\varepsilon}_{ref})} - 1 \tag{2.40}$$

$$F_X(\dot{\varepsilon}, \dot{\varepsilon}_{ref}) = \begin{cases} 1 & \text{if } \dot{\varepsilon} \leq \dot{\varepsilon}_{ref} \\ 1 + F_X^3 \left(\dot{\varepsilon}^{norm}\right)^{3\dot{\varepsilon}^{exp}} + F_X^2 \left(\dot{\varepsilon}^{norm}\right)^{2\dot{\varepsilon}^{exp}} + F_X^1 \left(\dot{\varepsilon}^{norm}\right)^{\dot{\varepsilon}^{exp}} & \text{if } \dot{\varepsilon} > \dot{\varepsilon}_{ref} \end{cases} \tag{2.41}$$

$$\dot{\varepsilon}_{12}^{norm} = ln\left(\frac{\dot{\gamma}_{12}}{\dot{\gamma}_{12,ref}}\right) \tag{2.42}$$

$$\dot{\varepsilon}_{11}^{norm} = \frac{\dot{\varepsilon}_{11}}{\dot{\varepsilon}_{11,ref}} \tag{2.43}$$

With X=$\{G_{12}^0, \sigma_{12}^0, \sigma_{12}^R, d_{12}^M, \alpha_{12}^1, E_{11/22}^0, \sigma_{11/22}^0, Y_{11/22}^R\}$. The value of G_{12}^0 at a certain strain rate $\dot{\gamma}_{12}$ is, for example, calculated by Equation 2.44.

$$G_{12}^0(\dot{\gamma}_{12}) = G_{12}^{0,QS} F_{G_{12}}(\dot{\gamma}_{12}, \dot{\gamma}_{12}^{ref}) \tag{2.44}$$

Protocol of mechanical properties identification

The shear mechanical properties identification follows a specific protocol (Figure 2.17) for all the tensile tests performed. Therefore, several stress-strain curves are obtained for each strain rate considered (reproducibility specimens). The material properties are defined from the averaged values obtained with the three reproducibility tensile tests per strain rate. Once the post-processing is done for the five strain rates considered, the viscous functions are identified following the process in the previous paragraph.

Conclusions on the post-processing, definition of the constitutive model and parameters identification

The work on GF/PA66 done during the COPERISIM-Crash was summarised in Sections 2.1 and 2.2. The influence of strain rate, temperature and RH on $0°$- and $45°$-oriented specimens were studied, the properties were measured, and a constitutive model was developed and implemented in a VUMAT subroutine for Abaqus/Explicit. The subroutine can be used at several strain rates for a fixed value of RH and T, i.e. the set of parameters for the subroutine are valid for a crash study at fixed moisture and temperature levels. A suitable correlation is observed between experiments and numerical results (Mbacké & Rozycki, 2018). The VUMAT subroutine calculates all the quantities required by the constitutive model; hence, they are accessible as output data of the simulations (plastic strains, the energy released rates, etc...). Therefore, these quantities can be used to improve the understanding of the behaviour compared to a more simplified one, which would only fit the stress-strain curves.

The use of this material was based on the strong experimental and numerical knowledge acquired in the COPERSIM-Crash project; hence, the work can focus on the behaviour of the welded joint. However, the project ended in 2018, and the material was stored for five years in an uncontrolled environment. The natural cycles of temperature/RH during the storage could result in fatigue or chemical ageing of

the material, thus leading to an evolution in the material behaviour. Therefore, some tensile tests are performed to eliminate this source of uncertainties for the study of welded GF/PA66 and to be able to apply an inverse method. The material behaviour will be well-known and modelled for the weld's behaviour study. The conditioning was necessary to control the RH level in the material. A testing temperature of 23 °C was chosen as a classical testing temperature, and RH 0 % was selected to control the moisture level in welded specimens and avoid non-uniform distribution. All the samples were dried according to the protocol defined in Section 2.1.1. The matrix and composite shear behaviour are significantly strain rate sensitive at that RH level.

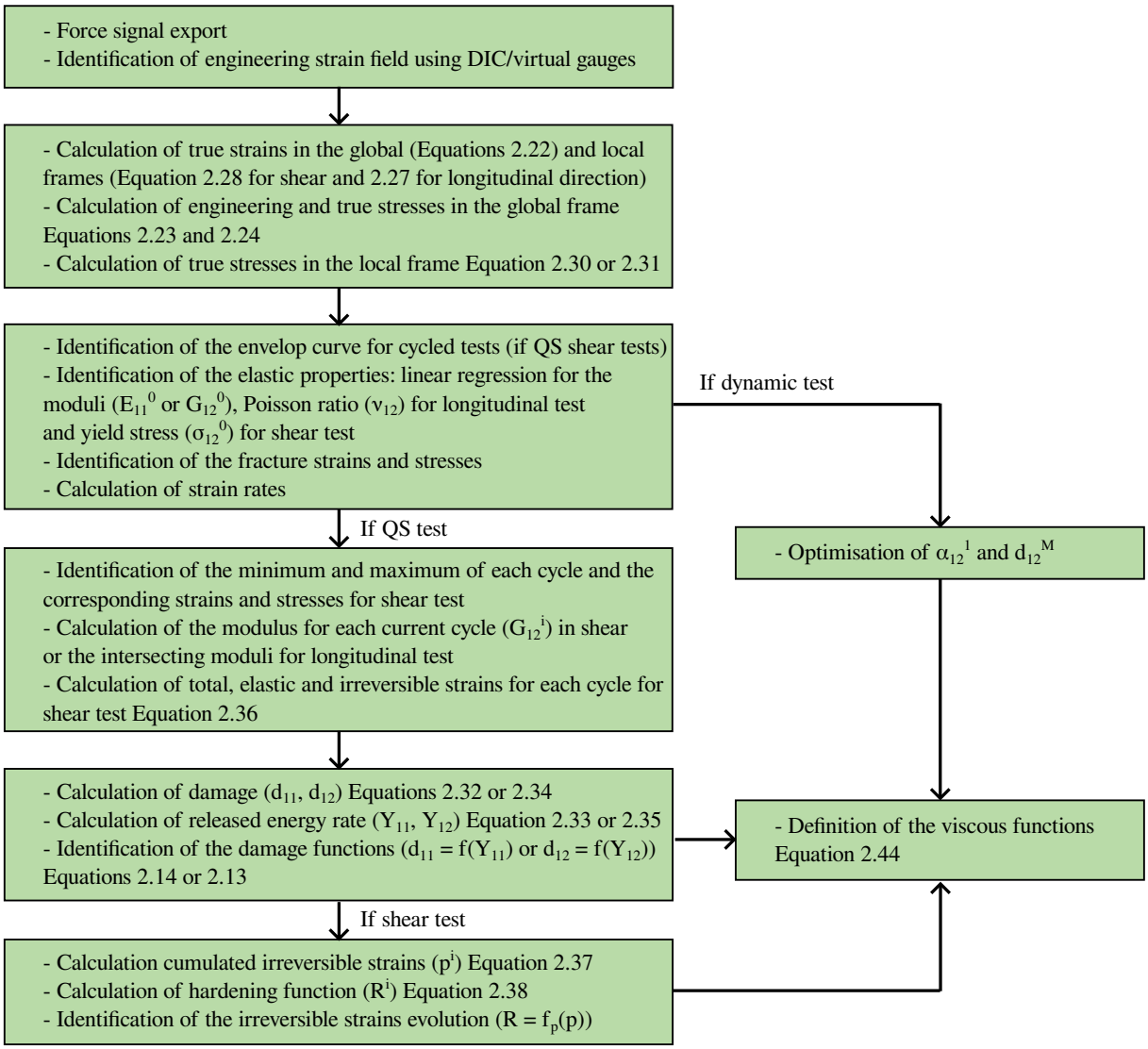

Figure 2.17 – Protocol for the identification of mechanical properties of GF/PA66

2.3 Control tests on the behaviour of GF/PA66

As presented in Section 2.1, GF/PA66 behaviour is significantly affected by temperature and RH. As the material was stored in ambient air for five years, it was necessary to control that no ageing phenomenon or natural temperature/RH cycles altered the composite behaviour (Bernstein & Gillen, 2010). This verification is required for the numerical aim of this study, which is the welded interface modelling: the knowledge of GF/PA66 in-plane behaviour is crucial to understand the behaviour of welded structures and being able to isolate the welded joint be-

haviour. In case of a significant difference between the previous study and the current tests, the constitutive model parameters that have changed will be updated for the final model to correlate with the new tensile tests results.

2.3.1 Tensile tests definition

Two in-plane behaviours are studied: longitudinal and shear (tensile tests on $[0]_4$ and $[45]_4$, respectively). A limited influence of strain rate was identified by Dau (2019) for the longitudinal behaviour compared to the shear behaviour. Therefore, tensile tests are performed only for quasi-static loading for the $0°$-oriented specimens. The tests are carried out from quasi-static to dynamic loadings for the $45°$ orientation.

Rectangular specimens of $250\,\text{mm} \times 25\,\text{mm} \times 2\,\text{mm}$ are used to characterise the longitudinal behaviour (Figure 2.1). The specimen width contains more than 1.5 RVE to ensure correct data extraction of the elementary ply behaviour (RVE of $15\,\text{mm} \times 15\,\text{mm}$ for the $0°$ ply and $10.6\,\text{mm} \times 10.6\,\text{mm}$ for the $45°$ ply). No tabs were used to avoid issues with the ageing and bounding processes. Sandpaper was placed between the specimen and the grip to improve adhesion. However, the slippage of the specimens can be more critical when the loading speed increases and the sandpaper becomes insufficient. Thus, a different geometry was considered for shear characterisation (Figure 2.18) with a stud and flange clamping system used for the grip. The dumbbell shape aims to concentrate the stress in the centre of the specimen for orientation $45°$. The width of the effective area contains more than 1.5 RVE. The same specimen geometry was used for all strain rate conditions to avoid the influence of structural changes. The testing rig and setup used will be presented in Subsection 3.2.3 with the tests on welded specimens. The desorption protocol and the mechanical testing setup will be detailed in Subsection 3.2.2.

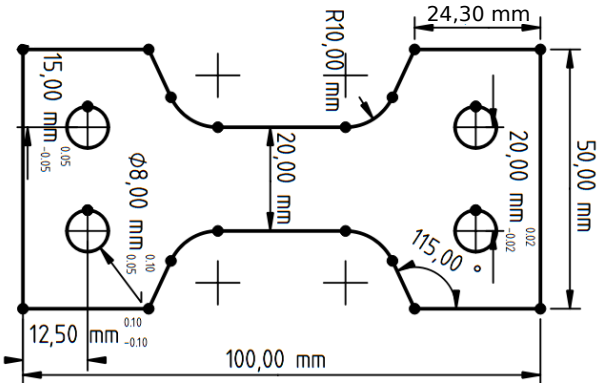

Figure 2.18 – Geometry of the specimens for shear characterisation from quasi-static to dynamic loadings

2.3.2 Tensile test results

Longitudinal behaviour

Tensile tests were conducted only in quasi-static for the $0°$-oriented material and the strain rate dependence is deactivated in constitutive model. The true strains and stresses calculation was done as described in Subsection 2.2.2. The stress-strain curves were plotted for the three tests performed (Figure 2.19). The behaviour is elastic-fragile with damage (slight decrease of the elasticity modulus along the tensile test). The three tests show good repeatability as indicated by standard deviations. In addition, the behaviour is similar to that obtained during the previous test campaign as presented by Table 2.2. For that reason, it is not necessary to modify the constitutive model and settings for the longitudinal behaviour of the composite [2]. Finally, the fracture occurred away from the grip for three specimens despite the rectangular shape (Figure 2.20). Therefore, the RVE behaviour identified is consistent up to fracture.

2. It is also valid for the transverse direction, as the fabric is assumed to be balanced.

An elastic-fragile behaviour could also have been considered for the longitudinal and transverse behaviours because the linear regression on the curve to failure gives a regression coefficient of about 0.999. Nevertheless, damage for longitudinal and transverse behaviours is considered for the rest of the study to keep a constitutive model as extensive as possible. Conclusions on the benefit of considering damage in the constitutive model should be discussed with the numerical results on welded specimens.

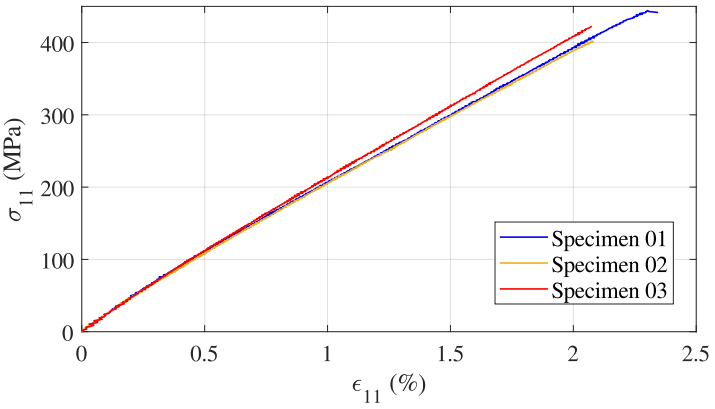

Figure 2.19 – Longitudinal behaviour of composite - tensile tests on $[0]_4$

	Thesis	COPERSIM-Crash
Elasticity modulus (GPa)	23.4 ± 0.7	22.8 ± 2.1
Damage initiation stress (MPa)	67.5 ± 19.6	54.4 ± 17.3
Strength (MPa)	422.8 ± 21.3	419.7 ± 113.5
Damage at fracture (-) (*For the reference curve*)	0.177	0.159

Table 2.2 – Material parameters identified for the longitudinal behaviour - current and COPERSIM-Crash project results comparison

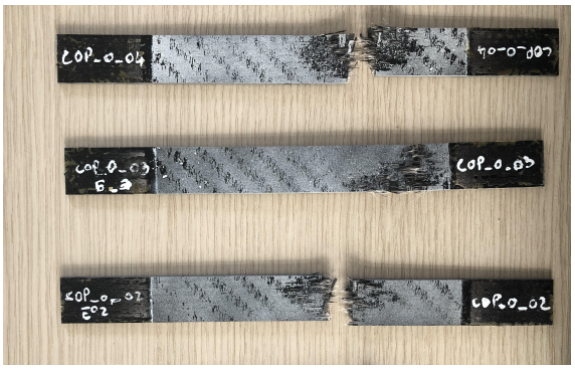

Figure 2.20 – Post-mortem specimens - tensile tests on $[0]_4$

Shear behaviour

The 45°-oriented specimens were tested at several strain rates to identify the shear behaviour from quasi-static to dynamic loadings. All the specimens broke in the narrow part near the fillets (Figure 2.21). It may have anticipated the fracture in comparison with traditional rectangular specimens. Tensile test data are treated following the post-processing explained in Subsection 2.2.2. Then, one sample among the three is selected for each loading speed to calculate the mechanical properties used in the model and plot the stress-strain curves (Figure 2.22). For this purpose, the three stress-strain curves are interpolated and averaged into one stress-strain curve. Then, the difference between each curve and the average curve is

calculated in the sense of the least squares method: for each strain point, the stress deviation is calculated, and then the values are summed over the entire strain range. Finally, the curve minimizing the difference is selected as the reference curve. An elastoplastic viscous behaviour with damage is observed in shear, as previously reported (Mbacké & Rozycki, 2018; Dau, 2019; Rozycki et al., 2019). The RVE behaviour identified for different strain rates shows an enhancement in yield strength and strain at failure with increasing strain rate (Figure 2.22). In addition, stiffening is observed with the augmentation in strain rate on the averaged properties (Figure 2.23). Viscosity is caused by the PA66 matrix behaviour.

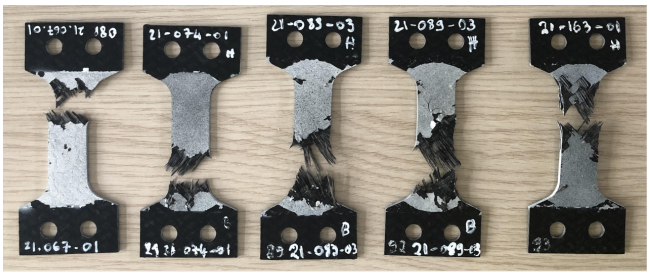

Figure 2.21 – Post-mortem specimens - tensile tests on $[45]_4$

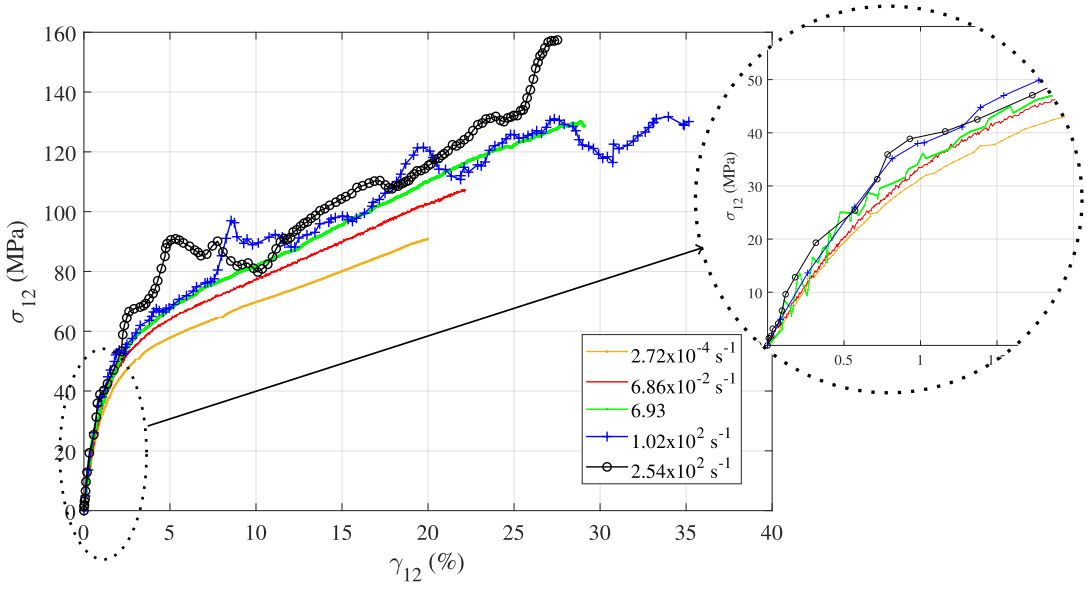

Figure 2.22 – Shear behaviour of composite - tensile tests on $[45]_4$

Figure 2.23 also highlights the positioning of the current results in relation to COPERSIM-Crash project ones. The comparison is made on G_{12}^0 and σ_{12}^0. The difference is small for the quasi-static tests, however, it is increasing at higher strain rates (especially beyond $60\,\mathrm{s}^{-1}$). Therefore, the evolution of these parameters with strain rate needs to be updated considering the values obtained for quasi-static to the highest strain rate tested.

Part of the elastic results differs from the first test campaign in which softening was observed for the higher strain rates. In addition, it is essential to note that Dau observed a self-heating of the laminate with a measured temperature of $+60\,°\mathrm{C}$ for a strain rate of $400\,\mathrm{s}^{-1}$ (Dau, 2019). The observed self-heating is presented as the cause of the softening because strain rate hardening competes with softening generated by a temperature increase. At RH0, the T_g is approximately $+60\,°\mathrm{C}$. Therefore, the laminate temperature may exceed the T_g during the tensile test resulting in a change in the behaviour of the matrix from solid to rubbery state. Overpassing the T_g changes the material state which leads to softening, as shown by Dau (2019) with tensile tests carried out at several temperatures on GF/PA66 and PA66. This softening observation was not reproduced in the present study with an increase of yield stress and shear modulus

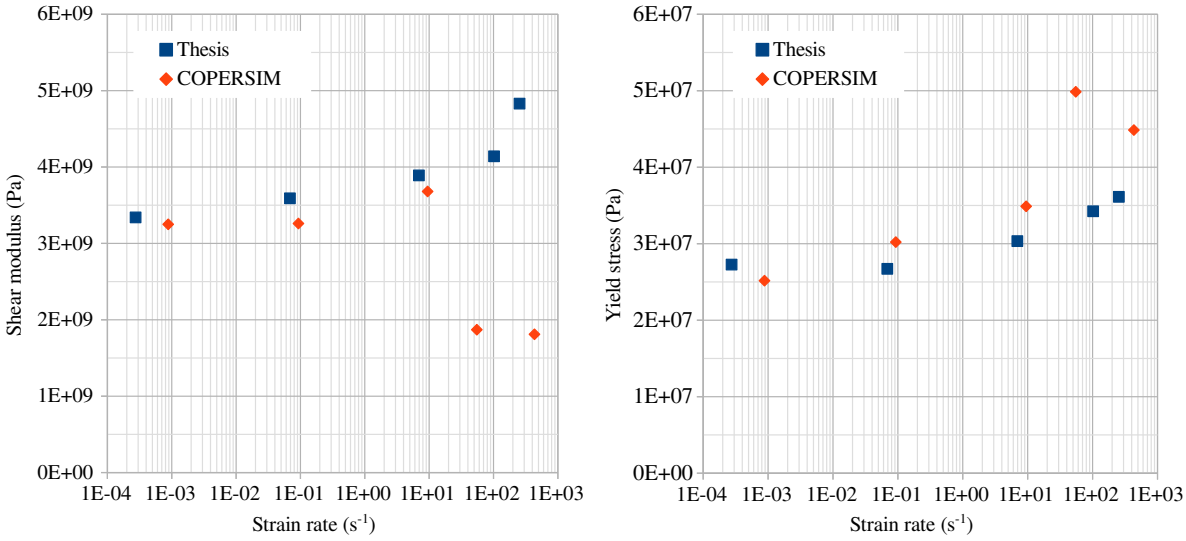

(a) Shear modulus

(b) Yield stress

Figure 2.23 – Comparison of the mechanical properties identified from COPERSIM and the last tensile tests

up to $254\,\mathrm{s}^{-1}$. At the same time, no actions were taken to avoid the potential laminate self-heating. For this reason and regarding the behaviour of bulk PA66 strengthening and stiffening with strain rate increase (Dau, 2019), it is assumed that another thermal source, such as lightning, may cause the decrease observed by Dau beyond $60\,\mathrm{s}^{-1}$. In the present study, softening at the highest strain rates may have been limited using cold lighting and a large working distance. However, no element prevents self-heating, which may have reduced shear stiffening with increasing strain rate at RH0/T23 °C. The comparison of COPERSIM-Crash and current work stress-strain curves in shear are presented in Appendix B.

2.3.3 Update of the constitutive model parameters

Some model parameters for shear behaviour (as the shear modulus and yield stress presented above) identified from the tensile tests performed in this work differ from previous work (Table 2.3). The validity of the updated parameters' was checked with elementary tests. Calculations made on one integration point were used to validate the RVE behaviour of the elementary ply. One shell element is loaded at a fixed velocity on one edge and embedded on the opposite edge. The strains and stresses are extracted at the integration point.

	Original parameters value	Updated parameters value
Elasticity	E_{11}, E_{22}, ν_{12}, ν_{21}	G^0_{12}
Inelasticity	β, m, Y^0_{11}, Y^0_{22}, Y^R_{11}, Y^R_{22}, α_1, α_2, α^2_{12}, d^{max}_{11}, d^{max}_{22}, d^{max}_{12}	σ^0_{12}, Y^0_{12}, α^1_{12}, d^M_{12}
Viscous functions	$\dot{\varepsilon}^{exp}_{12}$, $\dot{\varepsilon}^{ref}_{11}$, $\dot{\varepsilon}^{ref}_{22}$, $F^{1/2/3}_{Y^R_{11}}$, $F^{1/2/3}_{Y^R_{22}}$	$\dot{\varepsilon}^{ref}_{12}$,$F^{1/2/3}_{G^0_{12}}$, $F^{1/2/3}_{\sigma^0_{12}}$, $F^{1/2/3}_{\sigma^R_{12}}$, $F^{1/2/3}_{d^M_{12}}$, $F^{1/2/3}_{\alpha^1_{12}}$

Table 2.3 – VUMAT parameters for longitudinal behaviour

Concerning the longitudinal behaviour, Figure 2.24 highlights that COPERSIM reference test, the current one and the numerical result considering elastic-fragile-damage model are quasi-identical. Strain

rate sensitivity of longitudinal and transverse behaviour was not considered for the rest of the study. The final parameters used in the VUMAT for the longitudinal behaviour are summarised in Table 2.4.

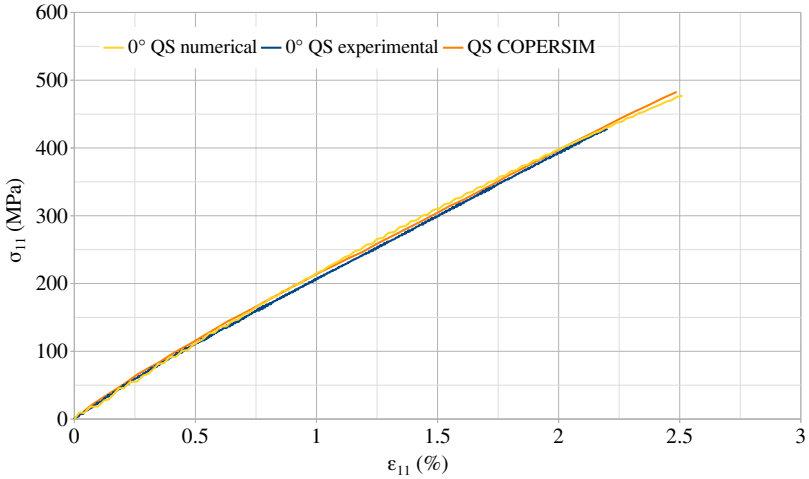

Figure 2.24 – Comparison of experimental and numerical results for the new tensile tests - longitudinal behaviour

E_{11}=E_{22} (Pa)	ν_{12} (-)	$\sqrt{Y^0_{11/12}}$ ($\sqrt{\text{Pa}}$)	$d^{max}_{11/22}$ (-)	$\sqrt{Y^R_{11/22}}$ ($\sqrt{\text{Pa}}$)
2.25×10^{10}	0.0199	3.66×10^2	0.177	2.69×10^3

Table 2.4 – VUMAT parameters for GF/PA66 longitudinal behaviour

Concerning shear behaviour, the shear modulus and its viscous function were modified from the experimental data identified by the process explained in Subsection 2.2.2. The same applies to the yield and fracture stresses, the damage threshold between logarithmic and linear damage evolution and the slope of logarithmic damage evolution. The polynomial regressions for G^0_{12}, σ^0_{12}, σ^R_{12}, d^M_{12} and α^1_{12} are available in Appendix C. Figure 2.25 exhibits the experimental and numerical stress-strain curves for the RVE (parameters from Table 2.5). The behaviour is suitably reproduced by the numerical tests on the entire strain range required by the shear tests. Moreover, the strain rate dependency is well-fitted numerically. The description of the shear behaviour, especially for the strains below $10\,\%$, is consistent with the experimental results. This achievement is essential for modelling the welded specimens as the substrates are not expected to undergo larger strains during the tensile tests.

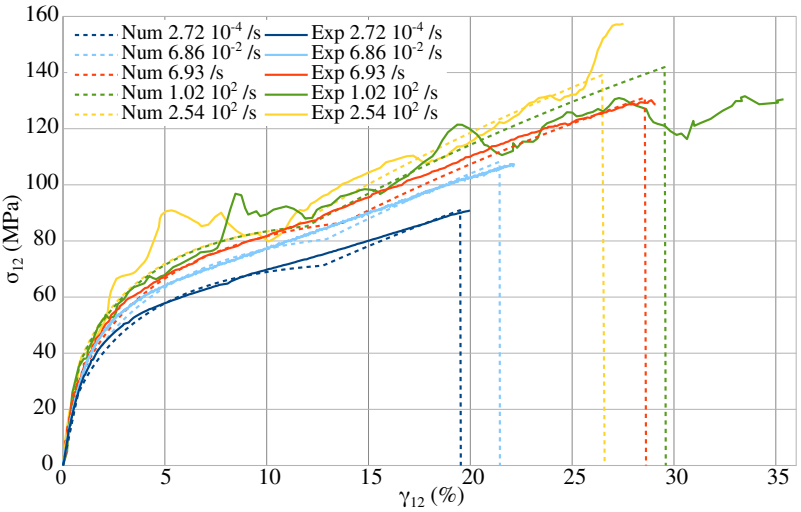

Figure 2.25 – Comparison of experimental and numerical results for the new tensile tests - shear behaviour

G_{12} (Pa)	σ^0_{12} (Pa)	β (MPa)	m	α^1_{12} (-)	$\sqrt{Y^0_{12}}$ ($\sqrt{\text{Pa}}$)
3.49×10^9	2.49×10^7	5.40×10^9	0.857	0.3089	298
$\sqrt{Y^R_{12}}$ ($\sqrt{\text{Pa}}$)	α^2_{12} ($\text{Pa}^{-0.5}$)	d^M_{12} (-)	d^{max}_{12} (-)	$\dot{\gamma}^{ref}_{12}$ (s^{-1})	$\dot{\gamma}^{max}_{12}$ (s^{-1})
3.18×10^3	2.04×10^{-5}	0.641	0.702	2.72×10^{-4}	2.55×10^2
$\dot{\gamma}^{exp}_{12}$ (-)	$F^{A3}_{G^0_{12}}$ (-)	$F^{A2}_{G^0_{12}}$ (-)	$F^{A1}_{G^0_{12}}$ (-)	$F^{A3}_{\sigma^0_{12}}$ (-)	$F^{A2}_{\sigma^0_{12}}$ (-)
1.5	3.71×10^{-6}	-1.04×10^{-4}	2.24×10^{-3}	6.62×10^{-6}	-4.54×10^{-4}
$F^{A1}_{\sigma^0_{12}}$ (-)	$F^{A3}_{d^M_{12}}$ (-)	$F^{A2}_{d^M_{12}}$ (-)	$F^{A1}_{d^M_{12}}$ (-)	$F^{A3}_{\alpha^1_{12}}$ (-)	$F^{A2}_{\alpha^1_{12}}$ (-)
1.52×10^{-2}	-2.30×10^{-6}	1.94×10^{-4}	-5.18×10^{-3}	1.55×10^{-6}	-3.69×10^{-5}
$F^{A1}_{\alpha^1_{12}}$ (-)					
-1.96×10^{-5}					

Table 2.5 – VUMAT parameters for GF/PA66 shear behaviour

2.4 Conclusions on the behaviour of GF/PA66

The previous work conducted during the COPERSIM-Crash project exposed the significant influence of strain rate, moisture and temperature on the shear behaviour of GF/PA66. Longitudinal and transverse behaviours are negligibly influenced by environmental parameters or strain rate. Based on these results, RH $0\,\%$ and room temperature (T $23\,^{\circ}\text{C}$) are chosen for the study of welded structures to limit the conditioning duration and ensure a uniform moisture level in the welded specimens. Control tensile tests and COPERSIM-Crash project results lead to a suitable knowledge of the material after storage in an uncontrolled environment (natural temperature/RH cycles for several years). The GF/PA66 composite shear behaviour is significantly affected by strain rate in a dry state and at room temperature. An increase in the shear modulus and yield stress is noticed. In addition, the fracture stress is enhanced by the strain rate increase. Some of these elements contrast with the results presented by Dau (2019) for the strain rate higher than $60\,\text{s}^{-1}$, which reported a softening behaviour caused by self-heating. These observations might diverge due to the geometry of the dumbbell-shaped specimen, which reduces the slippage in the grip, cold LED lighting and a large operating distance limiting the risk of material heating by the lighting. However, the self-heating could not be avoided and may lead to an overtaking of the T_g during the test, thus changing the mechanisms governing the composite behaviour. A thermal camera could have been used during the test to monitor the temperature evolution and its deviation from the T_g. The tensile tests were analysed to identify the constitutive model parameters and update those that evolved from the previous results. The VUMAT developed in (Mbacké & Rozycki, 2018) was employed as implemented, and the strain rate influence for in-axis behaviours was disabled for the rest of the study. The experimental results obtained in this work have updated some of the constitutive model input parameters. The numerical results on the RVE are consistent with experiments for longitudinal and shear directions. The strain rate sensitivity of the shear behaviour is also considered in the model and allows a faithful reproduction of the strain rate influence on the behaviour. Finally, the elastic and inelastic behaviours are close to the experiments up to $254\,\text{s}^{-1}$.

Knowledge of composite behaviour is essential for the welded structures study, especially for investigations on lap joint specimens using tensile tests. These research works aim to characterise and model the welded joints' behaviour from quasi-static to dynamic loadings. Therefore, all information about the composite to be welded is valuable to analyse the experimental characterisation tests on welded structures. Numerical simulation can then improve the understanding with access to several quantities

that are difficult to measure experimentally (damage, energy released rates, etc.). Moreover, the lap joint specimens' behaviour is driven by both the interface and the substrates. Therefore, the weld's behaviour can only be extracted by an inverse method for this specimen, which requires extensive modelling of the substrate's behaviour to isolate the welded joint behaviour. The following chapters investigate the welded joint's behaviour from an experimental and then numerical point of view.

Chapter 3

Characterisation of welded composite joints

Abstract: *The TP welded joints' performance is only studied for quasi-static or fatigue conditions in the literature, although some applications must withstand high dynamic loads. This chapter begins to fill this gap with the experimental characterisation of two welded specimen types for several loading speeds: single and double-lap joints. The specimens' geometry is described, and then the welding process is presented with the processing parameters choice. The steps of the experimental characterisation are reported: the specimen's drying, the testing rigs and the tensile tests post-processing. The experimental results are analysed using fractography, strength evaluation and load-displacement curves. The loading speed influences the behaviour of single-lap joint specimens by increasing their strength in dynamics. A stiffening behaviour is also observed for some configurations. The fracture mechanisms noticed are similar for all the loading speeds tested, with high strength inherited by fibre/matrix debonding mechanisms. As seen in Chapter 2, the viscous behaviour of the PA66 matrix leads to the stiffening and strengthening of GF/PA66 shear behaviour, which affects the global behaviour of the welded specimens. In addition, laminate strengthening reflects the improvement of the interfacial strength in the welded structures, which increases the specimen's strength due to the fibre/matrix debonding fracture mechanism.*

Contents

Introduction to the experimental characterisation of welded composite

The principal objective of these research works is to determine and model the behaviour of welded TP composite structures from quasi-static to dynamic loadings. Chapter 2 described the behaviour of the substrate based on previous research, the laminate behaviour validation after the material storage in an uncontrolled environment, and the constitutive model. This strong experimental and numerical basis allows for a better understanding of the study of welded structures because the substrates surround the weld; hence, their behaviour affects the structure's behaviour. This chapter presents the experimental characterisation of welded specimens with the methodology employed to analyse the structure's performances from quasi-static to dynamic loading. The objective is to study the welded specimens' behaviour and loading speed sensitivity; tensile tests also provide reference tests and inputs for the welded joint's modelling. The behaviour of the specimens used for the characterisation is a combination of the substrate and the weld's behaviour which will be separated using an inverse method on a numerical specimen (Chapter 4).

This chapter begins with the definition of the specimens and their geometry, which will be used to characterise the welded composite behaviour (first section). The configurations tested are detailed with the environmental conditions. The second section describes the experimental methods employed for the experimental characterisation. First, the welding process is described, with a short study to set the processing parameters before welding the specimens for characterisation. Second, the desiccation protocol application is briefly summarised. Third, the mechanical testing protocol is introduced with tensile test machines and cameras used. The fourth subsection explains the post-processing of data obtained from the tensile tests. The third section provides a description and analysis of the results. Several elements are analysed to get an overview of the welded specimens' behaviour: mesoscopic observations of the welds, fractography study, Load (**F**) - Displacement (**U**) curves (FU curves), and comparison of welded specimens' strength on the range of loading speeds considered. Finally, the conclusions of this experimental characterisation are drawn, taking into account the perspective of modelling the behaviour of welded joints.

3.1 Material and specimens for the experimental characterisation

The strategy employed for the experimental characterisation of welded structures is introduced in this section. The experiments were defined considering the reliable knowledge of the substrate behaviour for quasi-static and dynamic loadings (Chapter 2). The welded joint characterisation for a large range of loading speeds requires a suitable geometry for the specimens. The dumbbell-shaped specimens geometries are presented; SLJ and DLJ were selected to investigate the mixed mode I/II and mode II loadings, respectively. The influence of the substrate stiffness is investigated by welding several laminate orientations. Finally, the test cases matrix followed for these experiments is presented with loading speeds, number of specimens, substrates stacking sequences and environmental conditions.

3.1.1 Material and environmental conditions for testing

As presented in Chapter 2, GF/PA66 is a thermoplastic composite primarily used for the automotive industry. The reinforcement is quasi-balanced. Therefore, longitudinal and transverse properties are assumed to be identical. This composite was produced as four-ply laminates with a total thickness of 2 mm (0.5 mm thickness for each ply). PA66 matrix and GF/PA66 composite are sensitive to strain rate, temperature and RH. The previous results obtained in (Dau, 2019; Rozycki et al., 2019), summarised in Chapter 2, show a significant influence of strain rate, temperature and RH level on the shear behaviour of GF/PA66. For that reason, tests were conducted at fixed values of temperature and RH in the current

research works: $23\,°C$ and RH $0\,\%$ (dry state) to ensure an homogeneous moisture level in the welded specimens and limit the conditioning duration. Only the strain rate variations can affect the material behaviour in these conditions. The same plates as COPERSIM-Crash project are used; two stacking sequences were studied for the welded composite behaviour: $[0/45/45/0] = [0/45]_S$ and $[45/45/45/45] = [45]_4$.

3.1.2 Geometry of specimens and matrix of test cases

As in most studies in the literature, **S**ingle-**L**ap **S**hear (SLS) and **D**ouble-**L**ap **S**hear (DLS) tests were used to evaluate joint strength (Fernandez Villegas, 2014; Fernandez Villegas et al., 2015; Goto et al., 2019; Choudhury & Debnath, 2020). The tensile tests execution is relatively simple compared to conventional interface characterisation tests (DCB and ENF), especially for dynamic loading. In addition, the evaluation of fracture toughnesses from DCB and ENF tests may be distorted due to the fracture mechanisms encountered and inertia effects, as explained in Subsection 1.3.1. The purpose of the SLS tests is, theoretically, to load the welded interface in shear. This specimen is mainly used for adhesive and weld characterisation because its manufacturing is relatively simple, as well as the execution of tensile tests (ASTM D5868). However, in practice, the loading mode is a mixed mode I+II (peeling and shear) and not a pure mode II because of the specimen bending caused by the eccentricity of the loading (Figure 3.1) (Campilho et al., 2013). The DLJ specimen has the same overlap geometry as SLJ, although its symmetry limits the bending moment observed for the SLJ specimen (Figure 3.2) (Challita et al., 2011; Zhao et al., 2017). Therefore, the loading is closer to pure mode II.

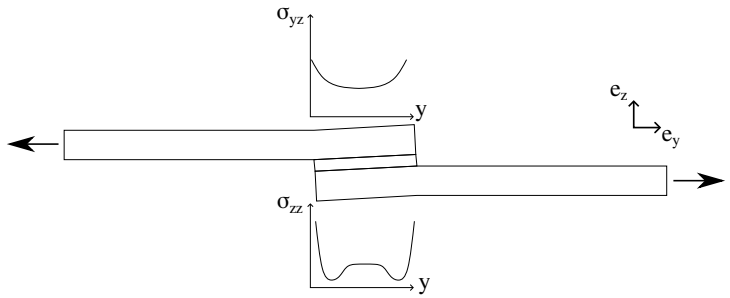

Figure 3.1 – Bending of SLJ specimen during tensile test

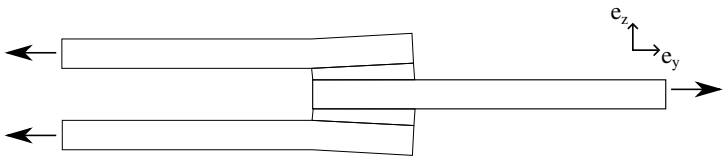

Figure 3.2 – Bending of DLJ specimen during tensile test

The geometries of SLJ and DLJ are similar to the specimens used for the laminate is Section 2.3.1 with dumbbell-shaped specimens (Figure 3.3). This geometry aims to concentrate the stress in the overlap zone. Moreover, it permits to prevent the slippage of the specimens in the grip using a stud and flange grip system. The same specimen geometry was used for all strain rate conditions to avoid the influence of structural changes.

The overlap geometry was chosen to include at least one RVE in the welded overlap. The largest RVE size in this study is $15\,\mathrm{mm} \times 15\,\mathrm{mm}$ (0°-oriented ply), so a geometry of $20\,\mathrm{mm} \times 20\,\mathrm{mm}$ has been defined for the overlap (Figure 3.3). Different stacking sequences are welded to study the influence of substrate stiffness on welded joint performance, the several configurations are: $[0/45]_S/[0/45]_S$, $[45]_4/[45]_4$ and $[0/45]_S/[45]_4$ for SLJ specimens and $[0/45]_S/[0/45]_S/[0/45]_S$ and $[45]_4/[45]_4/[45]_4$ for DLJ specimens. $[0/45]_S$ laminate is stiffer than $[45]_4$; in addition, the $45°$-oriented laminate has a ductile behaviour with large irreversible strains as opposed to the damage-elastic-fragile $[0/45]_S$ substrate. Therefore, the several configurations defined for SLJ and DLJ specimens will permit to study the influence of the substrates

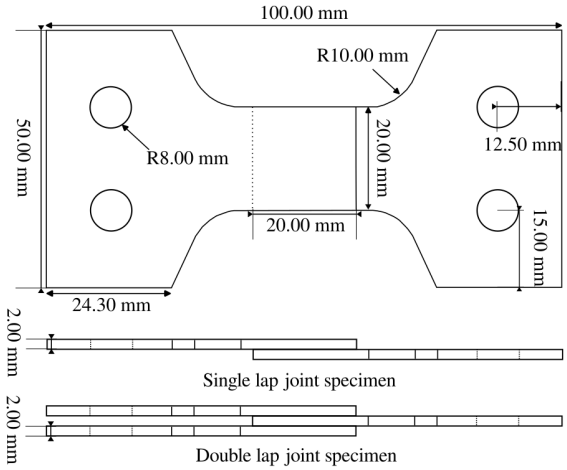

Figure 3.3 – Geometry of the welded specimens studied

stiffness and ductility on the weld behaviour. Three specimens are tested for each configuration and loading speeds to ensure repeatability. The test cases matrix is summarised in Table 3.1.

Specimen's type	Configurations	Loading speeds	Repeatability specimen	Total
SLJ	$[0/45]_S/[45]_4$ $[45]_4/[45]_4$ $[0/45]_S/[45]_4$	5 velocities from $2 \times 10^{-5}\,\mathrm{m\,s^{-1}}$ to $7\,\mathrm{m\,s^{-1}}$	3 specimens	75 tensile tests
DLJ	$[0/45]_S/[45]_4/[45]_4$ $[45]_4/[45]_4/[45]_4$			

Table 3.1 – Matrix of the test cases for the welded joints

The SLJ standard was created to study bonded joints under quasi-static loading and not for welded joints, so this specimen type might not be adapted for the study of welded joints. Fernandez Villegas and Rans (2021) questioned the relevance of using SLJ specimens to study the interfaces of welded polymer composites. According to them, the study of the welded specimens' mechanical strength alone is not sufficient to characterise these specimens. Their behaviour is a combination of the substrates' behaviour and the welded interface; therefore, it is also essential to know the initial state of the weld and the unwelded substrate behaviour. These elements can be examined by fractography, by studying the mesostructure of the joint and by mechanical tests on the non-welded substrate. These elements have been studied and are presented together with the joint mechanical performances.

3.2 Experimental methods

This section presents the methodologies and protocols used for the experimental characterisation: US welding, processing parameter choice, specimens' conditioning, tensile test configurations and post-processing. US welding process depends on various parameters to suitably join interfaces (thickness, material, reinforcement orientation, processing parameters ...). A short study was conducted to define the processing parameters based on tensile tests and macroscopic observations. The aim was to work with good-quality welds without doing a complete development of the joining process for the GF/PA66. The desiccation protocol applied before the tests to reach a dry state in the specimens is shortly presented. The tensile tests methodology is described with the testing rigs used to reach loading speed from $2 \times 10^{-5}\,\mathrm{m\,s^{-1}}$ *to* $7\,\mathrm{m\,s^{-1}}$*. Finally, the post-processing and data computation are explained to analyse the results with load-displacement curves and weld strength.*

3.2.1 Welding: process and setting of processing parameters

US welding is a process widely studied in the literature with a certain maturity acquired over the years; hence, it is now used in the industry for some type of parts. An industrial welding process was employed to conduct the study on welded joints close to what could be done in the industry. Initially, the welding phase was to be carried out by an industrial partner with robust control of the US welding process on its composite. However, due to several difficulties, the welding phase eventually had to be outsourced using our GF/PA66 composite. Therefore, the US welding process was set up based on the subcontractor's knowledge to weld a similar laminate and with a short study on the influence of the welding energy.

Welding process and definition of the tests on the processing parameters

The US welding of specimens was outsourced. Specimens were water-jet cut, and then **E**nergy **D**irectors (EDs) were integrated onto one substrate for SLJ and two substrates for DLJ specimens (Figure 3.4). EDs are made of neat PA6 matrix. As explained in Subsection 1.2.3, this addition of pure matrix concentrates the energy dissipation at the interface (friction and viscous dissipation) during the welding process and improves the weld quality. Without this addition, there would not be enough matrix involved in the adhesion process for the process employed, and deconsolidation could occur at the interface and in the substrates due to a large extent of the **H**eat-**A**ffected **Z**one (HAZ). Finally, the mechanical and thermal properties of PA6 are similar to PA66, as shown in Table 3.2, which makes its use as ED consistent.

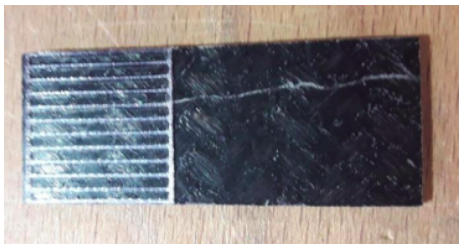

Figure 3.4 – Integration of energy directors on a specimen used for the processing parameters definition

Matrix	Young's modulus (MPa)	Poisson's ratio (-)	Yield stress (MPa)	Melting temperature (°C)	Glass transition temperature (°C)
PA66	3147	0.40	53.2	258	60 at RH0
PA6	3934	0.46	32.5	221	56 at RH0

Table 3.2 – Mechanical and thermal properties of PA66 and PA6 (Dau, 2019; Pivdiablyk, 2019; Ensinger, 2020)

The welding process employed is similar to the one presented in the literature review for individual samples welding (Subsection 1.2.3). It consists of the following steps:

- The elementary specimens are placed in a specific tooling after the EDs integration, which limits in-plane shifting of the samples and ensures planarity of the overlap (Figure 3.5),
- a sonotrode (or the horn) is placed in contact with the part to be welded,
- a welding force is applied to the joint while the sonotrode vibrates at a fixed amplitude ($60\,\mu m$) and frequency ($20\,kHz$),
- the vibration phase stops when the generator achieves the energy target,
- the solidification step starts with a holding force applied to the sample for a fixed duration to allow the interface to cool and limit deconsolidation in the interface and substrates.

Each interface of the DLJ specimen was welded separately, meaning that the first interface is joined in SLJ configuration, then the third elementary specimen is placed in the tooling, and the second interface

is welded with a tab placed between both arms of the DLJ to keep the distance between both external arms.

Figure 3.5 – Tooling used for specimens welding - DLJ configuration

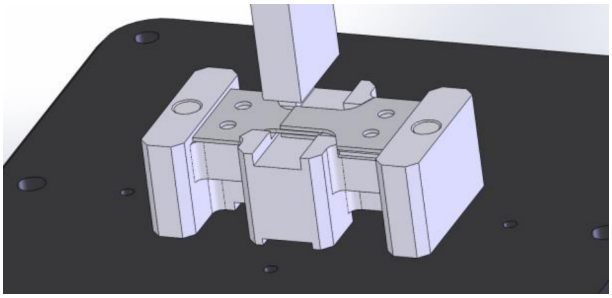

A set of processing parameters of the US welding had to be defined for the material used in this work. Thus a short study was conducted to determine adequate parameters leading to a suitable level of adhesion. To this end, three specimens were welded for each configuration with different process parameters. The process is energy-controlled, and then several energy levels were tested. Values are detailed in Table 3.3. The welding force, holding force and holding time are set to $50\,\mathrm{daN}$, $80\,\mathrm{daN}$ and $3\,\mathrm{s}$, respectively.

SLJ $[0/45]_S/[0/45]_S$ and $[45]_4/[45]_4$	SLJ $[0/45]_S/[45]_4$	DLJ $[45]_4/[45]_4/[45]_4$		DLJ $[0/45]_S/[0/45]_S/[0/45]_S$	
		Interface 1	Interface 2	Interface 1	Interface 2
550	650 (EDs on $[0/45]_S$)	600	700	650	700
600	650 (EDs on $[45]_4$) $\times$ 2 specimens	600	650	650	750
650		600	750	650	800

Table 3.3 – Energy levels tested for the development of the US welding process (energies in J)

The weld quality and performance were determined by tensile tests for all the development specimens. They were dried before mechanical testing to prevent the influence of RH (protocol detailed in Subsection 2.1.1 and desorption curves presented in Appendix D). The displacement and load signals were registered during testing to compare the performances. Tensile tests were conducted in quasi-static using a quasi-static tensile test machine INSTRON 5584 - $150\,\mathrm{kN}$ (Figure 3.6). Tabs cut in the same composite plates were placed, without being bonded, between the specimen and the grip to ensure symmetry in the load application and not to preload the specimen.

Tensile test results on developmental specimens and selection of parameters

Results from tensile tests on SLJ $[0/45]_S/[0/45]_S$ and $[45]_4/[45]_4$ are presented in Figure 3.7. The FU curves are similar for the three settings considered. In addition, a good reproducibility of the fracture load is noticed for both configurations (standard deviation less than $3.6\,\%$). Concerning the ultimate displacement of the upper grip, identical values are observed for SLJ $[0/45]_S/[0/45]_S$, but differences are noticed for SLJ $[45]_4/[45]_4$ ($7.6\,\%$ of standard deviation). The failure occurred along the welded joint with fibres tearing from the outermost ply of substrates and fibre/matrix debonding (Figure 3.8). Thus, any energy value tested could be used to study the interface behaviour.

For SLJ $[0/45]_S/[45]_4$ specimens, the FU curve varies depending on the integration of the EDs (Figure 3.9). Only one energy target was tested for this configuration, and the EDs was integrated either on the $[0/45]_S$ or $[45]_4$ laminate. Two specimens failed at the interface between the outermost ply of the

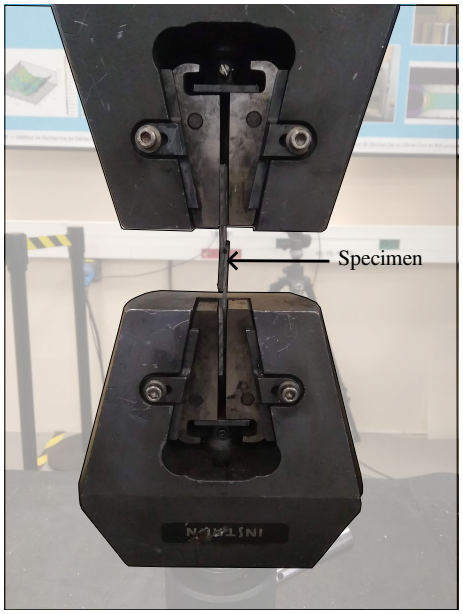

Figure 3.6 – Test setup for tensile test on specimens for the processing parameter choice

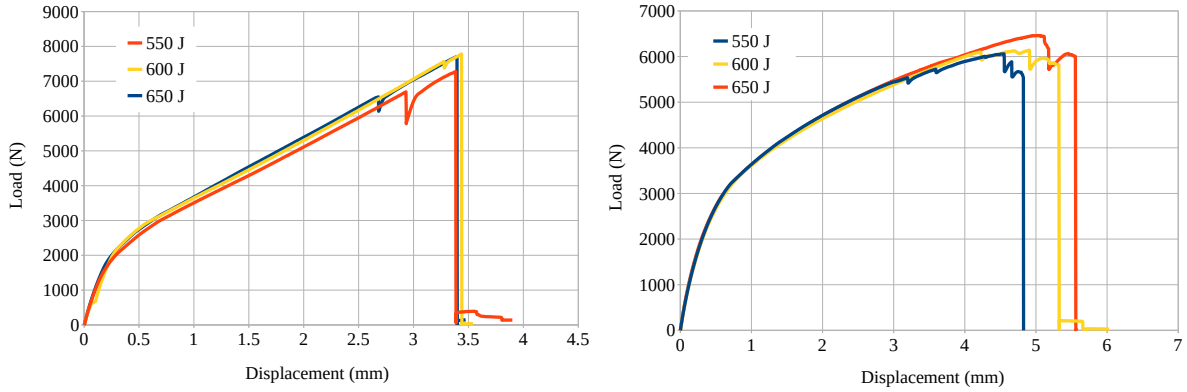

(a) SLJ $[0/45]_S/[0/45]_S$ (b) SLJ $[45]_4/[45]_4$

Figure 3.7 – FU curves for three levels of welding energy

(a) SLJ $[0/45]_S/[0/45]_S$ - 600 J (b) SLJ $[45]_4/[45]_4$ - 650 J

Figure 3.8 – Post-fracture SLJ specimens - study on the welding energy

laminate and the weld (mainly fibre/matrix debonding failure) also with cohesive fracture of the weld's matrix (Figure 3.10a). The third specimen failed with a mixed fibre/matrix debonding + adhesive fracture (Figure 3.10b). This latter type of failure is characteristic of variation which may occur in the extent of the welded zone, as the adhesion did not extend over the entire overlap. The yellow curve (Figure 3.9) corresponds to this mixed failure, and this specimen early fracture confirms the interface's low mechanical strength for the processing parameters considered. Moreover, these results show that scattering in the weld extent may occur even with a welding process using fixed parameters. Both specimens welded with an energy of 650 J presented different fracture types and performances. The tensile test with the highest fracture load corresponds to an integration of the EDs on the $[0/45]_S$ laminate. Finally, these welding parameters were selected for the SLJ specimens for the experimental characterisation of welds.

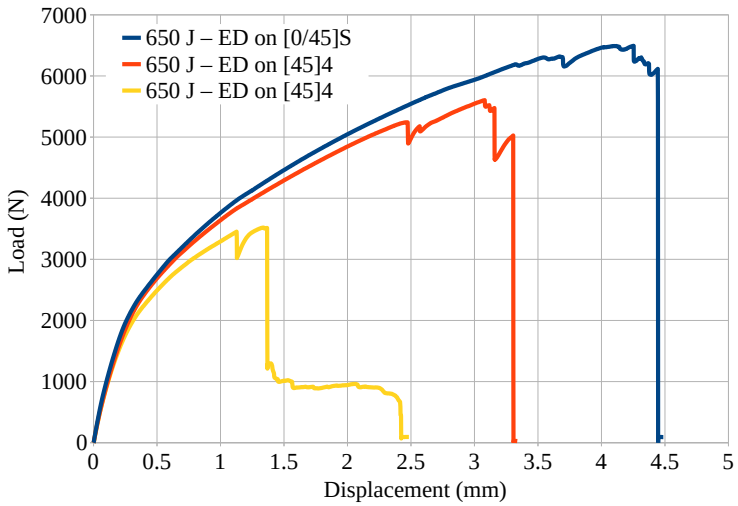

Figure 3.9 – FU curves for a 650 J welding energy and EDs integration on $[0/45]_S$ or $[45]_4$ substrate - SLJ $[0/45]_S/[45]_4$

(a) EDs on $[0/45]_S$ (b) EDs on $[45]_4$

Figure 3.10 – Post-fracture SLJ$[0/45]_S/[45]_4$ specimens - study on the welding energy

Two fracture types were observed for the DLJ specimens: substrate fracture and fracture of both welded interfaces. These two phenomena are identifiable on the FU curves (Figure 3.12). Indeed, the substrate fracture corresponds to the strictly increasing load over displacement until fracture (Figure 3.12a green and red curves, Figure 3.12b red and yellow curves), whereas a first interface fracture is noticed in the second case with a load drop followed by a load increase until the second interface fracture. The substrate fracture corresponds to the internal substrate fracture orthogonally to the welded interfaces (Figure 3.11). A double thickness is classically used for the middle laminate to overcome this stress concentration (Zhao et al., 2017), but this plate thickness was not available for this research study. The substrate rupture does not allow the characterisation of the interface behaviour until complete damage, so the parameters adopted are those characterised by the successive fracture of both interfaces.

Finally, the choice of energy target for the SLJ specimens was conditioned by the SLJ $[0/45]_S/[45]_4$ configuration. The energy target leading to the highest mechanical strength was chosen; consequently,

Figure 3.11 – Substrate fracture of DLJ specimen

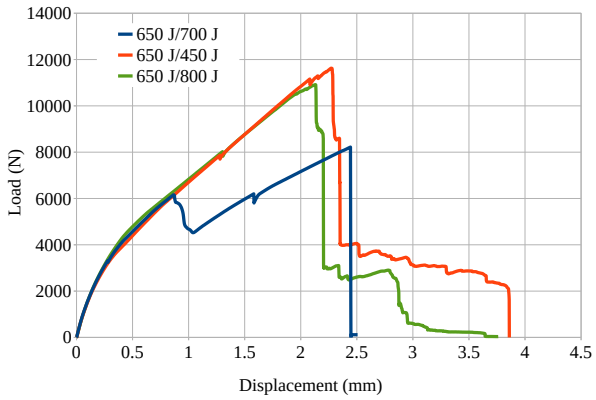

(a) DLJ $[0/45]_S/[0/45]_S/[0/45]_S$

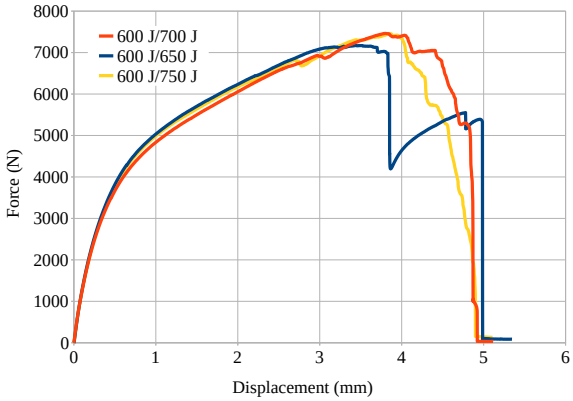

(b) DLJ $[45]_4/[45]_4/[45]_4$

Figure 3.12 – Post-fracture DLJ specimens - study on the welding energy

this welding energy will also be used for the unmixed joints ($[45]_4/[45]_4$ and $[0/45]_S/[0/45]_S$), as several values tested did not lead to significant variations in the interface behaviour. For the DLJ specimens, the parameters (650 J/700 J) and (600 J/650 J) are chosen for $[0/45]_S/[0/45]_S/[0/45]_S$ and $[45]_4/[45]_4/[45]_4$ respectively, because they allow the characterisation of the interface behaviour until fracture. Settings used for the experimental characterisation specimens are detailed in Table 3.4.

Configuration	Weld	Welding energy (J)	Welding force (N)	Holding force (N)	Holding time (s)
SLJs		650	50	80	3
DLJ $[0/45]_S/[0/45]_S/[0/45]_S$	interface 1	650			
	interface 2	700			
DLJ	interface 1	600			
$[45]_4/[45]_4/[45]_4$	interface 2	650			

Table 3.4 – Parameters for the ultrasonic welding process

Three outputs are measured during the welding process, and their averages are presented in Table 3.5 with the associated standard deviation. The generator supplies the power to reach the energy target. The welding distance corresponds to the sinking length in the specimen during the vibration phase. The total distance is the sum of the welding distance and the sinking distance during the holding phase. Finally, the welding time is the vibration phase duration. Despite using fixed values for the welding process, the process outputs vary depending on multiple factors: out-of-plane stiffness of the substrates, surface finish, void content, relative humidity, etc (Fernandez Villegas, 2014; Fernandez Villegas & Rans, 2021).

Conclusions on the US welding process setup

Different energy levels were tested to choose the most appropriate processing parameters for the weld characterisation. Concerning the SLJ specimens, the choice was based on the performance of SLJ $[0/45]_S/[45]_4$ as a significant difference was observed between the welding conditions and limited differences were obtained for SLJ $[0/45]_S/[0/45]_S$ and SLJ $[45]_4/[45]_4$. Nevertheless, two specimens were

Configuration		Power (W)	Welding distance (mm)	Total distance (mm)	Welding time (s)
SLJ $[0/45]_S/[0/45]_S$		675 ($\pm$ 34)	0.41 ($\pm$0.05)	0.53 ($\pm$ 0.06)	1.21 ($\pm$ 0.06)
SLJ $[45]_4/[45]_4$		720 ($\pm$ 57)	0.38 ($\pm$ 0.05)	0.52 ($\pm$ 0.06)	1.35 ($\pm$ 0.19)
SLJ $[0/45]_S/[45]_4$		699 ($\pm$ 39)	0.38 ($\pm$ 0.07)	0.50 ($\pm$ 0.08)	1.21 ($\pm$ 0.11)
DLJ $[0/45]_S/[0/45]_S/[0/45]_S$	int 1	703 ($\pm$ 43)	0.36 ($\pm$ 0.05)	0.48 ($\pm$ 0.06)	1.23 ($\pm$ 0.11)
	int 2	749 ($\pm$ 50)	0.38 ($\pm$ 0.04)	0.48 ($\pm$ 0.04)	1.14 ($\pm$ 0.05)
DLJ $[45]_4/[45]_4/[45]_4$	int 1	709 ($\pm$ 48)	0.44 ($\pm$ 0.05)	0.58 ($\pm$ 0.06)	1.38 ($\pm$ 0.13)
	int 2	781 ($\pm$ 65)	0.43 ($\pm$ 0.05)	0.53 ($\pm$ 0.06)	1.09 ($\pm$ 0.05)

Table 3.5 – Welding process outputs for the experimental characterisation specimens

welded with the same parameters and showed differences in the results (red and yellow curves in Figure 3.9). This gap is caused by a difference in the extent of the welded area in the overlap leading to reduced performance for the smaller welded surface area. Therefore, it underlines that some variability may occur in the extent of the welded portion of the overlap during the welding process as observed by several authors (Villegas & Bersee, 2010; Zhao et al., 2019; Zhi et al., 2022). Concerning the DLJ specimens, the parameters chosen for the experimental characterisation can lead to partially welded overlap for the secondly welded interface. Finally, only one test was performed for each processing parameter because of the limited resources for the PhD project, due to imponderables, that was not originally planned on this composite and based on the knowledge of the subcontractor on the welding of polyamide based $2\,\mathrm{mm}$ thick laminates. The objective was here to use a process which is close to what could be done in the industry. More tests should be required to have the highest weld performance and reproducibility in the area of the welded surface. Therefore, some variation in the extent of the welded area can be expected for the weld characterisation specimens. Specimens were welded and required conditioning before the tensile tests.

3.2.2 Specimen desiccation

The PA66 matrix behaviour is strongly dependent on the RH and temperature. The material used in this study was produced in 2016. Then it was stored in ambient air at a RH level higher than $50\,\%$ in average over five years. Therefore, the RH in the material is unknown and must be controlled before the characterisation tests to ensure consistency in the results from the moisture point of view. In that way, it is necessary to dry the specimens before the tests to control their moisture content as it was done for the specimens dedicated to GF/PA66 characterisation in Chapter 2.

Application of the desiccation protocol

The protocol presented in Section 2.1.1 was applied to the developmental specimens before the tests presented in Section 3.2.1 and for the welded specimens' characterisation from quasi-static to dynamic loadings. First, the mass loss measurements are presented in Appendix D for the specimens used for the preliminary study on the welding energy. Second, the same desorption protocol was applied to the specimens used for the experimental characterisation of welded specimens, except for the vacuum, due to issues with the pump. Two main difference are observed between the desorption process conducted in Chapter 2 - Subsection 2.1.1 and in this section: specimens are two or three times thicker due to the overlap zone and desorption is conducted at atmospheric pressure. Both of these elements may increase the desorption duration (Obeid, 2016). Therefore, mass measurements were conducted to follow the

desorption evolution over time and stop it after the right duration. A duration of $1200\ \sqrt{\text{s}}$ ($16.7\ \text{days}$) was needed for the three thicknesses of specimens (composite, SLJ and DLJ) for desorption at $+90\ °\text{C}$ and atmospheric pressure (Figure 3.13). Specimens were kept for 18 days in the desiccator as a precautionary measure. The duration is longer under atmospheric pressure (17 days at P_{atm} versus 4 days at $P = 6\ \text{mbar}$ - section 2.1.1); however, similar mass losses are obtained for desorption under vacuum and at atmospheric pressure.

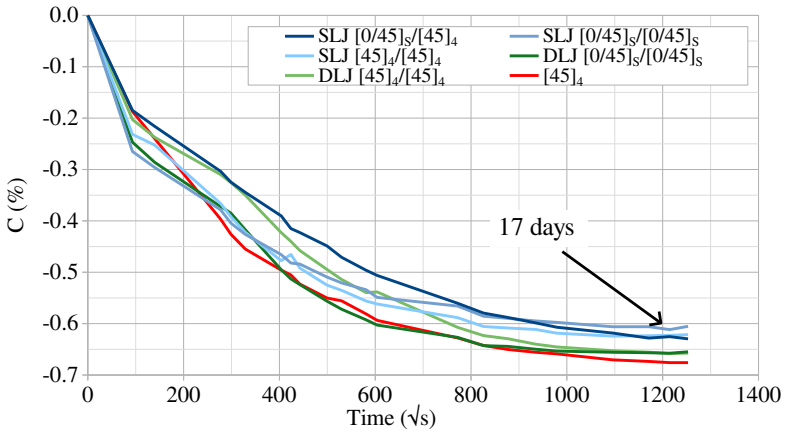

Figure 3.13 – Desorption curve of the samples for the weld's characterisation specimens

Once the desorption stage has ended, the samples are stored in quadruplex-layer PET aluminium OPA PE ($\pm 10\ \%$) bags (BERNHARDT company). The bag opening is then sealed with the BERNHARDT B235M impulse welder. This storage prevents change of RH in the material stored until the mechanical testing. The specimens are stored by three or six for each bag and are grouped by test loading speed.

3.2.3 Mechanical testing on welded specimens in quasi-static and dynamic

The characterisation was conducted at CRED located at École Centrale de Nantes. Two different tensile test machines were used to reach loading speeds from $2 \times 10^{-5}\ \text{m s}^{-1}$ to $7\ \text{m s}^{-1}$ using a quasi-static tensile test machine (INSTRON 5584 - $150\ \text{kN}$) and an hydraulic dynamic tensile test machine (MTS 819 - $20\ \text{kN}$). The highest loading speed considered is limited to $7\ \text{m s}^{-1}$ because of the camera used to record the tests; the windowing and acquisition frequency reached a limit for this loading speed, allowing a large enough area to be filmed and a sufficient number of points to be obtained throughout the test. The load is measured by the machines' load cell for all the tensile tests.

Concerning the operation of the hydraulic machine, the speed reached by machine's crosshead can be up to $10\ \text{m s}^{-1}$, hence, a suitable loading method is used to avoid a progressive increase of the speed during specimen loading and load the specimen at a quasi-constant loading speed. The sliding bar is connected to the actuator by an enclosing case; the bar can slide over a distance called "free fall", which controls the sliding speed. Once the "free fall" is complete, the bar drives the actuator at the target travel speed and loads the specimen. Concerning the load, the grip bar is mounted on an Hopkinson bar instrumented with strain gauges to measure the reaction force.

Displacements are measured using **D**igital **I**mage **C**orrelation (DIC) on the images recorded by high-speed cameras. For the GF/PA66 characterisation, one high-speed camera recorded the tensile tests. Concerning welded specimens, two cameras were used to register the specimen front and side (Stemmer AVT GT 6600) for the quasi-static tensile test (Figure 3.14a). The results from the front are used to extract the displacements, and then the images from the side highlight the specimen bending during the tests. For the dynamic tests, it was not possible to record the test from the front and side simultaneously due to the dynamic tensile test machine configuration. Therefore, images of the specimen are recorded from the front on both specimen faces using two high-speed cameras (Photron AX200 and Photron SA1 - Fi-

gure 3.14b with one camera visible). The use of two cameras also permits identifying the fracture of each interface for DLJ specimens in case of non-simultaneous fracture and accessing additional displacement or strain measurements which might differ on both sides due to the dynamic loading. Cold LED lighting illuminates the specimen to limit the material heating caused by the testing setup. A flange and stud system constitutes the grip for the specimen (Figure 3.15a). It avoids substrate slippage on the loading speed range considered; the two pins block the in-plane shifting, and the flange constrains the out-of-plane movements. Tabs were placed between one specimen end and the grip to load the SLJ specimen in the interface plane; they are not bonded to the specimen but placed on the grip. Another tab is placed between external substrates for the DLJ specimen (Figure 3.15b). These pieces were cut from the same composite plates as the substrates.

(a) SLJ specimen on the quasi-static test machine

(b) SLJ specimen on the dynamic tensile test machine

Figure 3.14 – Experimental setup for welds characterisation

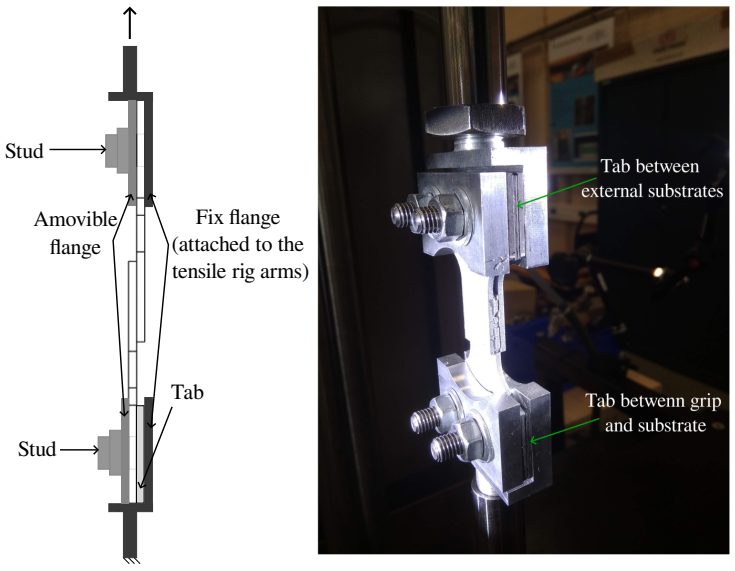

(a) Scheme of the system for a SLJ specimen

(b) DLJ specimen on the dynamic tensile test machine

Figure 3.15 – Stud and flange clamping system

Concerning environmental conditions, the room temperature is controlled and set at 23 °C, and the sealed bag is open less than three hours before the tests, the specimens' dimensions are measured and specimens are prepared for the tensile tests. In these conditions, the moisture uptake in the specimen is small as demonstrated by Pivdiablyk for GF/PA6 at 23 °C/RH 0 % (Pivdiablyk et al., 2020). A speckle

pattern required for DIC is placed on the samples with a first layer of white paint and a second layer of sprayed black.

3.2.4 Post-processing method for the tensile test on SLJ and DLJ specimens

After mechanical tests, images and load signal are post-processed to obtain FU curves. In addition, the post-mortem interfaces are studied to evaluate the fracture mechanisms. The protocols used are presented in the following paragraphs.

Extraction of FU curves

Displacements are extracted from the recorded images using DIC. As a first step, the tracking of points is done using virtual gauges on the software Ufreckles (Réthoré, 2018). A precise gauge location is defined to extract displacements at the same points for all the tensile tests, despite the change in windowing and resolution. Gauges are placed in the middle of the specimen, $4.5\,\mathrm{mm}$ in width. The gap between the gauge edge and the flange measures $4\,\mathrm{mm}$, and $5\,\mathrm{mm}$ separate the three gauges (Figure 3.16a). Displacements of the four vertexes are processed to calculate the elongation of the gauge considered over time. The displacements of the two top vertexes are averaged, the same is done for the bottom vertex. Then, both averaged values are subtracted to obtain the gauge elongation. This virtual gauge is close to how a gauge works experimentally with the measurement of a averaged strain over a surface from the displacements of edges. Finally, only the intermediate gauge is considered for post-processing as it is far enough from the bending zone and it is also below the grip system.

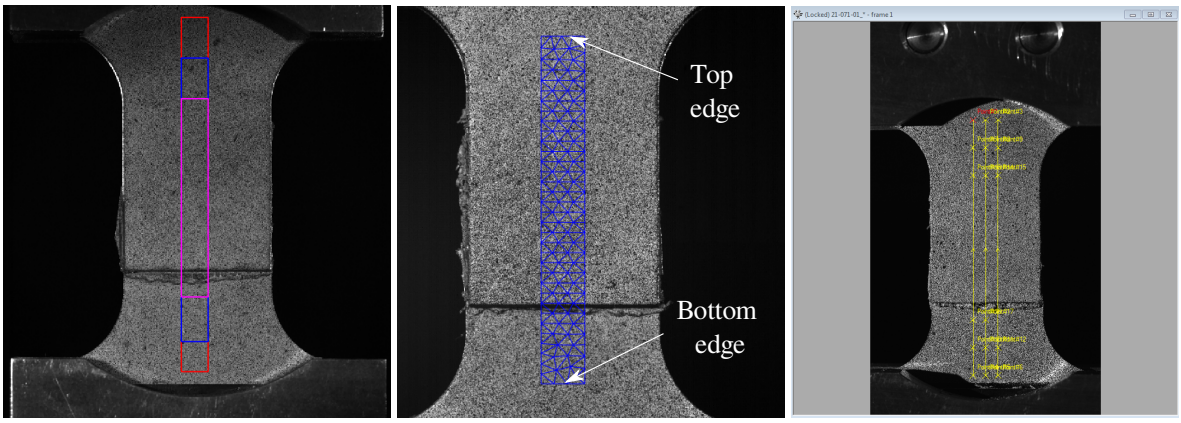

(a) Use of virtual gauges with Ufreckles (b) Use of mesh with Ufreckles (c) Point tracking with TEMA

Figure 3.16 – Several uses of DIC for the displacements extraction using Ufreckles and TEMA

These results are compared to measurements done using a mesh for the DIC, instead of a simple gauge over a surface, in order to use a method closer to what can be done numerically using finite element simulation (Figure 3.16b). Displacements were averaged on the top and bottom edges of the mesh and subtracted. The comparison in Figure 3.17a shows the difference between both methods before specimens' fracture. The deviation, caused by the substrate deformation, expands during the tensile test. The displacements measured at the top edge of the mesh differ for each node considered, but the gauges do not take this into account. Results are compared with those obtained with TEMA software using three vertical virtual gauges described by lines (Figure 3.16c). The mean elongation is calculated as the average of the three gauges. TEMA and Ufreckles results are similar (Figure 3.17b). Finally, the meshed option is used for the post-processing of all specimens using Ufreckles (Réthoré, 2018), this choice is closer to what will be done numerically using a finite element method.

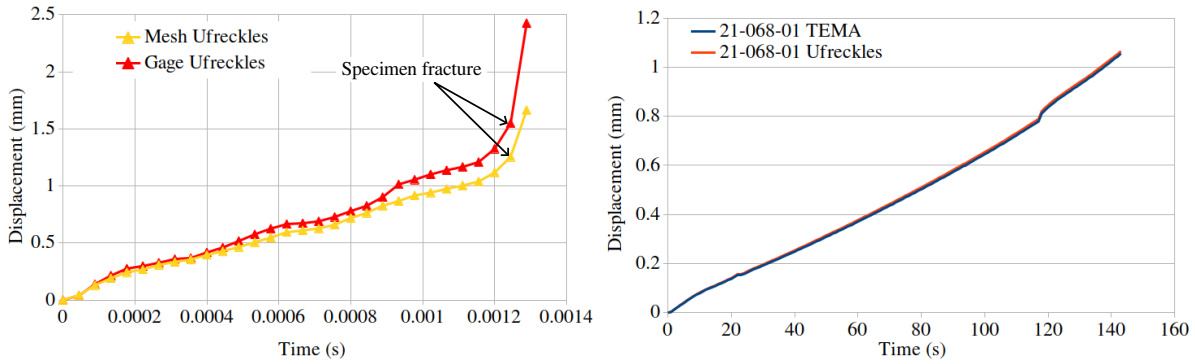

(a) Virtual gauge versus mesh using Ufreckles

(b) Ufreckles versus TEMA

Figure 3.17 – Comparison of displacements evolution over time using different extraction methods

Concerning the dynamic tests, camera and load registering start before the test begins because of the short duration of the tensile test and the loading method on the MTS dynamic tensile test machine. A trigger signal links the temporal reference of load and images. The reference ($\mathrm{t} = 0\,\mathrm{s}$) is not the beginning of specimen loading but the trigger (Figure 3.18). Therefore, the temporal adjustment of the displacement and load data follows the extraction. The beginning of the tensile test is identified for the load signal and displacement. Both signals have different frequencies ($500\ i/s$ to $125\,000\ i/s$ for displacements and $1\,\mathrm{kHz}$ to $1\,\mathrm{MHz}$ for the load depending on the loading rate), so interpolation of one signal is needed to obtain the FU curve. Therefore, load data are interpolated on the displacement extraction frequency to plot the FU curves for the welded joint behaviour analysis. The linear interpolation was made for the load signal and not for the displacement because a larger number of points existed for the load (higher acquisition frequencies of the cell than the camera), thus it avoids data creation.

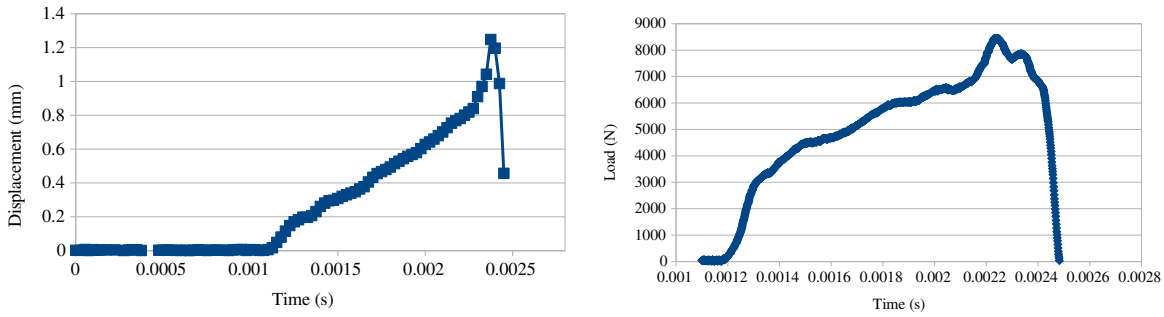

(a) Displacement signal

(b) Load signal

Figure 3.18 – Signals before interpolation and identification of the tensile test start

Some tensile tests are affected by out-of-plane movements of the grips, consequently of the specimen head. In quasi-static conditions, they affect the measurement quality due to the short operating distance between the camera and the specimen. In fact, for the configuration presented in Figure 3.19, the errors on the measured strains are calculated by Equation 3.1. Hence, a short operating distance can lead to a significant error in the displacements measured by DIC.

$$\Delta\varepsilon_{xx/yy} = \frac{\partial u\,(\Delta Z)}{\partial Z} = -\frac{\Delta Z}{Z} \tag{3.1}$$

The vertical displacements are corrected using the recordings made on the specimen side for the quasi-static tests. The displacements of nodes are extracted along a line from the front recording, at the

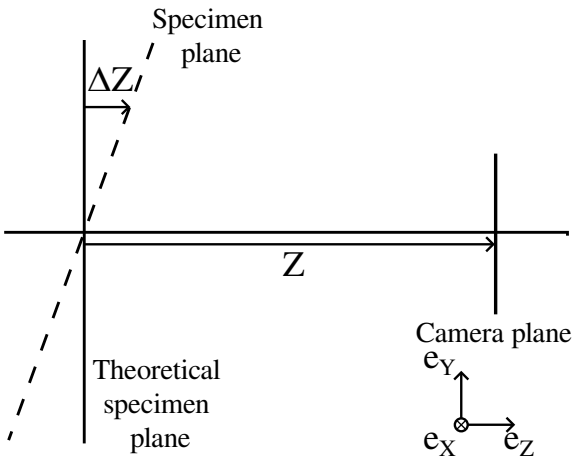

Figure 3.19 – Configuration of test with out-of-plan movements

specimen top and bottom (Figure 3.20a). Then, the vertical displacement of the top and bottom lines left end is extracted from the side recording (green point for the top line in Figure 3.20b). From these evaluations, the gap between the vertical displacements from the front and the side (U_Y^{front} and U_Y^{side} respectively) is calculated with Equation 3.2. This relative error (RE) is assumed to be equal throughout the specimen width, the corrected displacements along the line can be obtained by applying Equation 3.3 to the node considered. Then, the displacements along the top and bottom lines are plotted and saved. Finally, the elongation of the virtual gauge is calculated and plotted versus load. Figure 3.21 shows the shape of the FU curve with the first extracted data and corrected data; no loss of stiffness is observed at the beginning after correction. Concerning the other loading speeds, no camera was used on the specimen side as the tests were performed on the dynamic tensile test machine. Thus, the correction protocol described previously cannot be applied. Nevertheless, as the operation distances are more considerable for these tests, the effect of the out-of-plane movements on displacement extraction is reduced.

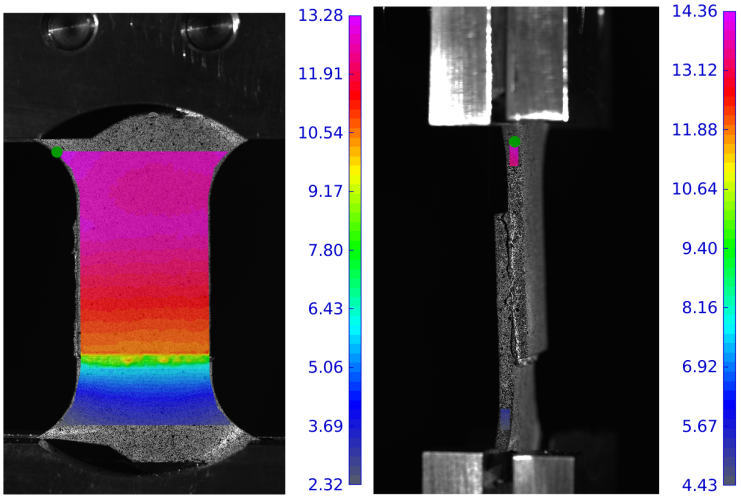

(a) Extraction from the front (b) Extraction from the side

Figure 3.20 – Extraction of displacement for the correction of data in quasi-static - vertical displacement in pixel

$$RE = \frac{U_y^{side} - U_y^{front}}{U_y^{side}} \quad (3.2)$$

$$U_{y,N_X}^{corrected} = U_{y,N_X}^{front} \times RE \quad (3.3)$$

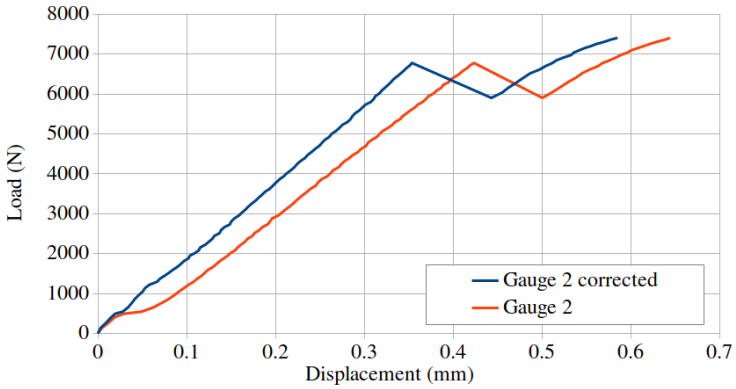

Figure 3.21 – FU curves before and after correction from side data - SLJ $[0/45]_S/[45]_4$ quasi-static

Measurements of welded area surface

The measurement of the welded area was made on the post-mortem specimens using the image processing software ImageJ (Schneider et al., 2012). This data permits the calculation of the joint performance called the **L**ap **S**hear **S**trength (LSS) as expressed in Equation 3.4. This quantity is mainly used in the literature to evaluate the weld quality as a comparison of different processing parameters (Villegas & Bersee, 2010; Goto et al., 2019). In this work, the LSS defines the joint performances and allows the study of the loading speed influence on this strength. The quantity S_{welded} corresponds to the welded area of the overlap. The images of the post-mortem interfaces are treated manually to identify the fibre/matrix debonding and matrix fracture zone, then the area is measured (Figure 3.22). F_{max} is extracted from the load signal recorded by the load cell before data interpolation to use the whole data measured. The number of points can be limited for the highest loading speeds ($2\,\mathrm{m\,s^{-1}}$ and $7\,\mathrm{m\,s^{-1}}$), then the maximum load could be less precisely evaluated from the FU curve (in practice a deviation of $2.5\,\%$ maximum was obtained, which is limited).

$$\mathrm{LSS} = \frac{F_{max}}{S_{welded}} \tag{3.4}$$

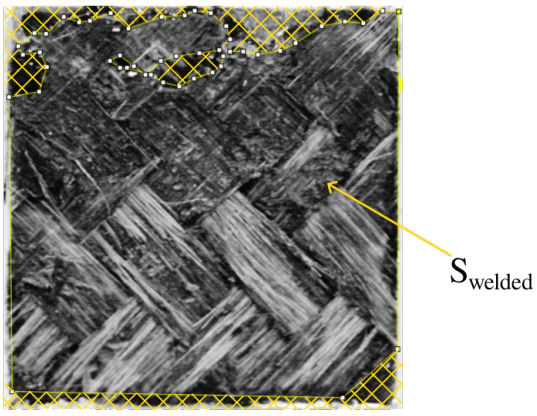

Figure 3.22 – Silhouetting of the welded interface using ImageJ

3.3 Aspect and behaviour of the welded joints

Previous sections presented all the methodological protocols to prepare and realise the characterisation tests. The results of the experimental characterisation conducted on the welded specimens are described and analysed in this section. First, observations are made on the macroscopic and mesoscopic aspects of welds cross-sections. These elements are useful to improve the understanding of joints behaviour and fracture mechanisms. Second, a fractography analysis presents the different fracture types observed and the prevailing fracture mechanism. Results highlight one

mechanism - combined fibre/matrix debonding and cohesive fracture of matrix - linked to high performance welds on which the analysis focuses. Then, the mechanical performances of the welded joints are presented in the last section of this chapter through the FU curves and the LSS. These results are analysed to determine to what extent the loading speed influences the behaviour of the welded specimens.

3.3.1 Macroscopic and mesoscopic observations of the welded interfaces

The specimens were welded with the same parameters of energy, welding force, holding force and welding time presented in Subsection 3.2.1. Despite the fixed processing parameters, the welds are not exactly identical because of the surface condition, RH and other parameters which may vary from one specimen to another. Several differences are observed; the welded interface edges are not altered by the welding process for $56\,\%$ of the specimens (Figure 3.23a). Parts of molten matrix can also be visible at the overlap edges; it led to fibres squeeze-out (Figures 3.23b and 3.23c lower left corner). In addition, for all specimens, part of the matrix flowed outside the overlap at the edges of the interface (white matrix visible at the interface edges). These elements were removed with a razor blade before the tests.

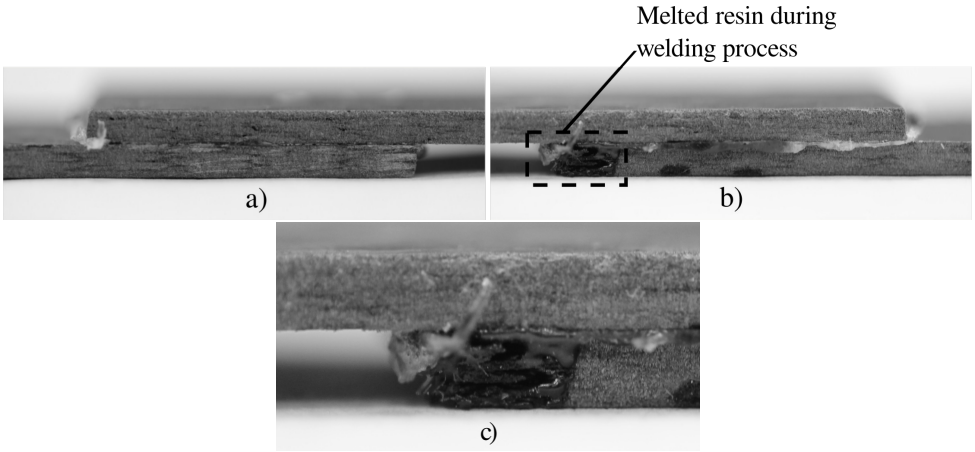

Figure 3.23 – Side of two SLJ specimens: a) edges without matrix flash, b) edges with matrix flash on bottom left corner and c) zoom on the circled zone of b)

One specimen of each configuration was cut out in the middle of the overlap, orthogonally to the loading direction and EDs, to observe the cross-section. These observations estimate the weld quality at that particular overlap location and measure the welded joint thickness. Overall, the EDs matrix blends with the laminate matrix (Figure 3.24). This mesostructure of welded joint reflect a high level of adhesion and healing between EDs and substrates matrices. The melting/softening of matrices on the short welding duration ($\sim 1\,\mathrm{s}$) is sufficient to create an intimate contact and erase the material interface between PA66 and PA6. However, voids are observed in some specimens, particularly at the overlap edges due to matrix squeeze-out. In this area, fibre movement is eased, resulting in the formation of voids. The voids may also be caused by moisture contained in the substrates, residual stresses or the welding process control. The specimens were not dried before welding, so the moisture contained in the laminate is heated during the welding process and might form the voids as observed by Shi et al. (2013) using resistance welding. Heating the interface may also relax residual stresses by changing the matrix state from solid to liquid or rubbery state (crystalline and amorphous part, respectively) (Amedewovo et al., 2022). Moreover, the energy-controlled process may be responsible for the presence of voids and differences between specimens. Fernandez Villegas (2014) showed that this way of controlling the process might lead to a difference in the welding stage reached. Therefore, specimens may have been submitted to vibration for too long, leading to the reinforcement deformation and the HAZ extension or for a too short duration,

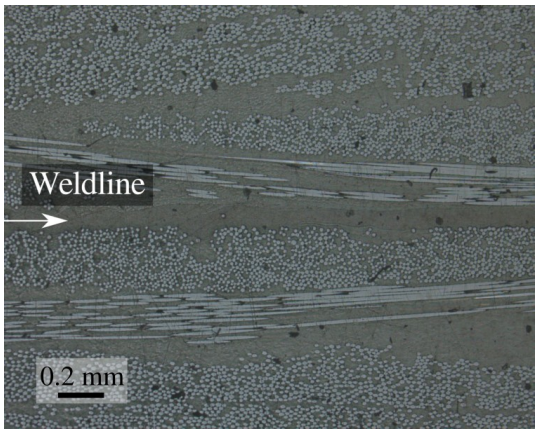

Figure 3.24 – $[0/45]_S/[0/45]_S$ cross-section micrograph at the overlap centre

leading to partial melting of EDs and laminates matrix. Unwelded zones are also noticed (Figure 3.25). These areas may be caused by the partial or slower melting of one or several EDs so that the matrix in a rubbery or liquid state could not flow to fill the gap, resulting in a hole in the final weld. These observations are local and were carried out only on one specimen for each type of overlap. Nevertheless, they provide information on the interface as the presence or absence of non-welded areas and an estimated thickness for the welded joint.

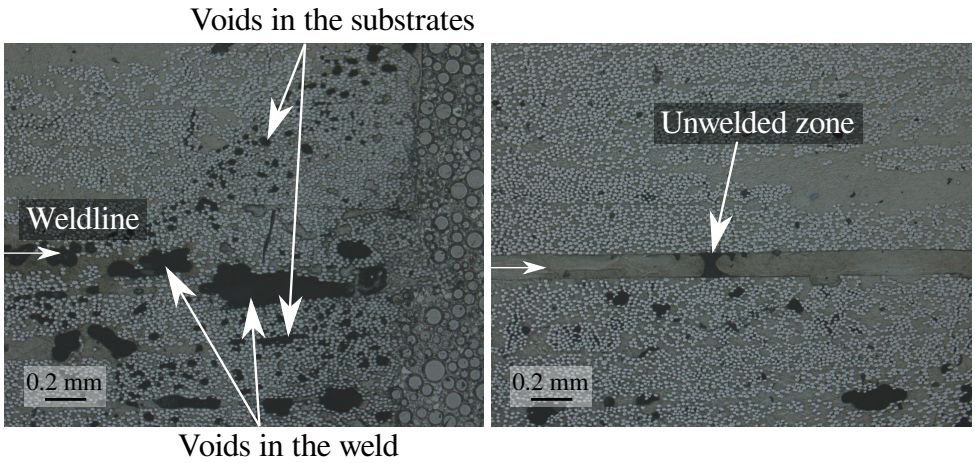

Figure 3.25 – $[45]_4/[45]_4$ cross-section micrographs on the overlap edge (left)) and overlap centre (right) (weldline indicated by the white arrow on the side)

In the case of the DLJ specimen cross-section, Figure 3.26 shows that the first welded interface is thin compared to the second one. Nevertheless, this weld is still thicker than the interply interface. For the second welded interface of the specimen in Figure 3.26, a non-welded zone is visible. Moreover, the interface between substrates and EDs matrix can be distinguished on either side of the non-welded area. These zones are also noticed on some SLJ and SLJ specimens' outside (Figure 3.27 green framed zone). EDs matrix flew out from some parts of the interface, as on the weld right side, and a small gap is spotted between both substrates elsewhere. Therefore, the welded area is expected to be smaller than the overlap for some specimens.

Measurement of the weld thickness

The welded joint thickness was estimated by measuring the overlap thickness with a micrometre at different points for all the characterisation specimens. The average non-welded laminate thickness is subtracted from the measurements, assuming that this thickness does not vary in the overlap area (no reduction in laminate thickness caused by the joining process). Therefore, an average value for the welded

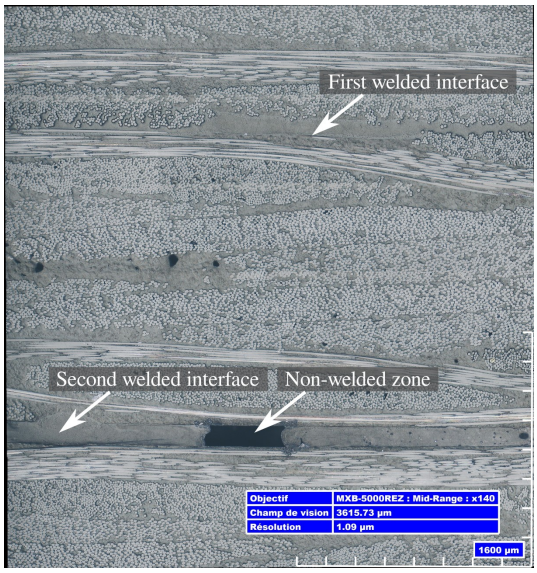

Figure 3.26 – $[0/45]_S/[0/45]_S/[0/45]_S$ cross-section micrographs

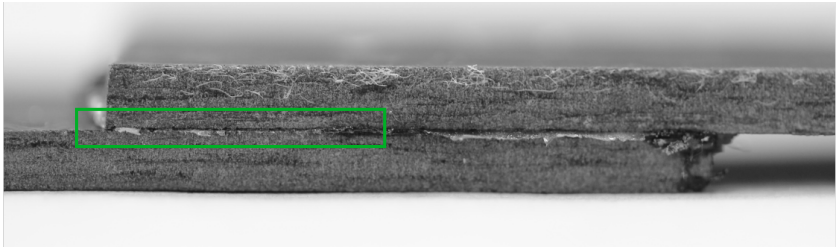

Figure 3.27 – Side of a SLJ specimen with a visible non welded zone on the overlap edge

joint thickness of $2.39 \times 10^{-5}\,\mathrm{m}$ is obtained, i.e. approximately ten times the thickness of the matrix-rich interply area. This macroscopic measurement was compared to a microscopic evaluation made with ImageJ software (Schneider et al., 2012) on the cross-section micrographs. The thickness was measured at different points along the cross-section, and then these values were averaged. Details about these measurements are given in Appendix E. A difference from 2 to $5\,\%$ is observed between the values obtained macroscopically and microscopically. Consequently, the thickness evaluated macroscopically will be used for the rest of the study.

Conclusions on the macroscopic and mesoscopic observations

These double-scale observations revealed areas with a strong adhesion between EDs and substrates with matrices blending in the interface. An average of $23.9\,\mu\mathrm{m}$ for the matrix-rich zone thickness was calculated from all the specimens welded, which is about ten times more than the interlaminar zone but thinner than bonded joints. Moreover, defects were observed in the weld and substrate, such as voids and partially welded zones; these elements can affect the joint performance and mechanical behaviour. Concerning DLJ specimens, a difference in thickness can be observed between both interfaces, hence it will influence these specimens' behaviour. These elements will be considered in the following analyses to understand tensile test results.

3.3.2 Fractography analysis

Fractography analysis aims to identify the fracture mechanism resulting from the tensile tests. These observations help to understand the mechanical performance of the welded joint. Moreover, the mechanisms identified can be explained by the weld mesostructures observed in the previous subsection.

Fracture types observed

Several types of failure were observed during the experimental characterisation: Cohesive + **F**ibre/**M**a-

trix **D**ebonding (FMD/cohesive), adhesive and mixed rupture types (FMD/cohesive + adhesive or FMD-/cohesive + delamination). Their occurrence among all the tested samples is quantified in Table 3.6 and post-fracture interfaces are presented in Figure 3.28.

Specimen type	FMD/Cohesive	Mixed adhesive + FMD/Cohesive	Mixed FMD/Cohesive + delamination	Adhesive
SLJ	23 (51.11 %)	21 (46.67 %)	1 (2.22 %)	0
DLJ	22 (36.67 %)	22 (36.67 %)	1 (1.67 %)	15 (25 %)

Table 3.6 – Number of interfaces observed for each fracture type

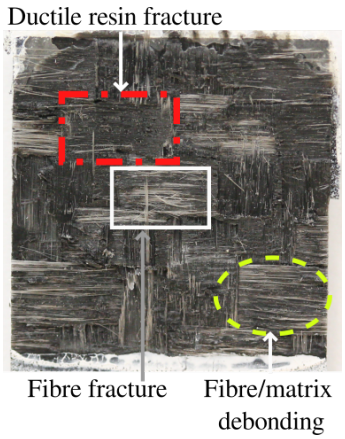

(a) FMD/cohesive fracture

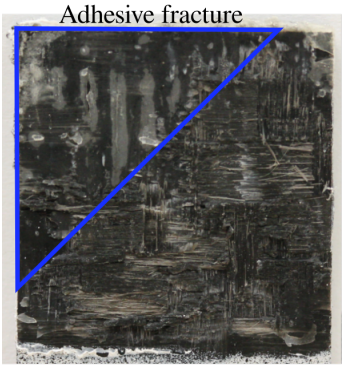

(b) Mixed FMD/cohesive + adhesive fracture

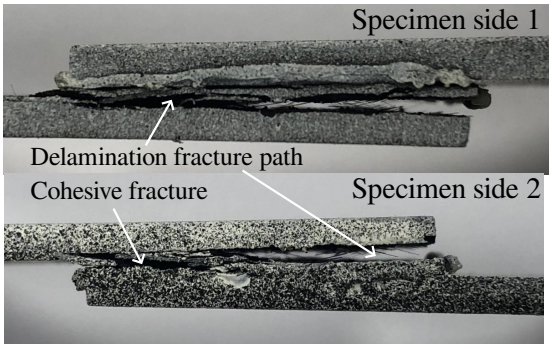

(c) Mixed delamination + FMD/cohesive fracture

(d) Adhesive fracture

Figure 3.28 – Post-fracture interfaces observed for both SLJ and DLJ

In this study, FMD/cohesive failure refers to a failure of the sample between the outermost ply of each substrate along the welded joint. Debonding at the fibre/matrix interface and matrix fracture characterise this type of rupture (Figure 3.28a). Fibre fracture is observed for some parts of the interfaces. Mixed FMD/Cohesive + adhesive failure is the second most common fracture type observed. These interfaces are firmly bonded in some areas (FMD/Cohesive failure) and weakly bonded in others (adhesive failure). Figure 3.28b illustrates this phenomenon, with the upper left corner corresponding to an adhesive break. In this area, residual parts of the EDs are still observable (vertical stripes) and underline the incomplete adhesion process (adhesion of the EDs with a single substrate). The adhesive fracture zones result from unwelded areas observed in Section 3.3.1 and the weak macromolecule interdiffusion at the interface between the substrate and the EDs. As a consequence, the FMD/Cohesive fracture zone

will later be referred to as S_{welded} because it is considered to be the surface carrying the load due to the significant adhesion level. The least observed is a mixed FMD/Cohesive + delamination type rupture (Figure 3.28c). On the one hand, the delamination occurs between the first and second ply of a substrate, and on the other hand, the failure occurs in the welded joint. The underlying reason for such an effect could be the voids in the substrate. Indeed, a high density of voids in the interply area can increase the weakness of substrates compared to the weldline (Figure 3.25). Hence, it promotes delamination from the overlap edges, mostly loading in peeling because of the specimen bending. Finally, adhesive fractures were observed for DLJ specimens, exclusively for the second welded interface (Figure 3.28d), which demonstrates the two steps welding process may cause weak adhesion.

Cohesive/FMD fracture mechanism

Cohesive/FMD fracture is characteristic of a good quality weld, which leads to a high mechanical strength of the interface. Visual and SEM observations of these post-mortem interfaces allow the study of the failure mechanisms involved in the weld. For many joints, both interfaces can be divided into two parts (Figure 3.29). The green boxed area is the zone where the matrix mostly is pulled out at the first ply. It is confirmed by the observations made under the SEM images (Figure 3.29a) where a majority of bare fibres are visible. The area framed in red has many matrix-rich areas with fewer exposed fibres;

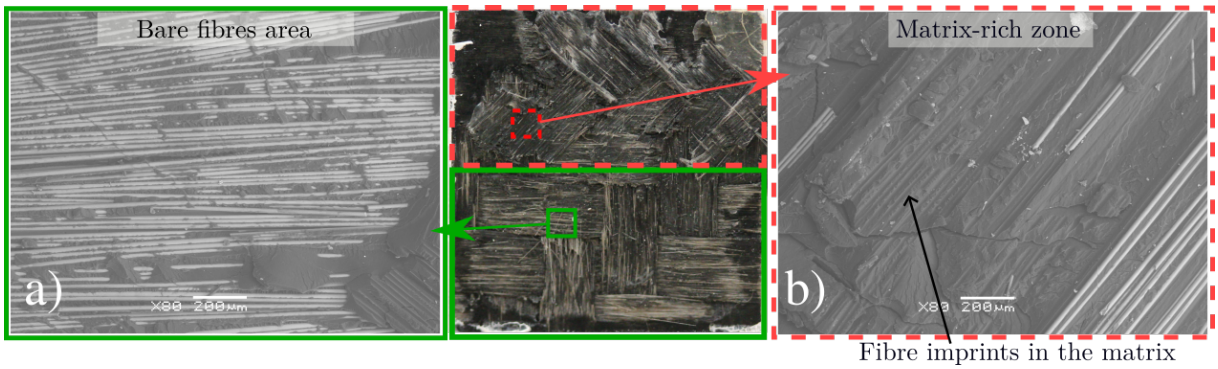

Figure 3.29 – Micrograph of an intralaminar post-fracture interface: a) in the neat fibre tearing area et b) in the ductile fracture zone

this is the matrix of the second substrate of the assembly and EDs. Figure 3.29b) exhibits the interface appearance in a matrix-rich zone. The matrix overlays most of the fibres, and fibres imprints are noticed highlighting the fibre/matrix debonding mechanism for this fracture type. The same observations are made on the second part of the specimen. Thus, we can assume that the interface breaks according to the path indicated in Figure 3.30. At the free edges, opening stress is caused by specimen bending and may be eased by voids in the edges in some cases. It causes the matrix-rich zone at the first ply in contact with the interface to pull away from each side of the substrate until it meets in the middle of the overlap (i.e. complete ruin of the specimen). This failure mechanism has been observed in the literature for CF/PA66 specimens welded without EDs. Here, the energy director is thin in the final assembly, so we can assume that this weld is close to the weld without EDs studied in (Goto et al., 2019).

Finally, these observations show the importance of the adhesion between fibres and matrix in the lap joint specimens' strength, as this interface is the primary fracture path for high welding quality. Therefore, interfacial strength plays a major role in the performance and failure of the weld.

Conclusions on the fractography analysis

Several fracture types are observed on the post-fracture specimens. They can be linked, to a certain extent, to the observations made on the welds' cross-section. On the one hand, the welds with EDs matrix

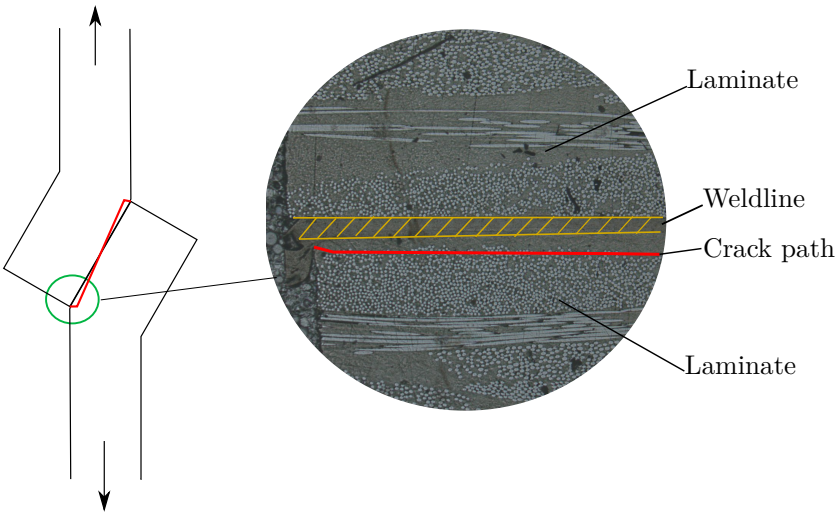

Figure 3.30 – Cohesive/FMD fracture mechanism

blending with substrate matrix (Figure 3.24) are more likely to show a Cohesive/FMD fracture. On the other hand, the specimens with unwelded zones or a distinguishable interface between EDs and substrates are more inclined to present a mixed adhesive + Cohesive/FMD fracture or purely adhesive. In addition, the mixed delamination + Cohesive/FMD fracture may be promoted by the voids content in the interply zone which constitutes a weakness compared to the welded joint. The performance observed for this fracture type is expected to be similar or greater than the one from FMD/cohesive fracture. Finally, the cohesive/FMD fracture characterises a high level of adhesion and no evolution in the fracture mechanism was observed with the evolution in the loading speed tested. This fracture type highlights the importance of the fibre/matrix adhesion and the interfacial strength in the welded joint failure. The mechanical results from tensile tests (FU curves and LSS) are analysed in the next parts considering the fracture types and the weld mesostructure and the performance is compared for several loading speeds.

3.3.3 Mechanical performances of welded joints

Performances of SLJ and DLJ specimens are analysed separately. First, results for each configuration and loading speed are studied to quantify the reproducibility of these tensile tests and understand the welded joint behaviour independently from the loading speed influence. Second, loading speed influence on the welded structures' behaviour is studied by confronting the results obtained for the five crosshead speeds considered.

3.3.3.1 Performances of SLJ specimens

Quasi-static tensile test results - Analysis of FU curves

FU curves extraction was conducted as explained in Section 3.2.4. Quasi-static results show a suitable reproducibility of the FU curve global shape for the three configurations. Furthermore, the behaviour is different depending on the substrate. As expected, the fracture displacement is more significant for the ductile substrates: $[45]_4$.

For SLJ $[0/45]_S/[0/45]_S$, a predominantly elastic behaviour followed by a drop in load and shift in displacement is observed followed by an increase in load until specimen's ruin (Figure 3.31). The load drop corresponds to the fracture initiation at the overlap edges caused by the significant opening mode loading. Figure 3.32 illustrates this fracture initiation with images extracted from three snapshots of the tensile test: the early stage of the tensile test, the last image before the complete fracture of the interface (fracture of the overlap edges framed in red) and complete fracture of the overlap. This fracture initiation also leads to a loss in the specimen stiffness until the complete fracture. Despite the identical shape

of curves, some differences appear in the stiffness and fracture loads. The '21-069-01' specimen is stiffer than both others and a difference in performance is noticed with fracture loads ranging from $3272\,\mathrm{N}$ to $7408\,\mathrm{N}$. The fracture mechanism leads to these substantial variations. As illustrated by Figure 3.31, the highest strength is related to the size of the FMD/cohesive fracture area. In the case of mixed fracture types (FMD/cohesive + adhesive), a higher rupture load is obtained for a larger size of FMD/cohesive zone fracture.

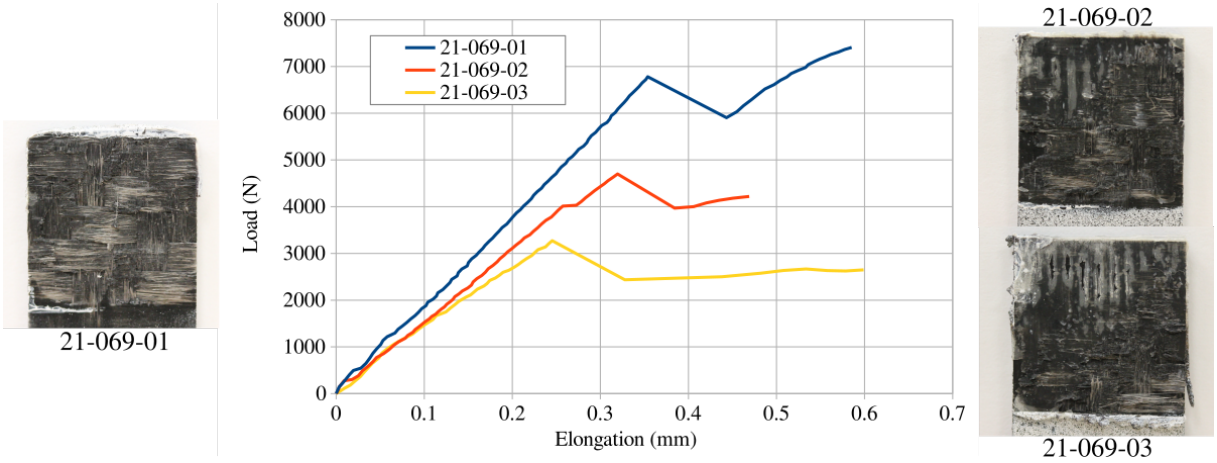

Figure 3.31 – FU curves $[0/45]_S/[0/45]_S$ quasi-static loading

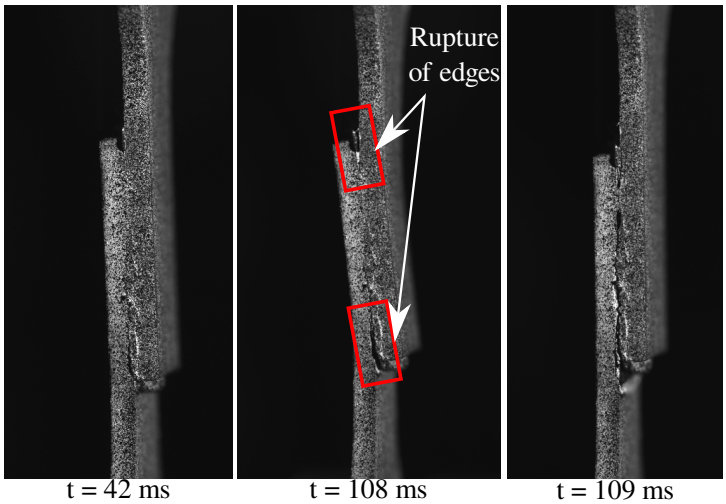

Figure 3.32 – Specimen side during tensile test - SLJ $[0/45]_S/[0/45]_S$ (specimen 21-069-01)

A high initial stiffness reproducibility is observed for the SLJ $[45]_4/[45]_4$ and $[0/45]_S/[45]_4$ (Figure 3.33 and 3.34). The fracture mechanism influences the behaviour of both other configurations in the same manner. For example, the specimen '21-070-03' breaks for a load level of $4426\,\mathrm{N}$ with $67\,\%$ of FMD/cohesive fracture in the overlap, while the specimen '21-077-02' breaks at $6938\,\mathrm{N}$ with a purely FMD/cohesive fracture. Therefore, an almost linear proportionality relation links the FMD/cohesive fracture area and the rupture load for these specimens as observed for SLJ $[0/45]_S/[0/45]_S$ (Figure 3.35). This element highlights the importance of FMD/cohesive fracture in the failure mechanism of welded TP composite. Almost only the zone of FMD/cohesive fracture carries the load in the interface. In addition, it emphasises the limited influence of the adhesive fracture occurring in this experimental characterisation and corresponding to weak adhesion or partially melted zones. The load-carrying capability of the adhesive fracture zone is not significant compared to FMD/cohesive fracture. Therefore, the welding area (S_{welded}) refers to the surface of FMD/cohesive fracture for the rest of the study, as first explained

in Subsection 3.3.2.

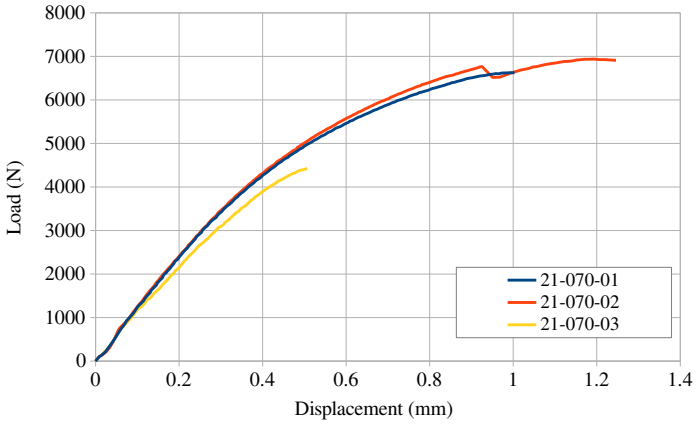

Figure 3.33 – FU curves for SLS $[45]_4/[45]_4$ quasi-static loading

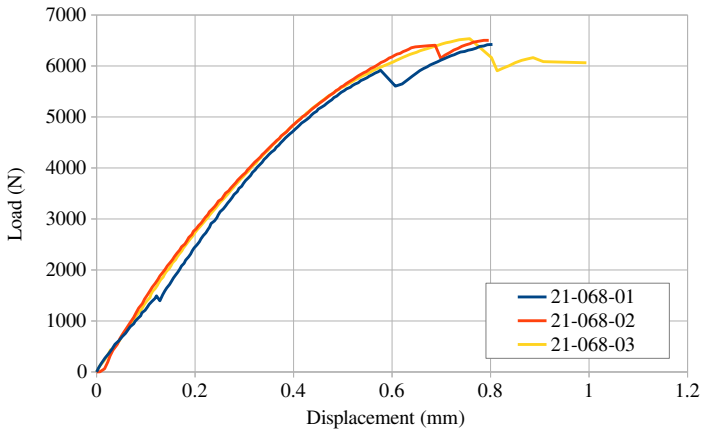

Figure 3.34 – FU curves $[0/45]_S/[45]_4$ quasi-static loading

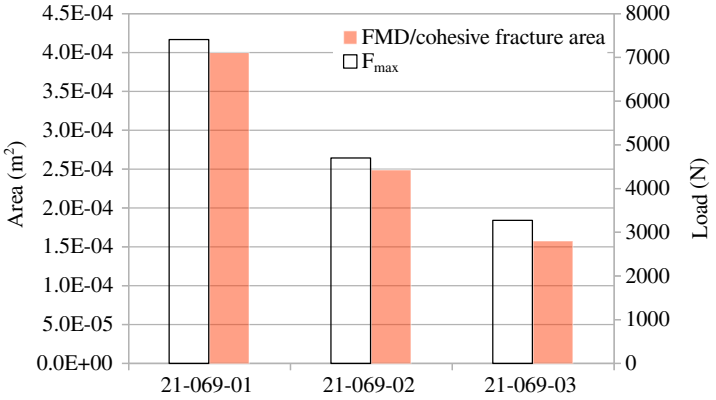

Figure 3.35 – F_{max} and S_{welded} for SLJ $[0/45]_S/[0/45]_S$ - Quasi-static tests

Influence of the loading speed on SLJ specimens' behaviour

Figure 3.36 enables the comparison of configuration performances (**L**ap **S**hear **S**trength - LSS - Equation 3.4) for several loading speeds but also to contrast the performances of the three configurations. All the averaged values are associated with their standard deviation. As can be seen, the average LSS improved with the increase in loading speed: $+11.2\,\%$ of LSS between quasi-static and $7\,\mathrm{m\,s^{-1}}$ tensile tests for the $[45]_4/[45]_4$ joints. A larger increase in LSS occurs for both other configurations tested: $+22.9\,\%$ and $+18.2\,\%$ between quasi-static and $7\,\mathrm{m\,s^{-1}}$ tests, for $[0/45]_S/[45]_4$ and $[0/45]_S/[0/45]_S$, respectively. The standard deviation is relatively small for most of the results; it demonstrates the reproducibility of the weld quality. For SLJ $[0/45]_S/[0/45]_S$ at $7\,\mathrm{m\,s^{-1}}$, only one specimen LSS was considered for Figure 3.36. The motivations for this are set out in the rest of the subsection.

T-tests were conducted to confirm the increasing trend of LSS from a statistical point of view. P-values are presented in Appendix F to evaluate the presumption against the following null hypothesis: "The mean LSS obtained in quasi-static and the mean LSS at V(i) are equal" with V = {$2\,\mathrm{mm\,s^{-1}}$, $200\,\mathrm{mm\,s^{-1}}$, $2\,\mathrm{m\,s^{-1}}$, $7\,\mathrm{m\,s^{-1}}$}. The increase in LSS from quasi-static to $7\,\mathrm{m\,s^{-1}}$ SLS tests on $[0/45]_S/[45]_4$ is confirmed by the T-test, with strong and very strong presumptions for the inequality of LSS average obtained in quasi-static and for each of the other speeds considered. For both other configurations, the results are more scattered with for SLJ $[0/45]_S/[0/45]_S$, strong and very strong presumption for LSS increase at $2\,\mathrm{mm\,s^{-1}}$ and $2\,\mathrm{m\,s^{-1}}$; and for $[45]_4/[45]_4$ a weak and a strong presumption at $200\,\mathrm{mm\,s^{-1}}$ and $7\,\mathrm{m\,s^{-1}}$. These results are in accordance with the averages and the standard deviations (Figure 3.36).

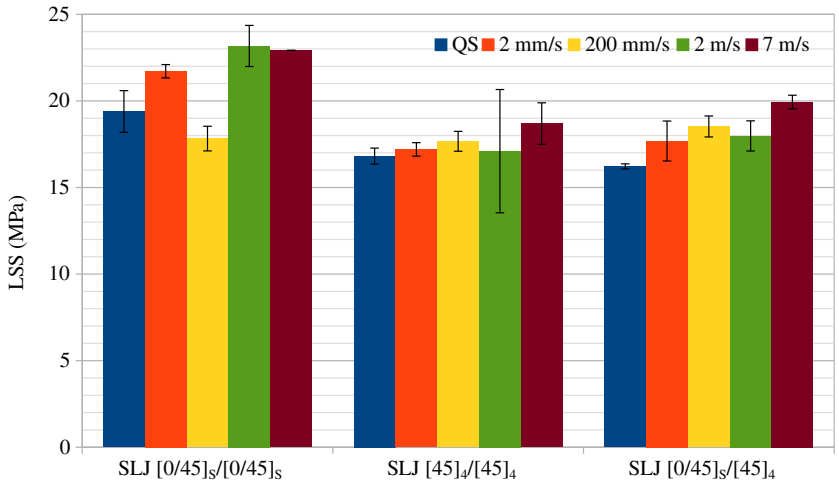

Figure 3.36 – LSS for the three SLJ configurations and the five loading speeds considered

The increase in LSS is caused by the viscous behaviour of PA66 and PA6 matrices. Chapter 2 presented the influence on the laminate shear behaviour with a rise in strength at high strain rates. This strengthening contributes to the increase in LSS with the increase in loading speed. Moreover, the viscous behaviour of polyamide may influence the behaviour of the matrix-rich zone constituting the welded joint. The stiffening and strengthening of these matrices at a high strain rate can affect the global performance of the SLJ specimen for dynamic loadings as observed by several authors for delamination (May, 2015; Machado et al., 2017). The fractography results presented in Subsection 3.3.2 highlighted the principal fracture mechanism involved, which is the fibre/matrix debonding for the five levels of speed investigated; hence, the interfacial strength is an important property affecting the SLJ specimen strength. As a consequence, another phenomenon improving the LSS with the loading speed increase can be the interfacial strength increase with strain rate. The strengthening of the in-plane shear behaviour of a laminate has been shown by several authors to be linked to the rise in interfacial strength (Madhukar & Drzal, 1991; Deng & Ye, 1999). As the GF/PA66 in-plane shear behaviour strengthens with the strain rate rise, it can be assumed that the interfacial strength follows the same evolving trend and thus improves the dynamic LSS of SLJ configurations tested. This phenomenon was observed by Koutras et al. (2018), with an influence of the interfacial strength degradation as the temperature increases on US welded CF/PPS.

As noticed with Figure 3.36 and the T-tests, some results deviate from the increasing tendency observed. On the one hand, for the configuration $[45]_4/[45]_4$, results obtained at $2\,\mathrm{m\,s^{-1}}$ are lower than expected with a high standard deviation. On the other hand, the strength of $[0/45]_S/[0/45]_S$ for a $200\,\mathrm{mm\,s^{-1}}$ loading speed is lower than the quasi-static test results. These deviations are caused by variability in the welding process. In the first case (SLJ $[45]_4/[45]_4$ - $2\,\mathrm{m\,s^{-1}}$), one specimen has a high LSS ($21\,\mathrm{MPa}$) while both other specimens have lower LSS ($14.4\,\mathrm{MPa}$ and $15.8\,\mathrm{MPa}$). The significant standard deviation may results from variation in the welding distance: sinking distance in the specimen during the welding phase. The phenomenon is associated with a more prolonged welding phase for one specimen among

the three tested (Figure 3.37). Both elements can lead to a thin welded surface, with strongly welded edges in that case caused by a more considerable time for interdiffusion of macromolecules. Indeed, the variation in thickness was evaluated to $4.9\,\%$ between these three specimens while it does not overpass $2.9\,\%$ for the other loading speed tested. The interface thickness plays an important role in the joint behaviour because it influences the stresses at the overlap edges. A thinner joint leads to lower shear and peel loads on the edges but also an increase of the average stresses in the overlap zone (Gleich et al., 2001; Villegas & Bersee, 2010; Fernandez Villegas, 2014). In contrast, thick weld and weakly welded overlap edges can ease fracture initiation. The welding quality of the overlap edges affects the joint strength due to the peeling load (Fernandez Villegas & Palardy, 2017).

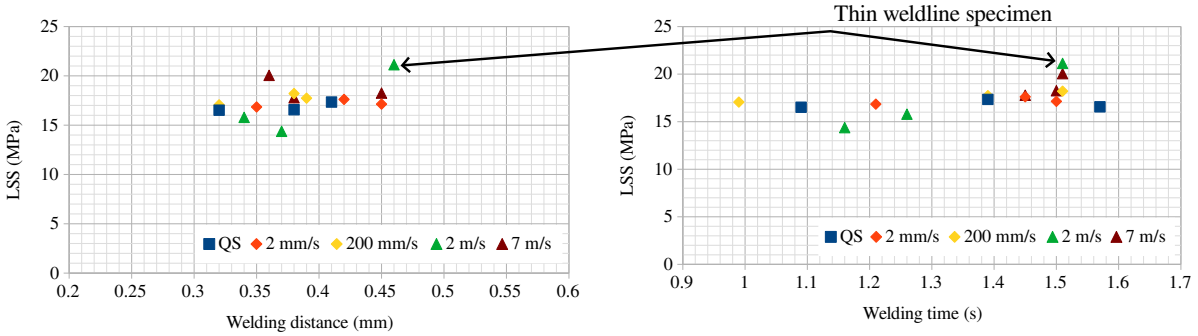

Figure 3.37 – Welding process outputs for SLJ $[45]_4/[45]_4$

The drop in strength for the $[0/45]_S/[0/45]_S$ configuration tested at $200\,\mathrm{mm\,s^{-1}}$ is induced by variability in the welding and total distances. These welding process outputs parameters are higher for this testing condition, which may have reduced the adhesion quality (Figure 3.38). The same observation was made for two specimens of $[0/45]_S/[0/45]_S$ for a $7\,\mathrm{m\,s^{-1}}$ loading speed with high welding distance but low power for two specimens. Hence, only the results of the specimen with consistent welding process outputs are presented in Figure 3.36.

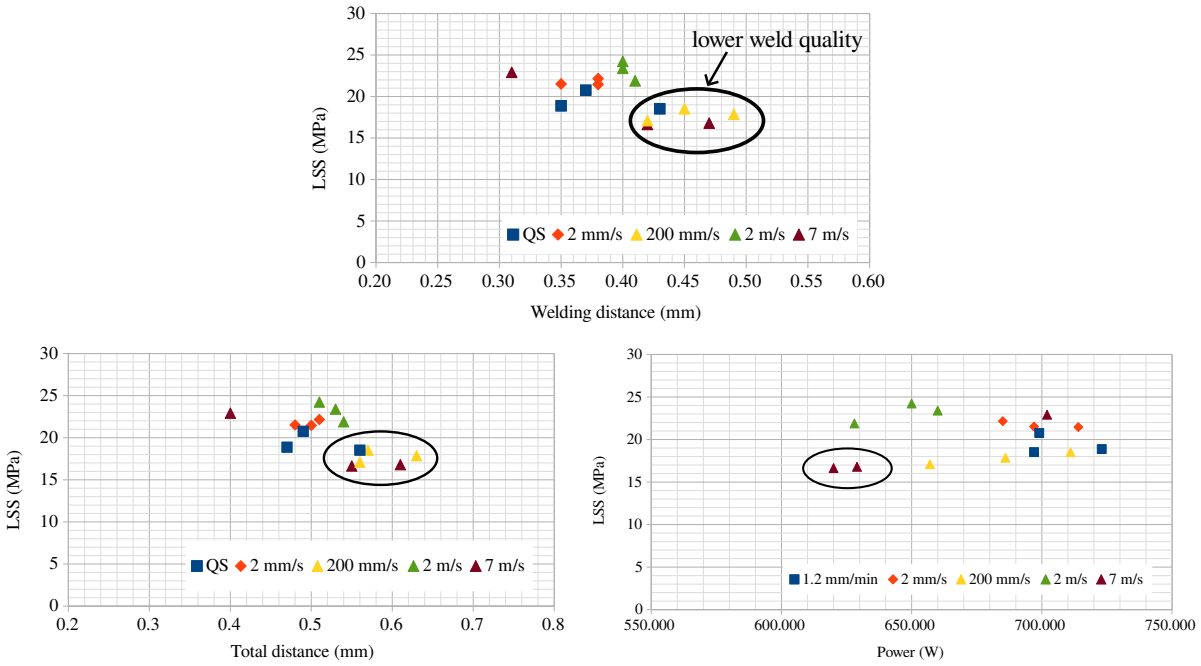

Figure 3.38 – Welding process outputs for SLJ $[0/45]_S/[0/45]_S$

The LSS differs according to substrate orientation. The stiffer the substrate is, the higher is LSS. The

mechanical behaviour of an SLJ specimen is dependent on substrate behaviour. Moreover, the stiffer the substrate is, the greater is the increase of LSS with growing loading speed. This phenomenon is most likely caused by the large ductility of $[45]_4$ substrate and its significant dependency on strain rate compared to $[0/45]_S$ one. The substrate is significantly deforming, which may reduce the importance of the joint's behaviour and its possible sensitivity to the loading speed. On the contrary, $[0/45]_S$ substrate strain level is lower, which may lead to a concentration of strain in the welded interface. Therefore, it may give greater importance to the sensitivity of the interface to the loading rate in the overall behaviour of the SLJ specimen.

Force-displacement results from quasi-static to dynamic loadings

Beyond the mechanical strength, FU curves are studied for several loading speeds. One specimen was selected for each loading speed as a reference for the configuration and the speed considered. This choice is made based on the fracture type. A purely FMD/cohesive fracture is selected whenever possible. In the case of several specimens satisfying this condition, the specimen with the highest rupture load is chosen. For the SLJ $[0/45]_S/[0/45]_S$, no purely FMD/cohesive fracture occurred for $2\,\mathrm{m\,s^{-1}}$ and $7\,\mathrm{m\,s^{-1}}$. Hence, the comparison is made for mixed fracture types ($\sim 63\,\%$ FMD/cohesive fracture and $\sim 37\,\%$ adhesive fracture - Figure 3.39b).

For the SLJ $[0/45]_S/[0/45]_S$, the specimen stiffness does not evolve with the change in loading speed (Figure 3.39). The improvement of the fracture load with the loading speed increase is observed only for three values in this figure: $2 \times 10^{-5}\,\mathrm{m\,s^{-1}}$, $2\,\mathrm{mm\,s^{-1}}$ and $2\,\mathrm{m\,s^{-1}}$. In contrast with the other configurations, the ultimate displacement seems to be negligibly influenced by the loading speed, with a value around $0.45\,\mathrm{mm}$. These observations are consistent with the limited strain rate influence on the behaviour of $0°$ orientation plies and the behaviour of PA66 and PA6 which are strain rate sensitive.

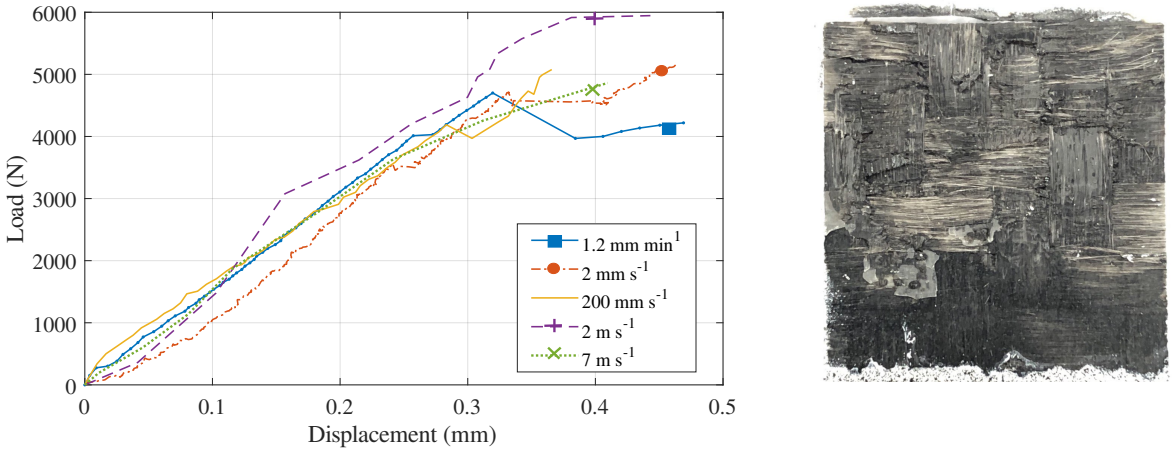

(a) FU curves

(b) Post-mortem interface

Figure 3.39 – FU curves and post-mortem interface - SLJ $[0/45]_S/[0/45]_S$ for several loading speeds

Figure 3.40 exhibits the strengthening of the SLJ $[45]_4/[45]_4$ structures as the loading speed increases. The ultimate displacement decreases while the maximum fracture improves for higher loading speeds. The same observations are made for the SLJ $[0/45]_4/[45]_4$ structure (Figure 3.41). Slight strengthening is also observed.

The change in FU curve shape at $2\,\mathrm{m\,s^{-1}}$ (Figure 3.41) is caused by the orientation of the specimen in the tensile test machine. For this loading speed, the $[45]_4$ was fixed to the loading grip while clamped to the embedded grip for the four other loading speeds. The first hypothesis is that the orientation of

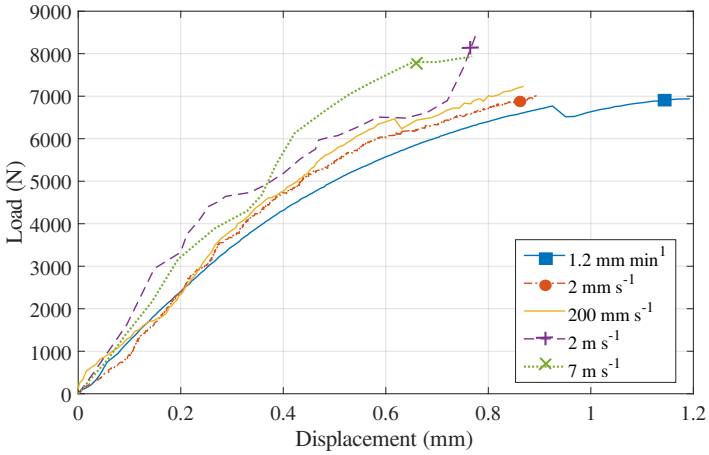

Figure 3.40 – FU curves for SLJ $[45]_4/[45]_4$

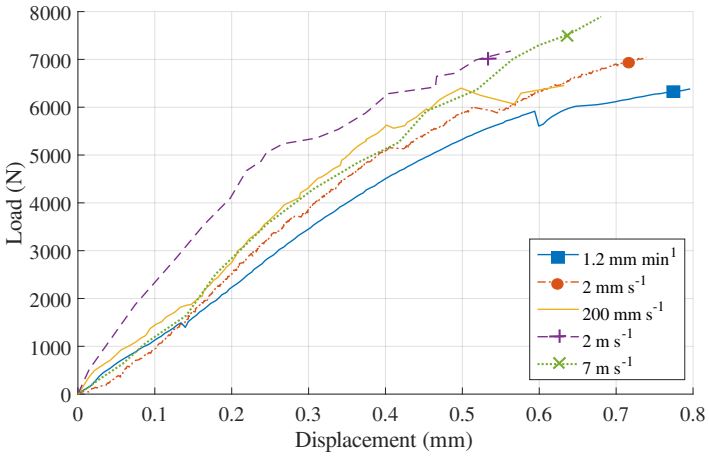

Figure 3.41 – FU curves for SLJ $[0/45]_S/[45]_4$

the specimen may influence the structure behaviour for dynamic loadings. The second one is the out-of-plane movements that may be eased by the $[45]_4$ substrate position. The horizontal movements of the lower tensile arm of the machine are not blocked. Thus, it is possible that for this arrangement or the other considered and due to the specimen dissymmetry, out-of-plane movements occurred and influenced the displacement measurement just as the FU curve.

The augmentation in maximum load is, as explained for the LSS, a combined effect of the substrates, the matrix-rich weld behaviour and the interfacial strength sensitivity to strain rate. These three phenomena are caused by PA66 and PA6 viscous behaviours. The strengthening of the laminate and matrices results in the SLJ specimen strength increase. The GF/PA66 stiffening shear behaviour leads to the stiffening observed for the configurations $[45]_4/[45]_4$ and $[0/45]_S/[45]_4$, with a significant impact of the substrates on the global behaviour of the structure. Nevertheless, the influence of the time dependence of the substrates and the weld on the welded specimens' performance cannot be easily separated from the results presented. It is a consequence of the difficulty of measuring quantities directly in the welded joint. Furthermore, the strain rate sensitivity of the laminate is well-known from the characterisation of the laminate; the weld's strain rate dependence, though, is still unknown and will be determined numerically using an inverse method. This method will be applied in the light of the results presented in this Chapter and the constitutive model developed previously for the GF/PA66 laminates (Mbacké & Rozycki, 2018).

Fracture load and FMD/cohesive fracture zone

Another form of LSS is used in the literature to quantify the weld performance and the welding pro-

cess efficiency (Villegas & Bersee, 2010; Goto et al., 2019). The entire overlap surface is considered for the strength calculation rather than the FMD/cohesive fracture zone and this quantity is named $LSS_{overlap}$ in this work (Equation 3.5). A more significant standard deviation than for the LSS is observed for all the configurations and loading speeds (Figure 3.42). The main reason is the variability of the fracture type (zone of FMD/cohesive and adhesive fracture, adhesion quality) and the variability in the welding process and the material. Nevertheless, an increasing trend of the LSS with the loading speed augmentation is still observed for the SLJ $[45]_4/[45]_4$ and $[0/45]_S/[0/45]_S$, on the range of loading speed considered and for the three smaller ones, respectively.

$$LSS_{overlap} = \frac{F_{max}}{S_{overlap}} \tag{3.5}$$

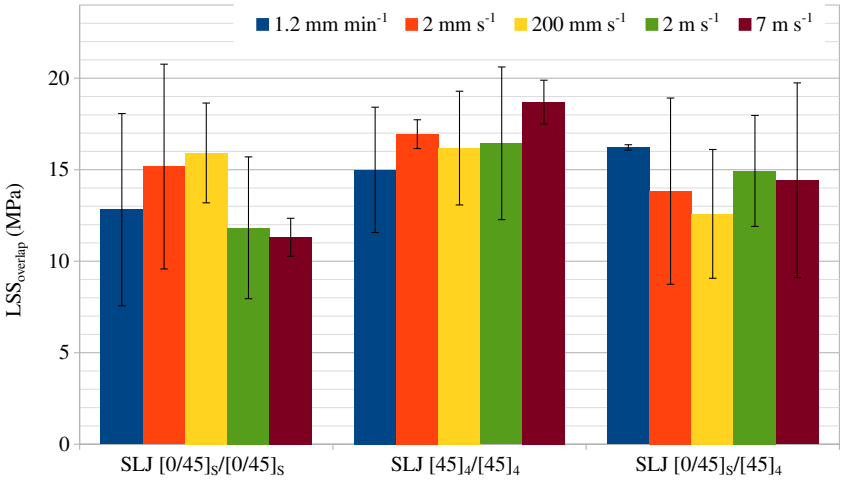

Figure 3.42 – LSS calculated from the overlap zone regardless of the fracture type

The fracture load strongly depends on the area of FMD/cohesive fracture zone. As shown in Figures 3.43, 3.44 and 3.45, these two quantities are linked by a linear relation for most loading speeds tested. Moreover, at a fixed value of FMD/cohesive fracture area, the fracture load is, on average, higher for the highest loading speeds, which is consistent with the observations made on the LSS and the FU curves. Nevertheless, some variability is observed. These observations are straightforward for the configurations $[0/45]_S/[45]_4$ and $[45]_4/[45]_4$ (Figure 3.43 and Figure 3.44). However, they are not totally validated for the third configuration ($[0/45]_S/[0/45]_S$ - Figure 3.45). Results obtained at $200\,\mathrm{mm\,s^{-1}}$ and $7\,\mathrm{m\,s^{-1}}$ are under the performances captured for the other loading speeds. This element is linked to some variability in the welding process, as explained previously for the LSS. To conclude, the processing parameters used for the SLJ $[0/45]_S/[0/45]_S$ might be improved for this configuration. The SLJ $[0/45]_S/[0/45]_S$ and $[0/45]_S/[45]_4$ configurations show a significant variation in S_{welded}. Greater welding energy could have improved the adhesion quality on the whole overlap.

Strain field in the substrates

Strain fields were extracted using DIC on the unwelded zone of the specimen, between the grip and the overlap. The extraction was made using Ufreckles (Réthoré, 2018) on the outermost side of the upper substrate for quasi-static loading. The shear strain field for an SLJ $[45]_4/[45]_4$ tested at $2 \times 10^{-5}\,\mathrm{m\,s^{-1}}$ is presented in Figure 3.46. The snapshot corresponds to the last image before the complete interface fracture. This field shows that the shear strain can overpass $10\,\%$, and it mainly lies between $2\,\%$ and $6\,\%$. The experimental characterisation on GF/PA66 in Chapter 2 identified the strain and stress at the end on the elastic domain. The strain level at yield stress is between $0.72\,\%$ and $0.82\,\%$, depending on the strain rate considered. Therefore, an extended part of the substrate is in its irreversible strain zone for these strain

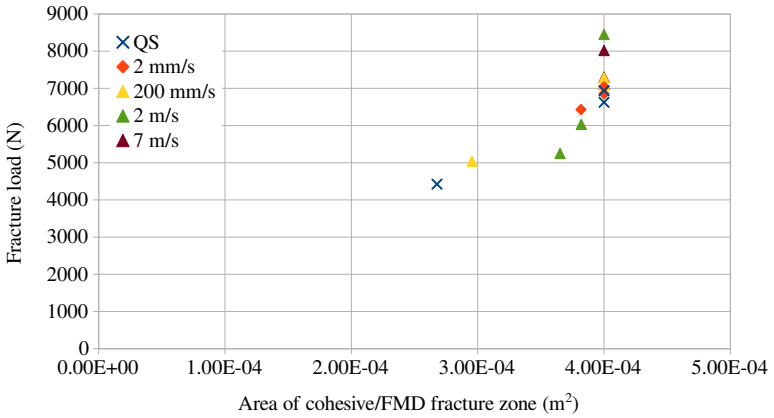

Figure 3.43 – Fracture load versus the area of the FMD/cohesive fracture zone - SLJ $[45]_4/[45]_4$

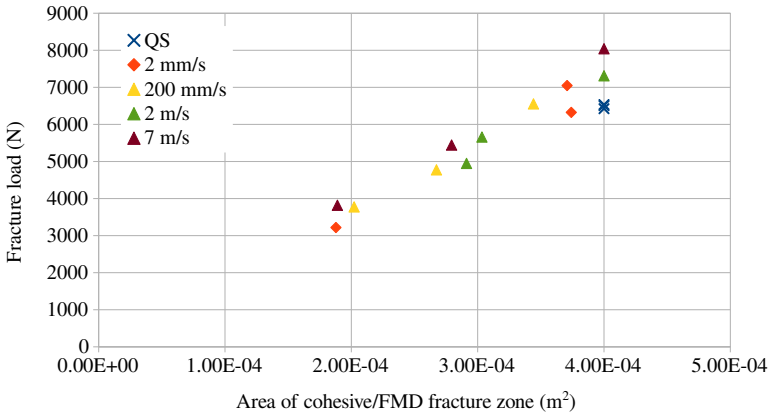

Figure 3.44 – Fracture load versus the area of the FMD/cohesive fracture zone - SLJ $[0/45]_S/[45]_4$

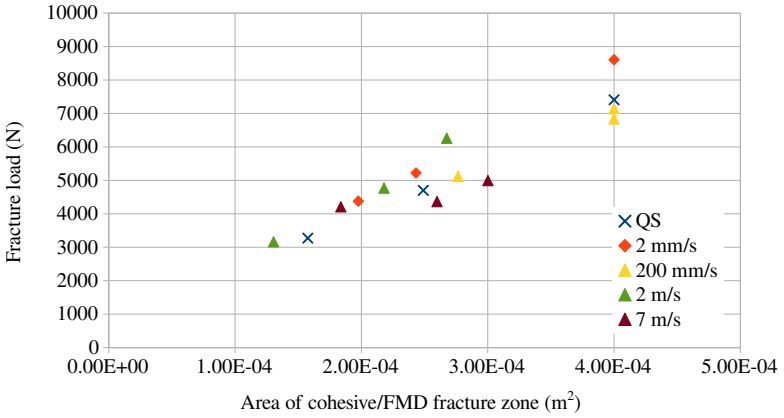

Figure 3.45 – Fracture load versus the area of the cohesive/FMD fracture zone - SLJ $[0/45]_S/[0/45]_S$

levels, as identified from the tensile tests on $[45]_4$. The substrate behaviour plays a significant role in the welded specimen behaviour with irreversible strains around the overlap. For this reason, this part of the behaviour must be considered in the welded specimens modelling to identify a consistent behaviour for the weld from the results of SLS tests. If the laminate constitutive model is considered purely elastic in shear, then the irreversible strains should only be taken into account through the weld's constitutive model, which is not consistent with the experiments.

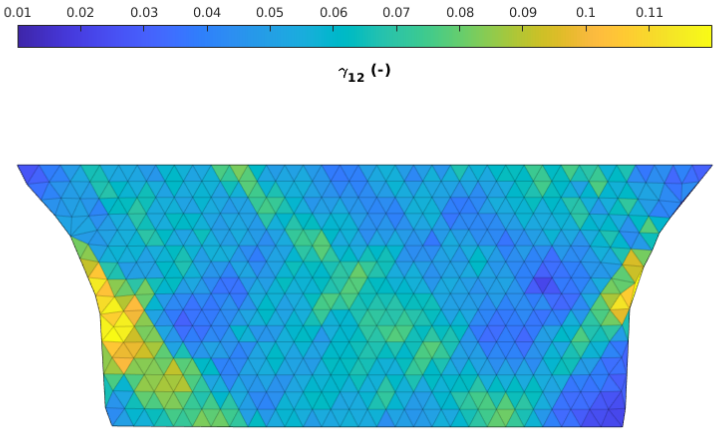

Figure 3.46 – Shear strain field in the substrates - SLJ $[45]_4/[45]_4$ - $2 \times 10^{-5}\,\mathrm{m\,s^{-1}}$

Conclusions on SLJ specimens

The single-lap shear tests showed an improvement in the mechanical strength with the loading speed increase for the three configurations tested. The increase is larger for the stiffer substrates joined. Moreover, the FU curves highlight the stiffening of the configurations $[45]_4/[45]_4$ and $[0/45]_S/[45]_4$ for dynamic loadings. The fracture extension decreases significantly for both configurations with the loading speed increase. The rise in strength and the stiffening are caused by the viscous behaviour of PA66 and PA6 matrices. The matrices behaviour affects the substrate strength and stiffness, as seen in Chapter 2; it may also influence the matrix-rich welded joint and the interfacial strength. All these effects contribute to the loading speed influence observed on SLJ specimens performance with an increase in LSS and a stiffening for the configurations $[45]_4/[45]_4$ and $[0/45]_S/[45]_4$. Moreover, the weld performance is proportional to the extent of the welded zone, i.e. the size of the FMD/cohesive fracture zone.

However, these behaviours and their strain rate sensitivity cannot be neither separated by a simple calculation nor quantified from these experimental results. Therefore, numerical modelling is required to separate these behaviours and quantify the strain rate sensitivity of the welded joints and their influence on the global specimens' behaviour. The identification of the resin-rich weld can be done using an inverse method based on the strong knowledge of the substrate behaviour on a large strain rates range. In addition, the SLJ specimens with one or two $[45]_4$ substrates (SLJ $[45]_4/[X]_4$) undergo irreversible strains in the substrates outside of the overlap. It is tremendous information to model the welded specimens as it requires the description of elastic and inelastic behaviours to obtain consistent results with the experiments.

3.3.3.2 Performances of DLJ specimens

The SLS test aim was to study the weld behaviour for a mixed mode loading: mainly shear load with peeling caused by bending of the specimen during the tensile test. DLS tests intend to investigate a quasi-pure shear mode of loading. Unlike the SLJ specimens, DLJ specimen interfaces' welding was more

challenging because two interfaces are welded in a two steps process. The joining quality varies significantly between both welds because of the lack of material to extend the study on processing parameters for US welding. 83 % of the DLJ specimens had partially welded interfaces (observation of either a mixed adhesive + FMD/cohesive fracture or an adhesive fracture). The weakest interface observed is always the secondly welded. These elements show that the second interface welded needs a substantial development phase to achieve high-quality welds for both interfaces, which could not be carried out in this work.

Force-displacement results

FU curves explicitly show that both welds are not equal. For most specimens, a first drop occurs during the test and corresponds to the first interface fracture. Then, a second drop is noticed for some specimens and coincides with the fracture initiation of the second interface due to peel load, and then total specimen fracture occurs. Figure 3.47 illustrates this phenomenon for quasi-static tensile tests. The FU curves are plotted for both welded interfaces of the specimen when they do not break simultaneously. A load drop and a change in the curve slope identify the first interface fracture. For example, the first fracture happened around 0.2 mm for the specimen '21-071-02' (Figure 3.47a). For the DLJ $[0/45]_S/[0/45]_S/[0/45]_S$, one specimen showed a simultaneous interfaces fracture '21-071-01' (Figure 3.47a). Its fracture load is significantly higher than the other specimens as both welds are correctly welded. A better reproducibility is observed for the stiffness of DLJ $[45]_4/[45]_4/[45]_4$ (Figure 3.47b). The fracture load is in the same range for all the specimens. However, the time at which the first break occurs affects the displacements in the specimens.

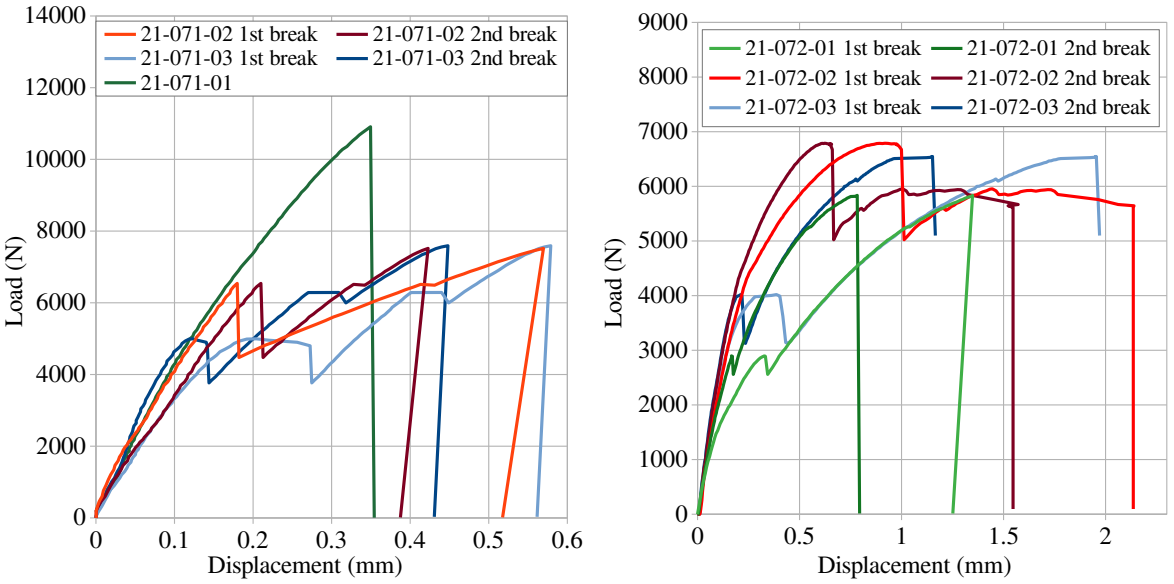

(a) DLJ $[0/45]_S/[0/45]_S/[0/45]_S$ (b) DLJ $[45]_4/[45]_4/[45]_4$

Figure 3.47 – FU curves for DLJ specimens in quasi-static

Concerning the influence of the loading speed on the behaviour of DLJ specimens, one FU curve is plotted for each speed following the same selection as for the SLJ specimens. The results are plotted only from one side of the specimen to make the analysis easier. Both configurations considered showed variation in the specimen's stiffness without an identifiable effect on the loading speed. For the DLJ $[0/45]_S/[0/45]_S/[0/45]_S$ two specimens failed with a simultaneous fracture of interfaces: quasi-static and $2\,\mathrm{m\,s^{-1}}$ tests. The fracture load is about 10.9 kN for the quasi-static and 13.5 kN at $2\,\mathrm{m\,s^{-1}}$. This difference may be caused by loading speed influence but also by the fracture type: purely FMD/cohesive for the

$2\,\mathrm{m\,s^{-1}}$ test and mixed FMD/cohesive + adhesive for both interfaces in quasi-static. Nevertheless, for two other loading speeds, namely $2\,\mathrm{mm\,s^{-1}}$ and $200\,\mathrm{mm\,s^{-1}}$, the first interface fracture occurs at particularly small elongations (about $0.1\,\mathrm{mm}$ and $0.2\,\mathrm{mm}$ respectively).

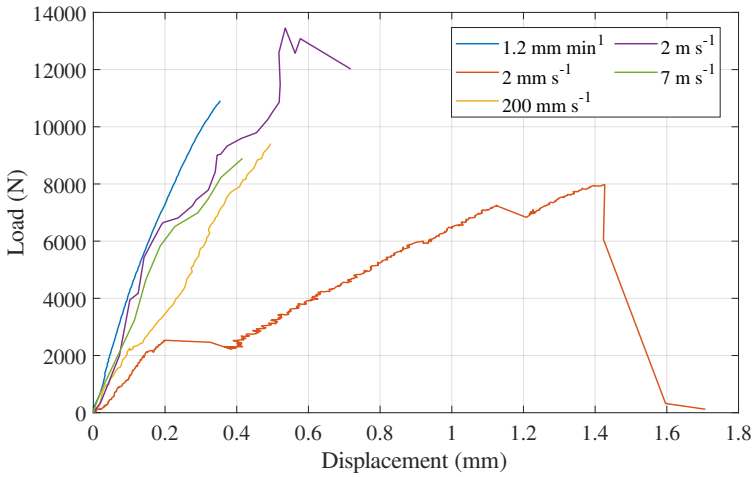

Figure 3.48 – FU curves for DLJ $[0/45]_S/[0/45]_S/[0/45]_S$

For the configuration DLJ $[45]_4/[45]_4/[45]_4$, the first interface fracture happens for larger elongation values for the five loading speeds, which means that the second welded interfaces have a better adhesion quality than what is observed, on average, for DLJ $[0/45]_S/[0/45]_S/[0/45]_S$. Therefore, both DLJ configurations would have needed a more extensive study to set the processing parameters and have a similar welding quality in both interfaces. DLJ $[0/45]_S/[0/45]_S/[0/45]_S$ especially needs improvement only purely adhesive fracture was observed for one interface for $2\,\mathrm{mm\,s^{-1}}$ and $200\,\mathrm{mm\,s^{-1}}$ loading speeds. It is in agreement with the SLJ specimens which obtained strong welds with $[45]_4$ substrates and more variability for SLJ $[0/45]_S/[0/45]_S$.

Figure 3.49 – FU curves for DLJ $[45]_4/[45]_4/[45]_4$

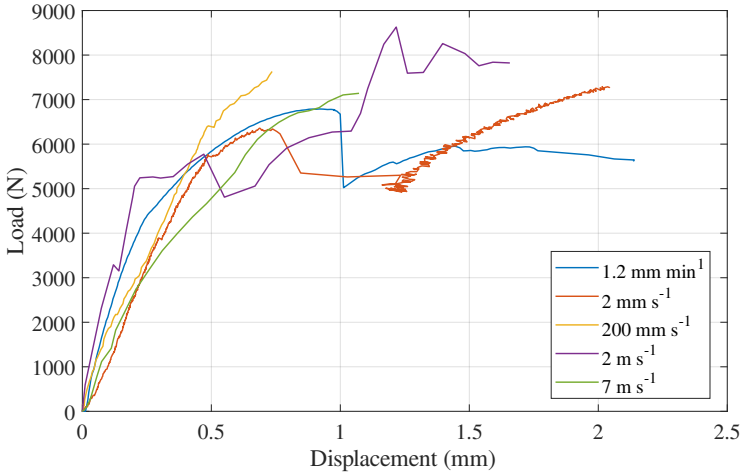

Analysis of the DLJ specimens performance

LSS was calculated as described by Equation 3.4. Data were averaged for every configuration and loading speed. Results plotted in Figures 3.50 and 3.51 show these values associated with their standard deviation and compared to the values obtained for SLJ specimens. The loading speed influence on the performance of DLJ $[0/45]_S/[0/45]_S/[0/45]_S$ cannot be clearly identified from the results in Figure 3.50. An increase in LSS is observed between $2\times10^{-5}\,\mathrm{m\,s^{-1}}$, $2\,\mathrm{mm\,s^{-1}}$ and $7\,\mathrm{m\,s^{-1}}$, however, the standard deviation for the highest loading speed is significant. Furthermore, the performances are lower than the LSS obtained for SLJ specimens for three speeds ($2\times10^{-5}\,\mathrm{m\,s^{-1}}$, $200\,\mathrm{mm\,s^{-1}}$ and $2\,\mathrm{m\,s^{-1}}$); it is caused

by the weaker adhesion level for the second welded interfaces and may also be linked to a lower welding quality for the firstly welded interface. The same observations are made for the DLJ $[45]_4/[45]_4/[45]_4$ (Figure 3.51) but with a limited visible increase of the strength with the loading rate increase. The standard deviation is broadly larger than for the SLJ $[45]_S/[45]_S$ specimens for the $2\,\mathrm{mm\,s^{-1}}$ tests, and the performance of the two largest loading speeds tested is higher than quasi-static and low loading speed values.

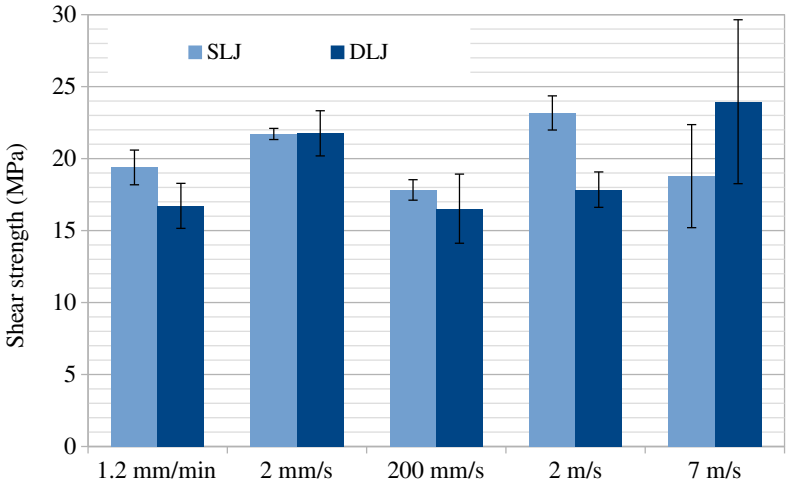

Figure 3.50 – LSS for DLJ $[0/45]_S/[0/45]_S/[0/45]_S$ at several loading speeds

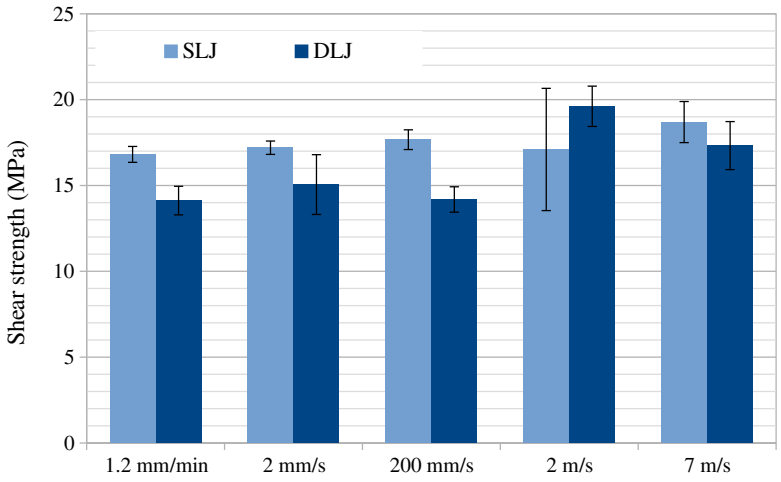

Figure 3.51 – LSS for DLJ $[45]_4/[45]_4/[45]_4$ at several loading speeds

A second quantity was calculated to evaluate the DLJ specimens' performance. This quantity aims to consider the early fracture of one interface for several DLS tests. If a premature interface fracture occurs during the tensile test, then all the load is carried by only one welded interface. Consequently, a new proposition is made here to assess the weld performance in case of early fracture of one interface. The specimen strength is then calculated based on the cohesive fracture area of the last breaking interface, the one handling the maximum load before specimen fracture. LSS_2 described by Equation 3.6 corresponds to this calculation of DLJ performance.

$$LSS_2 = \begin{cases} \dfrac{F_{max}}{S_{welded}} & \text{if no load drop is observed} \\ \dfrac{F_{max}}{S_{int1}} & \text{if a large load drop occurs during the tensile test} \end{cases} \tag{3.6}$$

S_{int1} equals the FMD/cohesive fracture area of the last breaking interface (it corresponds to the first welded interface for all the tested DLJ specimens) and $S_{welded} = S_{int1} + S_{int2}$, with S_{int2} the FMD/cohesive fracture area of the other interface. Results are presented in Figures 3.52 and 3.53.

Concerning the DLJ $[0/45]_S/[0/45]_S/[0/45]_S$, the observations are similar to those previously stated. The loading speed seems to affect the performances of this configuration based on the averaged values of LSS_2. Nevertheless, the standard deviation is too significant to conclude about this influence. For the second configuration, the loading speed influence is similar to the conclusions made for the SLJ $[45]_4/[45]_4$ specimens. For this substrate orientation, the SLJ and DLJ specimen performances are similar. The welded specimen performance slightly improves when the loading speed increases. Moreover, the LSS_2 consideration reduces the standard deviation for both highest loading speeds.

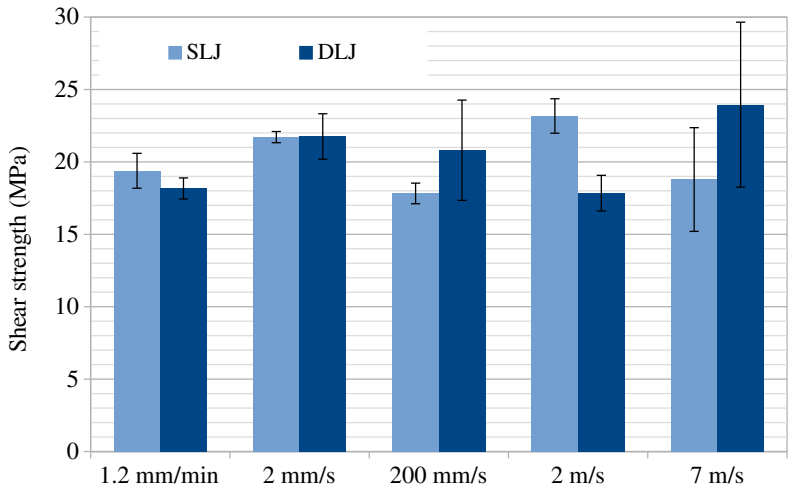

Figure 3.52 – LSS_2 for DLJ $[0/45]_S/[0/45]_S/[0/45]_S$ at several loading speeds

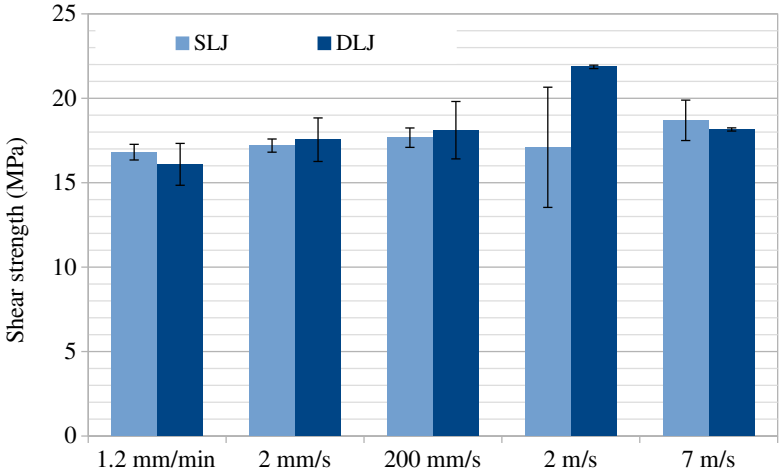

Figure 3.53 – LSS_2 for DLJ $[45]_4/[45]_4/[45]_4$ at several loading speeds

The variation in weld quality is too significant to conclude about the loading speed influence on the DLJ $[0/45]_S/[0/45]_S/[0/45]_S$ performance. Nonetheless, an increase in averaged performance is noticed for both DLJ configurations, with some exceptions as previously observed for the SLJ. More importantly from an industrial point of view, the quasi-static performance of DLJ welded specimens is not diminished for dynamic tensile loadings compared to quasi-static behaviour.

3.4 Conclusions on the experimental characterisation of welded composite joints

This chapter constitutes an experimental characterisation of welded TP composites from quasi-static to dynamic loadings. The aim was to study the behaviour of welded TP composites and the influence of loading speed on their performance. The tests were conducted to investigate the shear behaviour of the welded joint using DLJ specimens for a quasi-pure shear mode, and SLJ specimens for mixed shear/peeling modes.

Tensile test results on welded specimens showed the significance of the fracture mechanism involved. The three main fracture types identified: FMD/cohesive, adhesive and mixed (FMD/cohesive + adhesive), are the consequence of variability in the extent of the welded area. The FMD/cohesive fracture was identified as the fracture mechanism characterising the higher level of adhesion in this work, as in other studies in the literature about US welding of composites (Shi et al., 2013; Zhao et al., 2017; Goto et al., 2019; Fernandez Villegas & Rans, 2021). The relation between fracture load and the area of the FMD/cohesive fracture zone is linear for the SLJ configurations, showing that this is the primary mechanism responsible for the weld strength. The fracture mechanisms observed are not affected by the loading speed. An influence could have been expected because polyamide matrices such as PA66 can show a behaviour transition from ductile to fragile for an increase in strain rate. Dau (2019) reported this behaviour of PA66 at RH0 % and T23 °C without loss of strength but with a stiffening behaviour. Furthermore, the matrix behaviour may have been affected by its crystallinity as the high cooling speed of the joint leads to a majority of amorphous zones. The fibre/matrix debonding is the main factor in the interface fracture mechanism, which is corroborated by other studies (Shi et al., 2013; Koutras et al., 2018; Koutras et al., 2021).

This experimental characterisation conducted for loading speeds from quasi-static to moderate levels is an insight into the dynamic behaviour of welded TP composites. The SLJ specimens' performances improved with the increase in loading speed. This element is consistent with the behaviours of the PA66 matrix in the substrates and the PA6 matrix placed at the interface to enhance the welding process, which stiffens and strengthens at higher strain rates. The laminates and the matrix-rich weld can then inherit this strain rate dependent behaviour. The increasing shear strength of GF/PA66 in-plane behaviour also suggests the interfacial strength rise in the laminate and the welded joint. This phenomenon may significantly enhance the SLJ specimen's performance with the loading speed increase. In addition, a stiffening of the specimens SLJ $[45]_4/[45]_4$ and $[0/45]_S/[45]_4$ is noticed on the loading speed range considered and is strongly supposed to be the consequence of the strain rate dependence of GF/PA66 in-plane shear behaviour. Indeed, the welded specimen' performance is substantially dependent on the substrate behaviour. The experimental characterisation also highlighted the large substrate deformations going beyond the elastic domain for $[45]_4$ substrates. From an industrial point of view, this element is interesting for the repair of structures using US welding. The substrate irreversible strains condition the size of the area that must be removed from the structure and the size of the repairing patch. The influence of the substrate and welded joint on the SLJ specimen behaviour cannot be quantified readily from LSS and FU curves. GF/PA66 behaviour is well known and suitable modelled for quasi-static and dynamic loadings; hence, the weld's behaviour can be identified using an inverse method for the several loading speeds considered. This method will allow quantifying the strain rate sensitivity of the weld.

The behaviour of DLJ specimens was significantly affected by the variability in the welding process and the unavailability of double-thickness substrates for the intern arm. Moreover, the study on the processing parameters could not be as extended as needed. In spite of these observations, performances

of the DLJ $[45]_4/[45]_4/[45]_4$ are similar to the SLJ $[45]_4/[45]_4$, a slight increase is observed for higher loading speeds. For the second configuration, DLJ $[0/45]_S/[0/45]_S/[0/45]_S$, results are more contrasted despite an increase for the first loading speed tested due to the significant standard deviation.

The mechanical results obtained in this chapter can be used as the basis of the welded specimen numerical modelling. The model describing the welded interface will be established by comparison of numerical and experimental results minimising the deviation. Initially, the aim of the two geometry chosen for the weld characterisation was to fix the shear behaviour of the joint from the DLS results and then determine the opening behaviour from the mixed-mode loading of SLS tests. Nevertheless, the results obtained for DLJ specimens are too variable to follow this process. Therefore, the joint behaviour will be identified from the SLS results. Then, the parameters identified will be applied to numerical DLS tests. These elements are presented in the next chapter.

Chapter 4

Modelling the behaviour of welded composites

Abstract: *Cohesive elements are used to model the welded interface. Traction-separation laws were defined for the three SLJ configurations for quasi-static and dynamic loadings based on the experimental characterisation conducted in Chapter 3. A strain rate dependent formulation was implemented in a VUMAT subroutine, using viscous functions to describe the parameters' evolution with strain rate. First, the TSL parameters are identified by considering zero viscosity functions. The results show that SLJ* $[45]_4/[45]_4$ *and* $[45]_4/[0/45]_S$ *can be described using the parameters identified for the quasi-static tests. Therefore, these configurations do not require strain rate dependence in the traction-separation law to describe the weld's behaviour. The specimens' strengthening and stiffening are caused mainly by the laminate strain rate dependence in shear. However, the SLJ* $[0/45]_S/[0/45]_S$ *needs to consider an evolution of the traction-separation law parameters with the increase in loading speed. The viscous functions are defined based on the parameters identified for several loading speeds, then the strain rate dependent law is validated to describe SLJ* $[0/45]_S/[0/45]_S$ *dynamic behaviour. Several quantities are evaluated numerically to reinforce the conclusions obtained on the macroscopical specimens' behaviour. These elements also support explaining the need to consider a strain rate dependent traction-separation law for only one of the SLJ configurations tested.*

Contents

Introduction to the numerical modelling of welded joint

This final chapter presents the welded joint modelling and the definition of its parameters using an inverse method. A model is defined for the welded joint; then, the model's parameters are identified numerically knowing the substrates' behaviour (modelled by a strain rate dependent constitutive model, Chapter 2) and the experimental behaviour of SLJ specimens (Chapter 3). The numerical specimen's definition is presented in the first section with the models associated with the specimen's parts (substrates and weld) and the boundary conditions applied. Then, the inverse method process is presented. The welded joint is represented by cohesive elements using a bilinear **T**raction-**S**eparation **L**aw (TSL). The second section introduces the strain rate dependent TSL formulation defined and implemented in a VUMAT user subroutine. This definition uses viscous functions to describe the TSL parameters' evolution with the strain rate. The results of the parameters' identification are developed in the third section for the three SLJ configurations. The TSL parameters obtained for quasi-static loadings are applied to dynamic loadings; in case of a large gap with experiments, the parameters are re-identified for the loading speed considered. The results for several loading speed tests allow, if needed, the definition of viscous functions for the strain rate dependent TSL law. The need to add viscous functions for the TSL parameters allows concluding the significance of the weld's strain rate dependence on the global specimen's behaviour. On the contrary, if viscous functions are not required to describe an evolution of the parameters with strain rate, then the weld's strain rate dependence is negligible for the configuration in question. Finally, simulations were performed for DLS tests using the TLS parameters identified from SLS tests. These results permit drawing recommendations for the welded specimens testing.

4.1 Definition of the numerical specimen and protocol for the identification of the weld's constitutive model parameters

The specimens used to characterise the welded structures make experimental measurements in the welded joints difficult. Hence, it is impossible to directly identify the material parameters to describe the weld's behaviour. Nevertheless, proper knowledge of the substrate behaviour and its modelling allow the identification of a welded joint model's parameters from SLS tests using an inverse method. This requires reliable modelling of the substrate behaviour for the strain rates considered and boundary conditions. In this section, the specimen modelling is described with the geometry of the numerical specimen, the boundary conditions, and the post-processing of simulations. Finally, the protocol used for the weld's model identification is introduced by presenting the inverse method.

4.1.1 Definition of the numerical specimen

The numerical specimen is created with Abaqus and the simulations are performed with the dynamic/Explicit solver (*ABAQUS / Dynamic User's Manual*, 2019). Only the central part of the specimen is modelled; the parts tightened by the grips are not represented (Figure 4.1). Shell elements are used for the substrates, following the elementary ply constitutive model formulated in plane stress. Therefore, the substrate behaviour is extensively described from QS to dynamic loadings considering elastic and irreversible behaviours with damages. S4R elements are used (4-node general-purpose shell, reduced integration with hourglass control, finite membrane strains). Concerning the welded joint, a layer of cohesive elements models the welded joint (COH3D8 elements: 8-node three-dimensional cohesive element). The elements thickness is set to $23.9\,\mu m$ as measured on the specimens (Subsection 3.3.1). Both faces of the cohesive elements layer are linked to the substrate by a '*tie*' constraint to impose the displacements of the substrates (translations and rotations) on the weld's faces. This assumption is based

on the strong adhesion between the substrates and the EDs' matrix. The interface between the EDs and substrate matrix disappears in favour of interphase.

Three other elements must be defined in the model:

— Substrates behaviour - Constitutive model developed and presented in Chapter 2.

— Boundary conditions - Displacements of the specimens edges.

— Cohesive elements - TSL to be determined.

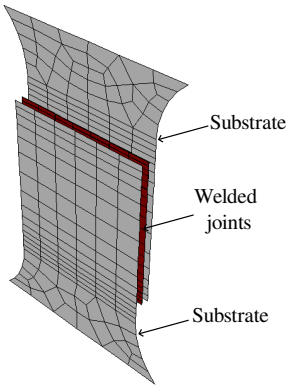

Figure 4.1 – Numerical SLJ specimen

A brief reminder on the GF/PA66 constitutive model used

The constitutive model presented in Chapter 2 defines the substrates' behaviour using a VUMAT material user subroutine. This implementation allows access to several quantities that could not be measured during the characterisation of welded specimens. The original model considered strain rate dependence of longitudinal, transverse and shear behaviour with damage for these three directions, as well as strain hardening of shear behaviour. The model used in this work was simplified by disabling the strain rate dependence of the in-axis direction because the influence is negligible compared to shear. The longitudinal and transverse damages are maintained, despite the quasi-elastic fragile in-axis behaviour, to describe accurately the loss of stiffness observed. Elastic and irreversible behaviours are defined to be strain rate dependent in shear up to $250\,\mathrm{s}^{-1}$. Beyond that limit, the mechanical properties are limited to the value at $250\,\mathrm{s}^{-1}$ (maximum strain rate tested). This model suitably reproduces the increase in shear modulus, yield stress and strength. The parameters used for the GF/PA66 elementary ply behaviour VUMAT are reported in Table 4.1. The laminate stacking sequence is defined in Abaqus by the thickness and orientation of each ply.

E_{11}=E_{22} (Pa)	ν_{12} (-)	G_{12} (Pa)	σ^0 (Pa)	β (Pa)	m
2.25×10^{10}	0.0199	3.49×10^9	2.49×10^7	5.40×10^9	0.857
α_{12}^1 (-)	$\sqrt{Y_{11/22}^R}$ ($\sqrt{\mathrm{Pa}}$)	$\sqrt{Y_{12}^R}$ ($\sqrt{\mathrm{Pa}}$)	α_{12}^2 ($\mathrm{Pa}^{-0.5}$)	d_{12}^M (-)	$d_{11/22}^{max}$ (-)
0.3089	2.69×10^3	3.18×10^3	2.04×10^{-5}	0.641	0.177
d_{12}^{max} (-)	$\dot{\gamma}_{12}^{ref}$ (s^{-1})	$\dot{\gamma}_{12}^{max}$ (s^{-1})	$\dot{\gamma}_{12}^{exp}$ (-)	$F_{G_{12}^0}^{A3}$ (-)	$F_{G_{12}^0}^{A2}$ (-)
0.702	2.72×10^{-4}	2.55×10^2	1.5	3.71×10^{-6}	-1.04×10^{-4}
$F_{G_{12}^0}^{A1}$ (-)	$F_{\sigma_{12}^0}^{A3}$ (-)	$F_{\sigma_{12}^0}^{A2}$ (-)	$F_{\sigma_{12}^0}^{A1}$ (-)	$F_{d_{12}^M}^{A3}$ (-)	$F_{d_{12}^M}^{A2}$ (-)
2.24×10^{-3}	6.62×10^{-6}	-4.54×10^{-4}	1.52×10^{-2}	-2.30×10^{-6}	1.94×10^{-4}
$F_{d_{12}^M}^{A1}$ (-)	$F_{\alpha_{12}^1}^{A3}$ (-)	$F_{\alpha_{12}^1}^{A2}$ (-)	$F_{\alpha_{12}^1}^{A1}$ (-)	$\sqrt{Y_{11/12}^0}$ ($\sqrt{\mathrm{Pa}}$)	$\alpha_{1/2}$ ($\sqrt{\mathrm{Pa}}$)
-5.18×10^{-3}	1.55×10^{-6}	-3.69×10^{-5}	-1.96×10^{-5}	3.66×10^2	7.6×10^{-5}
$\sqrt{Y_{12}^0}$ ($\sqrt{\mathrm{Pa}}$)					
298					

Table 4.1 – VUMAT parameters for GF/PA66

Boundary conditions

The boundary conditions are extracted from the experimental characterisation of welded specimens. This choice avoids the modelling of the stud and flange grip system, which is complex. As seen in Subsection 3.2.3 about the testing rig, the dynamic tests cannot be conducted at a highly precisely fixed and constant loading speed due to the loading strategy. Consequently, the crosshead speed may slightly vary during the tensile test. The boundary conditions applied here permit to load the specimen at the same loading speed as in the experiment, except for the QS loading, which will be presented later. Therefore, the use of boundary conditions extracted from the experiments allows it to be as close as possible to the experimental conditions. Extraction is done on specimens selected as reference for each configuration and loading speed tested. The longitudinal and transversal displacements of nodes on the upper and lower parts of the specimen are measured using DIC (Figure 4.2) (Ufreckles Réthoré, 2018) and converted into displacement amplitudes over time to be incorporated into Abaqus input file. Concerning the QS loading ($1.2\,\mathrm{mm\,min^{-1}}$), the time is divided by 10^5 to have a shorter computing time because the time increment is fixed by the Courant-Friedrich-Levy condition (time increment based on the smallest length and the worst mechanical properties of the finite elements Equation 4.1). Finally, the translations of both edges along the z-axis (out-of-plane translations) are fixed to zero because they are close to the grips.

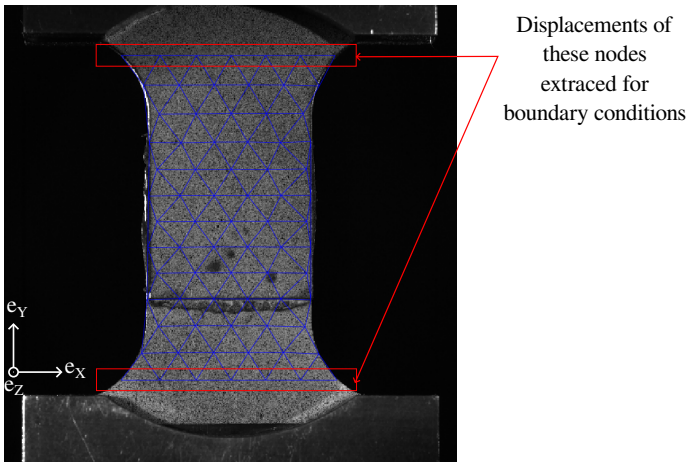

Figure 4.2 – Extraction of nodes longitudinal and transverse displacements for boundary conditions using (Réthoré, 2018)

$$dt \approx L\sqrt{\frac{\rho}{E}} \tag{4.1}$$

With L, the smallest element dimension in the part considered, ρ the material density and E the elastic modulus. The calculation is done for each part of the model, and the smallest one defines the time increment for the simulation. For these simulations, the cohesive elements rule the smallest critical time step due to their small thickness. At the beginning of the simulation, the time step is equal to $1.293 \times 10^{-8}\,\mathrm{s}$, and then it is slowly increasing due to the initiation of damage in the cohesive elements.

Traction-separation law for cohesive elements

TSLs are classically used to define the behaviour of cohesive elements, even though the constitutive model could also be defined using a continuum approach. These laws are simple; bilinear or trilinear evolutions are extensively used to describe elastic fragile or elastoplastic behaviours, for example. The TSL used in this work is based on a built-in law of Abaqus, considering mixed-mode. The damage initiation is controlled by a quadratic criterion on tractions (**QUAD**dratic nominal **S**tress criterion - 'QUADS') as defined in Camanho et al. (2003) for the delamination of composite (AS4/PEEK). The damage evolution is defined by a linear decrease in traction versus separation once the damage initiates. The energy

criterion BK is used to describe the energy in mixed-mode (Gong & Benzeggagh, 1995; Benzeggagh & Kenane, 1996). The law is set by defining the stiffnesses, the stresses at damage initiation, the fracture toughness for pure peel and shear modes (both shear mode laws are supposed to be equal) with the power function coefficient for mixed mode evolution. The element thickness is considered through the cohesive elements' geometry. The TSL definition will be detailed in Section 4.2, with its implementation in a VUMAT material subroutine.

Post-processing of simulations: plot of the FU curve and LSS calculation

Simulations are post-processed as the experiments. The reaction force is extracted on each node where displacement is applied, and values are summed for both specimen edges. The reaction force on the top edge is used to obtain the FU curves because the load is measured experimentally on the top grip. Node sets are created on the substrates to extract the displacements of the gauge's edges to measure the numerical elongation. The displacement is averaged for both gauge's edges as in the post-processing of experiments. The LSS calculation is made considering the size of the whole overlap zone as welded, i.e. $20\,\mathrm{mm} \times 20\,\mathrm{mm}$, and the maximum load reached, that is identified from the reaction load signal over time. Contrary to the experiments, numerical load and displacement data are obtained for the same time frequency; thus, no data interpolation is needed to plot the FU curve.

4.1.2 Strategy used for identification of the weld's constitutive model parameters

The parameters of the TSL describing the weld's behaviour were identified for the three SLJ configurations considered: $[0/45]_S/[0/45]_S$, $[45]_4/[45]_4$ and $[45]_4/[0/45]_S$. The three SLJ configurations investigate the weld's behaviour joining several ply orientations: $0°/0°$, $45°/45°$ and $45°/0°$, respectively. The QS test is studied in the first place with the identification of QS parameters for the TSL. If using the QS parameters for higher loading speeds correctly describes the experimental behaviour of the SLJ specimens, then it can be concluded that a strain rate independent constitutive model can be considered for the weld's behaviour in the present study. Otherwise, the TSL parameters are identified for each loading speed. Then, viscous functions can be defined from these identifications to describe the evolution of the TSL's parameters.

Parameters to be determined

Three parameters must be determined per mode to fix the TSL in pure modes (stiffnesses K, damage initiation stress σ^0 and fracture toughness G_C), and one parameter must be defined for the mixed-mode behaviour (power function coefficient for the mixed-mode fracture toughness η). The cohesive element stiffnesses can be estimated from literature data on PA6 (the ED matrix at the interface), by assuming equivalence between these two stiffnesses. Pivdiablyk (2019) measured the elastic modulus and Poisson's ratio of PA6 matrix for the QS load. Shear modulus can be calculated from these quantities (Equation 4.2), as the matrix behaviour is isotropic. The properties are grouped in Table 4.2. The stiffnesses value is not influencing the behaviour of the SLJ specimen significantly during the tensile test compared to the damage initiation stresses and fracture toughnesses (Figure 4.3); only a change in the order of magnitude may change the initial stiffness of the specimen which is not the case for change in crystallinity ratio. A relative difference of $2\,\%$ in the maximum load is observed when multiplying $K_{II}\,(= G/e)$ (the cohesive element shear stiffness) by three, and $4\,\%$ when multiplying $K_I\,(= E/e)$ by three. Consequently, the choice was made not to optimise the stiffnesses and use the values of Table 4.2.

$$G = \frac{E}{2\,(1+\nu)} \tag{4.2}$$

$E = K_I.e$ (GPa)	ν (-)	$G = K_{II}.e$ (GPa)	ρ (kg m^{-3})
3.934	0.463	1.344	1140

Table 4.2 – PA6 elastic properties (Pivdiablyk, 2019) and density

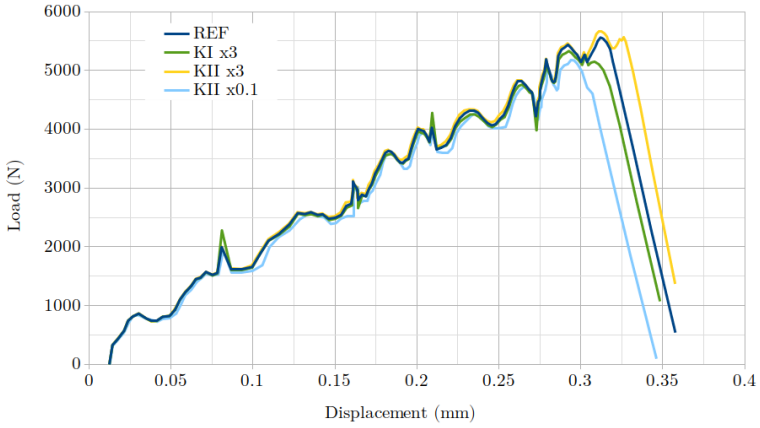

Figure 4.3 – Influence of the TSL stiffnesses on the global behaviour of a SLJ $[0/45]_S/[0/45]_S$

Concerning both other parameters (damage initiation stresses and fracture toughnesses), their value could also be based on literature results. Contrarily to the stiffness, these two parameters have a significant influence on the global response of the SLJ specimen. Damage initiation stress could be taken as the yield stress of the matrix; this quantity was estimated to 32.5 MPa (Pivdiablyk, 2019). However, this property may significantly differ according to the matrix crystallinity, which is unknown in this study (Felder et al., 2020). Therefore, this data from the literature constitutes an order of magnitude of the damage initiation stress but not a suitable value for the present problem. Concerning the fracture toughnesses, few values are available in the literature for GF/PA66. Todo et al. (1999) measured a mode II fracture toughness (G_{IIc}) of 4000 J m^{-1} $\pm$ 500 J m^{-1} for GF/PA66. No values were found for the mode I fracture toughness of this composite. Finally, the values of the damage initiation stresses and fracture toughnesses have to be identified from the tests conducted in this work. Data from the literature constitute starting points for the optimisation process to find TLS parameters adapted for the problem investigated in this work.

Inverse method

In this research work, cohesive elements are selected to describe the weld's behaviour because the specimens' fracture path is known in advance to occur in the welded joint. However, the TSL describing the weld's behaviour is unknown. The combined behaviour of substrates and the welded joint identified in Chapter 3 can only be separated numerically using FE simulations. Cohesive law parameters are determined by an inverse method using the results of SLS tests (Figure 4.4). The inverse method uses the definition of a numerical specimen in the FE software Abaqus (*ABAQUS / Dynamic User's Manual*, 2019), and it requires the control of the known behaviours and boundary conditions to let only one behaviour be unknown in the model. The experimental test is numerically simulated, and the same post-processing used experimentally is applied.

The identification was performed using Matlab's particle swarm optimisation function and minimising the error between the numerical and experimental FU curves in the least squares sense. Minimum and maximum boundaries are defined for the quantities to be identified based on initial simulations' results and literature references. The limits of this method are the choice of the error function and the number of parameters to be optimised in the problem. The optimisation was performed without restricting conditions between the parameters, and two parameters for each mode must be identified from

only one type of test. Therefore, final simulations were carried out to finalise the parameter identification manually by reducing the error between the numerical and experimental energy value of the FU curve (area under the curve).

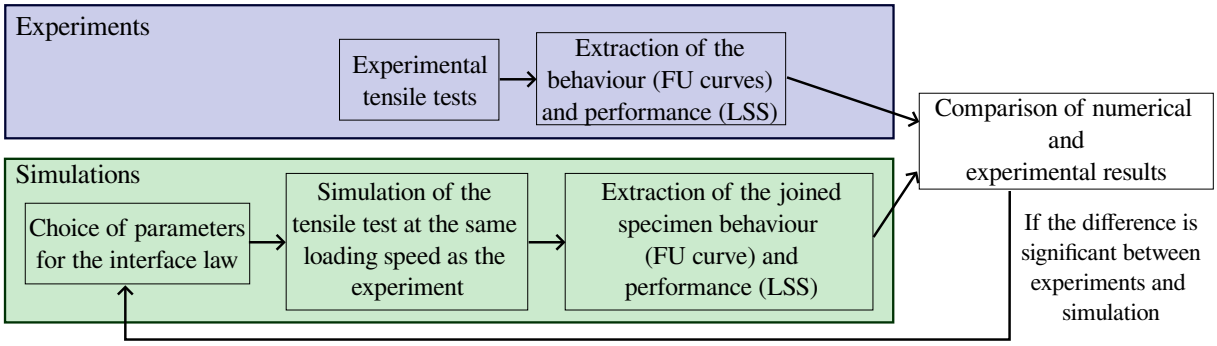

Figure 4.4 – Process of the interface model parameters using inverse method

Conclusion on the definition of the specimen and the inverse method protocol

The several elements used for the simulation of the numerical SLS test and its post-processing were presented in this section. The substrate modelling and the boundary conditions are known and controlled from experiments, allowing the application of an inverse method to identify the fracture toughnesses and damage initiation stresses for the weld's model. The following section presents the model chosen to describe the welded joint behaviour with cohesive elements.

4.2 Implementation and validation of a strain rate dependent traction-separation law

This section presents the bilinear law used for the welded joint constitutive model. This choice was made at first because it successfully described the behaviour of interfaces close to a composite welded joint: the delamination behaviour of TP composites such as AS4/PEEK (Camanho et al., 2003; Pinho et al., 2006) and bonded joints of composite materials (Marzi et al., 2009; Campilho et al., 2013). The behaviour is linear elastic until the damage initiation stress, named σ^0. Once this stress is reached, damage initiates in the element and propagates according to the TSL shape and the value of fracture toughness G_c. The quasi-static TSL formulation, implemented in a VUMAT subroutine, is presented in the first part based on the Abaqus built-in formulation considering quadratic nominal stress criterion for damage initiation, linear softening and BK criterion for mixed-mode fracture toughness. The second part presents the model extension to include strain rate dependence of the law's parameters and the VUMAT implementation.

4.2.1 Traction-separation law: pure and mixed-mode definition

The equations linking the traction evolution to the separation are presented first for pure mode loading. Then, the law definition is extended to mixed-mode loadings.

Pure modes

The following equations define the TSL for a pure loading mode j. This law was specified in (Camanho et al., 2003). Mode I refers to the normal opening, and modes II and III relate to both shear modes opening. The stress is linked to the separation between both cohesive element faces by Equation 4.3 (Figure 4.5). K_I is the stiffness in mode I and K_s for shear modes (mode II and mode III), both shear mode behaviours

are supposed to be equal. Stiffnesses can be expressed as $K_I = E/e$ and $K_s = K_{II} = K_{III} = G/e$, with E and G the elasticity and shear moduli of the ED matrix and e the thickness of cohesive elements. d is the damage variable representing the loss of stiffness in the degradation phase of the cohesive elements, after the initiation threshold. Normal opening mode contributes to the damage increase only for traction. In compression, the relation between δ_I and σ_I is purely elastic.

$$\sigma = \begin{cases} K\delta & \text{if } \delta \leq \delta^0 \\ (1-d)K\delta & \text{if } \delta^0 < \delta < \delta^f \\ 0 & \text{otherwise} \end{cases} \tag{4.3}$$

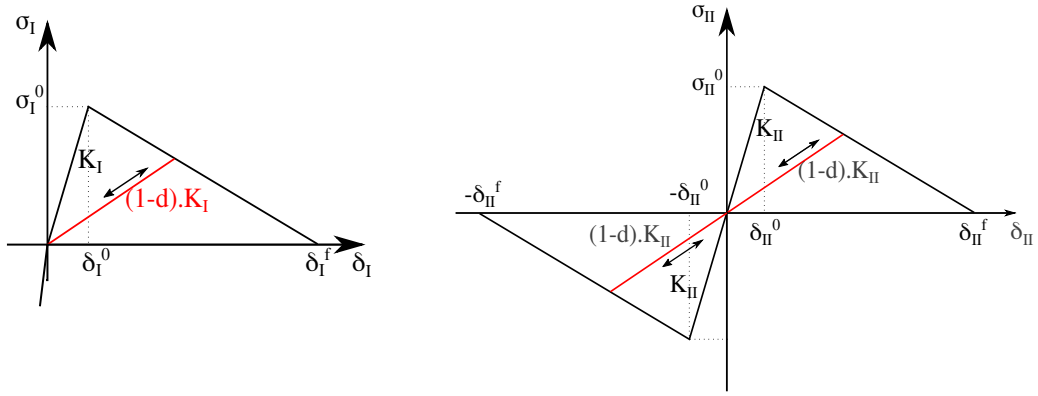

(a) Mode I (Normal opening)

(b) Mode II / mode III (Shear opening)

Figure 4.5 – Traction-separation laws for pure mode loadings

For a bilinear TSL, the damage is classically defined by a linear softening (Equation 4.4). δ^f is the separation at failure for the pure mode considered, δ^0 is the separation at damage initiation and $\delta^{max} = \underset{t>0}{max}\{\delta(t)\}$ is the maximum separation reached for the mode considered from the beginning of loading.

$$d = \begin{cases} 0 & \text{if } \delta \leq \delta_0 \\ \dfrac{\delta^f}{\delta^{max}} \dfrac{\delta^{max} - \delta^0}{\delta^f - \delta^0} & \text{if } \delta^0 < \delta < \delta^f \\ 1 & \text{otherwise} \end{cases} \tag{4.4}$$

The separation at the damage initiation is calculated with Equation 4.5 for a pure mode loading.

$$\delta_j^0 = \frac{\sigma_j^0}{K_j} \text{ with } j = \{I, II, III\} \tag{4.5}$$

Mixed modes

When in service, structures can be loaded under multiple modes simultaneously. Therefore, mixed-mode should be considered in the TSL (Figure 4.6). First, shear modes (II and III) are grouped in a shear separation δ_S calculated with Equation 4.6 (Camanho et al., 2003). In this work, both shear modes' laws are considered equal. Second, the effective separation δ_m is calculated (Equation 4.7).

$$\delta_S = \sqrt{{\delta_{II}}^2 + {\delta_{III}}^2} \tag{4.6}$$

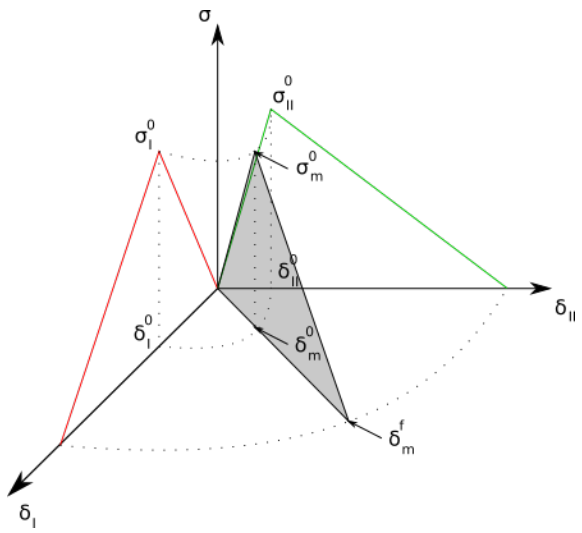

Figure 4.6 – Traction-separation law for a mixed-mode loading

$$\delta_m = \sqrt{{\delta_I}^2 + {\delta_S}^2} \tag{4.7}$$

A quadratic criterion defines damage initiation for mixed-mode loading (Equation 4.8). Normal compression does not affect the damage initiation.

$$\left(\frac{\langle\sigma_I\rangle_+}{\sigma_1^0}\right)^2 + \left(\frac{\sigma_{II}}{\sigma_{II}^0}\right)^2 + \left(\frac{\sigma_{III}}{\sigma_{III}^0}\right)^2 = 1 \tag{4.8}$$

At that point, by taking into account the definition of the mixed-mode separation (Equation 4.7) and the quadratic criterion for damage initiation (Equation 4.8), separation at the damage initiation in mixed-mode δ_m^0 is calculated with Equation 4.9.

$$\delta_m^0 = \begin{cases} \delta_I^0 \delta_S^0 \sqrt{\dfrac{1+\beta^2}{{\delta_S^0}^2 + (\beta\delta_1^0)^2}} & \text{if } \delta_I > 0 \\ \delta_S^0 & \text{if } \delta_I \leq 0 \end{cases} \tag{4.9}$$

$$\beta = \delta_S / \delta_I \tag{4.10}$$

With the assumption that the separation at damage initiation for pure shear mode is $\delta_S^0 = \delta_{II}^0 = \delta_{III}^0$. The mixity ratio β is defined by Equation 4.10 (Camanho et al., 2003). The mixed-mode are then taken into account for the fracture toughness with a Benzeggagh and Kenane law (Gong & Benzeggagh, 1995; Benzeggagh & Kenane, 1996).

$$G_C = G_{IC} + (G_{IIC} - G_{IC}) \left(\frac{G_S}{G_T}\right)^\eta \tag{4.11}$$

With $G_S = G_{II} + G_{III}$ and $G_T = G_I + G_S$. Then, the separation at damage initiation and at failure, considering a mixed-mode loading ($\delta_{j,m}^0$ at damage initiation and $\delta_{j,m}^f$ and failure), can be written for each mode (Equations 4.12 to 4.15).

$$\delta_{I,m}^0 = \frac{\delta_m^0}{\sqrt{1+\beta^2}} \tag{4.12}$$

$$\delta_{I,m}^f = \frac{\delta_m^f}{\sqrt{1+\beta^2}} \tag{4.13}$$

$$\delta_{s,m}^0 = \frac{\beta\delta_m^0}{\sqrt{1+\beta^2}} \tag{4.14}$$

$$\delta_{s,m}^f = \frac{\beta\delta_m^f}{\sqrt{1+\beta^2}} \tag{4.15}$$

The fracture toughness is defined in general terms by Equation 4.16. The vectors are written in bold.

$$G_C = \int_0^{\delta_f} \boldsymbol{\sigma} d\boldsymbol{\delta} = \int_0^{\delta_f} \left(K_I\delta_I\boldsymbol{n} + K_{II}\delta_S\boldsymbol{s}\right)\left(d\delta_I\boldsymbol{n} + d\delta_s\boldsymbol{s}\right) = \int_0^{\delta_f} \left(\sigma_I\delta_I d\delta_I\right) + \int_0^{\delta_f} \left(\sigma_s\delta_s d\delta_s\right) \tag{4.16}$$

Subsequently, the mixed separation corresponding to the element rupture δ_m^f (Equation 4.17) can be expressed from the mixed-mode fracture toughness (Equation 4.16) and the separations for each modes (Equations 4.12 to 4.15).

$$\delta_m^f = \begin{cases} \dfrac{2G_C}{\delta_m^0}\dfrac{1+\beta^2}{K_I+\beta^2K_{II}} & \text{if } \delta_I > 0 \\ \delta_{II}^f & \text{if } \delta_I \leq 0 \end{cases} \tag{4.17}$$

Once the separations and initiation stresses are defined in mixed-mode, as well as the energy and separation at rupture, then the damage can be calculated to obtain the stresses (Equation 4.18).

$$d = \begin{cases} 0 & \text{if } \delta_m^{max} < \delta_m^0 \\ \dfrac{\delta_m^f}{\delta_m^{max}}\dfrac{\delta_m^{max}-\delta_m^0}{\delta_m^f-\delta_m^0} & \text{if } \delta_m^0 \leq \delta_m^{max} \leq \delta_m^f \\ 1 & \text{otherwise} \end{cases} \tag{4.18}$$

Stresses are calculated with Equation 4.19, using the damaged stiffness matrix D (Equation 4.20).

$$\sigma_i = D_{ij}\delta_j \tag{4.19}$$

$$D_{jk} = \begin{cases} \underline{\delta}_{jk}K_j & \text{if } \delta_m^{max} \leq \delta_m^0 \\ \underline{\delta}_{jk}\left[(1-d)K_j + dK_j\dfrac{\langle-\delta_1\rangle}{-\delta_1}\underline{\delta}_{j1}\right] & \text{if } \delta_m^0 < \delta_m^{max} < \delta_m^f \\ \underline{\delta}_{j1}\underline{\delta}_{1k}\dfrac{\langle-\delta_1\rangle}{-\delta_1}K_j & \text{if } \delta_m^{max} \geq \delta_m^f \end{cases} \tag{4.20}$$

with $\underline{\delta}_{jk}$ the Kronecker delta.

The literature about composite delamination and bonded joints shows the significance of considering the strain rate sensitivity of the matrix at the interface in the constitutive model (Banea et al., 2015; May, 2015). Moreover, the results of SLS tests conducted on the welded specimens showed a loading speed sensitivity, which may result from the welded joint's strain rate sensitivity combined with the laminate's strain rate dependence. Therefore, the TSL should be extended to include the strain rate dependence of its parameters.

4.2.2 Addition of the strain rate dependence in the interface model and VUMAT implementation

For dynamic loadings, a strain rate sensitivity can be considered for the welded joint using independent viscous functions for each mode. Therefore, a TSL influenced by the strain rate is defined in this

work. This law introduces the evolution of the TSL parameters with strain rate (Marzi et al., 2009; May et al., 2014).

The strain rate can influence two properties in this law for each mode j: the damage initiation stresses (σ_j^0) and the fracture toughnesses (G_{jC}). The choice was made not to identify the TSL stiffnesses (K_I and K_{II}); therefore, stiffnesses are considered strain rate independent. Viscous functions are introduced in the same way as in the GF/PA66 constitutive model. The viscous function affecting a parameter $'X'$ is expressed by Equation 4.21. The function is defined from the evolution of the parameter value over strain rate. The comparison of the TSL for a QS and a dynamic loading is presented in Figure 4.7.

$$X\left(\dot{\varepsilon}\right) = X_{QS} f\left(\dot{\varepsilon}\right) \tag{4.21}$$

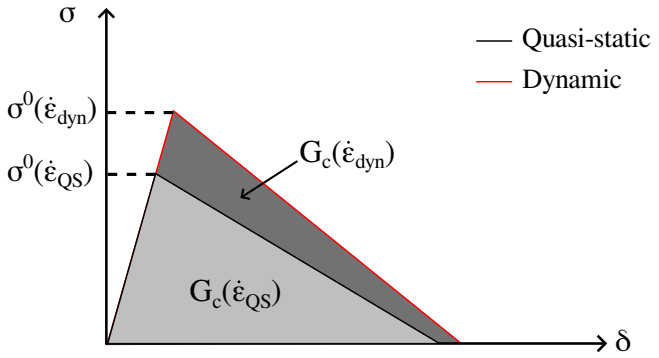

Figure 4.7 – Traction-separation law in QS and for a dynamic loading

Damage initiation stresses and fracture toughnesses are updated depending on the transient strain rate in the cohesive element until the damage initiation. When the damage initiates, the TSL in normal and shear modes' are fixed until fracture, i.e. evolution in strain rate does not affect the TSL parameters during softening.

Implementation of the VUMAT

The strain rate TSL was implemented in Abaqus using a VUMAT subroutine. The model is based on calculating the current separation δ^{i+1} for every increment. The calculation is made from the separation calculated at the previous increment δ^i and the strain increment $\Delta\varepsilon^{i+1}$ at the current increment calculated by Abaqus solver. The steps of the algorithm are described in Figure 4.8.

4.2.3 Results from the VUMAT on simple cases and comparison with Abaqus TSL

After implementing the TSL in a VUMAT subroutine, the behaviour was validated for QS loadings by comparing the results with Abaqus built-in TSL. The same hypotheses are used: quadratic nominal stress criterion for damage initiation and BK criterion for mixed-mode fracture toughness with the damage evolution defined by linear softening.

The model was first validated on simple cases of pure mode loading and then for mixed-mode loading. One element is considered with $\boldsymbol{e_z}$ the normal direction (Figure 4.9). An interaction constrains the displacements of the *'Reference Points'* to the corresponding surface (*'RP-1'* linked to the back surface and *'RP-2'* to the front surface). The back *'Reference Point'* is embedded and displacement is applied to the front *'Reference Point'*. It is first loaded in pure mode and then in mixed mode. The results are compared with Abaqus built-in TSL results with the same TSL parameters (Table 4.3).

Validation for pure modes

Mode I results are presented for a QS loading (Figure 4.10a). The red and yellow curves show that

VUMAT for Traction-Separation Law

— Retrieval of stresses σ_j^i and separation δ_j^i calculated at the previous increment.
— Retrieval of current strain increments from Abaqus $\Delta\varepsilon_j^{i+1}$.
— Calculation of current separations $\delta_j^{i+1} = \delta_j^i + \Delta\epsilon_j^{i+1} e$ with e the cohesive element thickness.
— Retrieval of energies at previous increment G_I^i, G_{II}^i and G_{III}^i.

Strain rate effect

— Retrieval of pure mode fracture toughness and damage initiation separation at previous increment: G_{IC}^i, G_{IIC}^i, $\sigma_I^{0,i}$, $\sigma_{II}^{0,i}$.
— Calculation of current strain rates: $\dot{\varepsilon}_j^{i+1} = \Delta\varepsilon_j^{i+1}/dt$ with dt the time increment.
— Calculation of current traction-separation law parameters at the current strain rate: $\sigma_I^{0,i+1}$, $\sigma_{II}^{0,i+1}$, G_{IC}^{i+1} and G_{IIC}^{i+1} (Equation 4.21 and Equation 4.22).

Mixed mode

— Calculation of current damage initiation separation: $\delta_I^{0\,i+1} = \sigma_I^{0\,i+1}/K_I$, $\delta_{II}^{0\,i+1} = \sigma_{II}^{0\,i+1}/K_{II}$.
— Calculation of current effective separation δ_m^{i+1} (Equation 4.7).
— Calculation of current mode mix ratio β^{i+1} (Equation 4.10).
— Calculation of current effective separation at damage initiation $\delta_m^{0\,i+1}$ (Equation 4.9).
— Calculation of the current fracture toughness G_C^{i+1} (Equation 4.11).
— Calculation of the effective separation at failure $\delta_m^{f\,i+1}$ (Equation 4.17).

Damage and stresses

— Calculation of current damage d^{i+1} (Equation 4.18).
— Calculation of current stresses σ_j^{i+1} (Equation 4.19 and Equation 4.20).
— Calculation of the accumulated energy for each mode at the increment *i+1* from the value at increment *i* and the increase in area at increment *i+1* calculated with trapezium: G_I^{i+1}, G_{II}^{i+1} and G_{III}^{i+1}.
— Safeguarding quantities of interest for each mode *j*: σ_j^{i+1}, δ_j^{i+1}, $\delta_m^{max,i+1}$, d^{i+1}, G_j^{i+1}, G_{jC}^{i+1}, $\delta_j^{0,i+1}$.

Figure 4.8 – Calculation protocol in the VUMAT

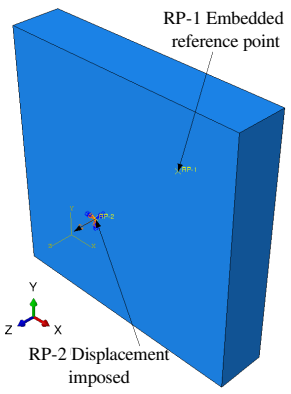

Figure 4.9 – VUMAT testing on one cohesive element - Mode I loading

VUMAT and Abaqus results for pure mode I loading are overlapping. Indeed, both laws are equal. The same observations are made for a pure mode II loading (Figure 4.10b).

$K_I.e$ (Pa)	$K_{II}.e$ (Pa)	σ_I^0 (Pa)	G_I^C (J m^{-2})	σ_{II}^0 (Pa)	G_{II}^C (J m^{-2})	e (m)	η
3×10^9	1×10^9	1.40×10^7	2000	3.20×10^7	4000	2×10^{-3}	2.284

Table 4.3 – Parameters for the VUMAT validation for TSL

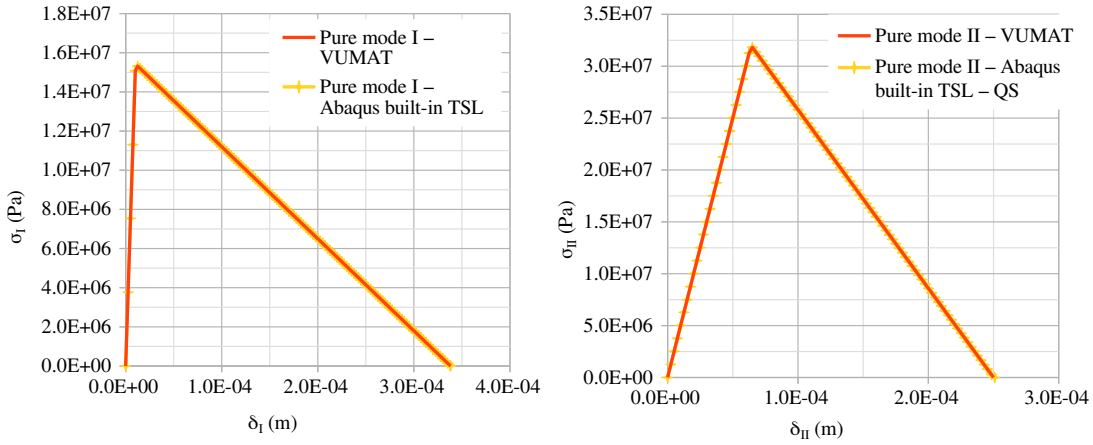

(a) Mode I (b) Mode II

Figure 4.10 – Pure mode loading using the VUMAT and ABAQUS built-in TSL

Validation for mix mode loading

Mixed modes are considered because the final application (SLS test modelling) is not a pure mode loading test. The TLS parameters used for pure mode tests are maintained for the mixed-mode simulation (Table 4.3), and two ratios are considered. The first ratio is $\beta = \delta_S/\delta_I = 10$ and the second is $\beta = 1$. These two ratios allow analysing of the mixed-mode behaviour for more significant loading in shear than in peeling and for equal loadings in both modes, respectively. The results obtained using Abaqus built-in TSL and the VUMAT subroutine are identical for both mixed-mode ratios considered (Figures 4.11 and 4.12).

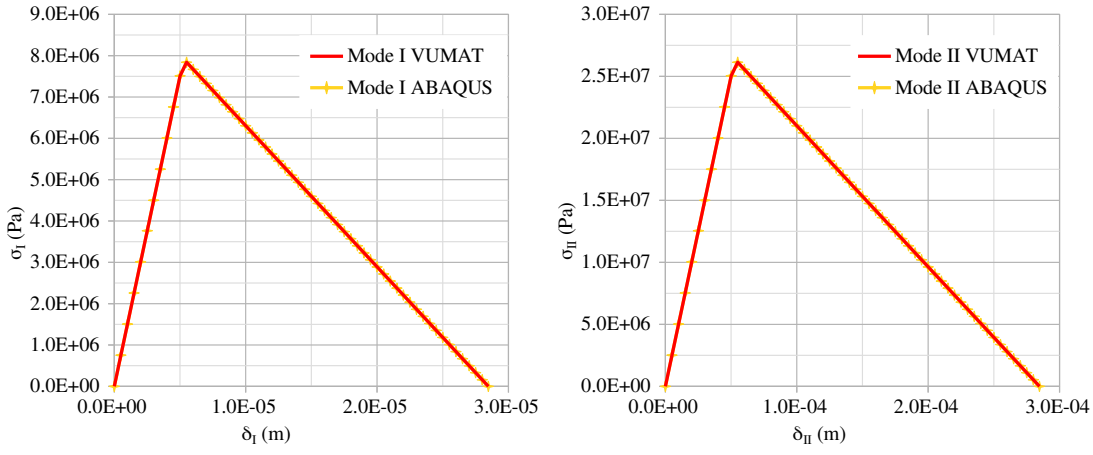

(a) Mode I (b) Mode II

Figure 4.11 – Mixed modes behaviour using the VUMAT - $\beta = 10$

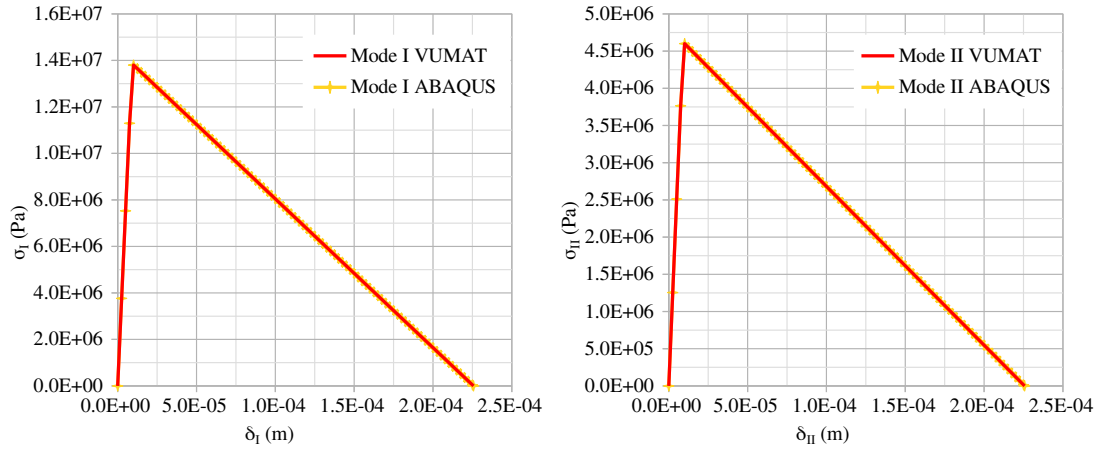

(a) Mode I (b) Mode II

Figure 4.12 – Mixed modes behaviour using the VUMAT - $\beta = 10$

4.2.4 Conclusion on the TSL defined in a VUMAT subroutine

The TSL was defined considering the interaction between modes. A quadratic nominal criterion was chosen for damage initiation and a BK criterion for the mixed-mode fracture toughness calculation. Viscous functions were included to be able to consider strain rate dependence in the weld's behaviour. Finally, the implementation was successfully validated on simple tests by comparing it with the Abaqus built-in TSL response. The following section presents the results from the inverse method application, with the TSL parameters identified for the three SLJ configurations.

4.3 Results of the TSL parameters identification

The numerical specimen, the TSL used to model the joints' behaviour, the boundary conditions and the post-processing of simulations were presented in the previous sections. Moreover, the inverse method process was introduced for the TSL parameters identification. This section outlines the TSL parameters' identification for the three welded SLJ configurations tested using the TSL implemented in a VUMAT. The parameters were identified from the QS tests; then, simulations were run for higher loading speeds using the same TSL parameters. If the numerical results match the experiments, then the QS TSL parameters successfully describe the specimens' behaviour from QS to dynamic. However, if a significant difference is observed (more than 10 % on the LSS), then a new set of TSL parameters is identified for the loading speed considered. The maximum relative error is set to 10 % because experimental scattering can be large for composite testing, especially for dynamic loadings. Therefore this gap could be acceptable under these conditions. The set of parameters identified is associated with the corresponding strain rate in the welded joint. These results allow identifying the viscous functions, thus completing the TSL parameters identification, including the strain rate dependence.

4.3.1 SLJ $[45]_4/[45]_4$ configuration

First, the TSL parameters identification is presented for a weld joining two 45°-oriented plies (SLJ $[45]_4/[45]_4$ - Figure 4.13). The set of TSL parameters identified for QS loading on the SLJ $[45]_4/[45]_4$ configuration is indicated in Table 4.4. The numerical FU curve conforms to the experimental results (Figure 4.14), and a relative error of 0.12 % is achieved on the LSS. The LSS comparison is made on the averaged values from Chapter 3 (Figure 3.36) (Bourda et al., 2023). A minor gap is observed between experimental and numerical FU curves, with a slightly stiffer numerical specimen than the experimental

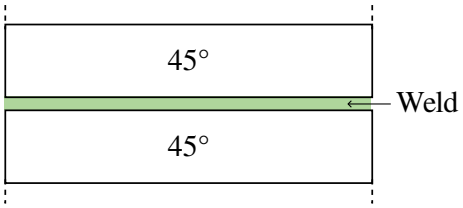

Figure 4.13 – Schematic cross section of the welded overlap for the SLJ $[45]_4/[45]_4$ configuration - weld $45°/45°$

one. Although, a relative difference of $1.29\,\%$ is obtained on the area under the curve, which is acceptable. The numerical area under the curve and the LSS validated the parameters identified for the QS test. Finally, the slight difference in stiffness may be caused by the out-of-plane movements observed experimentally in QS. It may introduce a limited error in displacement evaluation despite the data correction from side images. Nevertheless, the numerical results suitably reproduce the SLJ specimen behaviour and performance in QS. Concerning the consistency of the fracture toughnesses identified, the order of magnitude corresponds to the values measured or evaluated for TP composites (Chang & Lees, 1988; Camanho et al., 2003; Ma et al., 2016; Bhudolia et al., 2022) and more precisely for GF/PA66, one study reported a $4000\,\mathrm{J\,m^{-2}} \pm 500\,\mathrm{J\,m^{-2}}$ mode II fracture toughness (Todo et al., 1999). Moreover, these results show that using a bilinear TSL is appropriate to describe the behaviour of a weld surrounded by two $45°$-oriented plies for an SLS test.

$K_I.e$ (GPa)	σ_I^0 (MPa)	G_{Ic} ($\mathrm{J\,m^{-2}}$)	$K_{II}.e$ (GPa)	σ_{II}^0 (MPa)	G_{IIc} ($\mathrm{J\,m^{-2}}$)
3.9	14	3000	1.0	32	5000

Table 4.4 – Traction separation law parameters for SLJ $[45]_4/[45]_4$ specimens weld

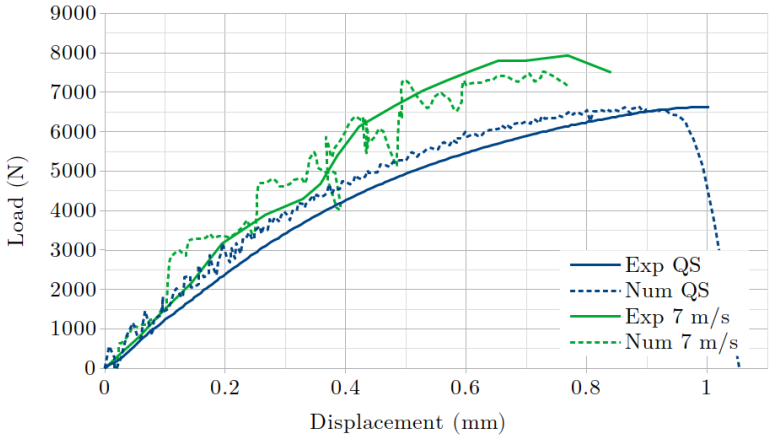

Figure 4.14 – Comparison of experimental and numerical FU curves for $1.2\,\mathrm{mm\,min^{-1}}$ (QS) and $7\,\mathrm{m\,s^{-1}}$ loading speeds - SLJ $[45]_4/[45]_4$

Simulations were performed for $200\,\mathrm{mm\,s^{-1}}$, $2\,\mathrm{m\,s^{-1}}$ and $7\,\mathrm{m\,s^{-1}}$ loading speeds with the QS TSL parameters (Table 4.4). FU curves agree with the experimental results (Figures 4.14 and 4.15), with similar initial stiffnesses and fracture occurring for similar displacement values. The comparison of numerical and experimental LSS values (Figure 4.16) shows minor differences. The gap is larger for the $2\,\mathrm{m\,s^{-1}}$ with $3.83\,\%$ more for numerical results, which is a limited error for a dynamic study. This scattering may be caused by variation in the characterisation tests, as a larger standard deviation was observed on the displacement for this crosshead speed. Therefore, the parameters identified for the QS test consistently describe the welded specimen's behaviour for dynamic loadings. This result implies that the loading speed influence observed on the LSS and FU curve (stiffening and strengthening) is caused by the strain rate sensitivity of the GF/PA66 shear behaviour. For the configuration tested in this work, no loading speed dependence is needed for the weld's TSL because of the relatively small weld's thickness, combined with the significant strain rate dependence of the $45°$-oriented ply. The author supposes that the

strain rate dependence of the weld's matrix is implicitly considered by the strain rate dependence of the surrounding plies because the stiffnesses are similar for the weld and the GF/PA66 shear behaviour. The influence of the parameters set on the global behaviour was investigated with two simulations run with a set of parameters different from the identified one. The results show that the choice of parameters affects the global behaviour of the SLJ specimen (Appendix G). Therefore, the consideration of a significant strain rate dependence of the TSL would negatively affect the numerical results obtained for this $45°/45°$ weld.

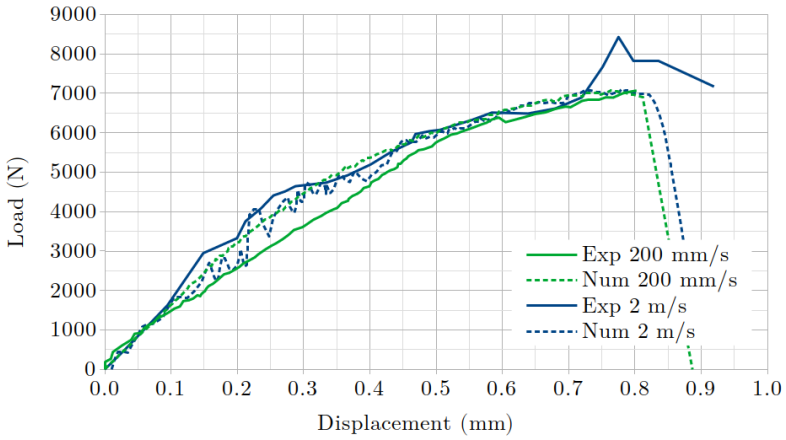

Figure 4.15 – Comparison of experimental and numerical FU curves for $200\,\mathrm{mm\,s^{-1}}$ (QS) and $2\,\mathrm{m\,s^{-1}}$ loading speeds - SLJ $[45]_4/[45]_4$

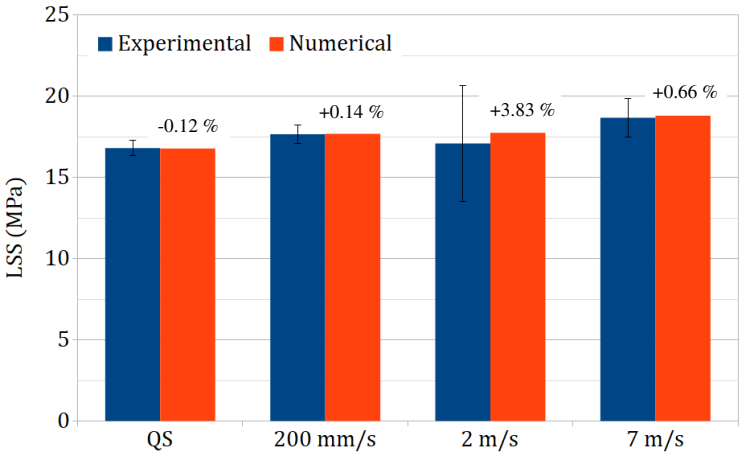

Figure 4.16 – Comparison of numerical and experimental LSS - SLJ $[45]_4/[45]_4$

Influence of the GF/PA66 strain rate dependence of the SLJ specimen's behaviour

Simulations were done without the strain rate dependence in the GF/PA66 substrates. The global behaviour is presented for a $2\,\mathrm{m\,s^{-1}}$ crosshead speed (Figure 4.17), for which the strain rate in the substrates is expected to be moderated (about 10 to $100\,\mathrm{s^{-1}}$). The FU curve obtained significantly differs from the experimental result with lower stiffness and strength for the TSL parameters identified in Table 4.4. No set of TSL parameters could be found to match the experimental FU curves, with always a lower load for a fixed displacement. Therefore, the viscous shear behaviour of GF/PA66 must be considered in the substrates' constitutive model to describe the behaviour of SLJ specimens.

Validation of the model consistency: comparison of quantities with experiments, analysis of numerical quantities

The TSL parameters identification was conducted by taking the FU curves and the LSS experimental values as a reference. These data correspond to the macroscale with comparison of data corresponding to the global behaviour of the substrates and the weld. Nevertheless, the validation can also be done at

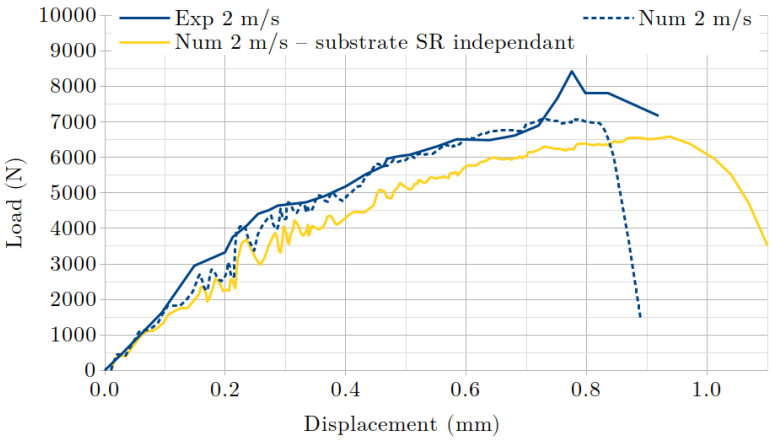

Figure 4.17 – FU curves for SLJ $[45]_4/[45]_S$ specimen at $2\,m\,s^{-1}$ with and without strain rate dependence of the GF/PA66 shear behaviour

a mesoscale by analysing quantities only in the substrates or the welded joint within the SLJ specimen. Some quantities can be compared between experiments and numerical results to validate the consistency of the weld's modelling. The several quantities analysed in this part are: the strain rates in the substrates above and below the welded joints and outside the overlap zone (compared with experiments whenever possible), damage in the substrates and stresses in the weld. These observations reinforce the conclusions presented on the $45°/45°$ weld modelling.

Validation in the substrates

It is essential to ensure the strain rate reached numerically in the substrates is similar to the experimental one to check on the modelling consistency. In the case of a strain rate dependent orientation of the substrates plies, similar experimental and numerical strain rates ensure that the correct parameters are used in the GF/PA66 constitutive law. Moreover, the same strain level in the substrates, experimentally and numerically, allows supporting the consistency of the weld's model and its parameters. The strain rate extraction is made first on a fixed zone outside the overlap (Figure 4.18a). Displacements are measured experimentally with the DIC software Ufreckles (Réthoré, 2018) on a meshed area and strains are calculated from these values. The data are averaged on the zone considered; the strain rate is estimated

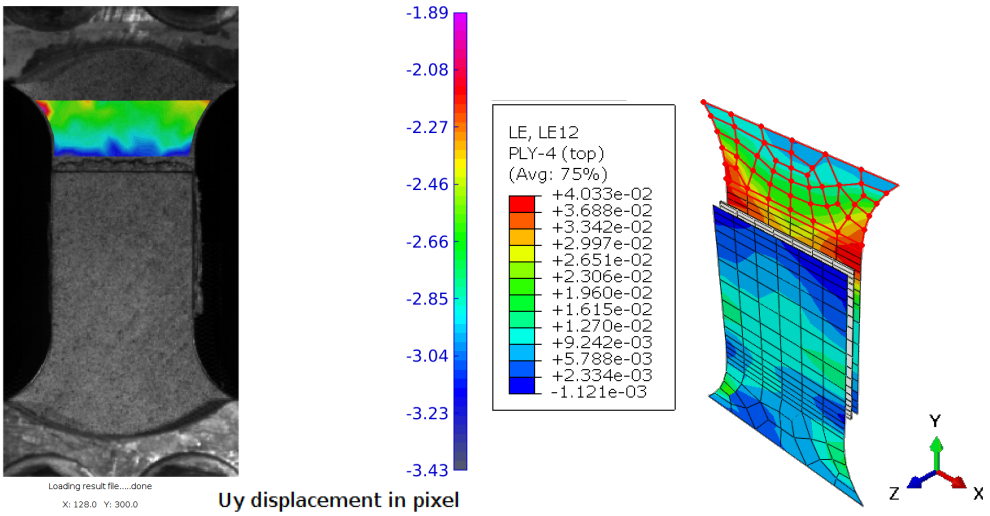

(a) Experimental strain extraction domain using Ufreckles (Réthoré, 2018)

(b) Numerical strain extraction domain

Figure 4.18 – Extraction of experimental and numerical strains for the strain rate evaluation

as the slope of strain over time from the tensile test beginning to the specimen's fracture (Figure 4.19a). The same extraction is made on the field outputs for the numerical results. Strains are extracted on the

outermost ply facing the camera during the experiments (elements circled in red in Figure 4.18b). As a second step, the strains are extracted numerically in the ply surrounding the weld, in the overlap area, to calculate the strain rates.

The shear strain rates obtained numerically for the configuration $[45]_4/[45]_4$ are smaller than the experimental ones (Figure 4.19b) outside the overlap zone. As expected, a significant increase in strain rate is observed between $200\,\mathrm{mm\,s^{-1}}$ and $7\,\mathrm{m\,s^{-1}}$ ($2.2\,\mathrm{s^{-1}}$ and $113.5\,\mathrm{s^{-1}}$, respectively). The relative differences observed in the strain rates are not leading to a large error in the material shear properties definition (modulus, yield stress, etc). Therefore, the weld's and substrates' constitutive law parameters are considered to be suitably defined at the loading speeds considered.

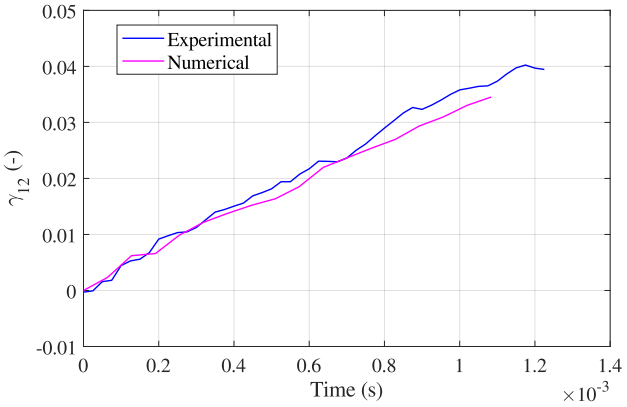

(a) Evolution of shear strain over time in a substrate - $2\,\mathrm{m\,s^{-1}}$

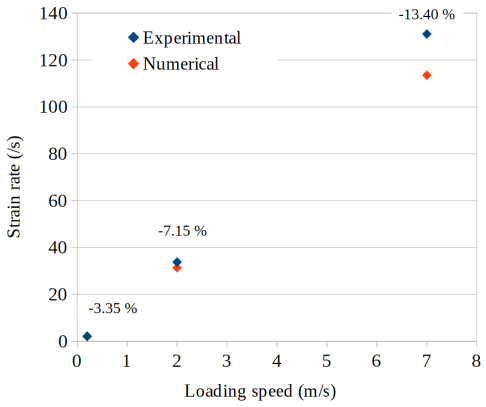

(b) SLJ $[45]_4/[45]_4$

Figure 4.19 – Experimental and numerical shear strain rate in $[45]_4$ substrates for $200\,\mathrm{mm\,s^{-1}}$, $2\,\mathrm{m\,s^{-1}}$ and $7\,\mathrm{m\,s^{-1}}$ loading speeds

As can be expected, the strain rate in the substrates increases quasi-linearly with the loading speed. In addition, the shear strain rate also rises in the substrate over the overlap zone at higher loading speeds (Figure 4.20). These levels of strain rate show that the state in the overlap is far from quasi-static conditions.

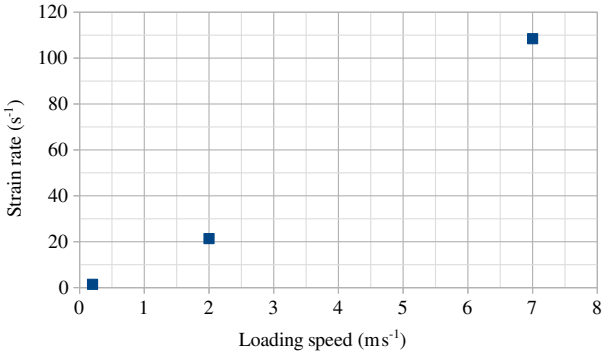

Figure 4.20 – Averaged $\dot{\gamma}_{12}$ above and below the welded joint - SLJ $[45]_4/[45]_4$

The strain fields in the substrates show a concentration of the strains near the overlap edge and fillets for QS and dynamic loadings (Figure 4.21). It results in higher damage values around the substrate fillets and the overlap edge (Figure 4.22). In addition, as the loading speed increases, the maximum damage in the substrates tends to decrease. This decrease in maximum damage is caused by the stiffening and strengthening shear behaviour of GF/PA66 composite: for the same strain level, the shear stress increases at a higher strain rate and damages are equivalent. For SLJ $[45]_4/[45]_4$, the maximum shear stress in the substrates tends to increase at higher loading speeds (Figure 4.23) and shear strain decreases (Figure 4.21), which justify the decrease in damage. These observations emphasise the significant influence of the substrate's behaviour on the global specimen's response, with large strains and damage up to fracture.

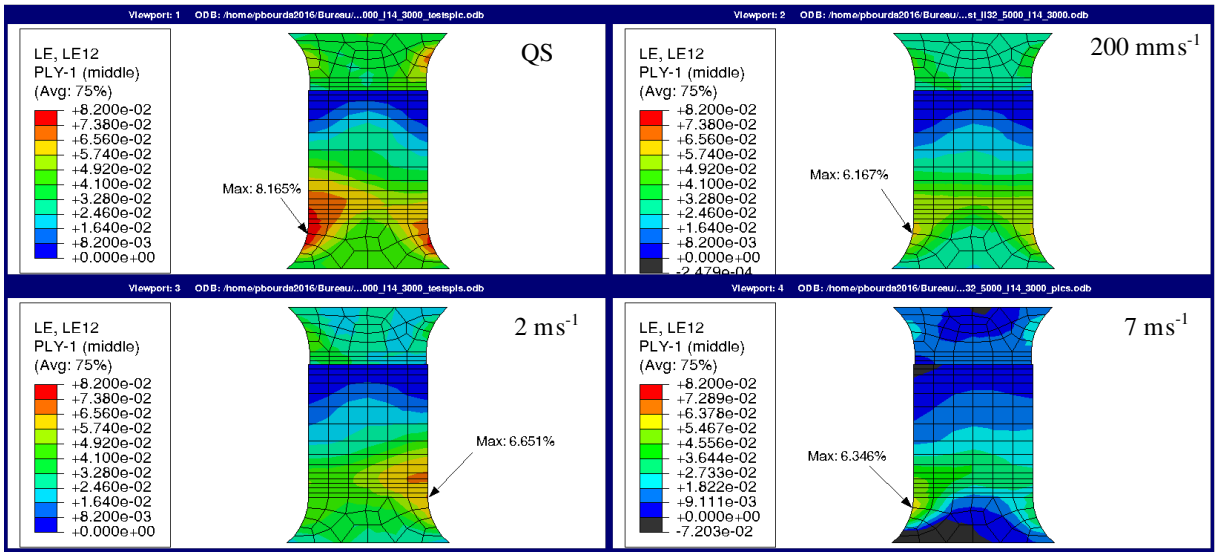

Figure 4.21 – Shear strain ε_{12} in the substrates - SLJ $[45]_4/[45]_4$ - QS, $200\,\mathrm{mm\,s^{-1}}$, $2\,\mathrm{m\,s^{-1}}$ and $7\,\mathrm{m\,s^{-1}}$

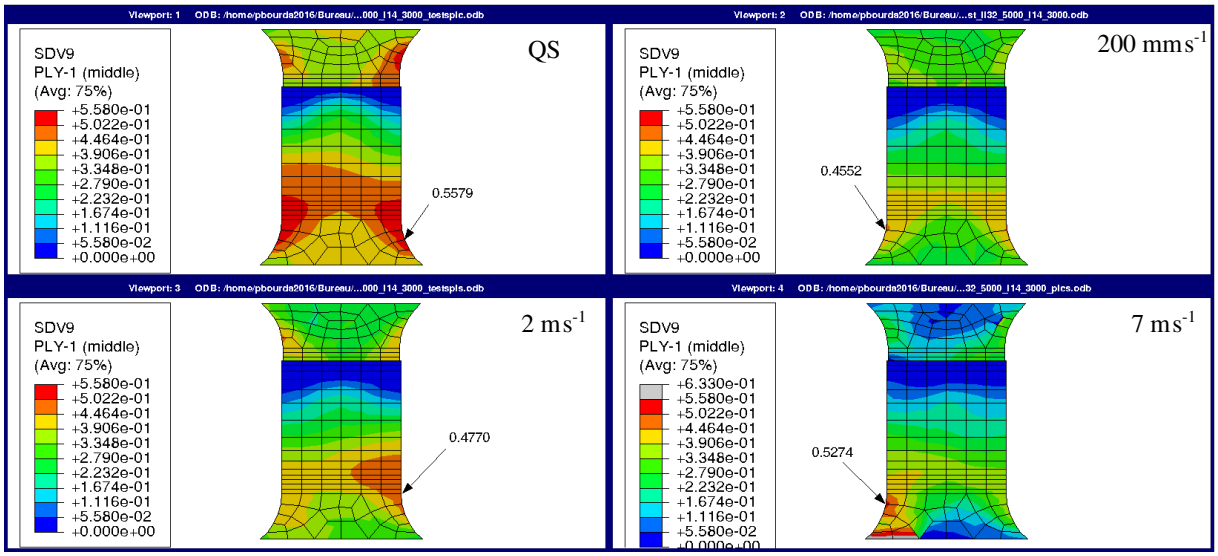

Figure 4.22 – Damage in shear d_{12} in the substrates - SLJ $[45]_4/[45]_4$ - QS, $200\,\mathrm{mm\,s^{-1}}$, $2\,\mathrm{m\,s^{-1}}$ and $7\,\mathrm{m\,s^{-1}}$

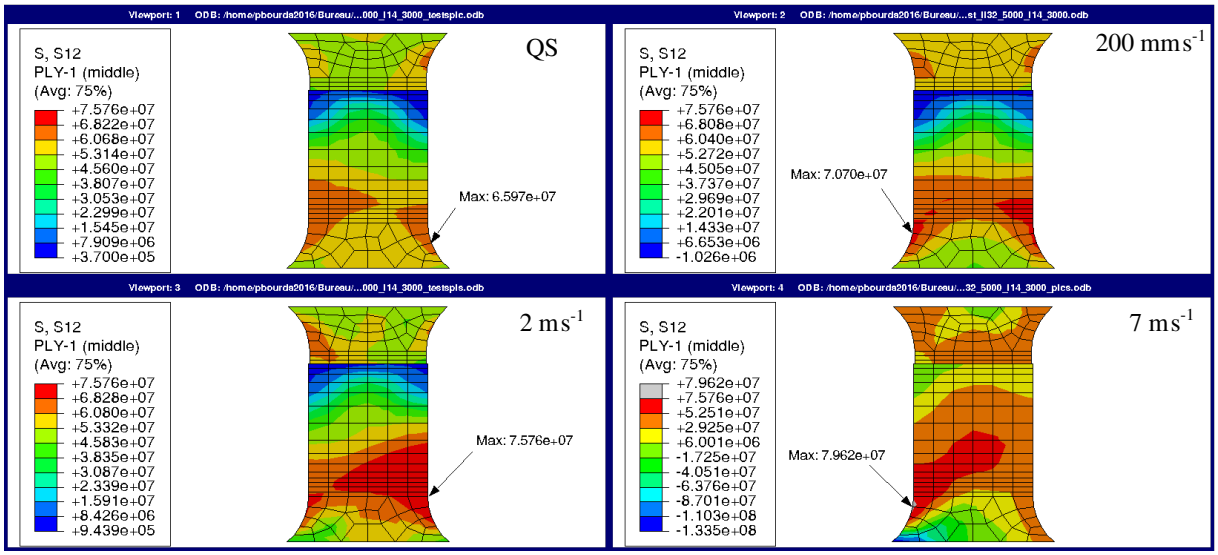

Figure 4.23 – Shear stress σ_{12} in the substrates - SLJ $[45]_4/[45]_4$ - QS, $200\,\mathrm{mm\,s^{-1}}$, $2\,\mathrm{m\,s^{-1}}$ and $7\,\mathrm{m\,s^{-1}}$

Analysis in the welded joint

Concerning the welded joint, the stress fields right before fracture are similar to the observations made in the literature for a SLS test (Figures 4.24a and 4.25a) (Campilho et al., 2013). The figures presented here consider the same level and field of damage in the weld. The stress evolutions along a vertical path in the middle of the weld (black line) show a concentration of normal stress on the edges of the weld (top and bottom edges). In addition, two peaks of compression are observed at one- and three-quarters of the length, as well as a plateau of low stresses in the centre of the overlap. The stress discontinuity is caused by the damage initiated in the outermost elements but not in the centre of the weld. Concerning the shear stresses, the peaks are noticed around one- and three-quarters of the overlap length. At the beginning of the loading, shear stress concentrates on the edges. Then, the peak propagates towards the overlap's centre due to the specimens' bending. Finally, the stresses fields are similar for the four loading speeds presented (QS, $200\,\mathrm{mm\,s^{-1}}$, $2\,\mathrm{m\,s^{-1}}$ and $7\,\mathrm{m\,s^{-1}}$, Appendix H).

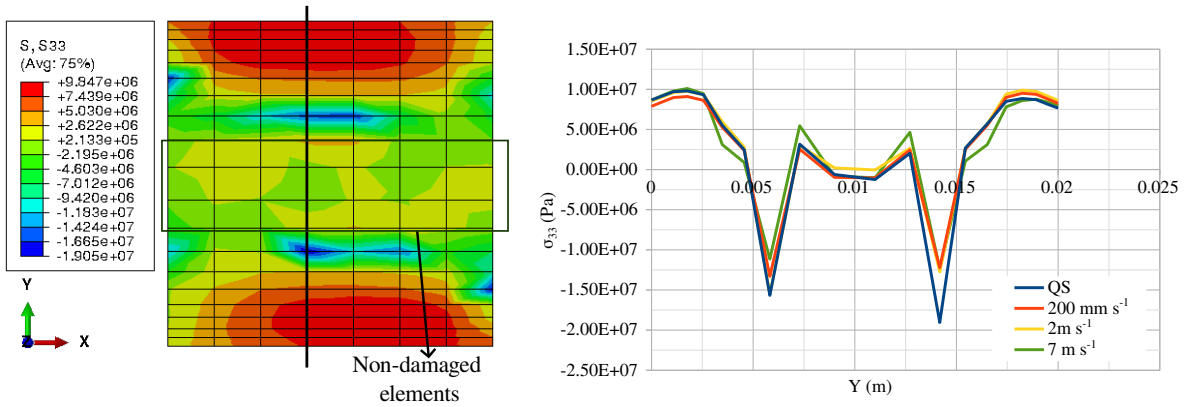

(a) Normal stress field - QS (b) Stress evolution along the path

Figure 4.24 – Normal stress before weld's fracture - SLJ $[45]_4/[45]_4$

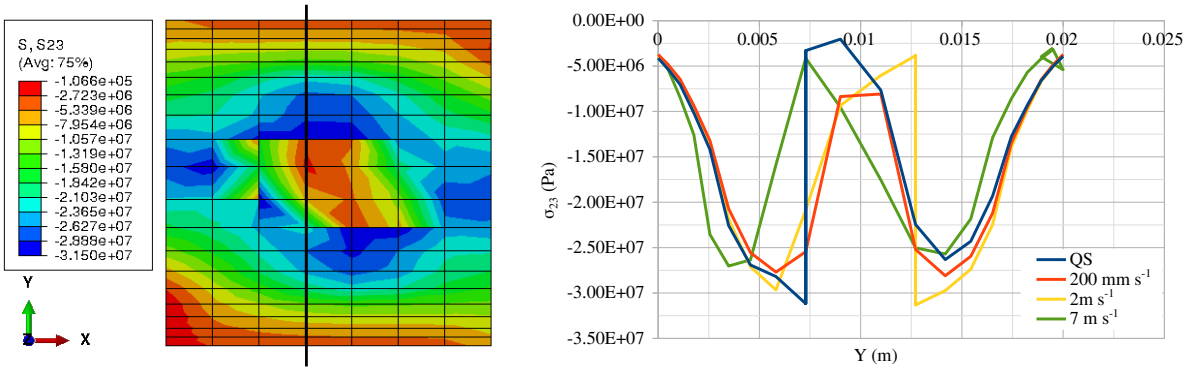

(a) Shear stress field- QS (b) Stress evolution along the path

Figure 4.25 – Shear stress before weld's fracture - SLJ $[45]_4/[45]_4$

Conclusions on the SLJ $[45]_4/[45]_4$ TSL identification

To conclude on the TSL parameters for the welded SLJ specimens $[45]_4/[45]_4$, the increases in LSS and rupture load, as well as the specimen's stiffening at higher loading speeds are suitably reproduced numerically (Figure 4.26). This phenomenon is mainly caused by the strain rate dependence of the GF/PA66 substrates shear behaviour. High damage levels are reached in the substrates near the overlap edges and outside the overlap, showing the significance of the substrates' in the SLJ's behaviour. The stress fields in the welded joint are similar for every loading speed considered. Finally, no significant strain rate de-

pendence of the TSL parameters was required to describe the $[45]_4/[45]_4$ weld's behaviour from QS to $7\,\mathrm{m\,s^{-1}}$. Therefore, no viscous functions are defined for the TSL describing the weld's behaviour between two $45°$-orientation plies. From all these elements, the author supposes that the weld thinness and the equivalence of stiffnesses between the substrates' plies and the weld's matrix lead to the non-necessity of viscosity in the TSL. The strain rate dependence would be included implicitly in the viscous shear behaviour of GF/PA66. However, this result may differ for a thicker weld.

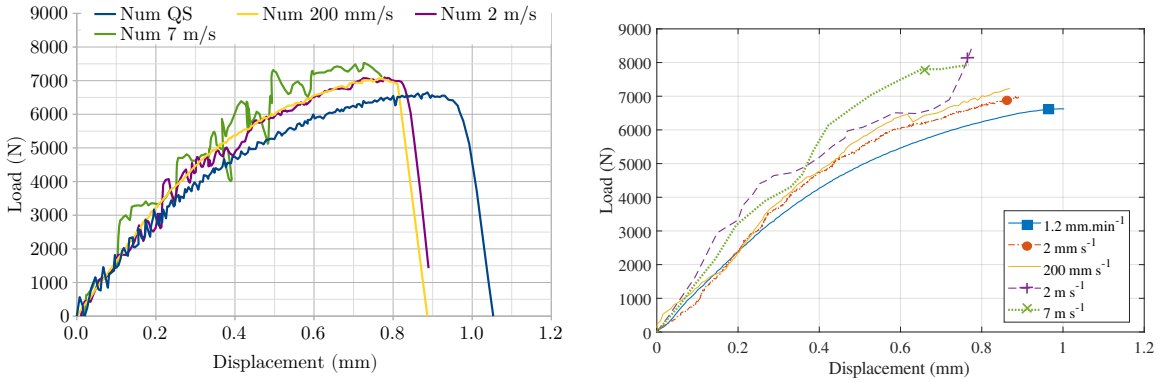

(a) Numerical (b) Experimental

Figure 4.26 – FU curves - SLJ $[45]_4/[45]_4$

4.3.2 SLJ $[45]_4/[0/45]_S$ configuration

The welded joint studied in this part joins a $0°$-oriented ply with a $45°$-oriented one (Figure 4.27). For this configuration, the simulation was done for the same specimen orientation as in the experiments: $[0/45]_S$ downward for QS and $2\,\mathrm{m\,s^{-1}}$ and $[45]_4$ upward and the opposite for $200\,\mathrm{m\,s^{-1}}$ and $7\,\mathrm{m\,s^{-1}}$ tests.

Figure 4.27 – Schematic cross section of the welded overlap for the SLJ $[0/45]_S/[45]_4$ configuration

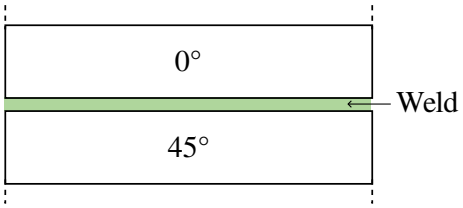

The TSL parameters were identified on QS tests for SLJ $[45]_4/[0/45]_S$ (Table 4.5). The parameters identified are equal to the ones obtained for the SLJ $[45]_4/[45]_4$ except for the smaller value of the mode II fracture toughness ($4500\,\mathrm{J\,m^{-2}}$ for SLJ $[45]_4/[0/45]_S$ compared to $5000\,\mathrm{J\,m^{-2}}$ for SLJ $[45]_4/[45]_4$). Therefore, the TSL parameters identified for the weld joining a $0°$-oriented and a $45°$-oriented plies show a weld's failure intervening at a lower energy level in shear compared to a weld between two $45°$-oriented plies. These results reinforce the link between the substrates' behaviour (more precisely the orientation of plies surrounding the weld) and the performance of the weld in the SLS test. In addition, these results corroborate with the observations of Machado, Marques, and da Silva (2018) on adhesive bonding. They stated that the most ductile substrate in the assembly has a significant influence on the behaviour of the SLJ specimen and its fracture.

$K_I.e$ (GPa)	σ_I^0 (MPa)	G_{Ic} ($\mathrm{J\,m^{-2}}$)	$K_{II}.e$ (GPa)	σ_{II}^0 (MPa)	G_{IIc} ($\mathrm{J\,m^{-2}}$)
3.9	14	3000	1.0	32	4500

Table 4.5 – Traction separation law parameters for SLJ $[45]_4/[0/45]_S$ specimens weld

The difference obtained between experimental and numerical LSS is limited with $0.89\,\%$ of relative difference (Figure 4.28). The performance is also validated at higher loading speeds using the TSL parameters identified for QS. Therefore, the same conclusion as for SLJ $[45]_4/[45]_4$ is drawn; the strain rate dependence of the substrate shear behaviour is necessary and sufficient to model the performance of SLJ $[45]_4/[0/45]_S$ and its evolution for dynamic loadings up to $7\,\mathrm{m\,s^{-1}}$. The welded joint considered in this study between one $0°$-oriented and one $45°$-oriented plies does not need a strain rate dependent model according to the numerical results.

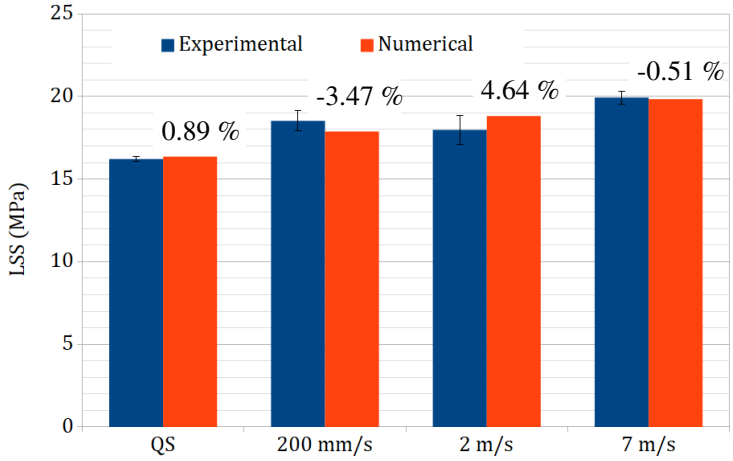

Figure 4.28 – Comparison of numerical and experimental LSS - SLJ $[45]_4/[0/45]_S$

Despite the limited deviation between numerical and experimental LSS, differences are observed in the shape of the FU curve (Figure 4.29). The experimental shape is more linear from the beginning, with larger displacements than numerical results at a fixed reaction force value. However, there is an exception at $2\,\mathrm{m\,s^{-1}}$ with a numerical evolution of the FU curve similar to the experiment. The stiffness deviation is caused by the realisation of tensile tests. As explained in Subsection 3.3.3.1, the orientation of

Figure 4.29 – Comparison of experimental and numerical FU curves for $1.2\,\mathrm{mm\,min^{-1}}$ (QS) and $7\,\mathrm{m\,s^{-1}}$ loading speeds - SLJ $[45]_4/[0/45]_S$

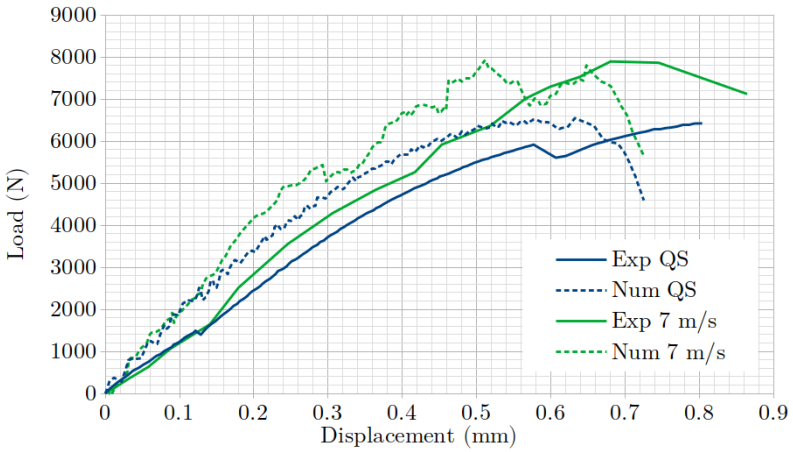

the specimen was different for $2\,\mathrm{m\,s^{-1}}$ than other loading speeds with the substrate $[0/45]_S$ fixed to the embedded arm. The author supposes that the specimen positioning prevented out-of-plane movements of the loading grip, which is not fully constrained to vertical displacement, compared to a tensile-torsion machine for example. However, for the other positioning ($[45]_4$ substrate attached to the embedded grip), out-of-plane displacement may have induced error in the displacement measurements. This results in the difference in the shape of the FU curves.

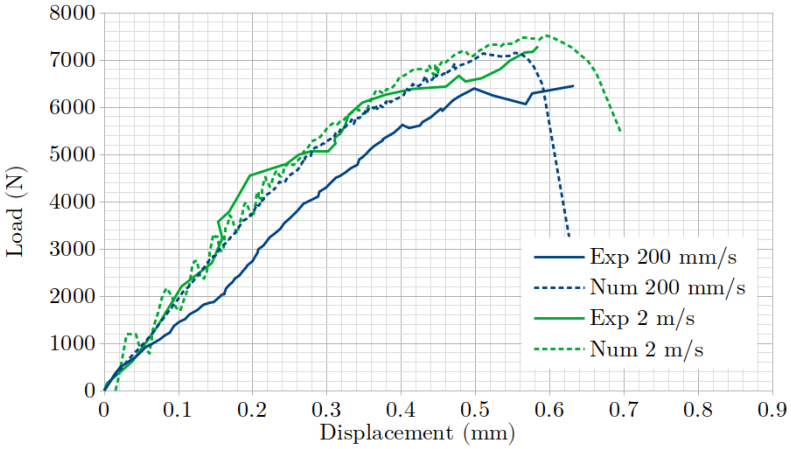

Figure 4.30 – Comparison of experimental and numerical FU curves for $200\,\mathrm{mm\,s^{-1}}$ (QS) and $2\,\mathrm{m\,s^{-1}}$ loading speeds - SLJ $[45]_4/[0/45]_S$

Validation of the model consistency: comparison of quantities with experiments, analysis of numerical quantities

The average strain rates in the $[45]_S$ substrate were extracted in the unwelded area (Subsection 4.3.1). The numerical results agree with the experiments, and the relative difference observed does not lead to a significant misestimation of constitutive law parameters for the substrate (Figure 4.31a). Similar extraction was done for the longitudinal strain rate in the $[0/45]_S$ substrate (Figure 4.31b). The differences are more significant for the $2\,\mathrm{m\,s^{-1}}$ and $7\,\mathrm{m\,s^{-1}}$ loading speeds (Figure 4.32). The evolution of the strain over time points out the difference caused by a stagnation of the strain from $5 \times 10^{-4}\,\mathrm{s}$ and $1 \times 10^{-4}\,\mathrm{s}$ for $2\,\mathrm{m\,s^{-1}}$ and $7\,\mathrm{m\,s^{-1}}$, respectively. This element is not observed numerically. Nevertheless, the initial slopes up to stagnation are in good agreement and the calculation of strain rate on these curve sections leads to a limited relative difference of $-4.49\,\%$ and $-11.76\,\%$ (instead of $46.67\,\%$ and $76.08\,\%$). From all

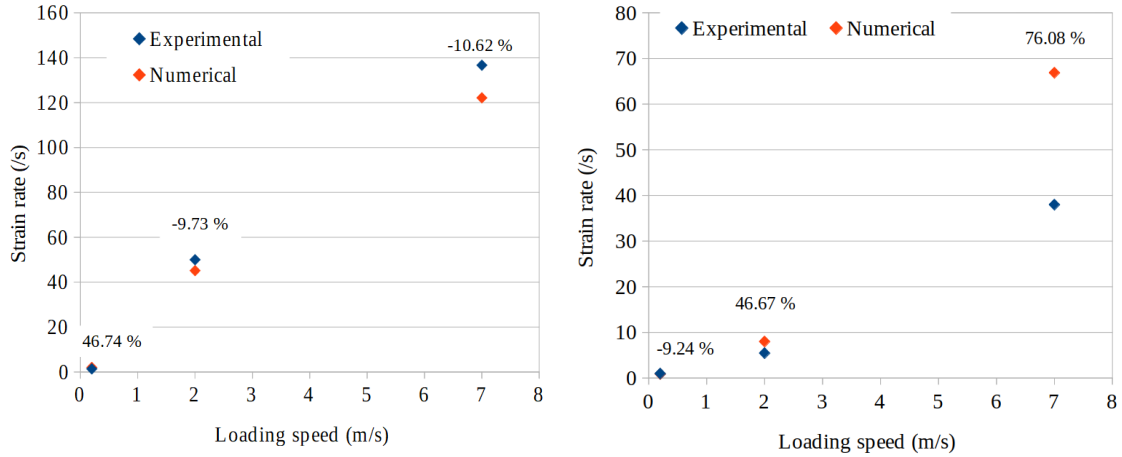

(a) Shear direction (b) Longitudinal direction

Figure 4.31 – Experimental and numerical strain rates for each substrate for $200\,\mathrm{mm\,s^{-1}}$, $2\,\mathrm{m\,s^{-1}}$ and $7\,\mathrm{m\,s^{-1}}$ loading speeds - SLJ $[45]_4/[0/45]_S$

these elements, it can be estimated that the constitutive laws defined for the substrates and weld lead to a consistent description of the behaviours occurring during the experiments. Nonetheless, improvements could still be made to the modelling.

The shear and longitudinal damages are concentrated around the fillet of the substrates and near the overlap edges (Figures 4.33 and 4.34), as observed for the previous SLJ configuration presented $[45]_4/[45]_4$. The shear damage level in the substrate is equivalent to the values obtained for the SLJ

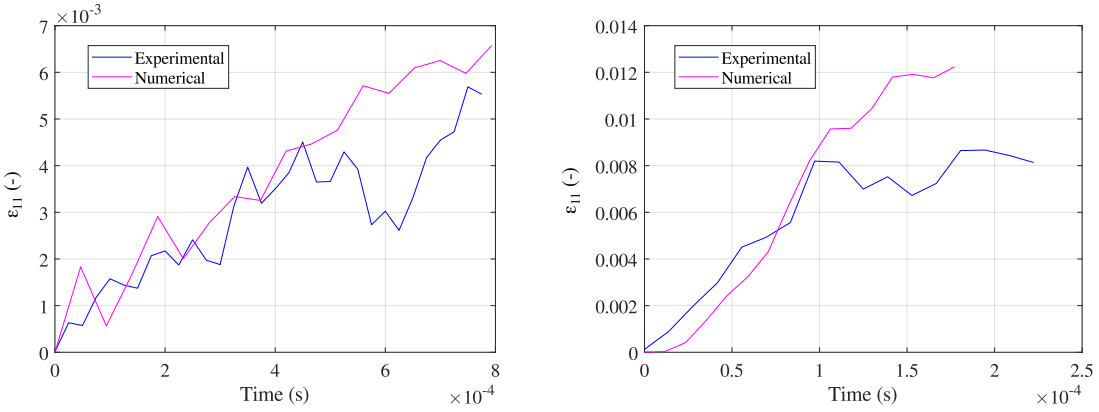

(a) Shear direction (b) Longitudinal direction

Figure 4.32 – Experimental and numerical longitudinal strain rate in $[0/45]_S$ substrates for $2\,\mathrm{m\,s^{-1}}$ and $7\,\mathrm{m\,s^{-1}}$ loading speeds - SLJ $[45]_4/[0/45]_S$

$[45]_4/[45]_4$ ($5.6\,\%$ for $[45]_4/[0/45]_S$ under QS loading versus $5.4\,\%$ for $[45]_4/[45]_4$). Moreover, a similar decrease in maximum damage in the substrate is observed for $[45]_4/[0/45]_S$ configuration. By contrast, the maximum longitudinal damage increases for dynamic loadings (Figure 4.34). This is caused by the largest stresses reached in the $[45]_4$ substrates, which equilibrate on the second substrate, leading to an increase in the longitudinal damage.

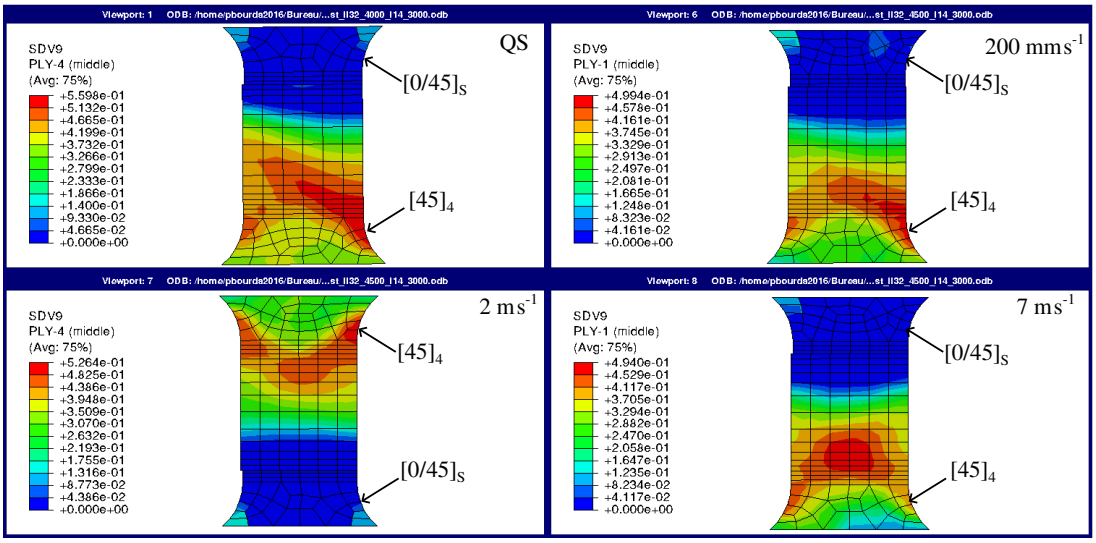

Figure 4.33 – Damage in shear d_{12} in the substrates - SLJ $[45]_4/[0/45]_S$ - QS, $200\,\mathrm{mm\,s^{-1}}$, $2\,\mathrm{m\,s^{-1}}$ and $7\,\mathrm{m\,s^{-1}}$

Concerning the stresses in the welded joint, the same evolutions are observed in normal and shear opening (Figures 4.35 and 4.36) at the four loading speeds tested (QS, $200\,\mathrm{mm\,s^{-1}}$, $2\,\mathrm{m\,s^{-1}}$ and $7\,\mathrm{m\,s^{-1}}$). The evolutions are also similar to the results obtained on SLJ $[45]_4/[45]_4$.

Conclusions on the SLJ $[45]_4/[0/45]_S$ TSL identification

The numerical results highlight a stiffening and strengthening behaviour at higher loading speeds (Figure 4.37) obtained by using only the TSL parameters identified from the QS test (Table 4.5). The increase in the maximum load is generated by the strain rate sensitivity of the GF/PA66 shear behaviour. The substrate $[45]_4$ properties are significantly affected by the strain rate sensitivity of the composite in shear, which is responsible for the strengthening and stiffening of this configuration for dynamic loads.

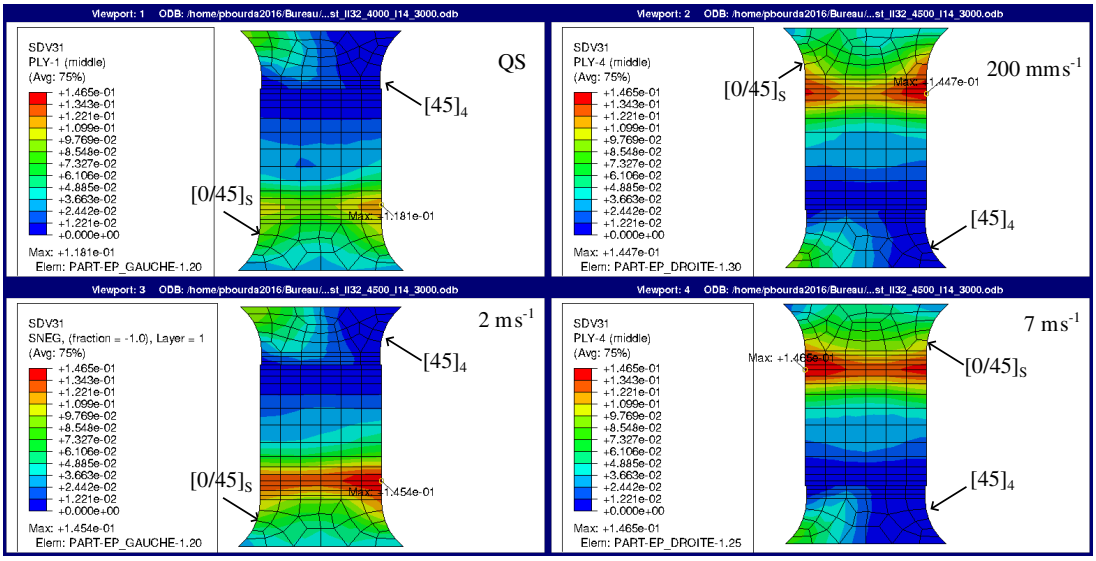

Figure 4.34 – Longitudinal damage d_{11} in the substrates - SLJ $[45]_4/[0/45]_S$ - QS, $200\,\mathrm{mm\,s^{-1}}$, $2\,\mathrm{m\,s^{-1}}$ and $7\,\mathrm{m\,s^{-1}}$

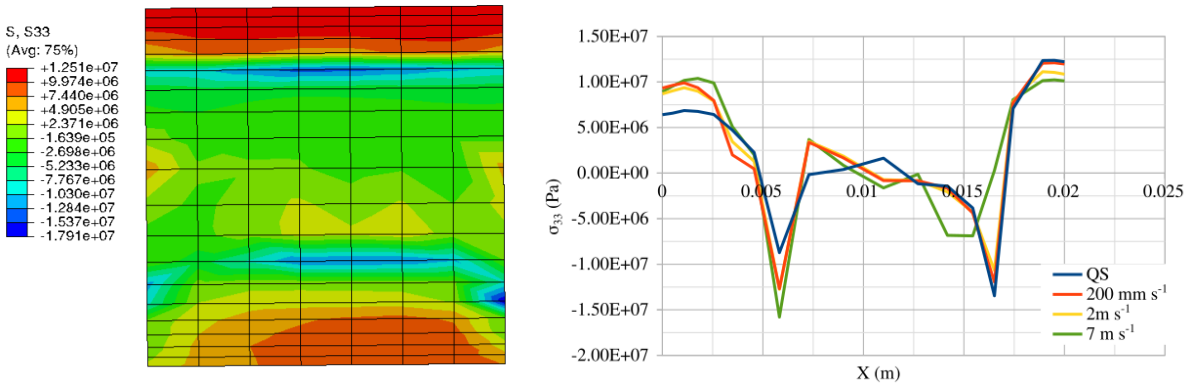

(a) Normal stress field - QS

(b) Stress evolution along the path

Figure 4.35 – Normal stress before weld's fracture - SLJ $[45]_4/[0/45]_S$

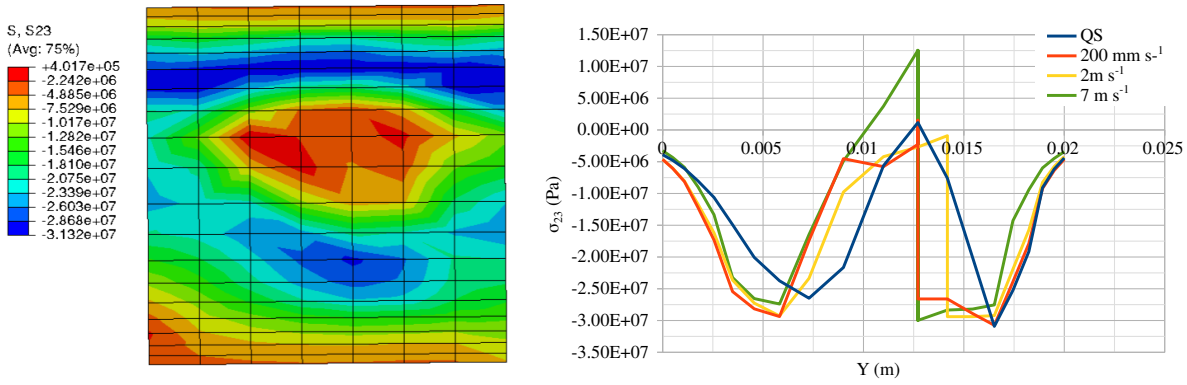

(a) Shear stress field- QS

(b) Stress evolution along the path

Figure 4.36 – Shear stress before weld's fracture - SLJ $[45]_4/[0/45]_S$

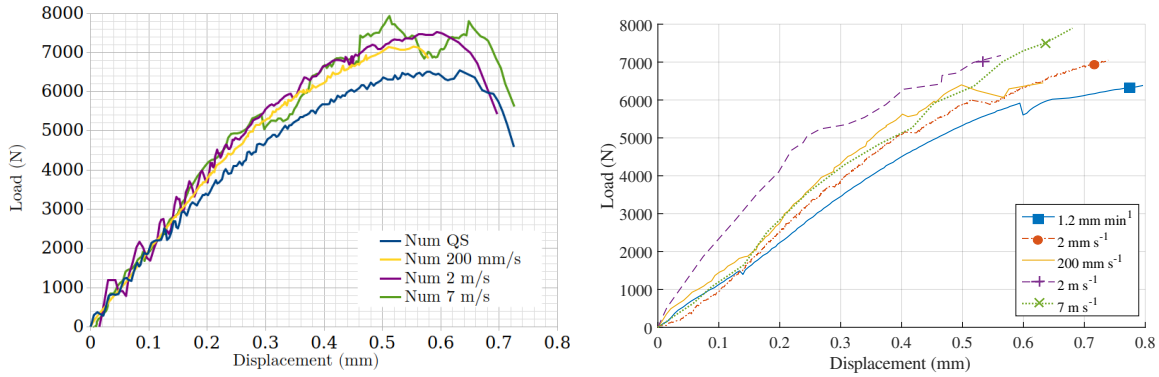

(a) Numerical (b) Experimental

Figure 4.37 – FU curves - SLJ $[45]_4/[0/45]_S$

As observed for the SLJ $[45]_4/[45]_4$, the substrates' behaviour plays a significant role in the SLJ specimen's behaviour. The strain rate dependence of the $[45]_4$ substrates seems to implicitly consider strain rate dependence of the weld's matrix (as observed for the $45°/45°$ weld). Therefore, a strain rate independent TSL is sufficient for the $0°/45°$ weld's modelling. Finally, an increase in the maximum longitudinal damage was observed in the $[0/45]_S$ substrate to balance the strengthening of $[45]_4$ substrates.

4.3.3 SLJ $[0/45]_S/[0/45]_S$ configuration

The results for the last welded joint studied are presented in this part. This weld joins two $0°$-oriented plies (Figure 4.38).

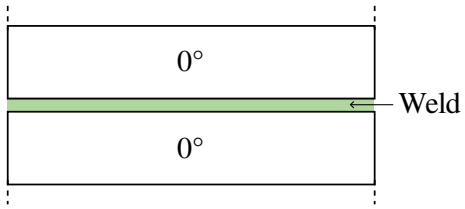

Figure 4.38 – Schematic cross section of the welded overlap for the SLJ $[0/45]_S/[0/45]_S$ configuration - weld $0°/0°$

4.3.3.1 Results from TSL parameters identification

Concerning the last SLJ specimen configuration $[0/45]_S/[0/45]_S$, the TSL parameters are identified first on the QS test. For the tests conducted at $2\,\mathrm{m\,s^{-1}}$ and $7\,\mathrm{m\,s^{-1}}$, no specimens experienced a purely FMD/cohesive fracture of the overlap. Only mixed cohesive/FMD + adhesive fracture was observed for these six specimens. Therefore, numerical FU curves obtained by considering the entire overlap as welded do not correspond to what is investigated experimentally for these two loadings speeds. For that reason, the welded surface measured on the reference specimen was considered in the model for both the highest loading speeds. Figure 4.39 represents the geometry considered for the numerical specimen with a partially welded overlap. Although, LSS values can be compared, as they are independent of the extent of the welded area.

The methodology was applied first to the QS test for validation before its application to the tensile tests at $2\,\mathrm{m\,s^{-1}}$ and $7\,\mathrm{m\,s^{-1}}$. One specimen tested in QS also broke with $63\,\%$ of cohesive/FMD fracture and $37\,\%$ of adhesive fracture. A loss of stiffness of $17.97\,\%$ is observed experimentally between an entire overlap welded and a $63\,\%$ of the overlap area welded. Numerically, the cohesive element area was reduced according to the geometry of S_{welded} for the reference specimens at the crosshead speed considered. The simulation was performed based on the geometry of the welded area ($S_{welded} = 0.63\,S_{overlap}$ in proportion) and using the TSL parameters determined for the QS loading (Table 4.6). The FU curve

Figure 4.39 – Numerical SLJ specimen - partially welded overlap corresponding to Figure 3.39b

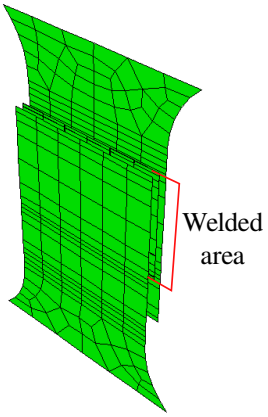

is similar to the experiment (Figure 4.40) considering the experimental area of the welded surface. It validates the consideration of a partially welded overlap to evaluate the TSL parameters.

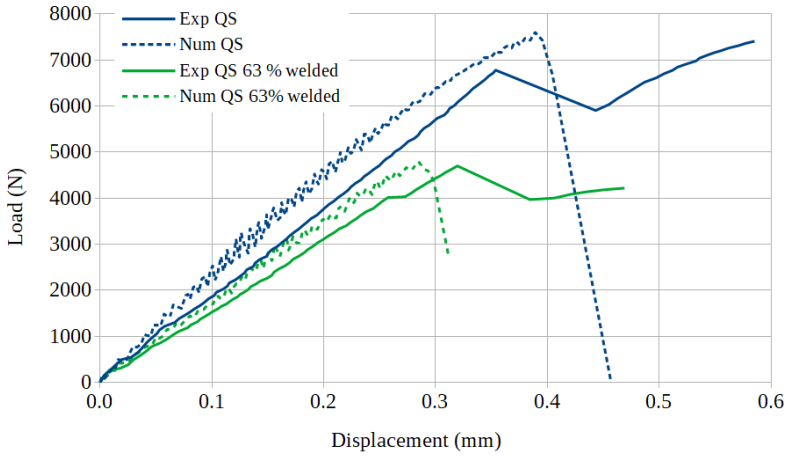

Figure 4.40 – Comparison of experimental and numerical FU curves for QS loading considering partially and totally welded overlap area - SLJ $[0/45]_S/[0/45]_S$

The parameters identified for the QS behaviour (Table 4.6) significantly differ from the identification on SLJ $[45]_4/[0/45]_S$ and $[45]_4/[45]_4$ with lower fracture toughnesses (2.25 to 2.50 times less for G_{IIc} and 1.5 times less fo G_{Ic}). Therefore, the energy required for the failure of a weld joining two $0°$-oriented plies is smaller than for the two other configurations tested. For QS loading, the initial stiffness is similar to the experiments (Figure 4.40) with a difference increasing throughout the tensile test and due to the out-of-plane movements of the specimen's edges (minor error on the displacement measured experimentally, cf Subsection 3.2.4). Moreover, fracture loads are analogous. The main difference between the experiments and the simulations is the drop in load which the model did not represent. It is caused by the fracture initiation at both edges of the overlap (Figure 3.32) also leading to a decrease in load and an increase in displacement. Nevertheless, the fracture load is only deviating by $2.60\,\%$, so the numerical results are considered in agreement with the experiments.

Loading speed	$K_I.e$ (GPa)	σ_I^0 (MPa)	G_{Ic} ($J\,m^{-2}$)	$K_{II}.e$ (GPa)	σ_{II}^0 (MPa)	G_{IIc} ($J\,m^{-2}$)
$1.2\,mm\,min^{-1}$	3.9	14	2000	1.0	32	2000
$2\,mm\,s^{-1}$	3.9	14	2600	1.0	32	3600
$2\,m\,s^{-1}$ and $7\,m\,s^{-1}$	3.9	14	3000	1.0	32	4500

Table 4.6 – Traction separation law parameters for SLJ $[0/45]_S/[0/45]_S$ specimens weld

The FU curve for $2\,\mathrm{m\,s^{-1}}$ test is compared to the experimental reference test (Figure 4.41). The numerical specimen stiffness reproduces the experiments. However, the maximum load reached was significantly lower than in the experiments using the QS parameters for TSL. This difference is then affecting the numerical LSS with an error about $13.75\,\%$ for the two highest loading speeds but also for a $2\,\mathrm{mm\,s^{-1}}$ loading speed (Figure 4.42). Therefore, a new set of TSL parameters was determined for $2\,\mathrm{mm\,s^{-1}}$, $2\,\mathrm{m\,s^{-1}}$, and $7\,\mathrm{m\,s^{-1}}$ tests to reduce the gap in LSS with experiments. An increase in mode I and mode II fracture toughnesses allows for a good fit with the experimental results (Figure 4.42 and Table 4.6).

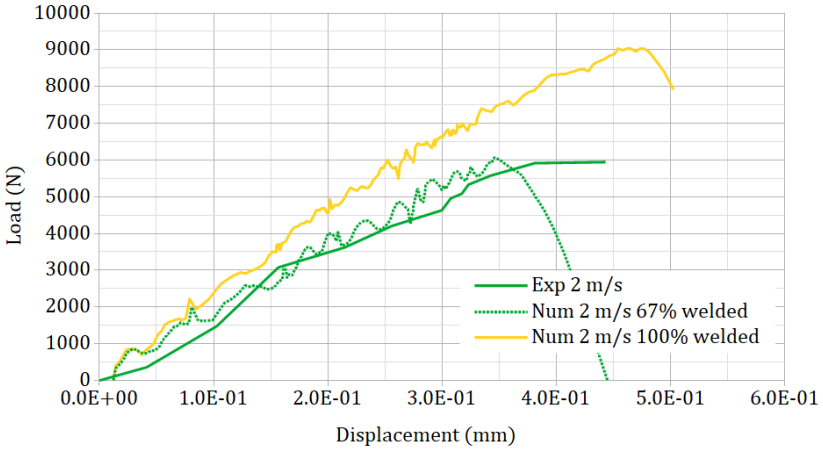

Figure 4.41 – Comparison of experimental and numerical FU curves for $2\,\mathrm{m\,s^{-1}}$ loading - SLJ $[0/45]_S/[0/45]_S$

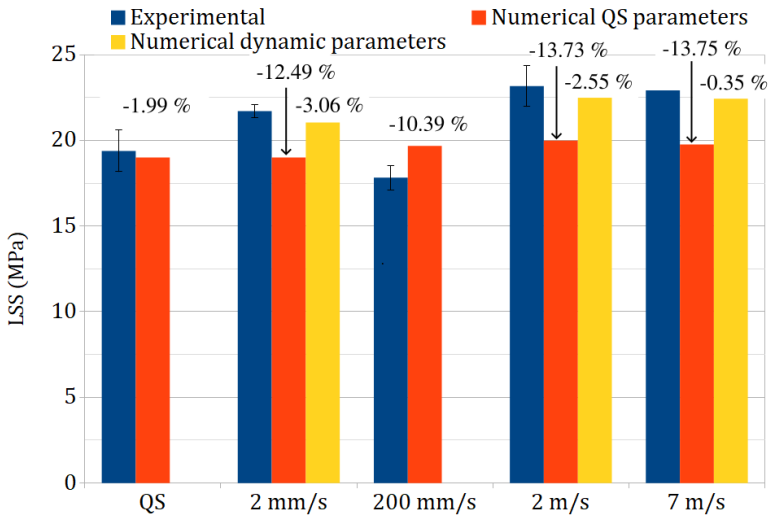

Figure 4.42 – Comparison of numerical and experimental LSS - SLJ $[0/45]_S/[0/45]_S$

The TSL parameters identification for SLJ $[0/45]_S/[0/45]_S$ differs from the identification made for the two other configurations. Indeed, results highlight that strain rate dependence should be considered in the TSL to obtain numerical results reliable to the experiments, as opposed to other configurations that only need the strain rate dependence in the substrate constitutive model. The smaller deformation of the substrates in the overlap area caused by the $0°$-oriented ply greater stiffness may increase the role played by the resin-rich layer constituting the weld which is strain rate-dependent (Shan et al., 2007b; Fabre et al., 2018; Dau, 2019).

Validation of the model consistency: comparison of quantities with experiments, analysis of numerical quantities

Experimental and numerical strain rates measured in the substrate and outside the overlap are compared (Figure 4.43a). The significant difference observed for the highest loading speed is caused by the

experimental decrease of strain, at about 0.6×10^{-4} s, leading to a smaller slope identified (Figure 4.43b). The two other loading speeds considered show good agreement with experiments.

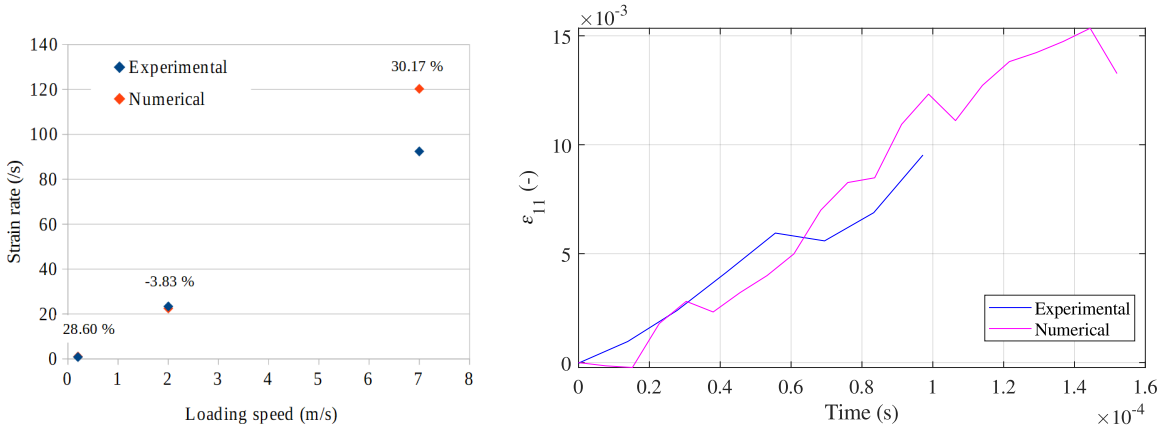

(a) SLJ $[45]_4/[45]_4$ (b) Evolution of shear strain over time in a substrate - $2\,\mathrm{m\,s^{-1}}$

Figure 4.43 – Experimental and numerical longitudinal strain rate in $[0/45]_S$ substrates for $200\,\mathrm{mm\,s^{-1}}$, $2\,\mathrm{m\,s^{-1}}$ and $7\,\mathrm{m\,s^{-1}}$ loading speeds

Longitudinal damage occurs in the substrates, especially in the ply joined to the weld. Longitudinal damage concentrates in the area near the overlap edge and not in the substrates' fillets contrary to both other SLJ configurations (Figure 4.44). The damage level is limited about 12 % to 15 %; however, these levels are close to the maximum longitudinal damage evaluated experimentally for the GF/PA66 constitutive model (17 %). In addition, the maximum damage increases for dynamic loadings, as observed for the $[45]_4/[0/45]_S$ configuration. The evolution of the TSL parameters with the strain rate leads to this phenomenon. Indeed, if the QS parameters are used for the dynamic loadings, then the maximum damage is about 12 % for all the loading speeds (Appendix I).

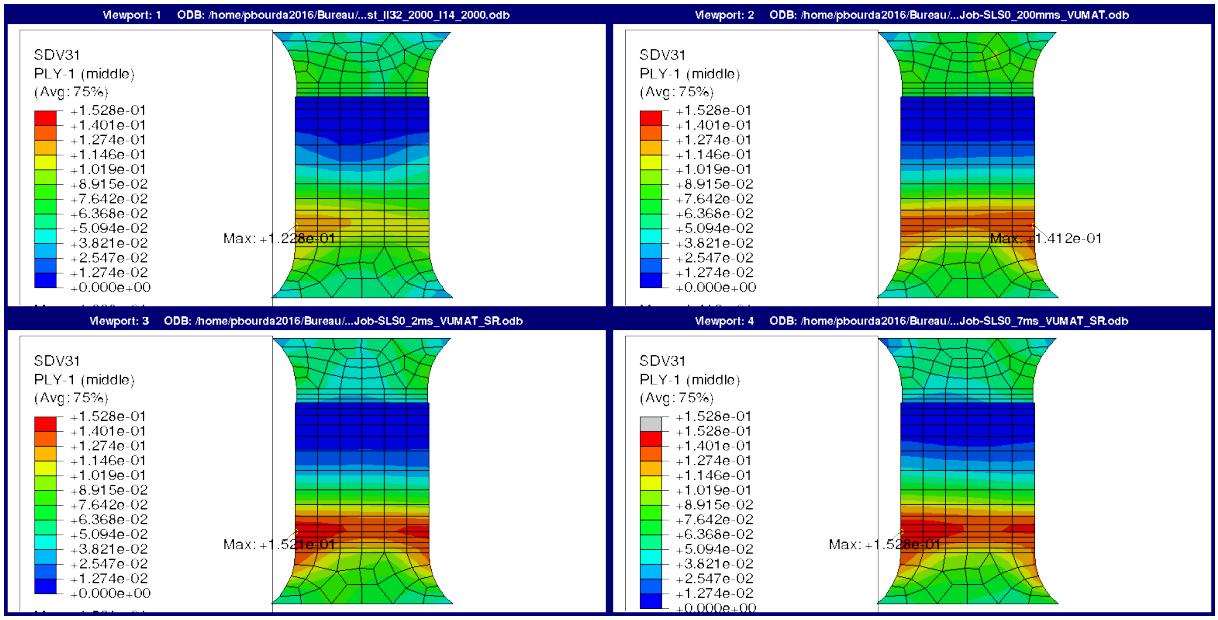

Figure 4.44 – Longitudinal damage d_{11} in the substrates - SLJ $[0/45]_S/[0/45]_S$ - QS, $200\,\mathrm{mm\,s^{-1}}$, $2\,\mathrm{m\,s^{-1}}$ and $7\,\mathrm{m\,s^{-1}}$

The normal stress along the overlap is similar for all the loading speeds tested (Figure 4.35). Moreover, the stresses are almost equal across the weld width (horizontally in Figure 4.45a). It is opposed to the

SLJs $[45]_4/[45]_4$ and $[45]_4/[0/45]_S$ in which the stresses are higher on the weld's sides and smaller in the centre of the overlap (Figures 4.24a and 4.35a).

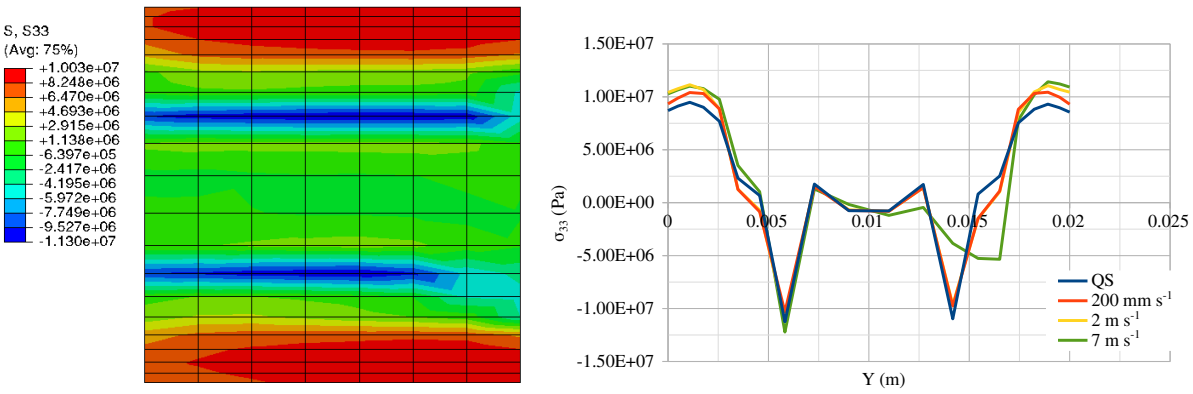

(a) Normal stress field - QS (b) Stress evolution along the path

Figure 4.45 – Normal stress before weld's fracture - SLJ $[0/45]_S/[0/45]_S$

Concerning the shear stresses, the evolutions along the weld are similar for the four loading speeds investigated (Figure 4.45). The extreme stresses are slightly higher for $200\,\mathrm{mm\,s^{-1}}$, $2\,\mathrm{m\,s^{-1}}$ and $7\,\mathrm{m\,s^{-1}}$ compared to QS (around $8.8\,\%$ higher), and the stresses peak are closer to the overlap edges, which corresponds to the observations made for the SLJ $[45]_4/[0/45]_S$.

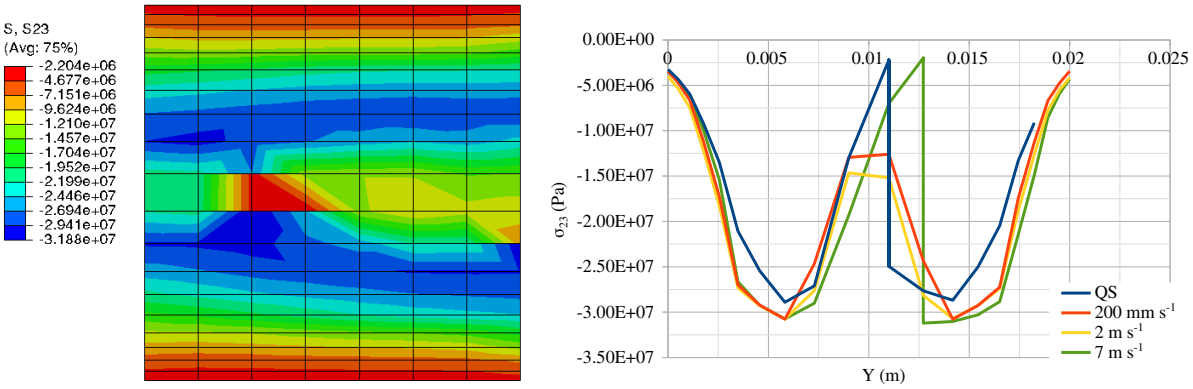

(a) Shear stress field- QS (b) Stress evolution along the path

Figure 4.46 – Shear stress before weld's fracture - SLJ $[0/45]_S/[0/45]_S$

Figure 4.47 – Shear stress before weld's fracture considering the QS TSL parameters - SLJ $[0/45]_S/[0/45]_S$

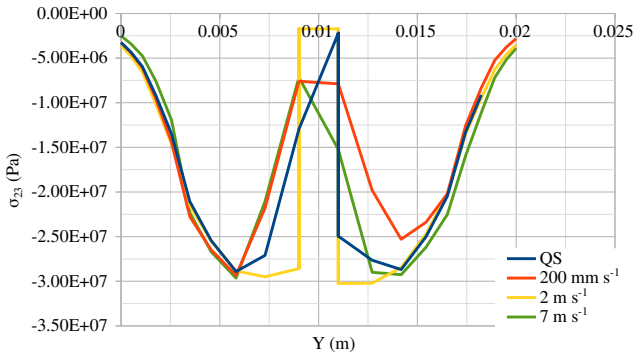

However, when using the QS TSL parameters to model the weld's behaviour under dynamic loadings, the stress evolutions are equal for each loading speed (Figure 4.47). The increase in stresses in the overlap for a fixed strain level in the weld permits modelling the specimen's strength for the SLJ $[0/45]_S/[0/45]_S$.

As the substrates' longitudinal orientation is not strain rate dependent, the strain rate dependence must be considered in the weld to affect the global behaviour.

Definition of a TSL parameters set without strain rate sensitivity

Finally, a last set of parameters was determined to describe the SLJ $[0/45]_S/[0/45]_S$ weld's behaviour for all the crosshead speeds tested. The aim was not to minimise the relative error but to get an acceptable gap for the four loading speeds. Considering that the investigation is conducted for dynamic loadings, an error about $10\,\%$ maximum could be acceptable given the experimental scatterings observed for these loadings. Therefore, the TSL parameters in Table 4.7 were used to model the weld's behaviour in QS and for several loading speeds. This set of parameters generates a more significant error on the numerical LSS compared to the experimental value. Nevertheless, the absolute relative error is lower than $10\,\%$, except for the $200\,\mathrm{mm\,s^{-1}}$ because of the experimental results. Therefore, this set of parameters could be used for the $0°/0°$ weld behaviour for quasi-static and dynamic loading without strain rate dependent behaviour. However, the relative error on LSS is larger than that obtained using the strain rate dependent TSL parameter.

K_Ie (GPa)	σ_I^0 (MPa)	G_{Ic} ($\mathrm{J\,m^{-2}}$)	$K_{II}e$ (GPa)	σ_{II}^0 (MPa)	G_{IIc} ($\mathrm{J\,m^{-2}}$)
3.9	14	2500	1.0	32	3250

Table 4.7 – Traction separation law parameters for SLJ $[0/45]_S/[0/45]_S$ specimens weld - Averaged parameters

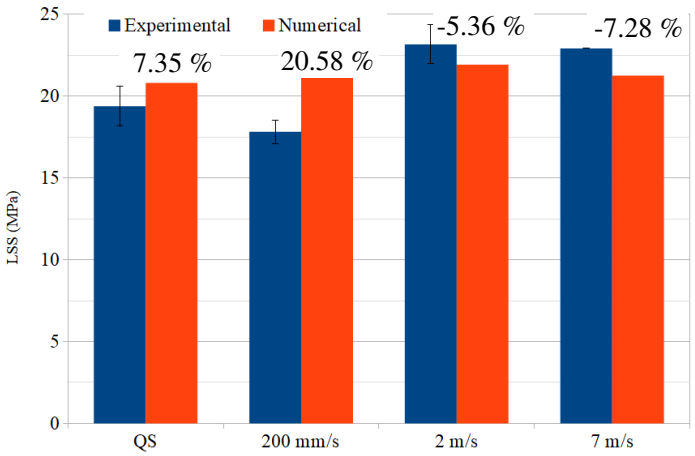

Figure 4.48 – Comparison of numerical and experimental LSS for the TSL parameter in Table 4.7 - SLJ $[0/45]_S/[0/45]_S$

4.3.3.2 Identification and validation of the TSL viscous functions for $[0/45]_S/[0/45]_S$ configuration

TSL parameters (damage initiation stresses and fracture toughnesses) have been identified and presented in the previous subsections for the several loading speeds investigated without considering the strain rate level in the weld. Viscous functions can be defined based on these results to establish the strain rate dependence of the parameters and include these functions in the TSL for the $0°/0°$ weld.

Identification of the viscous functions

The process employed for the TSL viscous functions definition is the following (Figure 4.49). The strain rates in the cohesive elements are obtained from the simulations presented in Subsection 4.3.3.1 (parameters Table 4.6). Therefore, the TSL parameters' evolution can be identified from these results by plotting the evolution of the fracture toughness depending on the strain rate and finding a suitable trend curve.

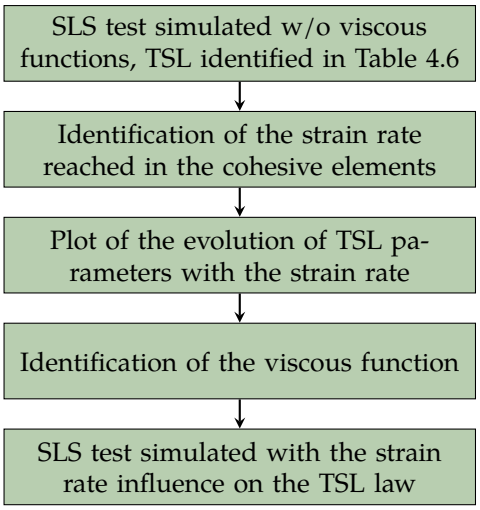

Figure 4.49 – Protocol used for the identification of the viscous function parameters for the TSL VUMAT subroutine

In more detail, the strain rate is identified at damage initiation on the edges of the overlap (the interface starts to break from the edges to the centre of the overlap). Figures 4.50 and 4.51 illustrate the normalised strain rate field for damage initiated in the edges.

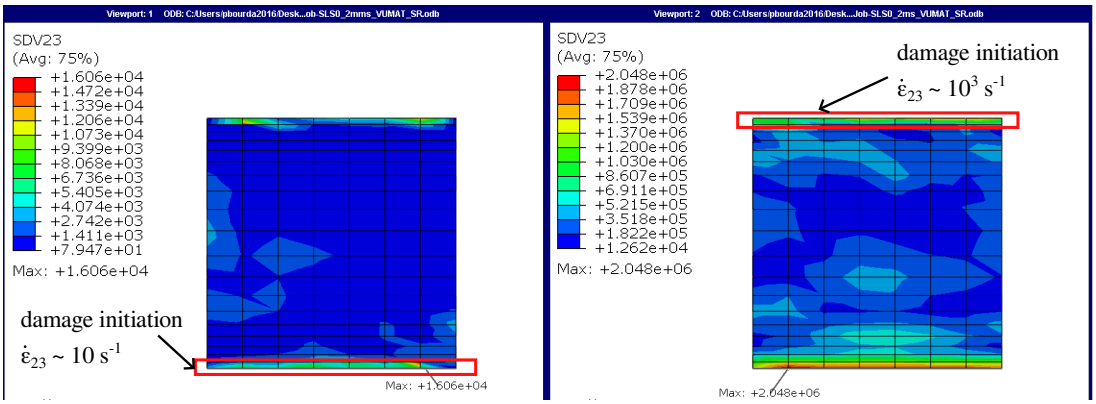

Figure 4.50 – Normalised strain rate field in shear - $2\,\mathrm{mm\,s^{-1}}$ and $2\,\mathrm{m\,s^{-1}}$

Figure 4.52 shows the evolution of the fracture toughnesses, identified for QS, $2\,\mathrm{mm\,s^{-1}}$ and $2\,\mathrm{m\,s^{-1}}$ loading speeds [1]. A linear evolution is observed between the fracture toughness and the logarithm of strain rate. Based on these results, viscous functions can be defined with similar evolutions to the ones used for the GF/PA66 constitutive model (Equation 4.22). The viscous function parameters C_I and C_{II} are identified from linear regressions on these data. The strain rates obtained in the cohesive elements at damage initiation for a $2\,\mathrm{m\,s^{-1}}$ loading speeds are about $7 \times 10^2\,\mathrm{s^{-1}}$ for mode I and $1 \times 10^3\,\mathrm{s^{-1}}$ for the mesh and TSL considered.

$$G_{jC}\left(\dot{\varepsilon}_j\right) = \begin{cases} G_{jC,QS} & \text{if } \dot{\varepsilon}_j \leq \dot{\varepsilon}_{j,ref} \\ G_{jC,QS}\left(1 + C_j \ln\left(\dfrac{\dot{\varepsilon}_j}{\dot{\varepsilon}_{j,ref}}\right)\right) & \text{if } \dot{\varepsilon}_{j,ref} < \dot{\varepsilon}_j < \dot{\varepsilon}_{j,max} \\ G_{jC,QS}\left(1 + C_j \ln\left(\dfrac{\dot{\varepsilon}_{j,max}}{\dot{\varepsilon}_{j,ref}}\right)\right) & \text{if } \dot{\varepsilon}_j \geq \dot{\varepsilon}_{j,max} \end{cases} \tag{4.22}$$

1. The fracture toughnesses determined for the $7\,\mathrm{m\,s^{-1}}$ loading speed are equal to the values identified at $2\,\mathrm{m\,s^{-1}}$. Therefore, the functions are supposed to be constant above the strain rate reached for a $2\,\mathrm{m\,s^{-1}}$ loading speed.

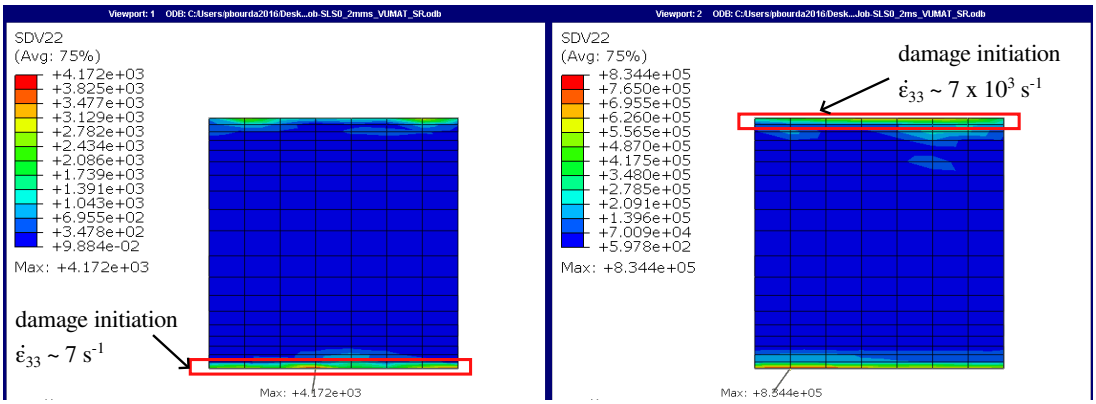

Figure 4.51 – Normalised strain rate field in normal opening - $2\,\mathrm{mm\,s^{-1}}$ and $2\,\mathrm{m\,s^{-1}}$

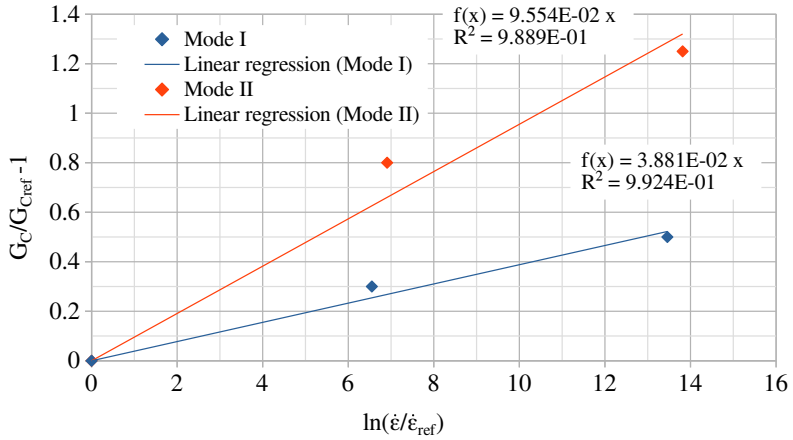

Figure 4.52 – Evolution of the fracture toughnesses versus strain rate for the SLJ $[0/45]_S/[0/45]_S$ TSL

Validation of the strain rate dependent TSL

Simulations were run for the five loading speeds studied experimentally (QS, $2\,\mathrm{m\,s^{-1}}$ [2], $200\,\mathrm{mm\,s^{-1}}$, $2\,\mathrm{m\,s^{-1}}$ and $7\,\mathrm{m\,s^{-1}}$) using the strain rate dependent TSL with the parameters defined in Table 4.8. The results obtained in terms of specimens' performance agree with the performances experimentally obtained (Figure 4.53). The increase in LSS from QS to $7\,\mathrm{m\,s^{-1}}$ loading speed is consistent with the experimental observation. In addition, the value reached numerically for $200\,\mathrm{mm\,s^{-1}}$ is well fitting the LSS increase with the rise in loading speed contrary to the experimental observation due to a lower adhesion for these specimens. A relative difference of maximum $3.06\,\%$ is noticed on the LSS numerical evaluation compared to experimental data (except for the $200\,\mathrm{mm\,s^{-1}}$).

E (Pa)	G (Pa)	$\sigma^0_{I,QS}$ (Pa)	$\sigma^0_{II,QS}$ (Pa)	$G_{IC,QS}$ ($\mathrm{J\,m^{-2}}$)	$G_{IIC,QS}$ ($\mathrm{J\,m^{-2}}$)	η	
3.9×10^9	1×10^9	1.4×10^7	3.2×10^7	2000	2000	2.284	
b_I	b_{II}	C_I	C_{II}	$\dot{\varepsilon}_{I,ref}$ ($\mathrm{s^{-1}}$)	$\dot{\varepsilon}_{II,ref}$ ($\mathrm{s^{-1}}$)	$\dot{\varepsilon}_{I,max}$ ($\mathrm{s^{-1}}$)	$\dot{\varepsilon}_{I,max}$ ($\mathrm{s^{-1}}$)
0	0	3.88×10^{-2}	9.55×10^{-2}	1×10^{-3}	1×10^{-3}	700	1000

Table 4.8 – VUMAT parameters for strain rate dependent TSL

2. The simulation of the $2\,\mathrm{mm\,s^{-1}}$ tensile test was not conducted by considering the actual test time evolution because of the calculation duration using Abaqus/Explicit solver. The time was multiplied by 1×10^3 as for QS simulations, and the fracture toughnesses are estimated from the strain rate in the cohesive elements and the viscous functions.

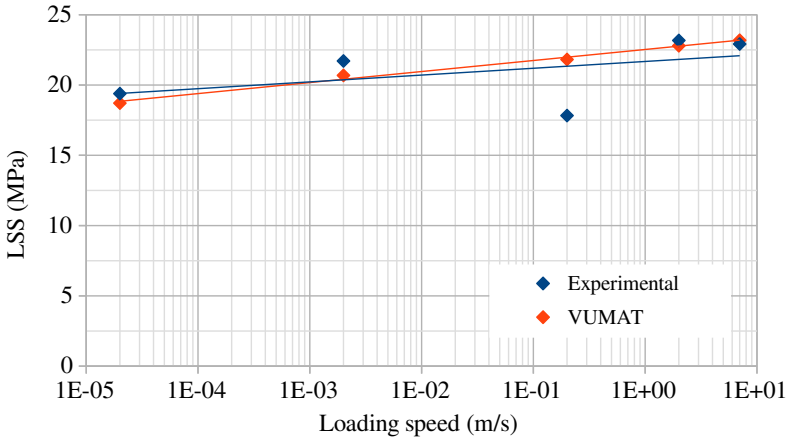

Figure 4.53 – Experimental and numerical LSS for five loading speeds from QS to $7\,\mathrm{m\,s^{-1}}$ - SLJ $[0/45]_S/[0/45]_S$

Conclusions on the SLJ $[0/45]_S/[0/45]_S$ TSL identification

The numerical results highlight a strengthening of the SLJ $[0/45]_S/[0/45]_S$ at higher loading speeds considering strain rate dependence in the substrates (in shear) and in the weld (Figure 4.54). This section exposed the need to define strain rate dependent TSL parameters to closely match the experimental results for the $0°/0°$ weld (Table 4.6). This inclusion was successfully validated by defining viscous functions. The maximum longitudinal damage in the substrates increases when considering the TSL viscosity, which is similar to the observations made for $0°/45°$ weld. Moreover, the stress fields in the weld show that the increase in shear mode fracture toughnesses allows higher stresses to be achieved in the weld, for similar damage levels, which contributes to the LSS increase. Finally, acceptable TSL parameters' set was found to describe the specimen's behaviour for all the loading speeds tested with an error on the LSS lower than $10\,\%$, which is reasonable (Table 4.7). Nevertheless, strain rate dependent TSL parameters are required to reduce the maximum relative error below $5\,\%$.

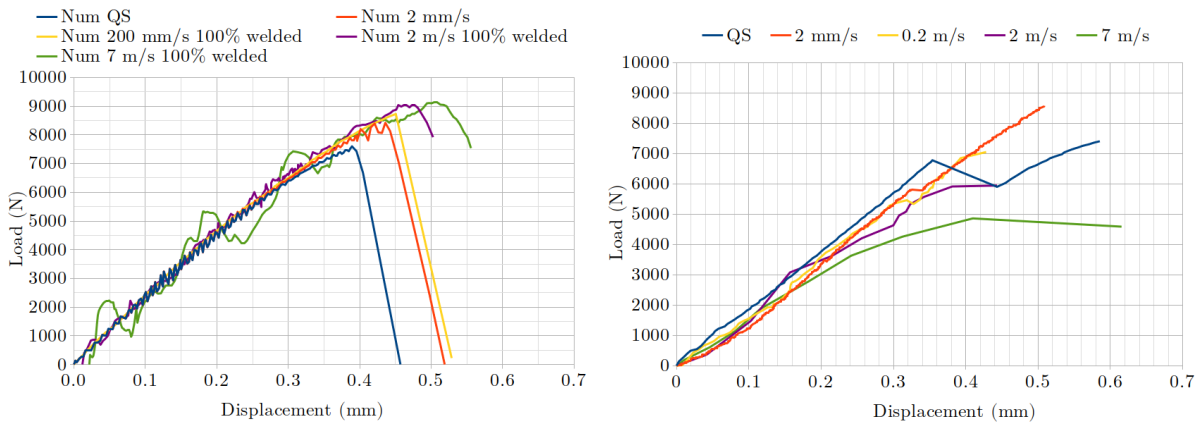

(a) Numerical

(b) Experimental - partially welded overlap for $2\,\mathrm{m\,s^{-1}}$ and $7\,\mathrm{m\,s^{-1}}$ tests

Figure 4.54 – FU curves - SLJ $[0/45]_S/[0/45]_S$

4.3.4 Conclusions on the identification of the traction-separation law parameters

A bilinear TSL defined and implemented in a VUMAT was used to model the behaviour of US welded joints. The parameters were identified using an inverse method by assuming that the substrate's behaviour is well-known and controlled, as well as the boundary conditions. Different TSL parameter sets were identified for each SLJ configuration. As the substrate stiffness increases, smaller shear fracture toughnesses have been determined. For the configurations SLJ $[45]_4/[45]_4$ and $[45]_4/[0/45]_S$, the TSL

parameters do not evolve depending on the loading speed considered. The stiffening and strengthening observed experimentally are reproduced considering the strain rate sensitivity of the GF/PA66 elementary ply shear behaviour. Concerning the configuration $[0/45]_S/[0/45]_S$, the TLS parameters are evolving with the loading speed to reach the experimental performances. An increase in fracture toughnesses with the strain rate enables a suitable reproducibility of the results obtained for dynamic loadings. The definition of viscous functions to describe the evolution of the fracture toughnesses with strain rate was successfully implemented in a VUMAT subroutine for the TSL. The natural logarithm evolution defined for the data evolution appears to be well suited to constitute the strain rate dependence of the SLJ $[0/45]_S/[0/45]_S$ weld fracture toughnesses. This model should be extended considering the influence of the transient change in strain rate on the TSL up to fracture.

Finally, the fracture toughness identified for the three SLJ configurations is different, while only the substrates' stacking sequence varies between the configuration. These differences may be caused by the local orientation of the plies above and below the weld. On the one hand, the weld configurations 45°/45° and 0°/45 do not require a strain rate dependent model for the SLS test. For these configurations, irreversible strains and damage in the substrates concentrates at the overlap edges and the specimen's fillets. The viscosity in shear provided by the 45°-oriented ply is sufficient to describe the SLJ specimen's strain rate dependence. The weld's small thickness compared to one ply and the difference in stiffness between the weld and the ply is negligible. Both elements may lead to an implicit consideration of the weld's strain rate dependence through the substrate behaviour. On the other hand, the weld configuration 0°/0° needs a strain rate dependent model. This phenomenon may be caused by the difference in stiffness between the weld and 0°-oriented ply. In this configuration, the plies have a strain rate independent tensile behaviour, which reinforces the need to model the weld's matrix strain rate dependent behaviour.

4.4 Model application to DLJ specimens

The DLS test was simulated using the TSL parameter identified from the SLS tests. The specimen modelling is similar to the SLS test with one layer of cohesive elements for each weld, joined using a "*tie*" constraint to both surrounding substrates (Figure 4.55). The boundary conditions are extracted from experiments. First, the simulation was performed for the DLJ $[0/45]_S/[0/45]_S/[0/45]_S$ by disabling the substrate fracture in the material model. Then, the stresses and damage in the substrate are analysed to determine if the fracture should occur in the substrates or the welded joints.

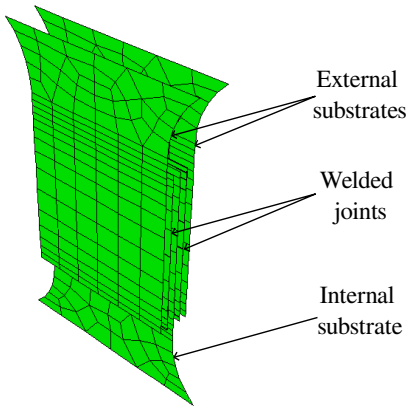

Figure 4.55 – Model for DLS test

4.4.1 DLJ $[0/45]_S/[0/45]_S/[0/45]_S$

The results obtained for DLJ $[0/45]_S/[0/45]_S/[0/45]_S$ specimens show good agreement on the structure stiffness between experimental and numerical results for QS and $2\,\mathrm{m\,s^{-1}}$ loading speeds (Figu-

re 4.56). Differences occur in the fracture load due to the lower performance of the welds observed for DLJ specimens compared to SLJ specimens (Subsection 3.3.3.2). The maximum load reached numerically for the $2\,\mathrm{m\,s^{-1}}$ cannot be reached because the ruin of the internal substrate would occur before the total damage of both welded surfaces, as indicated by the vertical line (Figure 4.56). At that displacement, the damage and longitudinal stress in the substrate coincide with the laminate fracture level. This phenomenon was observed for US welding processing parameter specimens. The concentration of stresses in the internal substrate leads to its fracture before the welds' fracture (Figure 4.57). Therefore, this type of specimen should be studied using a double-thickness laminate (here $4\,\mathrm{mm}$ instead of $2\,\mathrm{mm}$) for the internal substrate to reduce the stress concentration in this part.

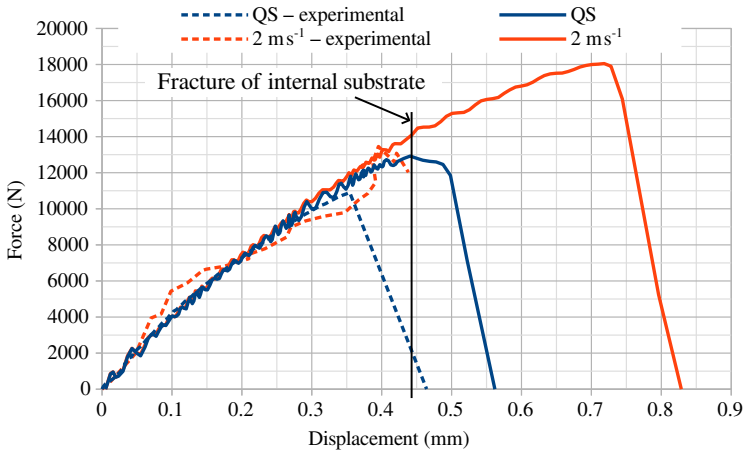

Figure 4.56 – Experimental and numerical FU curves for DLJ $[0/45]_S/[0/45]_S/[0/45]_S$ specimens - QS and $2\,\mathrm{m\,s^{-1}}$ loadings

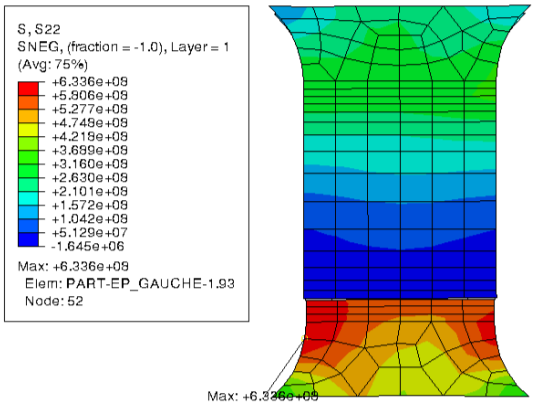

Figure 4.57 – Longitudinal stress field in DLJ $[0/45]_S/[0/45]_S/[0/45]_S$ specimens before interface fracture - $2\,\mathrm{m\,s^{-1}}$

4.4.2 DLJ $[45]_4/[45]_4/[45]_4$

Concerning the DLJ $[45]_4/[45]_4/[45]_4$, difficulties have been encountered in the specimen's modelling because no specimen broke with a significant welded area for both interfaces. Nevertheless, simulations were performed considering boundary conditions from the last breaking interface side.

The increase in damage in the internal substrate leads to a decrease in the load after a displacement of $0.7\,\mathrm{mm}$ and before the total fracture of the welds (Figure 4.58). Ultimate fracture of $8791\,\mathrm{N}$ in QS and $11\,481\,\mathrm{N}$ for $2\,\mathrm{m\,s^{-1}}$ loading speed were achieved, while $13\,448\,\mathrm{N}$ and $14\,954\,\mathrm{N}$ should have been reached according to the SLJ performance for QS and $2\,\mathrm{m\,s^{-1}}$ loading speed. However, the initial stiffness of the specimens is reproduced numerically. Welds fracture cannot be attained due to the simple-thickness internal substrate, which concentrates most of the stresses and leads to the specimens' softening until fracture in the substrates and the welds (Figure 4.59), or the weld's properties must be deteriorated.

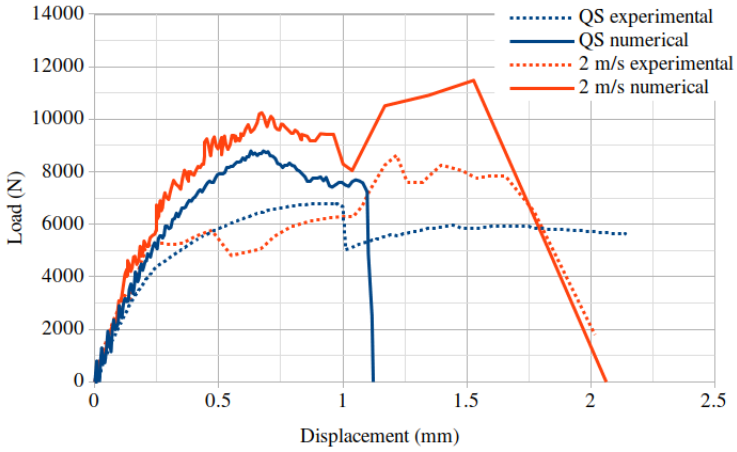

Figure 4.58 – Experimental and numerical FU curves for DLJ $[45]_4/[45]_4/[45]_4$ specimens - QS and $2\,\mathrm{m\,s^{-1}}$ loadings

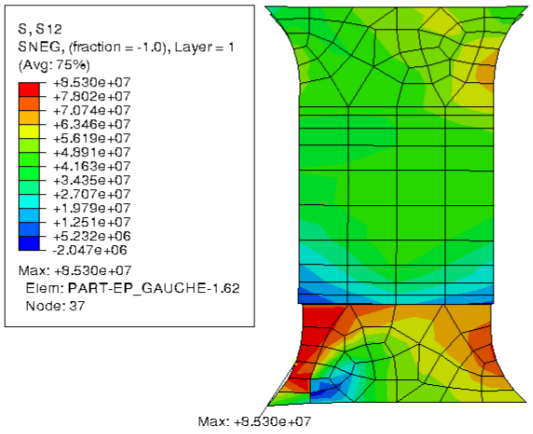

Figure 4.59 – Longitudinal stress field in DLJ $[45]_4/[45]_4/[45]_4$ specimens before interface fracture - $2\,\mathrm{m\,s^{-1}}$

4.4.3 Conclusions on the DLS test modelling

Using the TSL identified from the SLS tests highlights the need for a double-thickness internal substrate. The stresses are concentrated in this substrate, which leads to the substrate fracture instead of the welds fracture. Further simulations should be performed considering a thicker internal substrate (double the number of plies in the substrate, for example) to force the welds' fracture. Finally, these tests could have improved the validation of the TSL parameters identified with a quasi-pure mode II test. As a perspective, experimental tests should be performed on DLJ specimens with a double-thickness internal substrate to validate the mode II parameter. Tests could also be done on well-suited specimens for mode I loading characterisation, such as the cross-tensile tests (Goto et al., 2019). The testing rig should be adapted for dynamic loadings, and the measuring system must be suitably defined to control the boundary conditions for the modelling part.

4.5 Conclusions on the modelling of welded composite behaviour

The modelling of TP composite weld behaviour was presented in this chapter based on the use of a cohesive zone model. Acceptable outcomes were obtained from quasi-static to dynamic loads. The identification of appropriate parameters for the traction-separation law was successfully achieved using an inverse method for the three configurations tested. The results are similar for the configurations $[45]_4/[45]_4$ (45°/45° weld) and $[45]_4/[0/45]_S$ (45°/0° weld) with a lower mode II/mode III fracture toughness for the mixed substrates weld. The numerical results obtained without viscous functions in the TSL fit the experiments: the stiffening highlighted by the FU curves is suitably reproduced numerically, as well as

the increase in strength. The strain rate sensitivity implemented in the substrate constitutive model, according to the experimental behaviour of the elementary ply (Chapter 2), is required to describe the strain rate sensitivity of the welded structure. In addition, the definition of the irreversible phenomenon in the composite, in particular with shear damage, allowed the experimental results to be matched as closely as possible.

The last configuration, SLJ $[0/45]_S/[0/45]_S$ ($0°/0°$ weld), stands out from the other two because the TSL parameters identified for quasi-static loading lead to underestimated performances of the specimen for dynamic loadings. Therefore, strain rate sensitivity of the TSL is required in addition to the strain rate dependence of the substrate shear behaviour. The increase of mode I and mode II/mode III fracture toughnesses for higher strain rates is required to reach the experimental LSS. The integration of the strain rate dependence in the TSL using viscous functions showed appropriate results, in agreement with the experiments.

The analysis of several quantities in the substrate and the weld (damage, strains, strain rates) shows that consistency is obtained in the weld's matrix behaviour by the addition of strain rate dependence in the weld's behaviour only for the configuration $[0/45]_S/[0/45]_S$. In addition, this analysis emphasises the significance of damage and irreversible strains in the substrate on the fracture of the welded structure. Finally, the gap in stiffness between a $45°$-oriented ply and the weld's matrix is negligible, and the weld is 21 times thinner than a ply. Therefore, it is assumed that the weld strain rate dependent behaviour is absorbed by the substrates, for the $45°/45°$ and $0°/45°$ welds. However, it is no longer valid for the $0°/0°$ weld, for which the weld's strain rate dependence must be modelled.

The DLS tests should be performed with a double-thick internal specimen to concentrate stresses in the welded interface and thus to observe an FMD/cohesive fracture. Despite the impossibility of using these experimental results to identify the weld's shear behaviour, the inverse method applied to the SLS test gave appropriate results concerning the initial stiffness. In prospect, performing pure mode tests would be helpful to reinforce the phenomenon observed in this study and also to improve understanding of the difference between the several interfaces studied ($45°/45°$, $0°/45°$ and $0°/0°$).

CONCLUSIONS AND PERSPECTIVES

General conclusions

Despite the extensive research about thermoplastic composite welding, its potential application to structures in the transport industry still requires knowledge and control of the joined structures' behaviour to ensure structural integrity. In addition, structural parts can be subjected to dynamic, crash or impact loadings; several thermoplastic matrices are known as strain rate dependent, as well as interfaces such as inter-ply zones (delamination) or adhesive behaviour. Therefore, the welded composites' dynamic behaviour must be known to determine to what extent the strain rate affects the welded joint behaviour. In addition, modelling the weld's behaviour can be used to predict the behaviour of welded structures under quasi-static or dynamic loadings. In this context, this PhD thesis aims to:

1. Study the behaviour of welded structures.
2. Identify the influence of the strain rate on the welded joint behaviour.
3. Define a numerical model for the weld validated from quasi-static to dynamic loadings.

These investigations required the characterisation of welded specimens on a wide range of loading speeds. The difficulties arising from quantities measurements in the welded joints have led to the study of elementary structures. Single and double lap shear tests were performed to provide a relatively simple implementation for dynamic testing. The test results allow concluding of the strain rate dependence of welded composites. However, the substrates and weld's behaviours cannot be easily separated from the experimental results on elementary structures. Therefore, the substrates' and weld's behaviour are separated numerically. To this end, the substrates' behaviour is first identified from conventional tests on composite materials for several strain rates. These results allow the definition and identification of a constitutive model for the composite. Then, the weld's behaviour can be identified using an inverse analysis on the lap shear tests and considering the well-known substrates' constitutive model. Identification and validation of the weld's constitutive model for the dynamic tests indicate whether or not a strain-rate dependent model is required. In case the strain rate dependence is needed, then the parameters identification allows defining the time dependence required in the model.

The behaviour of GF/PA66 has been characterised for a range of strain rates, temperatures and relative humidities. These results from the COPERSIM-Crash project showed the negligible influence of these three parameters on the longitudinal behaviour due to the limited sensitivity of glass fibres' behaviour. They also highlighted a shear behaviour dependent on strain rate and environmental conditions. Tensile tests conducted at room temperature and dry state in the present work (due to potential chemical ageing) confirmed the viscous shear behaviour of GF/PA66 inherited from the matrix. The elasto-plastic-damage viscous behaviour was identified up to $250\,\mathrm{s}^{-1}$ and used in the constitutive model developed for this composite (Mbacké & Rozycki, 2018). Concerning the longitudinal behaviour, an elastic-fragile-damage behaviour was identified and used in the constitutive model to describe accurately the actual substrates' stiffness, which affects the lap joint specimens' behaviour. Comparisons of numerical and experimental behaviour on the relative volume elementary demonstrate the model's accuracy.

The welded structures have been characterised using single and double lap joint specimens in light of the well-known behaviour of GF/PA66. Three SLJs ($[45]_4/[45]_4$, $[0/45]_S/[0/45]_S$ and $[45]_4/[0/45]_S$) and two DLJs ($[45]_4/[45]_4/[45]_4$ and $[0/45]_S/[0/45]_S/[0/45]_S$) configurations were tested at room temperature and in a dry state for five loading speeds: from $1.2\,\mathrm{mm\,min^{-1}}$ to $7\,\mathrm{m\,s^{-1}}$. Significant results arise from these characterisation tests and contribute to a better understanding of the welded structures' behaviour.

— The welded structure shear performance (LSS) increases at higher loading speeds for the three single lap joint configurations tested.
— A stiffening of structures composed of at least one $[45]_4$ substrate was observed.
— The welded structures' performance is related to the substrates' stiffness, with a higher shear stress for stiffer substrates, and a more significant rise in performance as the strain rate increases.
— Fractography analysis highlighted that the fibre/matrix debonding associated with matrix fracture is obtained for high levels of adhesion in the weld.

The loading speed dependence of welded GF/PA66 is caused by the viscosity of PA66 and PA6 matrices affecting the substrates' and weld's behaviour (stiffening, strengthening and increase in interfacial strength). The laminate ductility and strain rate dependence in shear significantly affect the welded structure's behaviour. All these elements emphasise the significance of the matrix behaviour and the adhesion between fibre and matrix on the performance of welded joints. Experimental observations are an important step for understanding welded composites' dynamic behaviour. The strain rate influence observed comes from both the behaviour of the substrates and the weld; however, the weight of each influence on the overall behaviour is not experimentally quantifiable.

A strain rate dependent traction-separation law was implemented in a VUMAT subroutine to model the weld using a cohesive zone model. Numerical modelling of the welds was achieved using an inverse method to determine the model's parameters ($45°/45°$ weld for SLJ $[45]_4/[45]_4$, $0°/0°$ for SLJ $[0/45]_S/[0/45]_S$ and $45°/0°$ for SLJ $[45]_4/[0/45]_S$). Results highlight the need to consider the elasto-plastic-damage viscous shear constitutive model for GF/PA66, which describes by itself the strain rate dependent behaviour of SLJs $[45]_4/[45]_4$ and $[45]_4/[0/45]_S$. Therefore, no strain rate sensitivity is required in the traction-separation laws of $45°/45°$ and $45°/0°$ welds. Concerning the third configuration ($0°/0°$ weld - SLJ $[0/45]_S/[0/45]_S$), a strain rate dependent traction-separation law is needed to precisely describe the specimen's quasi-static and dynamic behaviours. Viscous functions successfully describe the fracture toughnesses evolution. The strain rate sensitivity of only one weld among the three configurations tested may be explained by the thickness of the welds, significantly smaller than a ply, and the difference in stiffness between the weld and its surrounding plies. Indeed, welds with equivalent stiffness to one or both the surrounding plies do not need a time-dependent model. Due to the thinness of the weld, the weld's matrix viscosity seems to be implicitly accounted for by the shear viscosity of the GF/PA66 constitutive model. Nevertheless, the stiffness jump in the interface of the $0°/0°$ weld, combined with the non-viscous longitudinal behaviour of GF/PA66 and the weld's matrix viscous behaviour, seems to force the addition of time-dependence in the weld's traction-separation law.

Perspectives of the study

This study's results constitute an insight into the dynamic behaviour of welded thermoplastic structures. The results presented are useful in developing the welding process for structural parts in the transport industry. Nevertheless, several elements should be studied to improve the global knowledge about composite welds' behaviour.

The tensile tests employed in this work are not pure mode testing, which led to the identification of several parameters (damage initiations stresses and fracture toughnesses for two modes) from only one type of test. Additional tests on a second geometry, as double lap shear tests were aimed for, should be implemented to improve the parameters identification by studying one pure mode at a time, then mixed mode. Pure mode I tests could be conducted on cross-tensile tests as in (Goto et al., 2019) using an adapted feature for dynamic loadings or on double U specimens (Morin, 2010; Argoud et al., 2016). However, these tests might be challenging in dynamic, especially in the method used for measuring quantities and test modelling. Decoupling modes in the experiments will also be useful to improve the understanding of the strain rate dependent model needed for the $0°/0°$ weld.

One major conclusion of the work is that the TSLs for $45°/45°$ and $0°/45°$ does not need to include strain rate dependence, despite the viscosity of PA6. The major supposition explaining this phenomenon is the small thickness of the weld compared to the ply thickness, and the equivalent stiffnesses for the $45°$-oriented ply and the weld matrix. Therefore, the matrix time-dependence would presumably already be included through the substrates' shear behaviour. However, these observations are valid for the weld's thickness investigated $(2.39 \times 10^{-5}\,\mathrm{m})$, which is significantly smaller than the ply thickness $(0.50 \times 10^{-3}\,\mathrm{m})$. Investigations should be conducted with thicker welds (in the limit of the joining process definition) to determine if the strain rate independent TLS and substrates' viscous constitutive model are still sufficient to describe the SLJ specimen's behaviour. The same investigation with smaller thicknesses is also relevant, especially for the $0°/0°$ weld, to determine if the strain rate dependent TLS identified in this work would still be needed or not. Finally, both extreme thicknesses approach bonding and delamination conditions.

Composite structures facing dynamic loadings might break in the joints of structures, nevertheless, delamination is also expected in the substrates. Therefore, the addition of inter-ply fracture in the model, using cohesive elements, for example, could enable the study of a complete model for a main structure such as a skin/stringer part. Moreover, the welded joint obtained with ultrasonic welding is, to some extent, close to the mesoscopic aspect of an inter-ply zone. Hence, comparing the weld's performance with co-consolidated or double thickness homogeneous specimens is worthwhile. Results from this investigation would be decisive on the need to distinguish the modelling of delamination and weld failure.

On another side of modelling the weld's behaviour, the computing efficiency could be improved using a different element type. The cohesive zone model used in this work significantly reduces the critical time step for dynamic/explicit simulations. Their use is acceptable for characterisation specimens at a research level, but computing time would skyrocket for a simulation on an industrial structure. Therefore, including a model for the weld in another element could reduce the computing time and makes it possible to model the welded joint for an entire structure. In addition, the welding process employed may lead to some scattering in the extent of the welded surface area, which affects the structure's response. In this way, the effect of this scattering should be considered in the weld's modelling through an evolution of the model's parameters according to the extent of the weld.

The composite and matrix characterisation conducted during the COPERSIM-Crash project highlighted the more significant strain rate dependence of the PA66 behaviour and GF/PA66 shear behaviour at higher RH or temperature (Dau, 2019). In addition, a limited number of studies investigated the influence of environmental conditions on the behaviour of welded joints. Humidity negligibly affects the performance of welded PPS/CF (Rohart, 2020). However, the PPS matrix absorbs small quantities of moisture compared to polyamides. Therefore, the strain rate influence study conducted during this PhD could be performed considering higher RH (needs to validate the ageing process for welded samples) and higher temperatures. The strain-rate sensitivity of the welded structure is expected to be more

significant than the results obtained in this work. In addition, a strain rate dependent model might be required for the three welds tested ($0°/0°$, $45°/45°$ and $0°/45°$) because the strain rate dependence of PA66 and PA6 intensifies at RH $50\,\%$ and $85\,\%$ (Dau, 2019).

BIBLIOGRAPHY

Dugdale, D. S. (1960). Yielding of steel sheets containing slits. *Journal of the Mechanics and Physics of Solids*, *8*(2), 100–104. https://doi.org/10.1016/0022-5096(60)90013-2

Barenblatt, G. I. (1962). The mathematical theory of equilibrium cracks in brittle fracture. *Advances in applied mechanics*, *7*, 55–129. https://doi.org/10.1016/S0065-2156(08)70121-2

Johnson, G. R. (1983). A constitutive model and data for materials subjected to large strains, high strain rates, and high temperatures. *Proc. 7th Inf. Sympo. Ballistics*, 541–547.

Mall, S., Law, G., & Katouzian, M. (1987). Loading rate effect on interlaminar fracture toughness of a thermoplastic composite. *Journal of composite materials*, *21*(6), 569–579. https://doi.org/10.1177/002199838702100607

Smiley, A., & Pipes, R. (1987a). Rate effects on mode I interlaminar fracture toughness in composite materials. *Journal of composite materials*, *21*(7), 670–687. https://doi.org/10.1177/002199838702100706

Smiley, A., & Pipes, R. (1987b). Rate sensitivity of mode II interlaminar fracture toughness in graphite/epoxy and graphite/PEEK composite materials. *Composites science and technology*, *29*(1), 1–15. https://doi.org/10.1016/0266-3538(87)90033-9

Chang, I., & Lees, J. (1988). Recent development in thermoplastic composites: a review of matrix systems and processing methods. *Journal of thermoplastic composite materials*, *1*(3), 277–296. https://doi.org/10.1177/089270578800100305

Béguelin, P., Barbezat, M., & Kausch, H. (1991). Mechanical characterization of polymers and composites with a servohydraulic high-speed tensile tester. *Journal de Physique III*, *1*(12), 1867–1880. https://doi.org/10.1051/jp3:1991238

Madhukar, M. S., & Drzal, L. T. (1991). Fiber-matrix adhesion and its effect on composite mechanical properties: I. Inplane and interlaminar shear behavior of graphite/epoxy composites. *Journal of Composite Materials*, *25*(8), 932–957.

Ladeveze, P., & LeDantec, E. (1992). Damage modelling of the elementary ply for laminated composites. *Composites science and technology*, *43*(3), 257–267. https://doi.org/10.1016/0266-3538(92)90097-M

Yuanming, X., Yuan, J., & Yang, B. (1994). A statistical model and experimental study of the strain-rate dependence of the strength of fibres. *Composites science and technology*, *52*(4), 499–504. https://doi.org/10.1016/0266-3538(94)90032-9

Blackman, B., Dear, J., Kinloch, A., Macgillivray, H., Wang, Y., Williams, J., & Yayla, P. (1995). The failure of fibre composites and adhesively bonded fibre composites under high rates of test. *Journal of Materials Science*, *30*(23), 5885–5900. https://doi.org/10.1007/BF01151502

Gong, X.-J., & Benzeggagh, M. (1995). Mixed mode interlaminar fracture toughness of unidirectional glass/epoxy composite. *Composite Materials: Fatigue and Fracture*, *5*, 100–123.

Benzeggagh, M. L., & Kenane, M. (1996). Measurement of mixed-mode delamination fracture toughness of unidirectional glass/epoxy composites with mixed-mode bending apparatus. *Composites Science and Technology*, *56*(4), 439–449. https://doi.org/10.1016/0266-3538(96)00005-X

Harras, B., Cole, K. C., & Vu-Khanh, T. (1996). Optimization of the ultrasonic welding of PEEK-carbon composites. *Journal of reinforced plastics and composites*, *15*(2), 174–182. https://doi.org/10.1177/073168449601500203

Kusaka, T., Hojo, M., Mai, Y.-W., Kurokawa, T., Nojima, T., & Ochiai, S. (1998). Rate dependence of mode I fracture behaviour in carbon-fibre/epoxy composite laminates. *Composites Science and Technology*, *58*(3-4), 591–602. https://doi.org/10.1016/S0266-3538(97)00176-0

Wang, Z., & Xia, Y. (1998). Experimental evaluation of the strength distribution of fibers under high strain rates by bimodal Weibull distribution. *Composites science and technology*, *57*(12), 1599–1607. https://doi.org/10.1016/S0266-3538(97)00092-4

Weeks, C., & Sun, C. (1998). Modeling non-linear rate-dependent behavior in fiber-reinforced composites. *Composites Science and Technology*, *58*(3-4), 603–611. https://doi.org/10.1016/S0266-3538(97)00183-8

Deng, S., & Ye, L. (1999). Influence of fiber-matrix adhesion on mechanical properties of graphite/epoxy composites: II. Interlaminar fracture and inplane shear behavior. *Journal of Reinforced Plastics and Composites*, *18*(11), 1041–1057.

Saheb, D. N., & Jog, J. P. (1999). Natural fiber polymer composites: a review. *Advances in Polymer Technology: Journal of the Polymer Processing Institute*, *18*(4), 351–363. https://doi.org/10.1002/(SICI)1098-2329(199924)18:4<351::AID-ADV6>3.0.CO;2-X

Todo, M., Nakamura, T., & Takahashi, K. (1999). Mode II interlaminar fracture behavior of fiber reinforced polyamide composites under static and dynamic loading conditions. *Journal of reinforced plastics and composites*, *18*(15), 1415–1427. https://doi.org/10.1177/073168449901801505

Rozycki, P. (2000). *Contribution au développement de lois de comportement pour matériaux composites soumis à l'impact.* (Doctoral dissertation). Université de Valenciennes et du Hainaut-Cambrésis.

Ageorges, C., Ye, L., & Hou, M. (2001). Advances in fusion bonding techniques for joining thermoplastic matrix composites: a review. *Composites Part A: applied science and manufacturing*, *32*(6), 839–857. https://doi.org/10.1016/S1359-835X(00)00166-4

Fracasso, R., Rink, M., Pavan, A., & Frassine, R. (2001). The effects of strain-rate and temperature on the interlaminar fracture toughness of interleaved PEEK/CF composites. *Composites science and technology*, *61*(1), 57–63. https://doi.org/10.1016/S0266-3538(00)00153-6

Gleich, D., Van Tooren, M., & Beukers, A. (2001). Analysis and evaluation of bondline thickness effects on failure load in adhesively bonded structures. *Journal of adhesion science and technology*, *15*(9), 1091–1101. https://doi.org/10.1163/156856101317035503

Kawai, M., Masuko, Y., Kawase, Y., & Negishi, R. (2001). Micromechanical analysis of the off-axis rate-dependent inelastic behavior of unidirectional AS4/PEEK at high temperature. *International journal of mechanical sciences*, *43*(9), 2069–2090. https://doi.org/10.1016/S0020-7403(01)00029-7

Li, Q., Mines, R., & Birch, R. (2001). Static and dynamic behaviour of composite riveted joints in tension. *International journal of mechanical sciences*, *43*(7), 1591–1610. https://doi.org/10.1016/S0020-7403(00)00099-0

Goldberg, R. K., & Stouffer, D. C. (2002). Strain rate dependent analysis of a polymer matrix composite utilizing a micromechanics approach. *Journal of composite materials*, *36*(7), 773–793. https://doi.org/10.1177/0021998302036007613

Rozycki, P., & Coutellier, D. (2002). Sensibilité à la vitesse de déformation des matériaux composites unidirectionnels: Applications au verre E/époxy à 60% de fibres. *Revue Européenne des Éléments*, *11*(2-4), 263–276. https://doi.org/10.3166/reef.11.263-276

Cady, C., Blumenthal, W., Gray III, G., & Idar, D. (2003). Determining the constitutive response of polymeric materials as a function of temperature and strain rate, In *Journal de Physique IV (Proceedings)*. EDP sciences.

Camanho, P. P., Davila, C. G., & de Moura, M. F. (2003). Numerical Simulation of Mixed-Mode Progressive Delamination in Composite Materials. *Journal of Composite Materials*, *37*(16), 1415–1438.

Yousefpour, A., Hojjati, M., & Immarigeon, J.-P. (2004). Fusion Bonding/Welding of Thermoplastic Composites. *Journal of Thermoplastic Composite Materials*, *17*(4), 303–341.

Jacob, G. C., Starbuck, J. M., Fellers, J. F., Simunovic, S., & Boeman, R. G. (2005). The effect of loading rate on the fracture toughness of fiber reinforced polymer composites. *Journal of applied polymer science*, *96*(3), 899–904. https://doi.org/10.1002/app.21535

Partridge, I. K., & Cartié, D. D. (2005). Delamination resistant laminates by Z-Fiber® pinning: Part I manufacture and fracture performance. *Composites Part A: applied science and manufacturing*, *36*(1), 55–64. https://doi.org/10.1016/j.compositesa.2004.06.029

Stavrov, D., & Bersee, H. (2005). Resistance welding of thermoplastic composites-an overview. *Composites Part A: Applied Science and Manufacturing*, *36*(1), 39–54. https://doi.org/10.1016/j.compositesa.2004.06.030

Ahmed, T., Stavrov, D., Bersee, H., & Beukers, A. (2006). Induction welding of thermoplastic composites—an overview. *Composites Part A: Applied Science and Manufacturing*, *37*(10), 1638–1651. https://doi.org/10.1016/j.compositesa.2005.10.009

Da Silva, L. F., Rodrigues, T., Figueiredo, M., De Moura, M., & Chousal, J. (2006). Effect of adhesive type and thickness on the lap shear strength. *The journal of adhesion*, *82*(11), 1091–1115. https://doi.org/10.1080/00218460600948511

Pinho, S., Iannucci, L., & Robinson, P. (2006). Formulation and implementation of decohesion elements in an explicit finite element code. *Composites Part A: Applied science and manufacturing*, *37*(5), 778–789. https://doi.org/10.1016/j.compositesa.2005.06.007

Galliot, C., Rousseau, J., & Verchery, G. (2007). Mecanismes de rupture d'assemblages colles de composites stratifies fracture mechanisms of adhesively bonded composite laminates joints.

Jiang, W.-G., Hallett, S. R., Green, B. G., & Wisnom, M. R. (2007). A concise interface constitutive law for analysis of delamination and splitting in composite materials and its application to scaled notched tensile specimens. *International journal for numerical methods in engineering*, *69*(9), 1982–1995. https://doi.org/10.1002/nme.1842

Marguet, S. (2007). *Contribution à la modélisation du comportement mécanique des structures sandwichs soumises à l'impact* (Doctoral dissertation). Ecole Centrale de Nantes (ECN).

Shan, G.-F., Yang, W., Yang, M.-b., Xie, B.-h., Feng, J.-m., & Fu, Q. (2007a). Effect of temperature and strain rate on the tensile deformation of polyamide 6. *Polymer*, *48*(10), 2958–2968. https://doi.org/10.1016/j.polymer.2007.03.013

Shan, G.-F., Yang, W., Yang, M.-b., Xie, B.-h., Feng, J.-m., & Fu, Q. (2007b). Effect of temperature and strain rate on the tensile deformation of polyamide 6. *Polymer*, *48*(10), 2958–2968. https://doi.org/10.1016/j.polymer.2007.03.013

Adamvalli, M., & Parameswaran, V. (2008). Dynamic strength of adhesive single lap joints at high temperature. *International Journal of Adhesion and Adhesives*, *28*(6), 321–327. https://doi.org/10.1016/j.ijadhadh.2007.10.005

Brunner, A., Blackman, B., & Davies, P. (2008). A status report on delamination resistance testing of polymer–matrix composites. *Engineering Fracture Mechanics*, *75*(9), 2779–2794. https://doi.org/10.1016/j.engfracmech.2007.03.012

Marzi, S., Hesebeck, O., Brede, M., & Kleiner, F. (2009). A rate-dependent cohesive zone model for adhesively bonded joints loaded in mode I. *Journal of adhesion science and technology*, *23*(6), 881–898. https://doi.org/10.1163/156856109X411238

VIC-2D CS Software. (2009). Correlated solutions. https://www.correlatedsolutions.com/vic-2d/

Bernstein, R., & Gillen, K. (2010). Nylon 6.6 accelerating aging studies: II. Long-term thermal-oxidative and hydrolysis results. *Polymer degradation and stability*, *95*(9), 1471–1479. https://doi.org/10.1016/j.polymdegradstab.2010.06.018

Morin, D. (2010). *Experiments and models until failure of bonded joints for crashworthiness* (Doctoral dissertation). Université de Valenciennes et du Hainaut-Cambrésis.

Villegas, I. F., & Bersee, H. E. (2010). Ultrasonic welding of advanced thermoplastic composites: An investigation on energy-directing surfaces. *Advances in Polymer Technology*, *29*(2), 112–121. https://doi.org/10.1002/adv.20178

Zhou, Y., Wang, Y., Xia, Y., & Jeelani, S. (2010). Tensile behavior of carbon fiber bundles at different strain rates. *Materials Letters*, *64*(3), 246–248. https://doi.org/10.1016/j.matlet.2009.10.045

Castagnetti, D., Spaggiari, A., & Dragoni, E. (2011). Effect of bondline thickness on the static strength of structural adhesives under nearly-homogeneous shear stresses. *The Journal of Adhesion*, *87*(7-8), 780–803. https://doi.org/10.1080/00218464.2011.597309

Challita, G., Othman, R., Casari, P., & Khalil, K. (2011). Experimental investigation of the shear dynamic behavior of double-lap adhesively bonded joints on a wide range of strain rates. *International Journal of Adhesion and Adhesives*, *31*(3), 146–153. https://doi.org/10.1016/j.ijadhadh.2010.11.014

Arao, Y., Taniguchi, N., Nishiwaki, T., Hirayama, N., & Kawada, H. (2012). Strain-rate dependence of the tensile strength of glass fibers. *Journal of Materials Science*, *47*(12), 4895–4903. https://doi.org/10.1007/s10853-012-6360-z

Blackman, B., Kinloch, A., Rodriguez-Sanchez, F., & Teo, W. (2012). The fracture behaviour of adhesively-bonded composite joints: Effects of rate of test and mode of loading. *International Journal of Solids and Structures*, *49*(13), 1434–1452. https://doi.org/10.1016/j.ijsolstr.2012.02.022

de Verdiere, M. C., Skordos, A., May, M., & Walton, A. (2012). Influence of loading rate on the delamination response of untufted and tufted carbon epoxy non crimp fabric composites: Mode I. *Engineering Fracture Mechanics*, *96*, 11–25. https://doi.org/10.1016/j.engfracmech.2012.05.015

de Verdiere, M. C., Skordos, A., Walton, A., & May, M. (2012). Influence of loading rate on the delamination response of untufted and tufted carbon epoxy non-crimp fabric composites/Mode II. *Engineering Fracture Mechanics*, *96*, 1–10. https://doi.org/10.1016/j.engfracmech.2011.12.011

Di Franco, G., Fratini, L., & Pasta, A. (2012). Influence of the distance between rivets in self-piercing riveting bonded joints made of carbon fiber panels and AA2024 blanks. *Materials & Design*, *35*, 342–349. https://doi.org/10.1016/j.matdes.2011.09.036

Galliot, C., Rousseau, J., & Verchery, G. (2012). Drop weight tensile impact testing of adhesively bonded carbon/epoxy laminate joints. *International Journal of Adhesion and Adhesives*, *35*, 68–75. https://doi.org/10.1016/j.ijadhadh.2012.02.002

Schneider, C. A., Rasband, W. S., & Eliceiri, K. W. (2012). NIH Image to ImageJ: 25 years of image analysis. *Nature methods*, *9*(7), 671–675.

Taniguchi, N., Arao, Y., Nishiwaki, T., Hirayama, N., Nakamura, K., & Kawada, H. (2012). Experimental study on impact tensile property of glass fiber. *Advanced Composite Materials*, *21*(2), 165–175. https://doi.org/10.1080/09243046.2012.688496

Vieille, B., Aucher, J., & Taleb, L. (2012). Comparative study on the behavior of woven-ply reinforced thermoplastic or thermosetting laminates under severe environmental conditions. *Materials & Design*, *35*, 707–719. https://doi.org/10.1016/j.matdes.2011.10.037

ASTM. (2013). ASTM D5528–13. *Standard test method for mode I interlaminar fracture toughness of unidirectional fiber-reinforced polymer matrix composites*.

Berthe, J. (2013). *Comportement thermo-visco-élastique des composites CMO–De la statique à la dynamique grande vitesse* (Doctoral dissertation). Ecole centrale de Lille.

Campilho, R. D., Banea, M. D., Neto, J., & da Silva, L. F. (2013). Modelling adhesive joints with cohesive zone models: effect of the cohesive law shape of the adhesive layer. *International journal of adhesion and adhesives*, *44*, 48–56. https://doi.org/10.1016/j.ijadhadh.2013.02.006

Govender, R., Langdon, G., Nurick, G., & Cloete, T. (2013). Impact delamination testing of fibre reinforced polymers using Hopkinson pressure bars. *Engineering Fracture Mechanics*, *101*, 80–90. https://doi.org/10.1016/j.engfracmech.2012.07.025

Heimbs, S., Schmeer, S., Blaurock, J., & Steeger, S. (2013). Static and dynamic failure behaviour of bolted joints in carbon fibre composites. *Composites Part A: Applied Science and Manufacturing*, *47*, 91–101. https://doi.org/10.1016/j.compositesa.2012.12.003

Musto, M., & Alfano, G. (2013). A novel rate-dependent cohesive-zone model combining damage and visco-elasticity. *Computers & Structures*, *118*, 126–133. https://doi.org/10.1016/j.compstruc.2012.12.020

Shi, H., Fernandez Villegas, I., & Bersee, H. (2013). Strength and failure modes in resistance welded thermoplastic composite joints: Effect of fibre–matrix adhesion and fibre orientation. *Composites Part A: Applied Science and Manufacturing*, *55*, 1–10. https://doi.org/10.1016/j.compositesa.2013.08.008

Silva, L., Tognana, S., & Salgueiro, W. (2013). Study of the water absorption and its influence on the Young's modulus in a commercial polyamide. *Polymer Testing*, *32*(1), 158–164. https://doi.org/10.1016/j.polymertesting.2012.10.003

Vieille, B., Casado, V. M., & Bouvet, C. (2013). About the impact behavior of woven-ply carbon fiber-reinforced thermoplastic-and thermosetting-composites: a comparative study. *Composite structures*, *101*, 9–21. https://doi.org/10.1016/j.compstruct.2013.01.025

Wu, W., Liu, Q., Zong, Z., Sun, G., & Li, Q. (2013). Experimental investigation into transverse crashworthiness of CFRP adhesively bonded joints in vehicle structure. *Composite Structures*, *106*, 581–589. https://doi.org/10.1016/j.compstruct.2013.07.009

ASTM. (2014a). ASTM D6671/D6671M–13. *Standard Test Method for Mixed Mode I-Mode II Interlaminar Fracture Toughness of Unidirectional Fiber Reinforced Polymer Matrix Composites*.

ASTM. (2014b). ASTM D7905/D7905M–14. *Standard Test Method for Determination of the Mode II Interlaminar Fracture Toughness of Unidirectional Fiber-Reinforced Polymer Matrix Composites*.

Esmaeili, F., Chakherlou, T., & Zehsaz, M. (2014). Prediction of fatigue life in aircraft double lap bolted joints using several multiaxial fatigue criteria. *Materials & Design*, *59*, 430–438. https://doi.org/10.1016/j.matdes.2014.03.019

Fernandez Villegas, I. (2014). Strength development versus process data in ultrasonic welding of thermoplastic composites with flat energy directors and its application to the definition of optimum processing parameters. *Composites Part A: Applied Science and Manufacturing*, *65*, 27–37. https://doi.org/10.1016/j.compositesa.2014.05.019

Levy, A., Le Corre, S., & Fernandez Villegas, I. (2014). Modeling of the heating phenomena in ultrasonic welding of thermoplastic composites with flat energy directors. *Journal of Materials Processing Technology*, *214*(7), 1361–1371. https://doi.org/10.1016/j.jmatprotec.2014.02.009

May, M., Voß, H., & Hiermaier, S. (2014). Predictive modeling of damage and failure in adhesively bonded metallic joints using cohesive interface elements. *International Journal of Adhesion and Adhesives*, *49*, 7–17. https://doi.org/10.1016/j.ijadhadh.2013.12.001

Banea, M. D., da Silva, L. F. M., & Campilho, R. D. (2015). The effect of adhesive thickness on the mechanical behavior of a structural polyurethane adhesive. *The Journal of Adhesion*, *91*(5), 331–346. https://doi.org/10.1080/00218464.2014.903802

Fernandez Villegas, I., Valle Grande, B., Bersee, H., & Benedictus, R. (2015). A comparative evaluation between flat and traditional energy directors for ultrasonic welding of CF/PPS thermoplastic composites. *Composite Interfaces*, *22*(8), 717–729. https://doi.org/10.1080/09276440.2015.1053753

Garcia-Gonzalez, D., Rusinek, A., Jankowiak, T., & Arias, A. (2015). Mechanical impact behavior of polyether–ether–ketone (PEEK). *Composite Structures*, *124*, 88–99. https://doi.org/10.1016/j.compstruct.2014.12.061

May, M. (2015). Numerical evaluation of cohesive zone models for modeling impact induced delamination in composite materials. *Composite Structures*, *133*, 16–21. https://doi.org/10.1016/j.compstruct.2015.07.032

May, M., Hesebeck, O., Marzi, S., Böhme, W., Lienhard, J., Kilchert, S., Brede, M., & Hiermaier, S. (2015). Rate dependent behavior of crash-optimized adhesives–Experimental characterization, model development, and simulation. *Engineering Fracture Mechanics*, *133*, 112–137. https://doi.org/10.1016/j.engfracmech.2014.11.006

Villegas, I. F., & Rubio, P. V. (2015). On avoiding thermal degradation during welding of high-performance thermoplastic composites to thermoset composites. *Composites Part A: Applied Science and Manufacturing*, *77*, 172–180. https://doi.org/10.1016/j.compositesa.2015.07.002

Zabala, H., Aretxabaleta, L., Castillo, G., & Aurrekoetxea, J. (2015). Loading rate dependency on mode I interlaminar fracture toughness of unidirectional and woven carbon fibre epoxy composites. *Composite Structures*, *121*, 75–82. https://doi.org/10.1016/j.compstruct.2014.11.001

Argoud, N., Rousseau, J., Piezel, B., Fiore, A., & Fontaine, S. (2016). Méthode d'essais multiaxiaux pour des assemblages composites thermoplastiques collés. *Matériaux & Techniques*, *104*(4), 402. https://doi.org/10.1051/mattech/2016030

Avendaño, R., Carbas, R., Marques, E., Da Silva, L., & Fernandes, A. (2016). Effect of temperature and strain rate on single lap joints with dissimilar lightweight adherends bonded with an acrylic adhesive. *Composite Structures*, *152*, 34–44. https://doi.org/10.1016/j.compstruct.2016.05.034

Frihi, D., Layachi, A., Gherib, S., Stoclet, G., Masenelli-Varlot, K., Satha, H., & Seguela, R. (2016). Crystallization of glass-fiber-reinforced polyamide 66 composites: Influence of glass-fiber content and cooling rate. *Composites Science and Technology*, *130*, 70–77. https://doi.org/10.1016/j.compscitech.2016.05.007

Gouin O'Shaughnessey, P., Dube, M., & Fernandez Villegas, I. (2016). Modeling and experimental investigation of induction welding of thermoplastic composites and comparison with other welding processes. *Journal of Composite Materials*, *50*(21), 2895–2910. https://doi.org/10.1177/0021998315614991

Ma, Y., Yang, Y., Sugahara, T., & Hamada, H. (2016). A study on the failure behavior and mechanical properties of unidirectional fiber reinforced thermosetting and thermoplastic composites. *Composites Part B: Engineering*, *99*, 162–172. https://doi.org/10.1016/j.compositesb.2016.06.005

May, M. (2016). Measuring the rate-dependent mode I fracture toughness of composites–A review. *Composites Part A: Applied Science and Manufacturing*, *81*, 1–12. https://doi.org/10.1016/j.compositesa.2015.10.033

Obeid, H. (2016). *Durabilité de composites à matrice thermoplastique sous chargement hygro-mécanique: étude multi-physique et multi-échelle des relations microstructure-propriétés-états mécaniques* (Doctoral dissertation). Nantes.

Paroissien, S. (2016). *Simulation numérique d'un assemblage métal/composite thermoplastique par CMT pins* (Doctoral dissertation). École centrale de Nantes.

Senders, F., van Beurden, M., Palardy, G., & Villegas, I. F. (2016). Zero-flow: A novel approach to continuous ultrasonic welding of CF/PPS thermoplastic composite plates. *Advanced Manufacturing: Polymer & Composites Science*, *2*(3-4), 83–92. https://doi.org/10.1080/20550340.2016.1253968

Coussa, F. (2017). *Du comportement dynamique de matériaux composites tissés à matrice polyamide* (Doctoral dissertation). Université Paris sciences et lettres.

Coussa, F., Renard, J., Joannes, S., Teissedre, J.-C., Bompoint, R., & Feld, N. (2017). A consistent experimental protocol for the strain rate characterization of thermoplastic fabrics. *Strain*, *53*(3), e12220. https://doi.org/10.1111/str.12220

Coussa, F., Renard, J., Joannès, S., Bompoint, R., & Feld, N. (2017). Influence de la vitesse sur le comportement mécanique de composites tissés à matrice thermoplastique, In *JNC 20-20èmes Journées Nationales sur les Composites*.

Dufour, L. (2017). *Caractérisation et modélisation du collage structural multi-matériaux sous sollicitation dynamique* (Doctoral dissertation). Université de Valenciennes et du Hainaut-Cambresis.

Fernandez Villegas, I., & Palardy, G. (2017). Ultrasonic welding of CF/PPS composites with integrated triangular energy directors: melting, flow and weld strength development. *Composite Interfaces*, *24*(5), 515–528. https://doi.org/10.1080/09276440.2017.1236626

Machado, J., Marques, E., Campilho, R., & da Silva, L. F. (2017). Mode II fracture toughness of CFRP as a function of temperature and strain rate. *Composites Part B: Engineering*, *114*, 311–318. https://doi.org/10.1016/j.compositesb.2017.02.013

May, M., & Lässig, T. (2017). Rate-dependent mode I delamination in ballistic composites–Experiment and simulation. *Composite Structures*, *180*, 596–605. https://doi.org/10.1016/j.compstruct.2017.08.045

Rozycki, P. (2017). *Essais expérimentaux sur éprouvettes (sergé 2x2 Verre/PA66 – 50%) - WorkPackage 1* [Internal report, IRT Jules Verne].

Valès, B. (2017). *Développement d'un essai Arcan dynamique* (Doctoral dissertation). Université Paul Sabatier - Toulouse III.

Wang, K., Shriver, D., Banu, M., Jack Hu, S., Xiao, G., Arinez, J., & Fan, H.-T. (2017). Performance prediction for ultrasonic spot welds of short carbon fiber-reinforced composites under shear loading. *Journal of Manufacturing Science and Engineering*, *139*(11). https://doi.org/10.1115/1.4037320

Yasaee, M., Mohamed, G., Pellegrino, A., Petrinic, N., & Hallett, S. R. (2017). Strain rate dependence of mode II delamination resistance in through thickness reinforced laminated composites. *International Journal of Impact Engineering*, *107*, 1–11. https://doi.org/10.1016/j.ijimpeng.2017.05.003

Zhao, T., Palardy, G., Fernandez Villegas, I., Rans, C., Martinez, M., & Benedictus, R. (2017). Mechanical behaviour of thermoplastic composites spot-welded and mechanically fastened joints: A preliminary comparison. *Composites Part B: Engineering*, *112*, 224–234. https://doi.org/10.1016/j.compositesb.2016.12.028

Abbasnezhad, N., Khavandi, A., Fitoussi, J., Arabi, H., Shirinbayan, M., & Tcharkhtchi, A. (2018). Influence of loading conditions on the overall mechanical behavior of polyether-ether-ketone (PEEK). *International Journal of Fatigue*, *109*, 83–92. https://doi.org/10.1016/j.ijfatigue.2017.12.010

Chen, C., Zhang, C., Liu, C., Miao, Y., Wong, S.-C., & Li, Y. (2018). Rate-dependent tensile failure behavior of short fiber reinforced PEEK. *Composites Part B: Engineering*, *136*, 187–196. https://doi.org/10.1016/j.compositesb.2017.10.031

Fabre, V., Quandalle, G., Billon, N., & Cantournet, S. (2018). Time-Temperature-Water content equivalence on dynamic mechanical response of polyamide 6, 6. *Polymer*, *137*, 22–29. https://doi.org/10.1016/j.polymer.2017.10.067

Francesconi, L., & Aymerich, F. (2018). Effect of Z-pinning on the impact resistance of composite laminates with different layups. *Composites Part A: Applied Science and Manufacturing*, *114*, 136–148. https://doi.org/10.1016/j.compositesa.2018.08.013

Koutras, N., Villegas, I. F., & Benedictus, R. (2018). Influence of temperature on the strength of resistance welded glass fibre reinforced PPS joints. *Composites Part A: Applied Science and Manufacturing*, *105*, 57–67. https://doi.org/10.1016/j.compositesa.2017.11.003

Liu, Y., van der Meer, F., & Sluys, L. J. (2018). Cohesive zone and interfacial thick level set modeling of the dynamic double cantilever beam test of composite laminate. *Theoretical and Applied Fracture Mechanics*, *96*, 617–630. https://doi.org/10.1016/j.tafmec.2018.07.004

Machado, J., Gamarra, P.-R., Marques, E., & da Silva, L. F. (2018). Improvement in impact strength of composite joints for the automotive industry. *Composites Part B: Engineering*, *138*, 243–255. https://doi.org/10.1016/j.compositesb.2017.11.038

Machado, J., Marques, E., & da Silva, L. F. (2018). Adhesives and adhesive joints under impact loadings: An overview. *The Journal of adhesion*, *94*(6), 421–452. https://doi.org/10.1080/00218464.2017.1282349

Mbacké, M. A., & Rozycki, P. (2018). Non-linear constitutive law for a glass-pa66 fabric composite dedicated to numerical simulations in crash studies, In *ECCM18-18th European conference on composite materials*.

Oshima, S., Yoshimura, A., Hirano, Y., & Ogasawara, T. (2018). Experimental method for mode I fracture toughness of composite laminates using wedge loaded double cantilever beam specimens. *Composites Part A: Applied Science and Manufacturing*, *112*, 119–125. https://doi.org/10.1016/j.compositesa.2018.05.036

Ponnusami, S. A., Cui, H., Erice, B., Pathan, M. V., & Petrinic, N. (2018). A wedge-DCB test methodology to characterise high rate mode-I interlaminar fracture properties of fibre composites, In *EPJ Web of Conferences*. EDP Sciences.

Réthoré, J. (2018). UFreckles [Language: en]. Zenodo. https://doi.org/10.5281/ZENODO.1433776

Rozycki, P., Mbacke, M. A., & Dau, A. T. (2018). Multiscale Homogenization of a glass-PA66 Fabric Composite Behavior for crash studies, In *ECCM18-18th European Conference on Composite Materials*.

Tutunjian, S., Dannemann, M., Fischer, F., Eroğlu, O., & Modler, N. (2018). A control method for the ultrasonic spot welding of fiber-reinforced thermoplastic laminates through the weld-power time derivative. *Journal of Manufacturing and Materials Processing*, *3*(1), 1. https://doi.org/10.3390/jmmp3010001

Viana, G., Machado, J., Carbas, R., Costa, M., Da Silva, L., Vaz, M., & Banea, M. (2018). Strain rate dependence of adhesive joints for the automotive industry at low and high temperatures. *Journal of adhesion science and Technology*, *32*(19), 2162–2179. https://doi.org/10.1080/01694243.2018.1464635

ABAQUS / Dynamic User's Manual. (2019). Version Version 2019. Providence, RI: Dassault Systèmes Simulia Corp.

Dau, A. T. (2019). *Elaboration d'un outil numérique reliant les échelles micro/méso d'un composite thermoplastique sensible à l'humidité et la température en quasi-statique* (Doctoral dissertation). Ecole centrale de Nantes.

Goto, K., Imai, K., Arai, M., & Ishikawa, T. (2019). Shear and tensile joint strengths of carbon fiber-reinforced thermoplastics using ultrasonic welding. *Composites Part A: Applied Science and Manufacturing*, *116*, 126–137. https://doi.org/10.1016/j.compositesa.2018.10.032

Pivdiablyk, I. (2019). *Durability of mechanical performance of prestressed bolted composite joints in a hygro - thermo - mechanical environment* (These de doctorat). Ecole centrale de Nantes. Retrieved February 19, 2021, from https://www.theses.fr/2019ECDN0068

Rozycki, P., Dau, A. T., & Mbacke, M. A. (2019). Identification du comportement quasi statique avec prise en compte des conditions environnementales d'un composite tissé thermoplastique par homogénéisation numérique, In *21ème Journées Nationales sur les Composites*.

Tao, W., Su, X., Wang, H., Zhang, Z., Li, H., & Chen, J. (2019). Influence mechanism of welding time and energy director to the thermoplastic composite joints by ultrasonic welding. *Journal of Manufacturing Processes*, *37*, 196–202. https://doi.org/10.1016/j.jmapro.2018.11.002

Zhao, T., Rans, C., Villegas, I. F., & Benedictus, R. (2019). On sequential ultrasonic spot welding as an alternative to mechanical fastening in thermoplastic composite assemblies: A study on single-column multi-row single-lap shear joints. *Composites Part A: Applied Science and Manufacturing*, *120*, 1–11. https://doi.org/10.1016/j.compositesa.2019.02.013

Barba, D., Arias, A., & Garcia-Gonzalez, D. (2020). Temperature and strain rate dependences on hardening and softening behaviours in semi-crystalline polymers: Application to PEEK. *International Journal of Solids and Structures*, *182*, 205–217. https://doi.org/10.1016/j.ijsolstr.2019.08.021

Borges, C., Nunes, P., Akhavan-Safar, A., Marques, E., Carbas, R., Alfonso, L., & Silva, L. (2020). A strain rate dependent cohesive zone element for mode I modeling of the fracture behavior of adhesives. *Proceedings of the Institution of Mechanical Engineers, Part L: Journal of Materials: Design and Applications*, *234*(4), 610–621. https://doi.org/10.1177/1464420720904026

Choudhury, M. R., & Debnath, K. (2020). Analysis of tensile failure load of single-lap green composite specimen welded by high-frequency ultrasonic vibration. *Materials Today: Proceedings*, *28*, 739–744. https://doi.org/10.1016/j.matpr.2019.12.290

Ensinger. (2020). *Datasheets : TECAMID 6 natural, TECAMID 66 natural*. https://www.ensingerplastics.com/fr-fr/produits-semi-finis/plastiques/pa66-tecamid-66-natural

Felder, S., Vu, N., Reese, S., & Simon, J.-W. (2020). Modeling the effect of temperature and degree of crystallinity on the mechanical response of Polyamide 6. *Mechanics of materials*, *148*, 103476. https://doi.org/10.1016/j.mechmat.2020.103476

Grefe, H., Kandula, M., & Dilger, K. (2020). Influence of the fibre orientation on the lap shear strength and fracture behaviour of adhesively bonded composite metal joints at high strain rates. *International Journal of Adhesion and Adhesives*, *97*, 102486. https://doi.org/10.1016/j.ijadhadh.2019.102486

Jongbloed, B., Teuwen, J., Benedictus, R., & Villegas, I. F. (2020). On differences and similarities between static and continuous ultrasonic welding of thermoplastic composites. *Composites Part B: Engineering*, *203*, 108466. https://doi.org/10.1016/j.compositesb.2020.108466

Jongbloed, B., Teuwen, J., Palardy, G., Fernandez Villegas, I., & Benedictus, R. (2020). Continuous ultrasonic welding of thermoplastic composites: Enhancing the weld uniformity by changing the energy director. *Journal of Composite Materials*, *54*(15), 2023–2035. https://doi.org/10.1177/0021998319890405

Lemaitre, J., Chaboche, J.-L., Benallal, A., & Desmorat, R. (2020). *Mécanique des matériaux solides-3e éd.* Dunod.

Manterola, J., Renart, J., Zurbitu, J., Turon, A., & Urresti, I. (2020). Mode I fracture characterisation of rigid and flexible bonded joints using an advanced Wedge-Driven Test. *Mechanics of Materials*, *148*, 103534. https://doi.org/10.1016/j.mechmat.2020.103534

May, M., Channammagari, H., & Hahn, P. (2020). High-rate mode II fracture toughness testing of polymer matrix composites–A review. *Composites Part A: Applied Science and Manufacturing*, *137*, 106019. https://doi.org/10.1016/j.compositesa.2020.106019

Pivdiablyk, I., Rozycki, P., Jacquemin, F., Gornet, L., & Auger, S. (2020). Experimental analysis of mechanical performance of glass fibre reinforced polyamide 6 under varying environmental conditions. *Composite Structures*, *245*, 112338. https://doi.org/10.1016/j.compstruct.2020.112338

Ramaswamy, K., O'Higgins, R. M., Kadiyala, A. K., McCarthy, M. A., & McCarthy, C. T. (2020). Evaluation of grit-blasting as a pre-treatment for carbon-fibre thermoplastic composite to aluminium bonded joints tested at static and dynamic loading rates. *Composites Part B: Engineering*, *185*, 107765. https://doi.org/10.1016/j.compositesb.2020.107765

Reis, J. P., de Moura, M., & Samborski, S. (2020). Thermoplastic Composites and Their Promising Applications in Joining and Repair Composites Structures: A Review. *Materials*, *13*(24), 5832. https://doi.org/10.3390/ma13245832

Rohart, V. (2020). *Impact des conditions environnementales sur la performance mécanique de composites thermoplastiques soudés par résistance avec un élément chauffant modifié* (Doctoral dissertation). École de technologie supérieure.

Rohart, V., Lebel, L. L., & Dubé, M. (2020). Effects of environmental conditions on the lap shear strength of resistance-welded carbon fibre/thermoplastic composite joints. *Composites Part B: Engineering*, *198*, 108239. https://doi.org/10.1016/j.compositesb.2020.108239

Tutunjian, S., Dannemann, M., Modler, N., Kucher, M., & Fellermayer, A. (2020). A numerical analysis of the temporal and spatial temperature development during the ultrasonic spot welding of fibre-reinforced thermoplastics. *Journal of Manufacturing and Materials Processing*, *4*(2), 30. https://doi.org/10.3390/jmmp4020030

Aisyah, H., Paridah, M., Sapuan, S., Ilyas, R., Khalina, A., Nurazzi, N., Lee, S., & Lee, C. (2021). A comprehensive review on advanced sustainable woven natural fibre polymer composites. *Polymers*, *13*(3), 471. https://doi.org/10.3390/polym13030471

Fernandez Villegas, I., & Rans, C. (2021). The dangers of single-lap shear testing in understanding polymer composite welded joints. *Philosophical Transactions of the Royal Society A*, *379*(2203), 20200296. https://doi.org/10.1098/rsta.2020.0296

Frederick, H., Li, W., & Palardy, G. (2021). Disassembly study of ultrasonically welded thermoplastic composite joints via resistance heating. *Materials*, *14*(10), 2521. https://doi.org/10.3390/ma14102521

Hsissou, R., Seghiri, R., Benzekri, Z., Hilali, M., Rafik, M., & Elharfi, A. (2021). Polymer composite materials: A comprehensive review. *Composite structures*, *262*, 113640. https://doi.org/10.1016/j.compstruct.2021.113640

Koutras, N., Benedictus, R., & Villegas, I. F. (2021). Thermal effects on the performance of ultrasonically welded CF/PPS joints and its correlation to the degree of crystallinity at the weldline. *Composites Part C: Open Access*, *4*, 100093. https://doi.org/10.1016/j.jcomc.2020.100093

Amedewovo, L., Le Corre, S., Du Plessix, B. d. P., Orgéas, L., & Lévy, A. (2022). Online characterization of fiber-reinforced thermoplastic composite deconsolidation, In *20th European Conference on Composite Materials, ECCM20*.

Bhudolia, S. K., Gohel, G., Vasudevan, D., Leong, K. F., & Gerard, P. (2022). On the mode II fracture toughness, failure, and toughening mechanisms of wholly thermoplastic composites with ultra-lightweight thermoplastic fabrics and innovative Elium® resin. *Composites Part A: Applied Science and Manufacturing*, *161*, 107115. https://doi.org/10.1016/j.compositesa.2022.107115

Zhi, Q., Li, Y., Shu, P., Tan, X., Tan, C., & Liu, Z. (2022). Double-Pulse Ultrasonic Welding of Carbon-Fiber-Reinforced Polyamide 66 Composite. *Polymers*, *14*(4), 714.

Bourda, P., Mbacké, M. A., & Rozycki, P. (2023). Experimental investigation of the loading speed effects on the performances of ultrasonically welded PA66/glass fabric composites. *Composites Part B: Engineering*, 110537.

TEMA Motion 3.4. (n.d.). Image systems. https://imagesystems.se/category/tema/

Appendix A

COPERSIM-Crash dynamic results - RH 50 % and 85 %

The strain rate sensitivity of PA66/GF was also investigated at RH 50 % and RH 85 % during COPERSIM-Crash project. The shear stress-strain curves in Figure A.1 and Figure A.2 exhibit a similar influence of the strain rate as for dry PA66/GF. Stiffening and increase in strength are observed until a threshold about $60\,s^{-1}$, then these quantities are limited due to the seft heating according to the authors. Overall, the fracture strain increases with the strain rate.

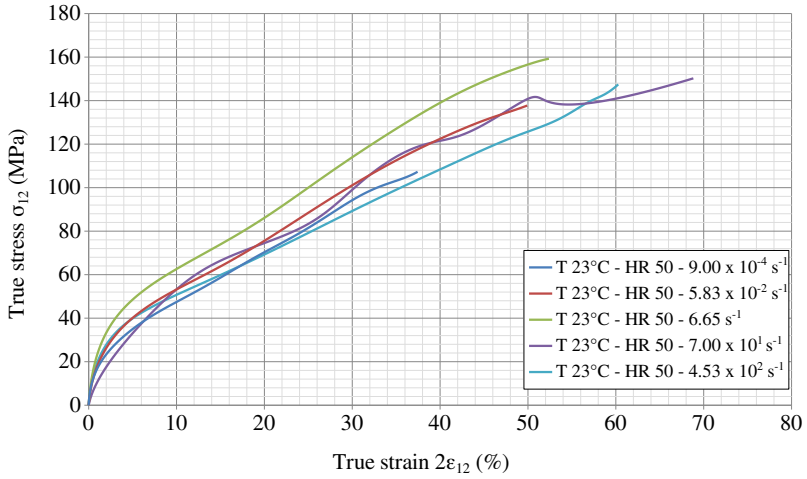

Figure A.1 – Shear behaviour for several strain rates at T 23 °C-RH 50 % (Dau, 2019)

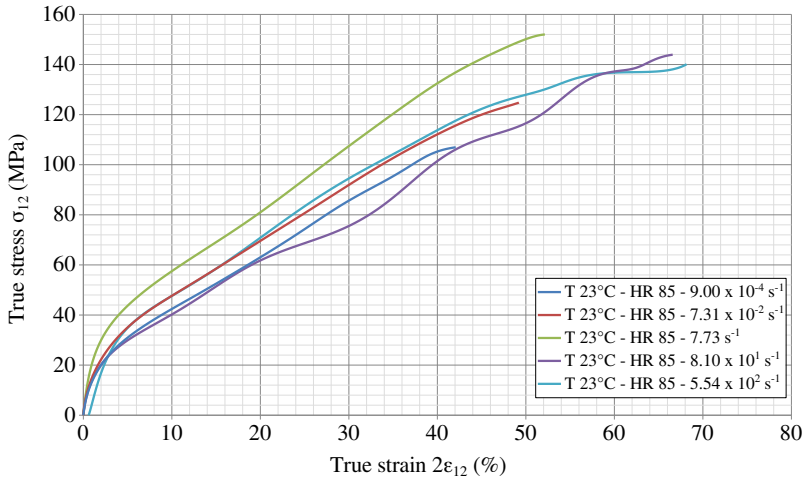

Figure A.2 – Shear behaviour for several strain rates at T 23 °C-RH 85 % (Dau, 2019)

Appendix B

Comparison of COPERSIM-Crash and current PA66/GF shear behaviour

The shear stress-strain curves are compared on four loading speeds: $1.2\,\mathrm{mm\,min^{-1}}$, $2\,\mathrm{mm\,s^{-1}}$, $0.2\,\mathrm{m\,s^{-1}}$ and $2\,\mathrm{m\,s^{-1}}$. For the fifth loading speed, COPERSIM tensile tests were conducted at $10\,\mathrm{m\,s^{-1}}$ which was not possible during the experimental campaign carried out during this thesis and limited to $7\,\mathrm{m\,s^{-1}}$. Therefore, the highest strain rate tested in this work is smaller than in COPERSIM-Crash project ($250\,\mathrm{s^{-1}}$ versus $450\,\mathrm{s^{-1}}$). The fracture of dumbbell-shaped specimens is observed for smaller strain values. It is most likely caused by the fracture occurring near the specimens fillet instead of the effective zone at the specimen's centre. Then, a significantly higher stiffness is noticed for the highest loading speed Figure B.4, which is most likely caused by the lightning used during the test leading to an evolution in the matrix state (from solid to rubbery). The moduli and yield stresses obtained from these tests are presented in Table B.1.

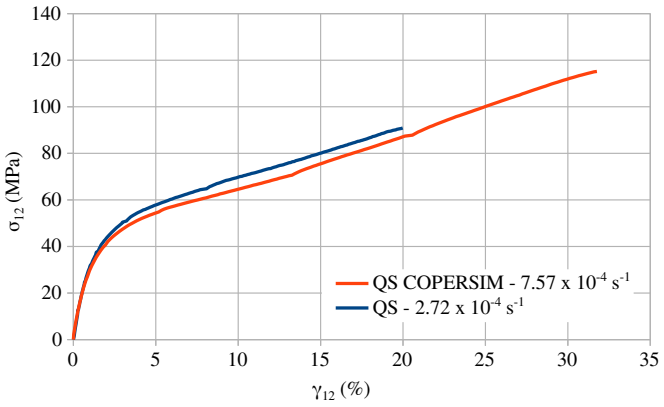

Figure B.1 – Quasi-static shear behaviour of PA66/GF - COPERSIM Crash and current work results

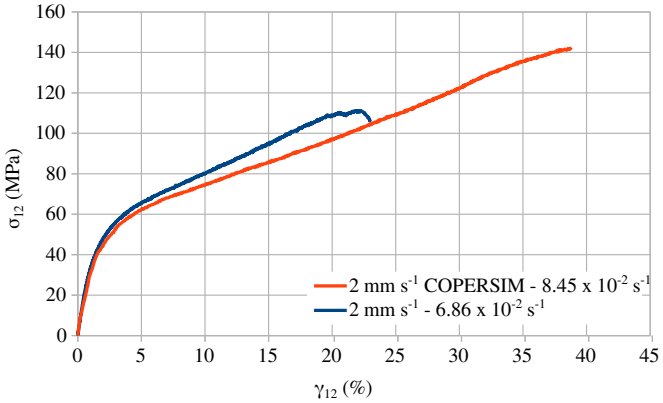

Figure B.2 – $2\,\mathrm{mm\,s^{-1}}$ shear behaviour of PA66/GF - COPERSIM Crash and current work results

Figure B.3 – $200\,\mathrm{mm\,s^{-1}}$ shear behaviour of PA66/GF - COPERSIM Crash and current work results

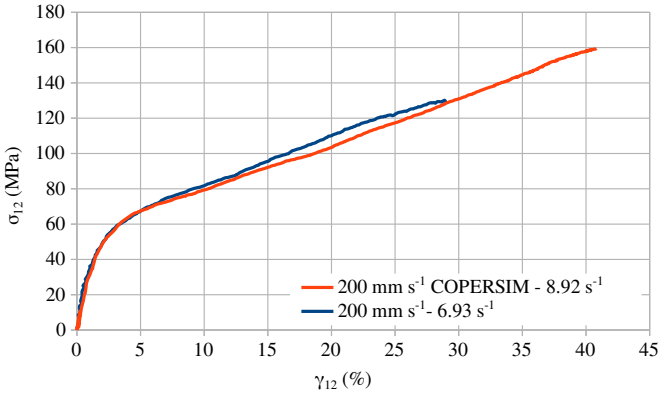

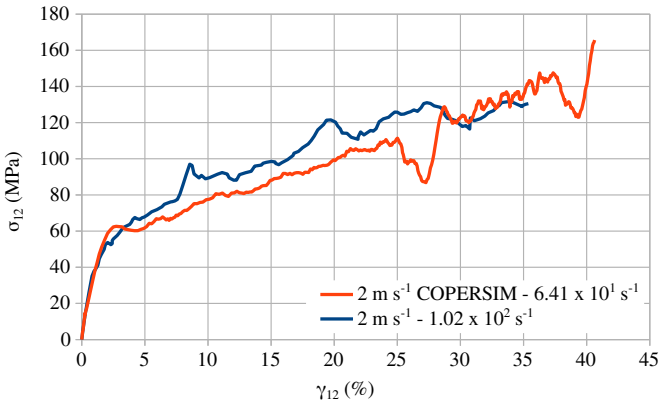

Figure B.4 – $2\,\mathrm{m\,s^{-1}}$ shear behaviour of PA66/GF - COPERSIM Crash and current work results

Figure B.5 – $10\,\mathrm{m\,s^{-1}}$ and $7\,\mathrm{m\,s^{-1}}$ shear behaviour of PA66/GF - COPERSIM Crash and current work results

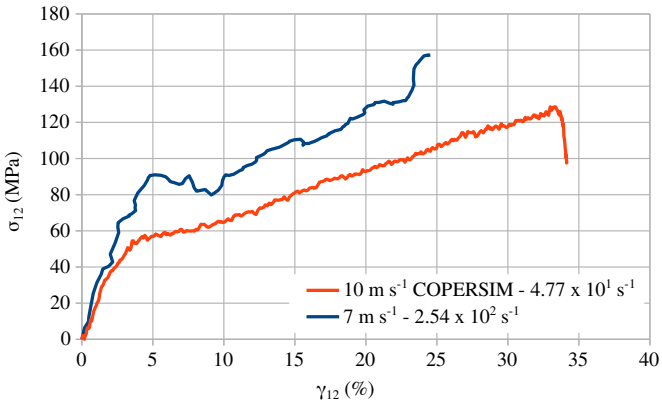

Strain rate ($\mathrm{s^{-1}}$)		Modulus (GPa)		Yield stress (MPa)	
Thesis	COPERSIM	Thesis	COPERSIM	Thesis	COPERSIM
2.74×10^{-4}	8.80×10^{-4}	3.34 ± 0.14	3.25 ± 0.22	27.27 ± 2.10	25.17 ± 0.54
6.86×10^{-2}	9.30×10^{-2}	3.59 ± 0.18	3.26 ± 0.17	26.72 ± 1.86	30.21 ± 0.36
6.93	9.47	3.89 ± 0.68	3.68 ± 0.26	30.34 ± 1.17	34.89 ± 0.20
1.02×10^{2}	5.51×10^{1}	4.14 ± 0.38	1.87 ± 0.22	34.24 ± 1.66	49.86 ± 0.44
2.54×10^{2}	4.33×10^{2}	4.83 ± 0.43	1.80 ± 0.60	36.13 ± 3.57	44.86 ± 0.17

Table B.1 – Shear modulus and yield stress of GF/PA66 at several strain rates

Appendix C

Viscous functions for the PA66/GF VUMAT

Here are presented the several polynomial regression to define the viscous functions for the material from experimental data. Tensile tests were conducted up to $250\,\mathrm{s}^{-1}$ on $45°$-oriented specimens. As a consequence, the viscous functions are set as a constant above this threshold.

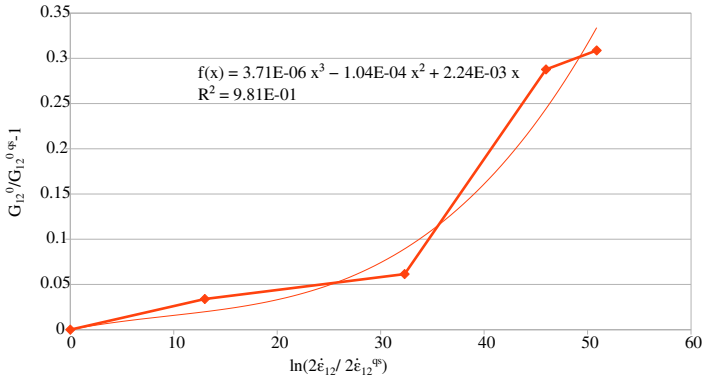

Figure C.1 – Polynomial regression of G_{12}^0

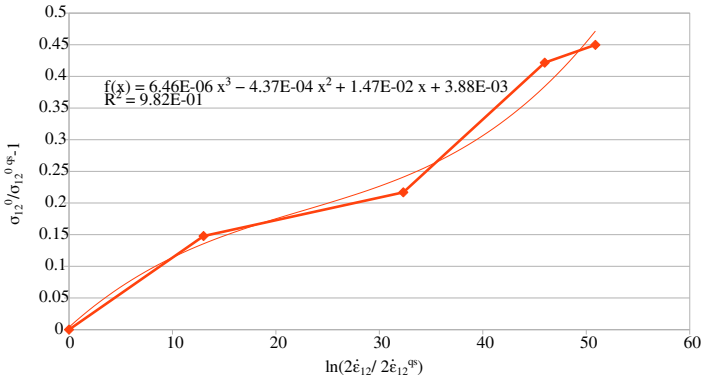

Figure C.2 – Polynomial regression of σ_{12}^0

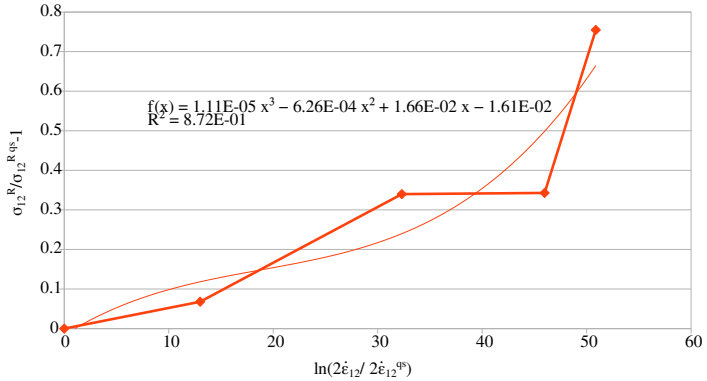

Figure C.3 – Polynomial regression of σ_{12}^R

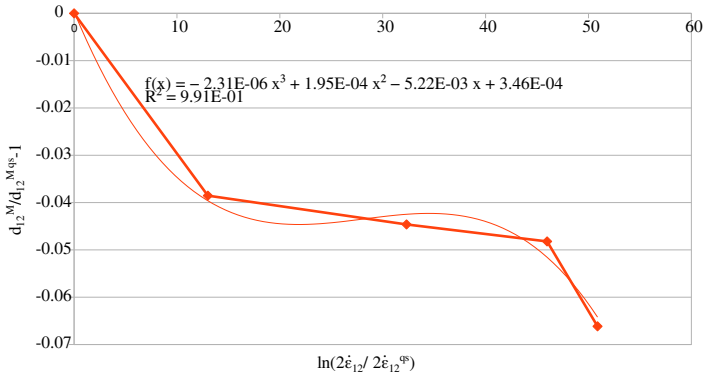

Figure C.4 – Polynomial regression of d_{12}^{M}

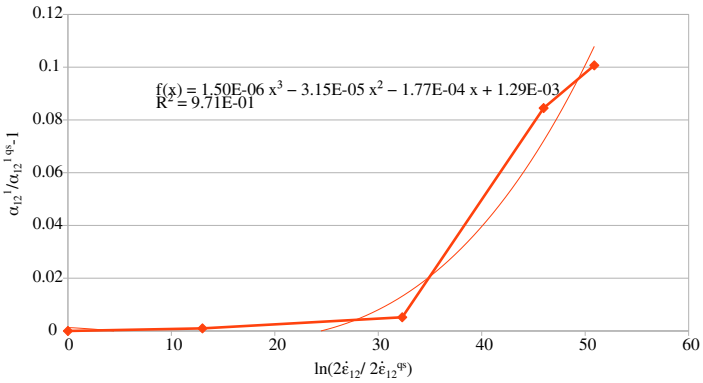

Figure C.5 – Polynomial regression of α_{12}^{1}

Appendix D

Desiccation protocol

Figure D.1 shows the mass loss curves over time for the specimens used for the processing parameters definition. The desorption is conducted at $+90\,°C$ and $6\,mbar$. For the SLJ specimens, the mass loss stabilises after 800 $\sqrt{s}$ (approximately eight days - Figure D.1). It is longer than the stabilisation time observed for the unwelded material during the COPERSIM-Crash project, which was about four days (Figure 2.3). This longer drying time is mostly caused by the greater thickness in the overlap area. A larger thickness leads to an increase in the water diffusion duration through the sample thickness (Figure D.2). Three extra-days of desorption are required to ensure that the mass loss plateau is reached. For the DLJ specimens, moisture loss reaches a maximum after 1216 $\sqrt{s}$ (approximately 17 days) for the three specimens measured. These results show that the desorption time depends on the overlap thickness. A thicker plate needs a longer time for the moisture to diffuse through the thickness.

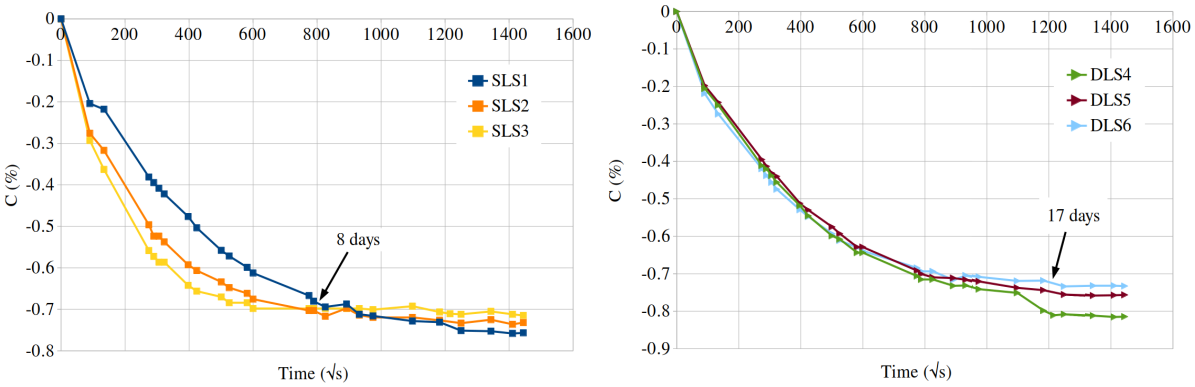

(a) Single Lap Joint specimens

(b) Double Lap Joint specimens

Figure D.1 – Mass loss versus root time curve for development specimens

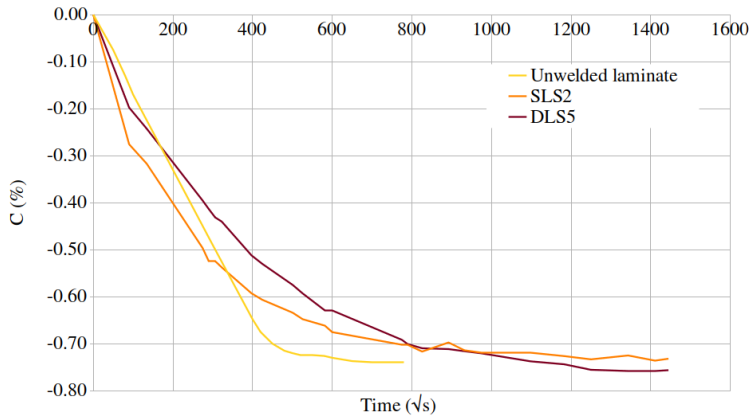

Figure D.2 – Mass loss versus the time for the three specimen types

Finally, the mass loss is plotted versus time divided by the specimen thickness ($4\,\mathrm{mm}$ for SLJs and $6\,\mathrm{mm}$ for DLJs). The evolutions are then similar which means that the desorption duration under vacuum is proportional to the specimen's thickness.

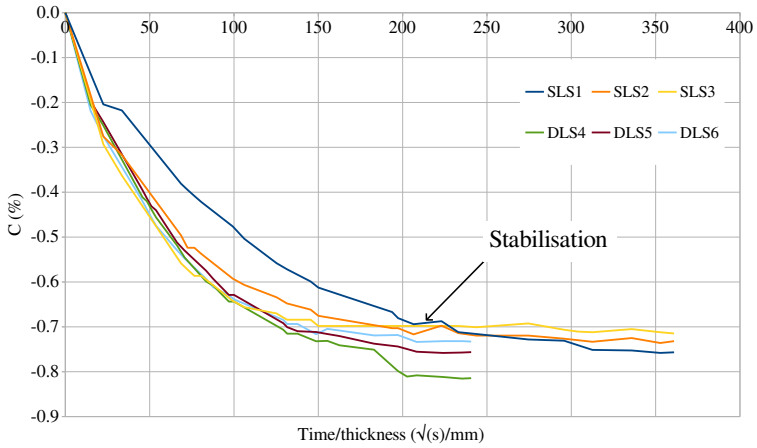

Figure D.3 – Mass loss versus the time divided by the maximum thickness of the specimen

Appendix E

Evaluation of the weld thickness

The thickness of the welds was estimated by measuring the overlap thickness at several points of the overlap. These measurement were carried out on all specimens for experimental characterisation. The average thickness of the substrate is subtracted from these measurements, considering that the laminate thickness was not affected by the welding process (no reduction of substrates' thickness in the overlap); it gives an average value for the welded joint thickness. The laminate thickness was measured on the several specimens tested for the longitudinal and shear characterisation. The average thickness of the laminate is $2.01\,\mathrm{mm}$ for $[45]_4$ laminates and $1.99\,\mathrm{mm}$ for $[0/45]_S$ laminates.

Measurements were conducted on cross-section micrographs for one specimen per configuration to confront results with macroscopical measurements. The joint thickness was measured over the overlap width using ImageJ, and an average value was obtained. Table E.1 presents the values identified with both methods on one specimen for each of the three SLJ configurations. A gap from $2\,\%$ to $5\,\%$ is observed between microscopical and macroscopical values. Therefore, the joint thickness evaluated macroscopically is used for the rest of the study.

	SLJ $[0/45]_S/[0/45]_S$	SLJ $[45]_4/[45]_4$	SLJ $[0/45]_S/[45]_4$
Thickness measured using Image J (mm)	0.094	0.091	0.081
Thickness evaluated from the overlap thickness measurement (mm)	0.089	0.089	0.077

Table E.1 – Measurement of the joint thickness of three specimens using two methods

Appendix F

T-Test for LSS

T-tests were conducted to conclude the significance of the LSS increasing trend observed with the increase in loading speed. The test alternative hypothesis is "The mean LSS in quasi-static is lower than the mean LSS at the loading speed V(i) with V=($2\,\mathrm{mm\,s^{-1}}$, $200\,\mathrm{mm\,s^{-1}}$, $2\,\mathrm{m\,s^{-1}}$ and $7\,\mathrm{m\,s^{-1}}$)". A two-sample t-test was conducted considering unequal variance due to the small number of specimens, and a left-tail test because we are focusing on the fact that the average at V(i) is larger than in QS. The Matlab ttest2 function was used. The null hypothesis is "that the population means (in QS and at V(i)) are equal". P-values are presented in Table F.1.

	SLJ $[0/45]_S/[0/45]_S$	SLJ $[45]_4/[45]_4$	SLJ $[45]_4/[0/45]_S$
$2\,\mathrm{mm\,s^{-1}}$	0.0300	0.1655	0.0785
$200\,\mathrm{mm\,s^{-1}}$	0.9292	0.0589	0.0089
$2\,\mathrm{m\,s^{-1}}$	0.0090	0.4512	0.0346
$7\,\mathrm{m\,s^{-1}}$	0.5982	0.0490	0.0007

Table F.1 – P-values calculated for the three configurations tested and the four crosshead speeds in comparison to quasi-static results

P-value < 0.01: Very strong presumption for the alternative hypothesis.
$0.01 \leq$ P-value < 0.05: Strong presumption for the alternative hypothesis.
$0.05 \leq$ P-value < 0.1: Weak presumption for the alternative hypothesis.
P-value ≥ 0.1: No presumption for the alternative hypothesis.

Appendix G

Influence of TSL parameters on SLJ $[45]_4/[45]_4$ modelling

The SLJ $[45]_4/[45]_4$ tensile behaviour is suitably described using a set of TSL parameters for quasi-static and dynamic loadings. Two other fracture toughnesses were considered for shear modes to evaluate the influence of TSL parameters on the global behaviour ($4000\,\mathrm{J\,m^{-2}}$ and $5500\,\mathrm{J\,m^{-2}}$). Figure G.1 highlights that the TSL shear fracture toughnesses affect the global behaviour of the SLJ despite the significant strain level in the substrates.

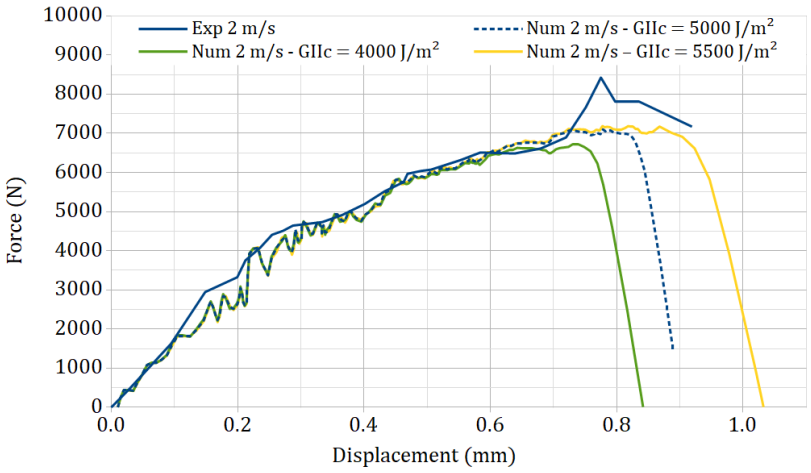

Figure G.1 – F-U curves for SLJ $[45]_4/[45]_4$ at $2\,\mathrm{m\,s^{-1}}$ considering different shear fracture toughnesses

Appendix H

Stresses in the weld of SLJ $[45]_4/[45]_4$

Stress fields in the weld $45°/45°$ are presented for three loading speeds (Figures H.1 and H.2). The stress fields are similar for the three loading speeds presented.

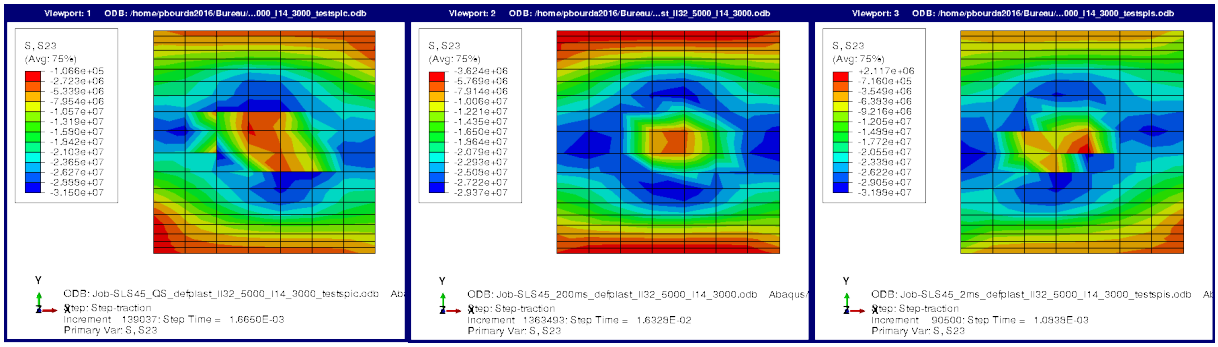

Figure H.1 – Shear stress in the weld for SLJ $[45]_4/[45]_4$ configuration for QS, $200\,\mathrm{mm\,s^{-1}}$ and $2\,\mathrm{m\,s^{-1}}$ loadings

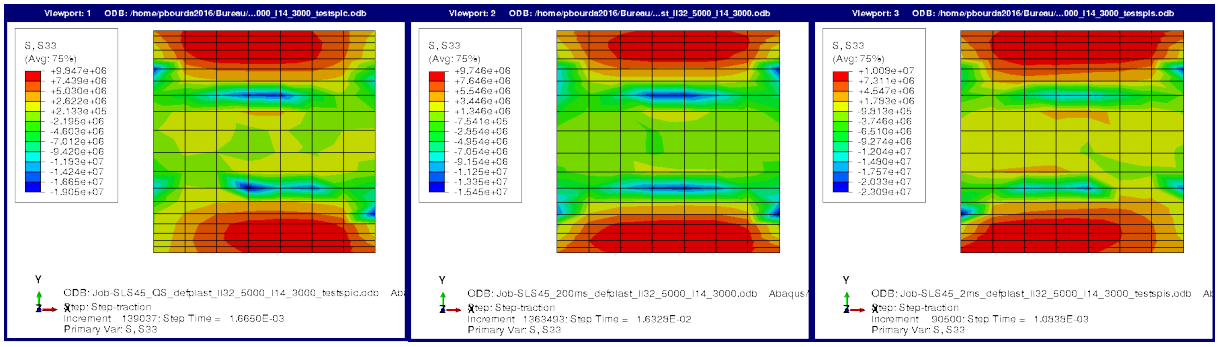

Figure H.2 – Normal stress in the weld for SLJ $[45]_4/[45]_4$ configuration for QS, $200\,\mathrm{mm\,s^{-1}}$ and $2\,\mathrm{m\,s^{-1}}$ loadings

Appendix I

Longitudinal damage for strain rate independent TSL parameters - SLJ $[0/45]_S/[0/45]_S$

The used of QS TSL parameters for the four loading speeds tested leads to a specimen's fracture occurring for a same level of longitudinal damage in the substrates about $12\,\%$ (Figure I.1). These observations are opposed to the results obtained for the weld's configuration $0°/45°$ for which the longitudinal damage was increasing in the substrates (from $11.8\,\%$ to $14.7\,\%$).

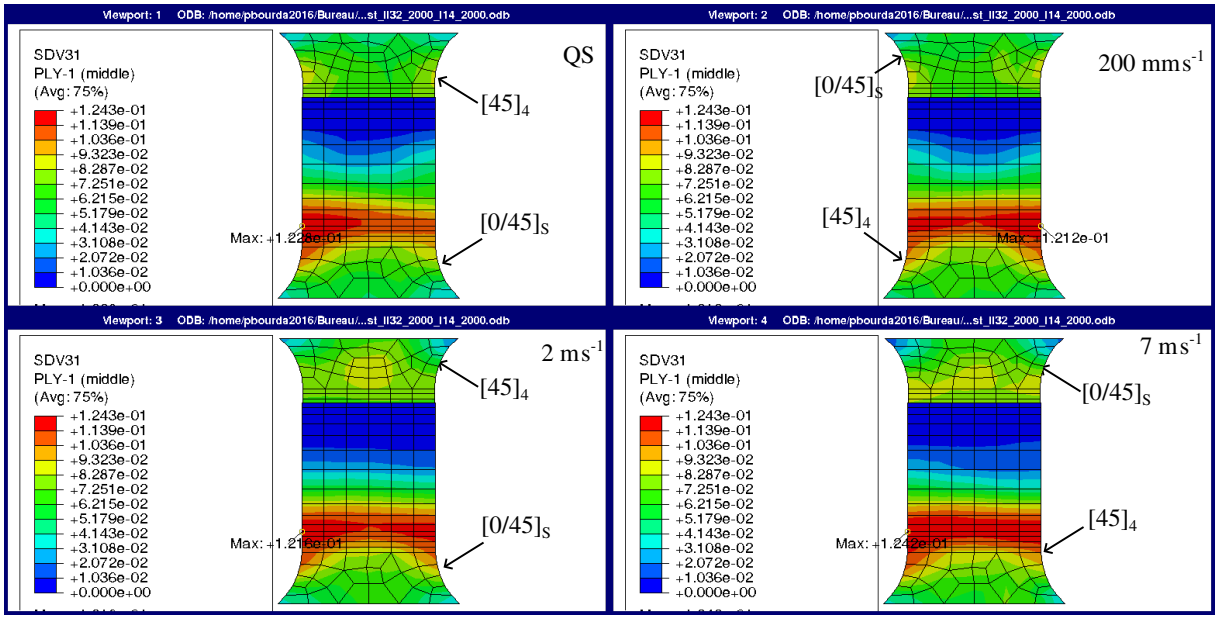

Figure I.1 – Longitudinal damage d_{11} in the substrates - SLJ $[0/45]_S/[0/45]_S$ using QS parameters for four loading speeds

Appendix J

Résumé des travaux de thèse

Ce chapitre constitue un résumé substantiel en français des travaux de thèse. La présentation est faite de façon synthétique avec des références aux figures présentées dans la thèse pour alléger ce résumé. L'introduction, la conclusion et les perspectives sont les seules parties entièrement développées.

J.1 Introduction

L'industrie des transports doit s'adapter au fil du temps aux évolutions sociaux-économiques et environnementales, que ce soit dans le secteur aéronautique, automobile ou naval. Les réglementations imposent des réductions de consommation en carburant des véhicules pour des raisons écologiques. Les constructeurs disposent de différents leviers pour réduire la consommation d'un moyen de transport : améliorer l'efficacité de la motorisation ou encore optimiser et réduire la masse des structures. Ainsi, le recours aux matériaux composites s'est largement développé avec notamment la fabrication de structures en composites thermodurcissables pour l'aviation. Néanmoins, les procédés de fabrications associés à ces matériaux, leurs conditions de stockage ainsi que leur faible recyclabilité ont conduit à élargir le champ d'expertise autour des composites thermoplastiques au cours des vingt dernières années. Ces composites se démarquent par leur résistance élevée à l'impact ainsi que par leurs procédés de fabrication et de mise en forme hors autoclave. Au-delà de la fabrication du composite en tant que telle, de nombreuses études se sont intéressées aux méthodes d'assemblage adaptées pour ces matériaux et particulièrement au soudage. L'assemblage par fusion ou soudage est rendu possible par la capacité des résines thermoplastiques de passer de manière réversible de l'état solide à l'état vitreux/liquide. Les procédés de soudage présentent différents intérêts tels que la rapidité du procédé (de l'ordre de la seconde), la continuité entre les pièces assemblées et la tenue mécanique élevée du joint soudé. Néanmoins, l'application de ce moyen d'assemblage à des structures dans l'industrie des transports nécessite la validation de son comportement mécanique selon diverses conditions environnementales, mais également pour des chargements dynamiques. Les études autour de ces deux phénomènes restent limitées dans la littérature avec quelques études concernant l'influence de la température et de l'humidité. À la connaissance de l'auteur, aucune étude sur l'influence de la vitesse de chargement sur les composites soudés n'a été publiée, et ce, malgré la sensibilité à la vitesse de déformation de plusieurs matrices thermoplastiques. La connaissance du comportement dynamique des joints soudés en composite thermoplastique est nécessaire pour leur application aux pièces structurelles, car ils peuvent être sensibles à la vitesse de déformation. En outre, la modélisation du comportement de la soudure est un outil indispensable à la conception des structures à l'aide de simulations.

Cette thèse a été réalisée en collaboration entre l'Institut de recherche en Génie civil et Mécanique et l'IRT Jules Verne dans le cadre du programme de thèse PERFORM. Les deux verrous scientifiques ayant menés à cette étude sont l'identification et la modélisation de l'influence de la vitesse de déformation et de la température sur le comportement de composite soudé. L'application finale de ces travaux étaient, à l'origine, de modéliser un essai de type impact d'oiseau sur une structure réelle (par exemple peau/raidisseur). Néanmoins, les objectifs de ces travaux ont été reconsidérés du fait du manque de don-

nées expérimentales sur le comportement du composite soudé considéré en quasi-statique ainsi que sur le comportement dynamique du composite non soudé. Cette modification des objectifs permet de réaliser à la fois la caractérisation et la modélisation des composites soudés sur une large plage de vitesse de chargement. Ainsi, l'étude s'est concentrée sur un composite GF/PA66 dont les comportements quasi-statique et dynamique sont connus et modélisés. Les objectifs ont été limités à l'étude expérimentale et numérique de l'influence de la vitesse de déformation sur le composite soudé à température ambiante. Ces travaux contribuent au domaine concerné de par la réalisation d'essais dynamiques sur composite soudé, et l'inclusion de la sensibilité à la vitesse de déformation dans le modèle de comportement de la soudure.

La modélisation du comportement d'un joint soudé sur une large plage de vitesses de déformation nécessite des résultats expérimentaux servant de référence à la définition d'un modèle et à l'identification de ces paramètres. Ainsi, une campagne de caractérisation de GF/PA66 soudé est proposée pour différentes vitesses de chargement, allant de la quasi-statique à des valeurs modérées, en utilisant des éprouvettes de recouvrement. Ces essais expérimentaux fournissent le comportement des structures élémentaires soudées et mettent en évidence l'effet de la vitesse de chargement sur ce comportement. Cependant, ces résultats ne permettent pas l'identification directe du comportement de la soudure. Par la suite, la modélisation de la soudure est faite en utilisant un modèle de zone cohésive et en déterminant des paramètres adaptés par méthode inverse. Cette méthode peut être appliquée du fait de la connaissance et la maitrise du comportement du composite, d'un point de vue expérimental et numérique, en quasi-statique et en dynamique. La dernière étape consiste à inclure la dépendance à la vitesse de déformation dans le modèle constitutif de la soudure et à valider la modélisation.

Le manuscrit est structuré en quatre chapitres pour étudier d'un point de vue expérimental le comportement de joints en composite thermoplastique soudés et de modéliser ce comportement de la quasi-statique à la dynamique.

Le Chapitre 1 constitue l'état de l'art sur les différents domaines abordés dans cette thèse. En premier lieu, les matériaux composites sont présentés de manière générale avec plus de précision sur le comportement des composites thermoplastiques et de leur dépendance à la vitesse de déformation. Les procédés de soudage des composites thermoplastiques sont introduits par la suite. Le soudage par ultrasons est présenté plus en détails, car c'est le procédé utilisé dans ces travaux de recherche. La troisième partie passe en revue les méthodes expérimentales de caractérisation du comportement d'interfaces collées ou interlaminaires pour de large gamme de vitesse de sollicitation et déformation. L'influence de la vitesse de déformation sur ces interfaces est également résumée. Enfin, différentes méthodes de modélisation du comportement des composites et de leurs interfaces en quasi-statique et dynamique sont présentées dans la dernière partie.

Le Chapitre 2 synthétise une partie des résultats de caractérisation du composite GF/PA66 étudié lors du projet COPERSIM Crash. Les comportements longitudinaux et en cisaillement ont été caractérisés pour une large gamme de vitesse de déformation, de température et d'hygrométrie relative. Un modèle de comportement a été développé, implémenté dans une sous-routine VUMAT dans le logiciel Abaqus et validé par rapport au comportement du composite (Mbacké & Rozycki, 2018). Au cours de ces travaux, quelques essais de traction ont été réalisés afin de valider le comportement du matériau identifié précédemment après son stockage durant cinq ans dans un environnement non contrôlé. Tous ces résultats permettent de valider la connaissance suffisante du comportement du composite, ainsi que sa modélisation adaptée pour différentes vitesses de déformation.

Le Chapitre 3 est dédié à la caractérisation du composite soudé. La mesure de grandeurs dans le joint soudé peut se révéler complexe expérimentalement. Ainsi, le choix a été fait de travailler sur le comportement d'une structure soudée, et d'utiliser une méthode inverse pour déterminer le comportement de

la soudure à partir du comportement de la structure. Ce choix repose sur la connaissance du comportement du substrat pour une large gamme de vitesse de déformation. La performance en cisaillement de la soudure est étudiée pour des chargements quasi-statiques ($1.2\,\mathrm{mm\,s^{-1}}$) à dynamiques ($7\,\mathrm{m\,s^{-1}}$) en utilisant des essais de traction sur des éprouvettes de recouvrement. Ces résultats constituent une première étape dans l'étude du comportement dynamique des soudures composites et permettent d'analyser l'évolution des performances et du comportement de la structure soudée en fonction de la vitesse de chargement (Bourda et al., 2023). Une analyse fractographique est également réalisée afin de mieux comprendre les mécanismes de rupture se produisant dans un joint soudé. Enfin, cette caractérisation expérimentale fournit des informations pour la définition d'un modèle de comportement de l'interface soudée : données d'entrée et essais de référence pour la validation du modèle.

Le Chapitre 4 introduit la stratégie de modélisation utilisée pour les éprouvettes soudées et présente son application. L'interface soudée est modélisée par des éléments cohésifs, car le chemin de rupture est connu à l'avance pour se situer au niveau de la soudure. Le modèle de zone cohésive est défini à l'aide d'une loi bilinéaire de traction-séparation dont les paramètres dépendent de la vitesse de déformation (fonctions visqueuses). Les paramètres de la loi constitutive sont identifiés par une méthode inverse sur les essais quasi-statiques, en utilisant les résultats expérimentaux comme référence. Par la suite, des simulations sont effectuées pour des chargements dynamiques afin de valider les paramètres ; en cas d'erreur relative significative entre les essais expérimentaux et les résultats numériques, les paramètres sont ré-identifiés pour la vitesse de chargement considérée. Les fonctions visqueuses décrivant l'évolution des paramètres avec la vitesse de déformation sont ainsi identifiées à partir des résultats numériques à chaque vitesse. Finalement, le comportement dépendant de la vitesse de déformation défini pour la soudure est validé.

Ce mémoire conclue par une synthèse des résultats principaux de ces travaux de recherches sur le comportement dynamique de composite soudé. Ces conclusions sont mises en perspectives avec des études à poursuivre afin d'améliorer et d'approfondir les connaissances sur le comportement de composites thermoplastiques soudés.

J.2 Comportement du composite GF sergé 2×2/PA66

Le composite PA66/GF utilisé dans cette étude a été caractérisé précédemment en quasi-statique et en dynamique, ainsi que pour différentes conditions de température et d'humidité (projet COPERSIM-Crash - Dau, 2019 ; Rozycki et al., 2019). Un modèle de comportement a été défini pour décrire le comportement du pli élémentaire en incluant la sensibilité à la vitesse de déformation. De plus ce modèle a été paramétré et validé pour être utilisé sur une large gamme de température et d'**H**umidité **R**elative (HR) (de $-40\,^{\circ}\mathrm{C}$ à $+80\,^{\circ}\mathrm{C}$ et de HR $0\,\%$ à HR $85\,\%$).

La préparation des éprouvettes pour les essais de caractérisation nécessite le conditionnement des échantillons dans un environnement contrôlé afin de maîtriser l'hygrométrie au sein de la matière. Pour cela, un protocole a été mis en place lors du projet COPERSIM-Crash. Le conditionnement débute par une phase de séchage dans un dessiccateur à $+90\,^{\circ}\mathrm{C}$. Des relevés de masse d'échantillons de référence au cours du séchage a permis d'identifier une durée de 4 jours afin d'atteindre une stabilisation de la masse (Figure 2.3). Les échantillons sont ensuite vieillis dans une chambre climatique, à une température de $+70\,^{\circ}\mathrm{C}$ et une hygrométrie correspondant aux HRs cibles $50\,\%$ et $85\,\%$. D'après les relevés de masse au cours du vieillissement, 14 jours sont nécessaires à la stabilisation de la masse et donc a une saturation de l'absorption d'humidité par l'échantillon (Figure 2.4).

Des essais de traction ont été réalisés au CRED (École Centrale de Nantes) à cinq vitesses de déformation, trois températures et trois hygrométries. Le comportement longitudinal identifié est élastique fragile endommageable (Figure 2.5). La sensibilité à la vitesse de déformation et aux deux conditions

environnementales sont négligeables du fait du comportement des fibres de verre. Le comportement en cisaillement est élasto-plastique visqueux endommageable (Figure 2.7). Un raidissement et une rigidification sont observés avec l'augmentation de la vitesse de déformation. Ce phénomène est observé jusqu'à une vitesse de déformation de $60\,\mathrm{s}^{-1}$, au-delà la raideur diminue. Cela est attribué par Dau (2019) à l'auto-échauffement du matériau à haute vitesse de déformation, ce qui entraine un chargement d'état de la résine au cours de l'essai, de l'état solide à l'état vitreux. De plus, la température et l'hygrométrie ont un effet significatif sur le comportement en cisaillement, conféré par le comportement de la matrice PA66. Lorsque ces conditions augmentent, alors l'écart entre la température d'essai et la température de transition vitreuse (T_g) diminue (Tableau 2.1), ainsi le matériau devient plus ductile avec une raideur initiale plus faible.

Quelques essais de traction ont été réalisés dans le cadre de la thèse afin de vérifier si le stockage du composite pendant cinq ans dans un environnement non contrôlé a modifié ou non le comportement du composite (causé par un vieillissement chimique du polymère, par exemple). Des essais quasi-statiques ont été menés dans la direction longitudinale et pour cinq vitesses de déformation en cisaillement. Contrairement aux essais réalisés dans le cadre du projet COPERSIM-Crash, une éprouvette en forme d'haltère a été utilisée (Figure 2.18) afin de limiter les complications expérimentales liées à l'utilisation de talons, notamment à grande vitesse.

Les essais de traction sur stratifié orienté à $45°$ confirment le comportement élasto-plastique visqueux endommageable du GF/PA66 en cisaillement. Le raidissement, la rigidification et l'augmentation de la contrainte à rupture sont observées jusqu'à $250\,\mathrm{s}^{-1}$. Aucune prévention n'a été faite lors des essais réalisés dans cette thèse afin de limiter l'auto-échauffement dans le matériau au cours de l'essai. Finalement, la perte de raideur observée par Dau (2019) est certainement causée par l'éclairage utilisé lors des essais, entrainant un échauffement du matériau. L'éclairage LED froid utilisé au cours de ces travaux de thèse, ainsi que les distances de travail importantes ont permis de limiter l'échauffement du matériau par des sources extérieures.

La caractérisation expérimentale du composite a ensuite donnée lieu au développement d'un modèle de comportement adapté aux simulations de crash (Mbacké & Rozycki, 2018). Le modèle est basé sur les développements faits au LMT à l'ENS Cachan par (Ladeveze & LeDantec, 1992) pour un composite thermodurcissable (TS) **U**ni-**D**irectionnel (UD). Ce modèle a été étendu pour la dynamique rapide (Rozycki, 2000) et aux composites tissés (Marguet, 2007). Dernièrement, il a également été étendu aux composites **T**hermo**P**lastique (TP) pour différentes température et hygrométries relatives (Mbacké & Rozycki, 2018). La mise en équation du modèle de comportement est présentée dans la Section 2.2 et se base sur une formulation thermodynamique. Ce modèle considère un comportement longitudinal élastique fragile endommageable, dont le comportement peut-être sensible à la vitesse de déformation. Dans la suite de ces travaux, cette orientation est considérée indépendante de la vitesse de déformation [1]. Le comportement en cisaillement est élasto-plastique visqueux endommageable. Un écrouissage isotrope est considérée en introduisant un potentiel de dissipation (Équations 2.16 à 2.18). Concernant l'endommagement, une fonction par morceau est considérée pour relier l'endommagement d_{12} au taux de restitution d'énergie $\overline{Y}_{12}$ (Équation 2.13). La première partie correspond à une évolution logarithmique suivie par une seconde évolution linéaire. Cela permet de décrire l'endommagement sur la grande plage de déformation ainsi que de prendre implicitement en compte la réorientation des fibres au cours de l'essai. Finalement, la viscosité en cisaillement est prise en compte via la définition de fonctions visqueuses faisant évoluer plusieurs paramètres du modèle constitutif selon la vitesse de déformation (Équation 2.19). Des fonctions visqueuses sont définies pour le module de cisaillement, la limite élastique, le taux de restitution d'énergie à rupture et les paramètres de la loi d'évolution de l'endommagement.

1. Idem pour le comportement transverse car le matériau est équilibré.

Le comportement longitudinal identifié aux cours de ces travaux est identique à celui identifié au cours du projet COPERSIM-Crash. Ainsi, les paramètres du modèle de comportement ne sont pas modifiés. Concernant le comportement en cisaillement, certaines différences ont été observées, notamment sur l'évolution du module de cisaillement et de la limite élastique (Figure 2.23). Par conséquent, certains paramètres ont été mis à jour en se basant sur les essais de travaux réalisés au cours de cette thèse. La liste des paramètres modifiés ou non est détaillée dans le Tableau 2.3. Pour conclure, la comparaison du comportement expérimental et numérique d'un VER en cisaillement montre une description adaptée du GF/PA66 en cisaillement jusqu'à une vitesse de déformation de $250\,\mathrm{s}^{-1}$ (Figure 2.25). Il en est de même pour le comportement longitudinal (Figure 2.24).

L'étude expérimentale et numérique du comportement du composite GF/PA66 est essentielle dans ces travaux afin de comprendre au mieux le comportement des structures élémentaires soudées. L'objectif final de cette thèse est l'étude expérimentale et la modélisation du comportement dynamique d'un composite soudé, ainsi toute information sur le comportement du composite seul est valorisable. Le comportement des éprouvettes de recouvrement résulte d'une combinaison entre le comportement des substrats et de la soudure. De plus, le comportement de la soudure ne peut être extrait que numériquement dans ces travaux, ce qui nécessite une modélisation suffisamment complète des substrats pour appliquer une méthode inverse. Les prochaines sections résument la campagne expérimentale sur les éprouvettes soudées puis leur modélisation.

J.3 Caractérisation de composites soudés

Le soudage par ultrasons est une méthode rapide d'assemblage pour les composites thermoplastiques. Un procédé de soudage statique a été utilisé dans ces travaux. Ce procédé consiste à placer les deux substrats à assembler dans un outillage (Figure 3.5), ensuite une sonotrode applique une force sur la zone de recouvrement puis vibre à haute fréquence et faible amplitude jusqu'à atteindre la valeur de consigne (ici en énergie). Ces vibrations entrainent l'échauffement de l'interface par frottement et dissipation visqueuse. La matrice contenue dans les plis proches de l'interface fond, les macromolécules peuvent ainsi diffuser à l'interface puis la soudure est solidifiée dans cet état (Figure 1.14). Pour améliorer le procédé, des lignes de résine pure (PA6 ici) sont intégrées sur un des substrats à assembler, ces éléments sont appelés directeurs d'énergie (Figure 3.4). Leur utilisation permet de concentrer l'énergie de vibration à l'interface afin de faire fondre la résine au niveau de l'interface (dans les substrats et les directeurs d'énergie) et de limiter l'étendue de la zone affectée thermiquement. Cela permet également d'ajouter de la résine entrant en jeu dans le processus d'adhésion et donc de limiter les zones non soudées. Ensuite la solidification du joint se fait sous pression de la sonotrode pour limiter la décohésion.

Trois configurations de simple recouvrement sont étudiées : $[0/45]_S/[0/45]_S$, $[45]_4/[45]_4$ et $[0/45]_S/[45]_4$. Deux configurations de double recouvrement sont testées : $[0/45]_S/[0/45]_S/[0/45]_S$ et $[45]_4/[45]_4/[45]_4$. Ces différentes configurations permettent de déterminer l'influence de la raideur des substrats et de l'orientation locale du pli en contact avec la soudure sur le comportement de l'éprouvette soudée. Une courte étude a été menée pour définir une énergie de soudure cible pour le procédé appliqué aux éprouvettes de caractérisation. Des éprouvettes ont été testées avec trois niveaux d'énergie différents, puis un essai de traction est réalisé sur chaque éprouvette. Pour les éprouvettes de simple recouvrement, une énergie de $650\,\mathrm{J}$ est choisie car elle permet d'atteindre un niveau d'adhésion élevée sur l'ensemble du recouvrement. Pour les doubles recouvrements, les deux interfaces sont soudées l'une après l'autre. Ainsi, un niveau d'énergie est fixé par soudure (Tableau 3.4). Les niveaux sont choisis de manière que la rupture se situe dans les interfaces et non dans le substrat interne (Figure 3.11).

La tenue mécanique des soudures et l'influence de la vitesse de chargement sur le comportement du GF/PA66 soudé sont étudiées à l'aide d'essais de traction sur des éprouvettes de simple et double recouvrement (Figure 3.3). Ces essais permettent l'étude du comportement du composite soudé respectivement sous sollicitation mixte mode I+II (ouverture normale + cisaillement) et en mode II quasi-pur. Les essais ont été réalisés à cinq vitesses différentes : $1.2\,\mathrm{mm\,min^{-1}}$, $2\,\mathrm{mm\,s^{-1}}$, $200\,\mathrm{mm\,s^{-1}}$, $2\,\mathrm{m\,s^{-1}}$ and $7\,\mathrm{m\,s^{-1}}$. Les conditions d'essais sont la température ambiante (T 23 °C) et l'état sec (HR 0 %). Pour cela, un protocole de désorption a été appliqué à toutes les éprouvettes avant la réalisation des essais, puis elles sont stockées dans des sachets quatre couches scellés par soudure pour éviter la reprise hydrique. Concernant la réalisation des essais, un système d'attache bride/goujon a été utilisé pour s'adapter à la géométrie en haltère des éprouvettes (Figure 3.15). Ce système permet de bloquer le glissement de l'éprouvette dans les mors, notamment à grande vitesse. Un mouchetis est réalisé sur les échantillons avant les essais pour accéder aux champs de déplacements/déformations en utilisant la corrélation par images. Les essais sont filmés avec des caméras rapides (Photron type SA1, AX). La force de réaction est quant à elle mesurée par la cellule force de la machine. Plusieurs éléments sont analysés afin d'obtenir une vue globale sur le comportement du GF/PA66 soudé et de l'influence de la vitesse de chargement sur ce comportement. D'une part, les échantillons sont observés avant les essais de traction (aspect externe et coupe transversale d'un échantillon par configuration) et les interfaces post-mortem sont observées dans le but d'étudier les types de rupture. D'un point de vue plus quantitatif, les courbes force-déplacement et la tenue mécanique sont étudiées.

L'observation macroscopique et microscopique de coupes transversales d'éprouvettes soudées met en avant le mélange des résines entre la soudure et la matrice des substrats (Figure 3.24). Néanmoins, le procédé de soudage peut conduire à la formation de porosités dans les substrats, surtout à proximité des bords du recouvrement, mais aussi dans la soudure (Figure 3.25). Ces porosités peuvent être formées à cause de la présence d'humidité dans le matériaux, mais aussi par les contraintes résiduelles libérées lors du procédé de soudage (passage de l'état solide à vitreux) (Shi et al., 2013 ; Amedewovo et al., 2022). L'épaisseur moyenne du joint soudé est évaluée à $2.39 \times 10^{-5}\,\mathrm{m}$, d'après les observations microscopiques associées à des mesures macroscopiques.

Une étude fractographique des éprouvettes post-mortem a permis de mettre en avant quatre types de rupture rencontrés au cours de la campagne expérimentale : la décohésion fibre/matrice associée à la rupture de matrice (FMD/cohésive), la rupture mixte adhésive + FMD/cohésive, la rupture mixte délaminage + FMD/cohésive et pour finir la rupture adhésive (Figure 3.28). Ces différents types de rupture sont liés aux degrés d'adhésion atteints au niveau de l'interface entre le directeur d'énergie et les substrats. La présence de porosité dans la soudure ou à l'interface entre la soudure et un substrat peut entrainer une rupture adhésive. D'autre part, les porosités localisées dans les substrats au niveau des zones interlaminaires peuvent conduire à une rupture par délaminage. La rupture par FMD/cohésive correspond au plus haut niveau de performance de la soudure atteinte dans cette étude et dans la littérature en général. Le faciès de rupture peut être découpé en deux zones : une première sur laquelle des fibres mises à nu sont visibles, et une deuxième plus riche en résine avec l'empreinte de fibres visibles (Figure 3.29). Ces observations permettent de supposer que l'amorce de la fissure se situe au niveau des bords libres du recouvrement, à l'interface entre le renfort fibreux d'un substrat et la zone riche en résine (Figure 3.30).

Les essais de traction réalisés à cinq niveaux de vitesse sont analysés avec les courbes force-déplacement (courbe FU) et la tenue mécanique des éprouvettes (LSS - Force maximale divisée par la surface de soudure). Les résultats principaux ressortant de la caractérisation expérimentale du composite soudé sont les suivants.

— La tenue mécanique est proportionnelle à l'étendue de la surface de rupture de type FMD/cohésive.
— La tenue mécanique des éprouvettes de simple recouvrement augmente avec la vitesse de déformation pour les trois configurations testées : $+11.2\,\%$ pour le SLJ $[45]_4/[45]_4$, $+22.9\,\%$ pour le SLJ $[45]_4/[0/45]_S$ et $+18.2\,\%$ pour le SLJ $[0/45]_S/[0/45]_S$.
— La raideur des configurations SLJ $[45]_4/[45]_4$ et SLJ $[45]_4/[0/45]_S$ augmentent avec la vitesse de chargement.
— Des niveaux de déformation élevés sont atteints dans les substrats $[45]_4$ en dehors de la zone soudée - $5\,\%$ à $12\,\%$. Le matériau n'est donc plus dans une zone d'élasticité pure, ainsi la phase de modélisation requière la prise en compte des phénomènes irréversibles dans les substrats (Figure 3.46).

La viscosité observée pour les éprouvettes de simple recouvrement est causée par le caractère visqueux des matrices PA66 et PA6. L'augmentation de la contrainte à rupture et de la raideur en cisaillement du GF/PA66 contribue à l'augmentation de la tenue mécanique de la structure soudée sous sollicitation dynamique. De plus, le caractère visqueux du PA6 peut également jouer sur le comportement de la soudure. L'étude fractographique a mis en avant l'importance de la décohésion fibre/matrice dans le mécanisme de rupture de l'interface. Par conséquent, l'adhésion fibre/matrice est un élément important dans le comportement de l'assemblage soudé. Plusieurs études ont montré un lien entre l'augmentation de la contrainte à rupture pour des essais de traction dans le plan sur un stratifié et l'augmentation de la tenue interfaciale. La contrainte à rupture en cisaillement du GF/PA66 augmente avec la vitesse de chargement, ainsi, il peut être supposé que la tenue interfaciale est aussi améliorée en dynamique. Ce phénomène est une troisième source d'accroissement du LSS pour des chargements dynamiques. Ces résultats corroborent les observations de Koutras et al. (2018) sur l'influence de la température sur le comportement de CF/PPS soudé. Par ailleurs, le raidissement observé pour les structures contenant un substrat $[45]_4$ est engendré par le raidissement du GF/PA66 en cisaillement. Finalement, la viscosité du PA66 et PA6 contribue à la dépendance à la vitesse de chargement des éprouvettes testées dans ces travaux à travers les substrats, la soudure et les différentes interfaces. Néanmoins, le poids de chacune de ces influences sur le comportement global ne peut pas être quantifié expérimentalement à partir des essais réalisés, car les mesures dans le joint soudé sont particulièrement complexes. Par conséquent, les comportements des substrats et de la soudure vont être découplés numériquement à partir des résultats expérimentaux sur le composite et sur les éprouvettes soudées. Les paramètres d'un modèle de comportement de la soudure peuvent ainsi être déterminés par méthode inverse. Ces résultats permettront de quantifier la dépendance à la vitesse de déformation nécessaire dans le modèle de comportement de la soudure.

Quelques difficultés ont été rencontrées pour les éprouvettes de double recouvrement. Pour certaines éprouvettes, la rupture de la première interface est intervenue très rapidement au cours de l'essai de traction à cause d'une différence significative de niveau d'adhésion entre les deux interfaces. Néanmoins, l'étude de la tenue mécanique de ces éprouvettes montre que pour la configuration $[45]_4/[45]_4/[45]_4$, des niveaux similaires à ceux pour les éprouvettes de simple recouvrement sont obtenus. La tenue mécanique augmente avec la vitesse de chargement. Pour la configuration $[0/45]_S/[0/45]_S/[0/45]_S$, une plus grande variabilité est observée dans la qualité des soudures. Ainsi, les conclusions émises à partir des résultats sur les éprouvettes de simple recouvrement ne peuvent pas être confirmées sur la configuration de double recouvrement.

La campagne expérimentale menée sur le GF/PA66 soudé permet de mettre en avant l'influence de la vitesse de chargement sur le comportement et la performance des structures soudées. Cependant, tels quels, ces résultats ne permettent pas de quantifier l'influence des substrats et de la soudure sur le com-

portement global. Ainsi, les résultats expérimentaux servent de base pour la modélisation numérique des assemblages soudés. Un modèle de comportement est établi pour la soudure dans la suite de ces travaux. Les paramètres de ce modèle sont déterminés par comparaison et minimisation des écarts entre résultats numériques et expérimentaux. Initialement, les résultats sur les éprouvettes de double recouvrement devaient être utilisés pour définir le comportement de l'interface en cisaillement pur, puis les éprouvettes de simple recouvrement devaient permettre la définition de la mixité des modes et du mode I. La variabilité des résultats sur les éprouvettes de double recouvrement ne permet pas l'application de ce protocole, ainsi les paramètres du modèle constitutif de l'interface sont définis uniquement à partir des résultats sur éprouvettes de simple recouvrement. La modélisation est résumée dans la section suivante.

J.4 Modélisation numérique du comportement de joint soudé

Une modélisation du comportement du joint soudé est proposée en utilisant un modèle de zone cohésive. L'éprouvette de simple recouvrement est modélisée en utilisant le modèle de comportement présenté précédemment pour les substrats (Figure 4.1). La couche d'éléments cohésifs représentant la soudure est liée de part et d'autre aux substrats avec une contrainte rigide de type 'tie' (les déplacements et rotations sont contraintes à celles des substrats dans la zone correspondante). Des conditions aux limites en déplacements sont appliquées de part et d'autre de l'éprouvette de simple recouvrement. Ces déplacements sont extraits par corrélation d'images à partir des essais expérimentaux pour appliquer le même chargement qu'expérimentalement, et ainsi charger les éprouvettes numériques à la même vitesse (Figure 4.2). Par conséquent, seuls les paramètres de la loi cohésive sont inconnus dans le modèle, ainsi ils sont déterminés par méthode inverse. Pour cela, une fonction d'optimisation a été utilisée avec le logiciel Matlab ('Particle Swarm optimisation'). Des bornes maximales et minimales sont définies pour les paramètres à identifier en se basant sur des données issues de la littérature. La fonction objectif à minimiser quantifie l'écart entre les courbes FU numérique et expérimentale au sens des moindres carrés. Quatre paramètres (contraintes d'initiation de l'endommagement et énergies de rupture) doivent être déterminés à partir des essais de simple recouvrement, et la fonction d'optimisation choisie ici n'est pas suffisamment restrictive, ainsi quelques simulations sont réalisées manuellement pour finaliser l'identification des paramètres.

La loi de traction-séparation décrivant le comportement de la soudure a été implémentée dans une subroutine VUMAT. La loi choisie est disponible dans Abaqus, cependant une sensibilité à la vitesse de déformation des différents paramètres de la loi a été ajoutée dans le modèle implémenté au cours de ces travaux de thèse. Cette loi relie la contrainte au saut de déplacement entre les deux faces d'un élément cohésif (Figure 4.5). Une loi bilinéaire est considérée dans ces travaux avec une interaction entre les modes (Figure 4.6). Pour cela, un critère quadratique sur la traction défini l'initiation de l'endommagement en mode mixte (Équation 4.8), et l'énergie de rupture en mode mixte est spécifiée par le critère Benzeggagh-Kenane (Gong & Benzeggagh, 1995 ; Benzeggagh & Kenane, 1996) (Équation 4.11). Toutes les équations du modèle de comportement sont détaillées dans la section 4.2.1. La sensibilité à la vitesse de déformation est intégrée via des fonctions visqueuses (Équation 4.21). Ces fonctions font évoluer les propriétés de la loi de comportement selon la vitesse de déformation atteinte. Les paramètres de la loi évoluent selon la vitesse de déformation transitoire tant que l'endommagement n'est pas initié dans l'élément (Figure 4.7). Une fois l'endommagement non nul, la loi de traction-séparation est figée jusqu'à la rupture de l'élément.

En pratique, les paramètres de la loi de traction-séparation sont déterminés par méthode inverse en utilisant une fonction d'optimisation sur l'essai quasi-statique. Le jeu de paramètre minimisant l'écart entre les courbes FU numérique et expérimental est retenu. Ces paramètres quasi-statiques sont par la

suite utilisés pour simuler un essai dynamique. Si l'écart avec l'expérimental est trop grand (plus de $10\,\%$ d'écart relatif sur la tenue mécanique), alors un nouveau jeu de paramètres est déterminé pour se rapprocher des résultats expérimentaux à la vitesse considérée. Enfin, si nécessaire, des fonctions visqueuses sont définies à partir des différents paramètres obtenus pour chaque vitesse de chargement. Les paramètres ayant été déterminés pour les cinq vitesses de chargement, il est possible de déterminer une loi d'évolution de ces paramètres selon la vitesse de déformation dans la soudure.

La définition des paramètres de la loi de comportement se base sur des données macroscopiques (courbes FU et tenue mécanique). De là, plusieurs quantités à l'échelle mésoscopique sont étudiées afin de valider la cohérence de la modélisation en se basant sur des données plus locales. La comparaison des vitesses de déformation dans les substrats, en-dehors de la zone soudée, montre que les résultats numériques sont globalement proches des résultats expérimentaux. Les champs de contrainte dans la soudure, inaccessibles expérimentalement, sont cohérents avec les observations faites dans la littérature.

Finalement, les résultats principaux ressortant de la modélisation du comportement du joint soudé sont les suivants.

- La loi de traction-séparation bilinéaire est adaptée pour modéliser le comportement des soudures considérées dans ces travaux en quasi-statique et dynamique.
- La modélisation du caractère visqueux du GF/PA66 en cisaillement est nécessaire pour modéliser correctement le comportement des éprouvettes soudées. Le raidissement et la rigidification observés pour les configurations SLJs $[0/45]_S/[45]_4$ and $[45]_4/[45]_4$ sont représentés correctement en considérant uniquement la viscosité des substrats en cisaillement.
- Il est nécessaire de considérer un comportement visqueux pour la soudure $0°/0°$ afin de réduire l'écart relatif avec les résultats expérimentaux.
- Les niveaux de déformation et d'endommagement des substrats sont non négligeables : l'endommagement en cisaillement diminue dans les substrats $[45]_4$ avec l'augmentation de la vitesse de chargement pour les configurations $45°/45°$ et $45°/0°$, tandis que l'endommagement longitudinal augmente pour les configurations $45°/0°$ et $0°/0°$ (si prise en compte de la viscosité de l'interface pour cette dernière configuration).

Les résultats numériques mettent en avant une différence entre les soudures étudiées. D'un côté, les soudures $45°/45°$ et $45°/0°$ pour lesquelles un modèle de comportement de la soudure indépendant de la vitesse de déformation est suffisant. De l'autre, la soudure $0°/0°$ pour laquelle un modèle dépendant de la vitesse de déformation permet de réduire significativement l'écart avec les résultats expérimentaux. Cette différence est certainement causée par la faible épaisseur du joint soudé devant l'épaisseur du pli, et ce associé à la similitude du module du joint soudé et du module de cisaillement du GF/PA66. Ces deux éléments entraineraient une prise en compte implicite de la viscosité de la soudure via la loi de comportement en cisaillement du substrat, pour les configurations $45°/45°$ et $45°/0°$. Cependant, la différence de raideur entre les plis environnants et la soudure est importante pour la configuration $0°/0°$. De plus, les plis orientés à $0°$ ne sont pas sensibles à la vitesse de déformation. Ces deux éléments semblent alors forcer la nécessité de prendre en compte le comportement visqueux de la résine dans le modèle de comportement de la soudure.

Des simulations sur éprouvettes de double recouvrement ont montré la nécessité d'utiliser un substrat interne d'épaisseur double afin de localiser la concentration de contrainte dans les soudures et donc observer une rupture des interfaces de type FMD/cohésive. Malgré l'impossibilité de déterminer les propriétés d'interface en cisaillement à partir des essais expérimentaux de double recouvrement (variabilité dans la qualité d'interface trop importante), les simulations numériques montrent une raideur initiale cohérente avec l'expérimental (en utilisant les paramètres déterminés sur les éprouvettes de simple recouvrement).

J.5 Conclusions et perspectives

Conclusions générales

Malgré les recherches approfondies sur le soudage des composites thermoplastiques, son application potentielle aux structures dans l'industrie du transport nécessite encore de connaître et de contrôler le comportement des structures assemblées afin de garantir leur intégrité. En outre, les structures peuvent être soumises à des chargements dynamiques, comme des chutes d'outils ou des impacts. De plus, plusieurs matrices thermoplastiques sont connues pour leur comportement dépendant de la vitesse de déformation, tout comme les interfaces telles que les zones inter-plis (délaminage) ou le comportement des adhésifs. Par conséquent, le comportement dynamique des composites soudés doit être connu pour déterminer dans quelle mesure la vitesse de déformation affecte le comportement du joint soudé. Enfin, la modélisation du comportement de la soudure peut être utilisée pour prédire le comportement des structures soudées sous divers chargements, quasi-statiques ou dynamiques. Dans ce contexte, cette thèse de doctorat a eu pour objectif :

1. d'étudier le comportement des structures soudées,
2. d'identifier l'influence de la vitesse de déformation sur le comportement du joint soudé et
3. de définir un modèle numérique pour la soudure validé pour des chargements quasi-statiques à dynamiques.

Ces travaux ont nécessité la caractérisation de composite soudé pour une large plage de vitesses de chargement. Les difficultés liées aux mesures de quantités dans les joints soudés ont conduit à l'étude de structures élémentaires. Des essais de traction sur éprouvettes de simple et double recouvrement ont été menés afin de proposer une méthode de caractérisation relativement simple en dynamique. Les résultats d'essais permettent de statuer sur la sensibilité du GF/PA66 soudé à la vitesse de chargement. Néanmoins, le comportement du substrat et celui de la soudure ne peuvent être séparés facilement d'un point de vue purement expérimental. Par conséquent, les comportements sont séparés numériquement. Pour ce faire, le comportement des substrats a été identifié, dans un premier temps, à partir d'essais conventionnels sur le matériau composite à diverses vitesses de déformation. Ces résultats permettent de définir et d'identifier un modèle de comportement pour le composite. De là, le comportement des soudures peut être identifié en utilisant une analyse inverse sur les essais de recouvrement et en considérant le modèle, connu et maîtrisé, défini pour les substrats. L'identification et la validation du modèle de comportement de la soudure pour des essais dynamiques permet de déterminer si l'ajout de dépendance à la vitesse de déformation est nécessaire ou non. Si la viscosité est requise, alors l'identification des paramètres du modèle de comportement est utilisée pour définir la dépendance à la vitesse du modèle.

Le comportement du GF/PA66 a été caractérisé pour diverses vitesses de déformation, températures et humidités relatives. Ces résultats du projet COPERSIM-Crash ont mis en évidence l'effet négligeable de ces paramètres sur le comportement longitudinal causé par la faible sensibilité du comportement des fibres de verre. Ils montrent également la sensibilité à la vitesse de déformation et aux paramètres environnementaux du comportement en cisaillement. Les essais de traction réalisés aux cours de ces travaux de thèse, à température ambiante et à l'état sec, confirment le comportement visqueux du GF/PA66 en cisaillement, hérité du comportement de la matrice PA66. Le comportement élasto-plastique visqueux endommageable a été identifié jusqu'à $250\,\mathrm{s}^{-1}$ et il a été utilisé pour paramétrer le modèle de comportement développé précédemment pour ce composite (Mbacké & Rozycki, 2018). Concernant le comportement longitudinal, un comportement élastique fragile endommageable a été identifié et retenu afin de décrire

le plus correctement possible la raideur courante du matériau, ce paramètre influant sur le comportement des échantillons soudés. La comparaison des résultats numériques et expérimentaux sur le volume élémentaire de référence démontre la précision du modèle.

Les structures soudées ont été caractérisées à l'aide d'éprouvettes de simple et double recouvrement, compte tenu du comportement connu et contrôlé du GF/PA66. Trois configurations de simple recouvrement ont été considérées ($[45]_4/[45]_4$, $[0/45]_S/[0/45]_S$ et $[0/45]_S/[45]_4$) et deux configurations de double recouvrement ($[45]_4/[45]_4/[45]_4$ et $[0/45]_S/[0/45]_S/[0/45]_S$). Les essais sont réalisés à température ambiante et à l'état sec, pour cinq vitesses de chargement (de $1.2\,\mathrm{mm\,min^{-1}}$ à $7\,\mathrm{m\,s^{-1}}$). Des résultats significatifs proviennent de cette campagne expérimentale et contribuent à l'amélioration de la compréhension des composites soudés.

— La performance en cisaillement du GF/PA66 soudé (LSS) augmente avec la vitesse de chargement pour les trois configurations d'éprouvette de simple recouvrement testées.
— Un raidissement est observé pour les structures composées d'au moins un substrat $[45]_4$.
— La performance des structures soudées est fortement liée à la raideur des substrats, avec notamment une tenue mécanique plus importante et un accroissement de la performance plus grand pour les substrats les plus rigides.
— L'étude fractographique a mis en avant la rupture de type décohésion fibre/matrice associée à la rupture de matrice pour les éprouvettes soudées les plus performantes.

La dépendance à la vitesse de chargement du GF/PA66 soudé est causée par la viscosité des matrices PA66 et du PA6 affectant le comportement du substrat et de la soudure (raidissement, rigidification, augmentation de la tenue interfaciale). La ductilité en cisaillement du stratifié et sa dépendance à la vitesse de déformation jouent sur le comportement global de la structure soudée. Tous ces éléments soulignent l'importance du rôle de la matrice et de l'adhésion entre les fibres et la matrice sur la performance des joints soudés. Les observations et conclusions expérimentales constituent une étape importante pour la compréhension du comportement dynamique du GF/PA66 soudé. La dépendance à la vitesse de chargement observée est engendrée par le comportement des substrats et de la soudure ; cependant, le poids de chaque sensibilité sur le comportement de la structure ne peut pas être quantifié expérimentalement.

Une loi de traction-séparation sensible à la vitesse de déformation a été implémentée dans une sous-routine VUMAT pour modéliser le comportement de la soudure en utilisant un modèle de zone cohésive. La modélisation numérique est réalisée par application d'une méthode inverse pour déterminer les paramètres du modèle pour les différentes soudures étudiées (soudure entre les plis $45°/45°$ pour un SLJ $[45]_4/[45]_4$, $0°/0°$ pour un SLJ $[0/45]_S/[0/45]_S$ et $45°/0°$ pour un SLJ $[45]_4/[0/45]_S$). Les résultats mettent en évidence la nécessité de considérer le comportement élastoplatique visqueux endommageable en cisaillement dans le modèle de comportement du GF/PA66. En effet, cette propriété permet à elle seule de décrire la dépendance à la vitesse de chargement du comportement des éprouvettes de simple recouvrement $[45]_4/[45]_4$ et $[45]_4/[0/45]_S$. Ainsi, aucune sensibilité à la vitesse de déformation n'est requise pour les lois de traction-séparation décrivant le comportement des soudures $45°/45°$ et $45°/0°$. Concernant la troisième configuration de soudure ($0°/0°$), une loi de traction-séparation sensible à la vitesse de déformation est nécessaire pour décrire correctement les comportements quasi-statique et dynamique de l'éprouvette considérée. Des fonctions visqueuses permettent de décrire avec succès l'évolution des paramètres (ténacités) de la loi de traction-séparation avec la vitesse de déformation. La sensibilité à la vitesse d'une seule configuration de soudure testée parmi les trois peut s'expliquer par l'épaisseur des joints soudés, faible devant l'épaisseur d'un pli, et par la différence de raideur entre la soudure et les plis avoisinants la soudure. En effet, les configurations ayant une similitude entre la raideur de la soudure et d'un ou des deux plis environnants ne nécessite pas de loi de traction-séparation dépendante à la

vitesse de déformation. Du fait de la très faible épaisseur de la soudure, la viscosité du matériau constituant la soudure semble être prise en compte implicitement via le modèle de comportement du substrat (visqueux en cisaillement). Néanmoins, la différence de raideur à l'interface pour la soudure $0°/0°$, associée à l'absence de viscosité du comportement longitudinal du GF/PA66, semblent forcer l'ajout de dépendance à la vitesse de déformation dans le modèle de comportement de la soudure.

Perspectives de ces travaux de recherche

Les résultats de cette étude constituent un aperçu du comportement dynamique de structures soudées en composite thermoplastique. Ces observations et analyses sont intéressantes pour le développement et l'application du soudage ultrasons à des pièces de structures pour l'industrie des transports. Néanmoins, différents éléments restent à étudier pour approfondir les connaissances sur le comportement des composites soudés.

Les essais de traction employés dans ces travaux de recherche ne sont pas des essais de mode pur. Ainsi, l'identification des différents paramètres de la loi de traction-séparation (contraintes d'initiation de l'endommagement, ténacité, mixité des modes) ont dû être déterminées à partir d'un seul type d'essai. Des essais additionnels doivent donc être réalisés au moins sur une deuxième géométrie (objectif initial des essais sur les éprouvettes de double recouvrement), afin d'améliorer l'identification des paramètres à partir d'essai en mode pur ou quasi-pur puis en mode mixte. Les essais de pur mode I pourraient être fait à l'aide d'essais de traction sur éprouvette en croix (Goto et al., 2019) ou sur des éprouvettes en double U (Morin, 2010; Argoud et al., 2016). Ces essais nécessiteraient l'adaptation des équipements pour les chargements dynamiques. Cependant, la mise en œuvre de ces essais (notamment pour l'éprouvette en croix) est difficile, surtout au niveau des méthodes de mesure utilisées et de leur exploitation à des fins de modélisation. Le découplage des modes expérimentalement est également intéressant afin de mieux comprendre la nécessité de considérer un modèle sensible à la vitesse de déformation uniquement pour la soudure $0°/0°$.

Une des conclusions majeures de cette étude est l'indépendance à la vitesse de déformation des lois de traction-séparation des soudures $0°/45°$ et $45°/45°$, malgré la viscosité du PA6. Les suppositions principales expliquant ce phénomène sont d'une part la faible épaisseur du joint soudé par rapport à un pli, d'autre part la raideur similaire entre ces deux éléments. Par conséquent, la sensibilité à la vitesse de déformation de la matrice serait prise en compte implicitement dans le modèle de comportement des plis adjacents, dont le comportement en cisaillement est visqueux. Néanmoins, ces observations sont valident sur l'épaisseur étudiée ici $(2.39 \times 10^{-5}\,\mathrm{m})$, ce qui est nettement inférieur à l'épaisseur du pli $(0.5 \times 10^{-3}\,\mathrm{m})$. Il serait intéressant d'étudier des joints de soudure plus épais (dans la limite des caractéristiques du procédé de soudage) afin de déterminer si la viscosité du substrat est encore suffisante pour décrire le comportement des SLJ dans ces conditions. La même étude peut être menée pour des épaisseurs plus faibles, notamment pour la soudure $0°/0°$, afin d'établir la nécessité ou non de considérer le caractère visqueux dans la loi de traction-séparation.

Les structures en composite sous chargement dynamique peuvent rompre dans les zones d'assemblage mais également par délaminage. L'ajout de la rupture interlaminaire permettrait de compléter le modèle pour une structure soudée. De plus, le joint soudé obtenu est, dans une certaine mesure, proche d'une zone interlaminaire. Par conséquent, la comparaison des performances d'une soudure avec le comportement en délaminage du composite (co-consolidation ou pièce d'épaisseur double) vaut la peine d'être étudiée. Ces résultats permettraient de trancher sur la nécessité de distinguer la modélisation d'une soudure et du délaminage.

D'un autre point de vue numérique, le temps de calcul pourrait être amélioré en utilisant par exemple des éléments autres que les éléments cohésifs. Ces derniers réduisent considérablement le pas de temps critique pour des simulations de dynamique/Explicite. Leur utilisation reste acceptable au niveau recherche sur des éprouvettes élémentaires, cependant le temps de calcul augmenterait considérablement pour une structure industrielle. Par conséquent, l'inclusion du modèle de comportement de la soudure dans des éléments différents des éléments cohésifs pourrait diminuer le temps de calcul. Enfin, la prise en compte des variabilités dans l'étendu de la surface soudée sur le comportement de la soudure serait intéressant pour limiter les modifications de géométrie. Cela pourrait se faire via des fonctions d'évolution des paramètres du modèle selon la surface soudée.

Finalement, la dernière perspective principale est l'étude de l'influence de l'humidité relative sur le comportement de la soudure. Les campagnes d'essais réalisées lors du projet COPERSIM-Crash ont mis en lumière une sensibilité à la vitesse de déformation d'autant plus importante à des niveaux d'humidité de $50\,\%$ et $85\,\%$ (Dau, 2019). Peu d'études se sont intéressées à l'influence de l'hygrométrie sur le comportement d'un composite soudé. L'influence est négligeable pour un CF/PSS d'après Rohart et al. (2020) ; cependant, l'absorption d'humidité d'un PPS est très faible par rapport aux polyamides. Ainsi, l'étude menée aux cours de cette thèse pourraient être menée pour un niveau d'humidité plus grand mais aussi à une température plus élevée. La sensibilité à la vitesse étant plus importante pour ces conditions environnementales, il pourrait donc être nécessaire de considérer un modèle de comportement de la soudure sensible à la vitesse de déformation quelle que soit la configuration.

COLLEGE SCIENCES
DOCTORAL DE L'INGENIERIE
PAYS DE LA LOIRE ET DES SYSTEMES

CENTRALE NANTES

Titre : Caractérisation expérimentale et modélisation numérique du comportement de l'assemblage de structures composites thermoplastiques soudées de la quasi-statique à la dynamique

Mot clés : Composite thermoplastique, soudage ultrasons, chargements dynamiques, éléments cohésifs

Résumé : Le recours aux composites thermoplastiques est grandissant dans l'industrie des transports. Le soudage se distingue comme une méthode d'assemblage rapide pour ces matériaux, créant une continuité entre les pièces assemblées et offrant une tenue mécanique élevée. Son application aux structures dans le secteur des transports peut néanmoins poser des questions quant aux chargements dynamiques combinés à la sensibilité à la vitesse de déformation de diverses matrices thermoplastiques. Malgré l'étendu de la littérature sur le soudage de composites, aucune étude sur la sensibilité à la vitesse de déformation n'a été trouvée. Les objectifs de cette thèse sont d'étudier le comportement d'un composite (GF/PA66 tissé) soudé pour des chargements quasi-statique et dynamique d'un point de vue expérimental et de proposer un modèle de comportement valide sur la plage de vitesses considérées.

La méthode employée repose sur la connaissance du comportement quasi-statique et dynamique des substrats, expérimentalement et numériquement. L'influence de la vitesse de chargement sur le composite soudé est étudiée à l'aide d'essais de traction sur des éprouvettes de recouvrement, en quasi-statique et à vitesse modérées de chargement. L'influence de la vitesse de déformation sur la soudure ne peut pas être tranchée expérimentalement, car le comportement des éprouvettes mêle les comportements de la soudure et des substrats. Ainsi, les comportements sont découplés numériquement en utilisant un modèle élasto-plastique endommageable visqueux pour le stratifié et une loi de traction-séparation pour la soudure (éléments cohésifs). La loi cohésive est identifiée en quasi-statique puis appliquée aux essais dynamiques. Le modèle final, pouvant inclure de la viscosité, est validé de la quasi-statique à la dynamique, permettant de conclure sur la nécessité ou non d'inclure des fonctions de viscosité pour décrire le comportement des soudures.

Title: Experimental characterisation and numerical modelling of the assembly of welded thermoplastic composite structures' behaviour from quasi-static to dynamic

Keywords: Thermoplastic composites, ultrasonic welding, dynamic loadings, cohesive elements

Abstract: Thermoplastic composites utilisation is increasing in the transport industry. Welding is a fast joining method for these materials, creating continuity between the assembled parts and offering high mechanical strength. However, its application to transport structures can raise questions due to the dynamic loading that may occur and the strain rate sensitivity of various thermoplastic matrices. Despite the extensive literature on composite welding, no studies have been found on the strain rate sensitivity of welds. This thesis aims to study the behaviour of a welded composite (GF/PA66 fabric) for quasi-static and dynamic loadings from an experimental point of view and propose a numerical model of the welded zone, including strain rate sensitivity.

The methodology is based on an accurate knowledge of the substrates' behaviour for an extensive strain rate range, both experimentally and numerically. The welded composite time dependency is investigated from quasi-static until moderate loading speeds using tensile tests on lap joint specimens. The strain rate dependence of the weld is difficult to quantify experimentally since the sample behaviour combines the behaviours of the weld and the substrates. Therefore, a numerical uncoupling is achieved using a viscous elastoplastic damage model for the substrates and a traction separation law for the weld (cohesive elements). The cohesive law is identified in quasi-static and then applied to dynamic tests. The final model, which may include viscosity, is validated from quasi-static to dynamic, allowing conclusions on whether or not viscous functions are necessary to describe the behaviour of the welds.